



**HAL**  
open science

# Corrosion inhibition of galvanized steel by LDH - inhibitor hybrids: Mechanisms of Inhibitor Release and Corrosion Reactions

Viacheslav Shkirskiy

► **To cite this version:**

Viacheslav Shkirskiy. Corrosion inhibition of galvanized steel by LDH - inhibitor hybrids: Mechanisms of Inhibitor Release and Corrosion Reactions. Chemical Physics [physics.chem-ph]. Université Pierre et Marie Curie - Paris VI, 2015. English. NNT: 2015PA066216 . tel-01230884

**HAL Id: tel-01230884**

**<https://theses.hal.science/tel-01230884>**

Submitted on 19 Nov 2015

**HAL** is a multi-disciplinary open access archive for the deposit and dissemination of scientific research documents, whether they are published or not. The documents may come from teaching and research institutions in France or abroad, or from public or private research centers.

L'archive ouverte pluridisciplinaire **HAL**, est destinée au dépôt et à la diffusion de documents scientifiques de niveau recherche, publiés ou non, émanant des établissements d'enseignement et de recherche français ou étrangers, des laboratoires publics ou privés.



**PROJET DE THÈSE DE DOCTORAT DE  
L'UNIVERSITÉ PIERRE ET MARIE CURIE**

Spécialité

Chimie Physique et Chimie Analytique

Présentée par

**Viacheslav SHKIRSKIY**

Pour obtenir le grade de

**DOCTEUR de l'UNIVERSITÉ PIERRE ET MARIE CURIE**

Sujet de la thèse:

**Corrosion inhibition of galvanized steel by LDH – inhibitor hybrids:  
Mechanisms of Inhibitor Release and Corrosion Reactions**

soutenue le 24 septembre 2015

devant le jury composé de: (préciser la qualité de chacun des membres).

P. Volovitch	Maître de conférences (HDR) à ChimieParistech	Directeur de thèse
K. Ogle	Professeur à Chimie Paristech	Co-directeur de thèse
M. Rohwerder	Professeur de recherche à Max-Planck institute	Rapporteur
B. Vuillemin	Professeur à Université de Bourgogne	Rapporteur
P. Keil	Chercheur à BASF	Examineur
V. Vivier	Directeur de recherche au CNRS	Examineur
N. McMurray	Professeur à Swansea university	Examineur



*“La dernière chose qu’on trouve en laissant un ouvrage est de savoir celle qu’il faut  
mettre la première.”*

*“The last thing one discovers in composing a work is what to put first.”*

*“Лишь в конце работы мы обычно узнаём, с чего её нужно было начать.”*

Blaise Pascal (Pensées, Section 1, 19)



---

# Curriculum vitae

---

## Viacheslav SHKIRSKIY

### PERSONAL DATA

---

PLACE AND DATE OF BIRTH: Karpilovka, Russia | 14 June 1990  
ADDRESS: 11 rue Pierre et Marie Curie, 75005 Paris  
WEB-SITE: [www.shkirskiy.org](http://www.shkirskiy.org)  
EMAIL: [viacheslav@shkirskiy.com](mailto:viacheslav@shkirskiy.com)

### EDUCATION

---

2012-2015 PhD in Physical and Analytical chemistry (**diploma with honors**)  
*University Pierre et Marie Curie (UMPC)*, Paris,  
UMR-CNRS Chimie ParisTech 8247

2007-2012 Bachelor+Master programme (**M. Sc. diploma with honours**)  
in Chemistry, *Lomonosov Moscow State University*, Moscow

2005-2007 BacS (**diploma with honours**), secondary school diploma,  
equivalent to A level, *Puskin Bryansk Public Lyceum №1*,  
*class of Physics and Mathematics*, Bryansk

### SCIENTIFIC INTERNSHIPS

---

MARCH-  
MAY 2012 Master internship, *Chimie ParisTech*, Paris

2007-2012 Scientific works in physical, organic, analytical and inorganic  
chemistry laboratories *Lomonosov Moscow State University*, Moscow.

---

## PROFESSIONAL ACTIVITY

---

2014-2015     **Teaching assistant**  
Practical Works in physical and analytical chemistry, level L3,  
Chimie ParisTech, Paris.

2014-  
PRESENT     **Reviewer** for Electrochimica Acta and ChemElectroChem

## RELEVANT SKILLS

---

**ANALYTICAL TECHNIQUES:** stationary and non-stationary electrochemical techniques (potentiodynamic and potentiostatic polarization, EIS), analytical chemistry spectroscopic techniques (ICP-OES, UV-Vis Spectroscopy), quantification of element release (immersion test, weight loss measurement), surface analytical techniques (SEM, XPS).

**PROPERTIES AND PHENOMENA:** corrosion mechanisms, corrosion inhibitors, passivity, interaction electrolyte species and material.

**PERSONAL ACHIEVEMENTS:** electrochemical flow cell development, species distribution modelling, design of experiments.

**SOFTWARE TOOLS:** MS Office, Matlab, Origin, Latex, Basic knowledge of C/C++ and Python

## LANGUAGES

---

**ENGLISH:** C1 level  
**FRENCH:** B1 level  
**RUSSIAN:** mother tongue

---

# Acknowledgements

---

Three years of my PhD thesis have given me an immeasurable scientific and life experience. I have significantly evolved during this time and I know that without the great help and support of many people my doctoral thesis would not be possible.

Firstly, I would like to express my sincere gratitude to my advisor Polina Volovitch for the continuous support of my PhD study and related research, for her patience, motivation, and immense knowledge. Thank you for your guidance and at the same time liberty that you gave me. You were always there for me, even if it meant redacting manuscripts together at the lab until midnight. I would also like to thank my co-advisor Kevin Ogle for his insightful comments and encouragement. Thank you for sharing my passion for the chess and for teaching me numerous power point tips and tricks. I would like to thank you both for the hard questions, which incited me to widen my research from various perspectives.

I would also like to thank BASF Coatings GmbH for the financial support of this work. My sincere gratitude goes to Horst Hintze-Bruening and Patrick Keil, especially for agreeing to be a member of the jury committee. I was glad to collaborate with the laboratory of Université Blaise Pascal in Clermont-Ferrand, especially with Fabrice Leroux, Thomas Stimpfling and Pierre Vialat. Thank you all for the fruitful discussions during our meetings and supplying various materials for the aim of the work. Without your precious support it would not be possible to conduct this research.

I also thank Michael Rohwerder and Bruno Vuillemin for kindly agreeing to evaluate this work as reviewers. I would like to thank Neil McMurray and Vincent Vivier for agreeing to participate in my thesis committee.

I am grateful to Patrick Chapon from Horiba Jobin Yvon, François Brisset and Diana Dragoë from Institut de Chimie Moléculaire et des Matériaux d'Orsay, and Grégory Lefèvre from Chimie ParisTech who always opened their labs for me to use GD-OES, SEM, XPS and ATR-IR instruments, helped with the processing and interpretation of data and gave the information on the instrumentations.

I would also like to thank Nick Birbilis for his endless energy, enthusiasm and open mind and especially for the re-thinking the words “nebulizer”, “monochromator”, “le”, “convolution” and the significance of the upper two dots.

---

I also want to say thanks to Michel Cassir, the director of our group, Armelle Ringuede, Virginie Lair and Valerie Albin, who welcomed and helped me since my first days at the lab. I would also like to thank the secretaries: Elisabeth Brochet, Sylvie Gandziarski and Marie-José Michel, as well as the secretary of doctoral school Soobrayen Koonavadee for their help with administrative procedures, which were never trivial to me, and their patience regarding my French language skills.

My warm thanks go to Marion, Deborah and Peng for sharing the office with me, making hard days easier with jokes and fun that we had and for endless discussions about similarities between Russian and French: our list of words will be only longer! Life at the lab would not be so good without Hazem Mubarak and Oumaïma Gharbi with their readiness to teach me Arabic, shukran jazīlan! Regarding my language skills, my Ukrainian still needs improvement, Katya, Denis and Tanya thank you for initializing it, дякую. Apart from linguistic lessons, I will not forget the wave-board master classes by Kirill in pauses between his beam-times.

I do not know a more patient person than Noémie, who spent so much of her time reading some of my raw manuscripts and fighting me with German thoroughness to prove her point, thank you for that! My gratitude goes to Oxana, for translating some parts of this thesis to French, even if she understood nothing in a chemical blah-blah. I also wish to thank Maria and Sophie, who helped me a lot with the AESEC instrumentation and patiently answered all my questions on the first and the most difficult steps of learning this technique. Of course, many thanks to my lab-mates not mentioned yet: Mattheu, Rémi, Zuzana, Sveta, Alina, Shadi, Emna, Arturo, Amandine, Mohamed, Fatima, Stéphanie, Cédrik, François, Marcelle, Bing Bing, Hao, . . . for the good spirits you make prevail at work.

I would like to unconditionally thank my parents Zoya and Vitaliy for their support even when I did not listen to their wise advises and of course my sister Pepun for enduring all my sarcastic jokes and saving my spirit.

Finally, I would like to thank my beloved Nastëna for her stoical patience during redaction of this PhD thesis, for re-reading it, for guidance in LaTeX and Python. Thank you for your odessian sense of humor, the emotional support and encouraging my crazy hobbies - Solomon is just the beginning! Спасибо большое!

---

# Notation

---

$M(n)$	oxidation state $n$ of element M in an ion where $n$ can be I, II, etc
$M^n$	oxidation state $n$ of ion M where $n$ can be +1, -1, etc
$X$	variable
$\mathbf{X}$	vector of variable $X$
$E$	electrical potential
$E^0$	standard $E$
$E_{oc}$	$E$ at open circuit
$j_e$	total current measured by potentiostat
$j_e^*$	convoluted $j_e$
$j_{Zn}$	Zn current corresponded to formation of soluble Zn cations measured by AESEC
$j_{Zn}^{ins}$	Zn current corresponded to formation of insoluble Zn oxides
$j_{Zn}^{**}$	deconvoluted $j_{Zn}$
$j_c^*$	cathodic current calculated as $j_e^* - j_{Zn}$
$j_c^{**}$	cathodic current calculated as $j_e - j_{Zn}^{**}$
$j_{partial}$	$j_{Zn}$ or $j_c$
$j_{corr}$	corrosion current
$j_{corr}^E$	corrosion current estimated by the direct measurement of $j_{Zn}^{**}$ from polarization curves at $E(j_e = 0)$
$j_{corr}^{ET}$	corrosion current estimated by Tafel extrapolation of $j_e$ to $E(j_e = 0)$
$j_{corr}^{AESEC}$	corrosion current estimated from Stern Geary relation
$j_{corr}^{SG}$	corrosion current estimated from Zn dissolution under open circuit
$b_a$	anodic Tafel slope
$b_c$	cathodic Tafel slope
$C$	capacitance
$C_x$	concentration of $x$ specie
$C_x^f$	formal concentration of $x$ specie
$C_x^r$	residual concentration of $x$ specie
$\varepsilon$	conversion of a chemical process
$G_x^0$	standard Gibbs free energy of $x$ process

---

$a_x$	activity of $x$ species
$K_x$	equilibrium constant of $x$ process
$\theta$	surface coverage
$\eta$	inhibition efficiency
$n$	number of electrons in electrochemical reactions
$Q_X$	quantity of $X$
$F$	Faradays constant
$A$	surface of working electrode
$v_X$	rate of dissolution of specie X
$v_X^s$	steady state rate of $v_X$
$z$	value of charge of ion
$t$	time
$T$	temperature
$t_c$	time constant
$w$	frequency of AC perturbation
$f_e$	flow rate of electrolyte in the feed capillary
$f_s$	flows of substance
$A$	surface area
$T$	temperature
$R_x$	resistance of $x$ element
$Re$	Reynolds number
$i$	input discrete signal
$i^*$	output discrete signal
$i^{**}$	deconvoluted $i^*$ signal
$h(t)$	transfer function or residence time distribution
$\beta$ and $\tau$	parameters of $h$
$\delta$	interface thickness
$\rho$	density
$c$	the speed of light
$E_n$	energy level $n$
$h$	Planck constant
$n_n$	initial population of electrons
$N$	total population of considered ionization state
$g_n$	statistical weight of considered level
$k$	Boltzmann constant
$\lambda$	wavelength
$E^e$	excitation energy
$P$	probability of possible transitions per unite of time
$Z$	partition function
$S$	slope of calibration curve
$I$	corrosion current estimated from Zn dissolution under open circuit

---

$u$	velocity
$p$	pressure
$\nu$	kinematic viscosity
$L$	characteristic length of fluid
$D$	diffusion coefficient
$R$	universal gas constant
$s_i$	stoichiometric coefficient of specie $i$
$J_i$	flux of $i$ specie
$\mu$	electrochemical potential
$\mu^0$	standard electrochemical potential
$k$	kinetic constant
$V$	volume



---

## List of acronyms

---

AESEC	atomic emission spectroelectrochemistry
ICP-AES	inductively coupled plasma atomic emission spectrometer
LDH	layered double hydroxide
OCP	open circuit potential
SHE	standard hydrogen electrode
SHE	saturated calomel electrode
PP	primarily prepared
RSH	L-cysteine
RSSR	L-cystine
IE	inhibition efficiency
HDG	hot dip galvanized steel
CRS	cold rolled steel
SST	salt spray test
ORR	oxygen reduction reaction
HER	hydrogen reduction reaction
WE	working electrode
EIS	electrochemical impedance spectroscopy
XPS	X-ray photoelectron spectroscopy
XRD	X-ray powder diffraction
SEM	scanning electron microscopy

---

EDX	energy-dispersive X-ray spectroscopy
GD-OES	glow discharge optical emission spectrometer
ICP-MS	inductively coupled plasma mass spectrometer
ATR-IR	attenuated total reflectance infrared spectroscopy
SKP	scanning kelvin probe
SVET	scanning vibrating electrode technique
ZHC	zinc hydroxy chloride
ZHS	zinc hydroxysulfate
HZ	Zinc hydroxy carbonate
ZSC	sodium zinc chlorohydroxy sulfate
SZC	sodium zinc carbonate
RDE	rotating disk electrode
RRDE	rotating ring disk electrode

---

# Contents

---

<b>Contents</b>	<b>i</b>
<b>Résumé de la thèse</b>	<b>1</b>
<b>A. Introductory section</b>	<b>10</b>
<b>1 Introduction</b>	<b>13</b>
1.1 Origin and objectives of the PhD study . . . . .	13
1.2 Milestones of the work . . . . .	14
1.3 Summary and structure of the PhD dissertation . . . . .	15
1.4 List of publications . . . . .	18
<b>2 Towards inhibition of Zn reactivity</b>	<b>21</b>
2.1 Origins of Zn protection in inhibitor free media . . . . .	22
2.2 Zn reactivity in the presence of inhibitors . . . . .	27
2.2.1 Reduction of anionic species to low soluble oxides . . . . .	27
2.2.2 Acid-base precipitation of external cations to oxides/hydroxides . . . . .	29
2.2.3 Anion enhanced precipitation of Zn(II) compounds . . . . .	32
2.2.4 Adsorption on Zn surface . . . . .	35
<b>3 Controlled inhibition by hybrid anticorrosion coatings</b>	<b>39</b>
3.1 Desorption controlled release . . . . .	40
3.2 pH-controlled release . . . . .	41
3.3 Ion-exchange controlled release . . . . .	43
3.4 General conclusions from the literature review . . . . .	46
<b>B. Experimental section</b>	<b>47</b>
<b>4 AESEC technique</b>	<b>51</b>
4.1 Introduction . . . . .	51
4.2 Electrochemical flow cell . . . . .	52

4.3	Inductively coupled plasma atomic emission spectroscopy . . . . .	53
4.4	Fast electronics . . . . .	57
4.5	AESEC data treatment . . . . .	57
4.5.1	Development of deconvolution algorithm . . . . .	59
4.6	Summary . . . . .	62
<b>C.</b>	<b>Results section</b>	<b>62</b>
<b>5</b>	<b>Observation of anodic zinc dissolution during cathodic polarization and its consequences for corrosion rate measurements</b>	<b>65</b>
5.1	Introduction . . . . .	66
5.2	Experimental . . . . .	67
5.2.1	Materials . . . . .	67
5.2.2	Aeration of L-cysteine solutions . . . . .	67
5.2.3	AESEC technique . . . . .	68
5.3	Results and Discussions . . . . .	70
5.3.1	Equilibrium considerations . . . . .	70
5.3.2	AESEC polarization experiments . . . . .	71
5.3.3	EIS/AESEC experiments . . . . .	76
5.3.4	Corrosion rate measurements . . . . .	81
5.4	Conclusions . . . . .	83
<b>6</b>	<b>The effects of L-cysteine on the inhibition and accelerated dissolution processes of zinc metal</b>	<b>85</b>
6.1	Introduction . . . . .	86
6.2	Experimental . . . . .	88
6.2.1	Materials . . . . .	88
6.2.2	AESEC technique . . . . .	89
6.2.3	UV/Vis spectroscopy . . . . .	90
6.2.4	Immersion tests . . . . .	90
6.2.5	Surface characterization . . . . .	91
6.3	Results . . . . .	91
6.3.1	Dimerization of L-cysteine to L-cystine in aerated aqueous solutions	91
6.3.2	Real time dissolution measurement . . . . .	93
6.3.3	Zn reactivity in immersion tests . . . . .	98
6.3.4	Surface characterization after immersion tests . . . . .	99
6.4	Discussion . . . . .	102
6.4.1	Effect of dimerization of L-cysteine on initial Zn reactivity . . . . .	102
6.4.2	Competitive actions of L-cysteine on Zn dissolution . . . . .	104
6.5	Conclusions . . . . .	107
<b>7</b>	<b>MoO<sub>4</sub><sup>2-</sup> as a soluble inhibitor for Zn in neutral and alkaline solutions</b>	<b>109</b>
7.1	Introduction . . . . .	110
7.2	Experimental . . . . .	113

7.2.1	Materials . . . . .	113
7.2.2	AESEC technique . . . . .	114
7.2.3	Surface characterization . . . . .	116
7.3	Results . . . . .	117
7.3.1	AESEC measurement of Zn spontaneous dissolution . . . . .	117
7.3.2	Film characterization . . . . .	122
7.4	Discussion . . . . .	126
7.4.1	Inhibition efficiency of molybdate and the composition of the film . . . . .	126
7.4.2	Universality of Cr(VI) action on Zn at pH 4 -13 . . . . .	126
7.4.3	Role of flow conditions for Zn reactivity in $10^{-2}$ M $\text{Na}_2\text{MoO}_4$ solutions . . . . .	127
7.5	Conclusions . . . . .	129
<b>8</b>	<b>Factors affecting <math>\text{MoO}_4^{2-}</math> inhibitor release from a <math>\text{Zn}_2\text{Al}/</math>-based LDH and their implication in protecting HDG by means of organic coatings.</b>	<b>131</b>
8.1	Introduction . . . . .	133
8.2	Experimental . . . . .	136
8.2.1	Preparation of $\text{Zn}_2\text{Al}/$ - $\text{MoO}_4^{2-}$ LDH phase . . . . .	136
8.2.2	Coating preparation . . . . .	136
8.2.3	Release studies from LDH powder . . . . .	137
8.2.4	Tests of coated HDG samples . . . . .	139
8.3	Results . . . . .	140
8.3.1	$\text{MoO}_4^{2-}$ release from LDH powders . . . . .	140
8.3.2	Molybdate release and effect of $\text{Zn}_2\text{Al}/$ - $\text{MoO}_4^{2-}$ LDH fillers on the corrosion of coated samples . . . . .	147
8.4	Discussion . . . . .	151
8.4.1	Mechanisms of $\text{MoO}_4^{2-}$ release from $\text{Zn}_2\text{Al}/$ -LDH framework . . . . .	151
8.4.2	Effect of carbonates on the corrosion behavior of coated samples . . . . .	154
8.5	Conclusions . . . . .	154
<b>D.</b>	<b>Concluding remarks</b>	<b>155</b>
<b>9</b>	<b>Conclusions and perspectives</b>	<b>159</b>
<b>Appendix A</b>	<b>On the time resolution of AESEC method</b>	<b>169</b>
<b>Appendix B</b>	<b>Action of L-phenylalanine on galvanized steel</b>	<b>179</b>
<b>Appendix C</b>	<b>Comparison the actions of L-cysteine, L-phenylalanine, <math>\text{CrO}_4^{2-}</math> and <math>\text{MoO}_4^{2-}</math> water soluble inhibitors on low carbon CRS</b>	<b>182</b>
<b>Appendix D</b>	<b>Methodology verification for leaching studies from LDH</b>	<b>183</b>
<b>Appendix E</b>	<b>Python code for numerical convolution and deconvolution of AESEC data</b>	<b>185</b>

<b>Appendix F</b>	<b>A novel coupling of EIS with AESEC: application to the open circuit dissolution of Zn</b>	<b>189</b>
<b>Appendix G</b>	<b>Salt spray test results of HDG panels coated with a model coating</b>	<b>201</b>
<b>Bibliography</b>		<b>203</b>

---

# Résumé de la thèse

---

## L'origine et les objectifs de l'étude doctorale

L'une des stratégies courantes utilisées pour la protection des substrats métalliques contre la corrosion est une application de revêtements organiques, qui servent de barrière physique entre le métal et les milieux corrosifs [1–6]. Cependant, des sollicitations environnementales, telles que par exemple, la radiation ultraviolette, la température ou l'action mécanique (des rayures ou des fissures) peuvent conduire à une détérioration du revêtement organique en ouvrant le passage des espèces agressives (l'eau, l'oxygène etc) vers l'interface métal / oxyde / polymère, par des pores et des fissures ce qui favorise l'initiation de la corrosion du substrat [1–5, 7–9]. Afin d'augmenter la durée de vie du revêtement, les pigments inhibiteurs hydrosolubles peuvent être ajoutés directement à la formulation du revêtement [1, 3–5, 7]. Cependant, l'addition des inhibiteurs directement dans le polymère peut altérer les propriétés mécaniques qui provoque aussi une lixiviation spontanée des pigments inhibiteurs et, par conséquent, les mesures de protection seront « perdues » en relativement peu de temps [1, 3–5, 7]. Pour éviter cela, une solution élégante consiste à embarquer les espèces actives (inhibiteurs hydrosolubles) dans un réservoir nanométrique avant leur incorporation dans le film protecteur, ce qui permet de contrôler à la fois les propriétés mécaniques et la libération de l'inhibiteur en prolongeant la durée de vie de substrat [7, 10–12]. Les derniers revêtements hybrides sont souvent qualifiés dans la littérature de revêtements autocratisant ou « intelligents ».

Les hydroxydes doubles lamellaires (HDL) ont récemment été étudiés comme les structures hôtes pour des inhibiteurs de corrosion dans les revêtements organiques [12–19]. Quelques auteurs ont proposé un grand nombre de formulations HDL - inhibiteur et ont démontré l'efficacité de ces formulations pour la protection anticorrosion des alliages d'Al [12–19]; quelques hypothèses mécanistiques ont été proposées pour leur action sur ce type de substrat. Cependant, même pour le substrat d'Al, qui reste à ce jour le plus étudié pour ce type de revêtements, la cinétique de lixiviation en lien avec l'évolution de l'effet d'inhibition n'ont pas été suivis de façon systématique et quantitative car ceci nécessite une meilleure compréhension des mécanismes de lixiviation et des réactions de corrosion de substrat ainsi qu'un nouveau développement méthodologique. Moins d'études ont été faites pour tester l'effet et comprendre les mécanismes d'action des inhibiteurs embarqués

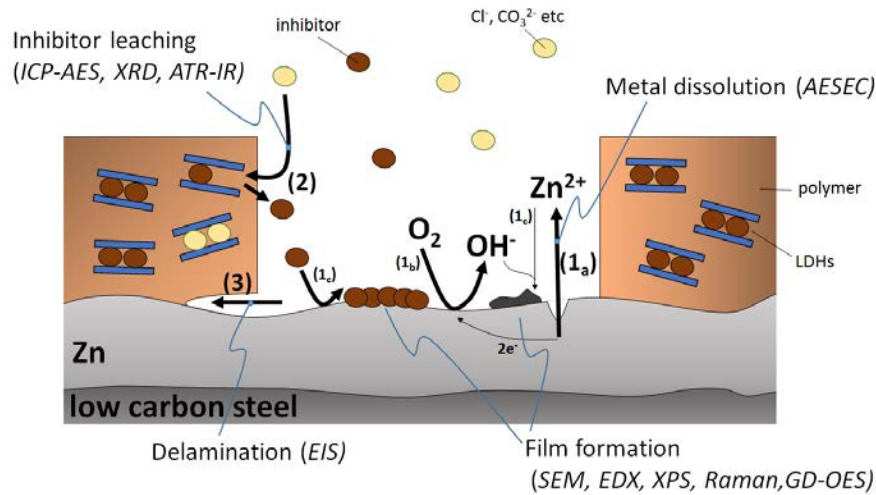


Figure 1: Schéma de l'inhibition de la corrosion de l'acier galvanisé par HDL - inhibiteur hybrides dans la formulation de revêtement. Les principaux procédés étudiés dans ce travail sont présentés : (1<sub>a</sub>) dissolution électrochimique du substrat accompagnée par (1<sub>b</sub>) réduction de l'oxygène cathodique et la formation de films insolubles (processus 1<sub>c</sub>), (2) lixiviation de l'inhibiteur à partir de HDL et (3) délamination du revêtement.

dans les HDL pour la protection des aciers galvanisés.

Le travail présenté dans ce manuscrit essaie de comprendre les mécanismes de l'action d'un inhibiteur de corrosion présent dans un revêtement hybride sous forme de pigments intercalés dans l'HDL pour la protection de l'acier galvanisé. Afin d'identifier les candidats potentiels, il faut à la fois comprendre les mécanismes de lixiviation de l'inhibiteur et ses interactions avec le substrat et les produits de corrosion du substrat ce qui demande de développer une approche méthodologique spécifique à cette application.

- ✓ **L'objectif principal de ce travail consiste à trouver une méthodologie qui permet d'identifier un système HDL-inhibiteur de corrosion potentiellement intéressant pour l'application dans de revêtements hybrides et de comprendre les mécanismes fondamentaux de corrosion aqueuse dans le système revêtu en identifiant et étudiant les réactions élémentaires.**

## Les points clés de l'étude

En général, la réactivité des revêtements hybrides contenant les inhibiteurs embarqués dans les molécules hôtes peut être vue dans une série de processus simultanés présentés schématiquement sur la Fig. 1.

1. **Réactions de corrosion de substrat** en présence de l'inhibiteur telles que la dissolution anodique ( $1_a$  sur la figure), la formation et dégradation des films insolubles et des produits de corrosion ( $1_c$ ) et la réduction cathodique de l'oxygène ( $1_b$ ).
2. **Réactions provoquant la lixiviation de l'inhibiteur** (2 sur la figure) par les réactions d'échange ionique ou par la destruction de l'hôte.
3. **Dégradation du système revêtu** (3 sur la figure, délamination du revêtement) à cause de l'endommagement de l'interface métal / oxyde / polymère.

En tenant compte de la différence entre les zones revêtues (et donc moins actives) et des défauts (plus actives) on peut s'attendre à ce que la réaction cathodique (processus  $1_b$ ) se passe majoritairement sous le polymère [20–22]. L'évacuation des espèces de la zone confinée étant lente, une forte alcalinisation est attendue sous le polymère. L'inhibiteur retenu doit donc être efficace à pH alcalins ce qui est rarement testé même pour des inhibiteurs courants. De plus, compte tenu de la rapidité avec laquelle l'inhibiteur doit bloquer la corrosion, il faut que son action une fois libéré soit immédiate ; donc les aspects cinétiques de son action sont primordiaux.

Sur la base de trois types de processus influant sur le système complet, les trois étapes clés ont été donc choisies pour ce travail :

1. **Identification d'un inhibiteur de corrosion hydrosoluble** pour les substrats de l'acier galvanisé (donc zinc et acier) à partir de quelques candidats potentiels avec une **compréhension de la réactivité** de l'acier galvanisé en présence de ces inhibiteurs dans les conditions définies par l'utilisation dans les revêtements organiques (large gamme de pH incluant le domaine alcalin, une cinétique de protection rapide).
2. Compréhension **des facteurs et des mécanismes contrôlant la libération de l'inhibiteur** sélectionné lors de la première partie à partir d'un système hybride HDL-inhibiteur de corrosion en tant que paramètre principal définissant la libération de l'inhibiteur à la demande.
3. Compréhension **des mécanismes de protection dans un système modèle avec le revêtement hybride**. Dans ce système les pigments HDL-inhibiteur sélectionnés lors de la première partie sont incorporés dans le polymère et la cinétique de lixiviation est mesurée en lien avec l'efficacité du système en variant les paramètres externes définis lors de la seconde partie.

Dans ce travail nous nous sommes concentrés sur les étapes initiales de dégradation dans lesquels l'acier n'est pas encore exposé. C'est pour cela que la plupart des résultats en étape 1 concerne la réactivité du Zinc en présence des inhibiteurs et beaucoup moins la réactivité de l'acier.

## Le résumé et la structure de la thèse de doctorat

Cette thèse est organisée en **4 parties principales**: (A) partie introductive qui présente les questions scientifiques à travers une revue bibliographique, (B) partie qui présente la technique principale utilisées dans ce travail, (C) la partie des résultats qui expose les résultats principaux et leur discussion, et la partie (D) avec les conclusions et les perspectives.

La **1ère partie** contient 3 chapitres. Le **chapitre 1** présente un aperçu global de la thèse. Les **2ème et 3ème chapitres** détaillent l'état des connaissances concernant les mécanismes de la corrosion de Zinc et les moyens de sa protection par des inhibiteurs hydrosolubles (**Chapitre 2**), ainsi que les paramètres contrôlant la libération d'inhibiteurs hydrosolubles à la demande de différents types de revêtements intelligents (**Chapitre 3**). Les œuvres les plus importantes sont répertoriées et les stratégies et les mécanismes proposés sur la protection du Zinc par les inhibiteurs hydrosolubles et la libération contrôlée de l'inhibiteur des revêtements intelligents sont analysés. Selon l'analyse documentaire, L-cystéine, L-phénylalanine et les ions de  $\text{MoO}_4^{2-}$  ont été choisis en tant qu'inhibiteurs hydrosolubles potentiels pour le Zn. Le système hôte avec  $\text{Zn}_2\text{Al}/\text{-HDL}$  a été proposé pour les revêtements hybrides. En marge de la partie A, chaque chapitre comprend une étude bibliographique en partie C.

La 2ème partie contient 2 chapitres. Le **chapitre 4** décrit la méthodologie principale utilisée pour le screening intelligent d'inhibiteurs hydrosolubles – la technique de la

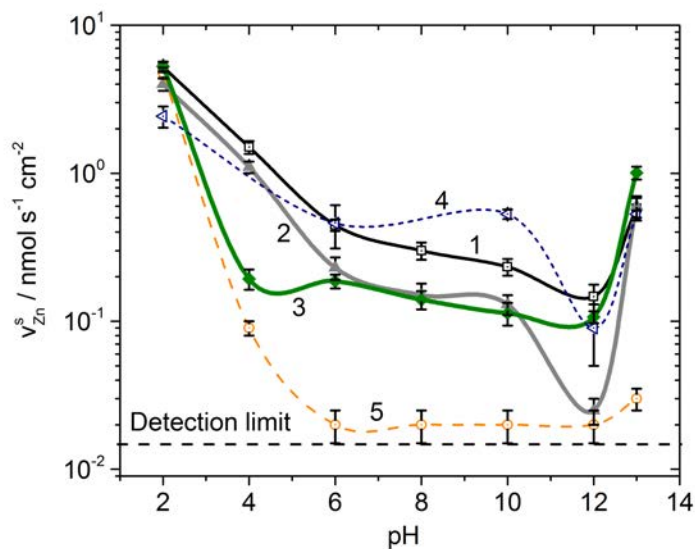


Figure 2: Les valeurs des vitesses de dissolution de Zn en fonction du pH à 0,5 M de NaCl dans (1) une solution sans inhibiteur, (2) à  $10^{-2}$  M  $\text{Na}_2\text{MoO}_4$ , (3) à  $10^{-3}$  M L-cystéine, (4) à  $10^{-2}$  M L-phénylalanine et (5) à  $10^{-2}$  M  $\text{K}_2\text{CrO}_4$ .

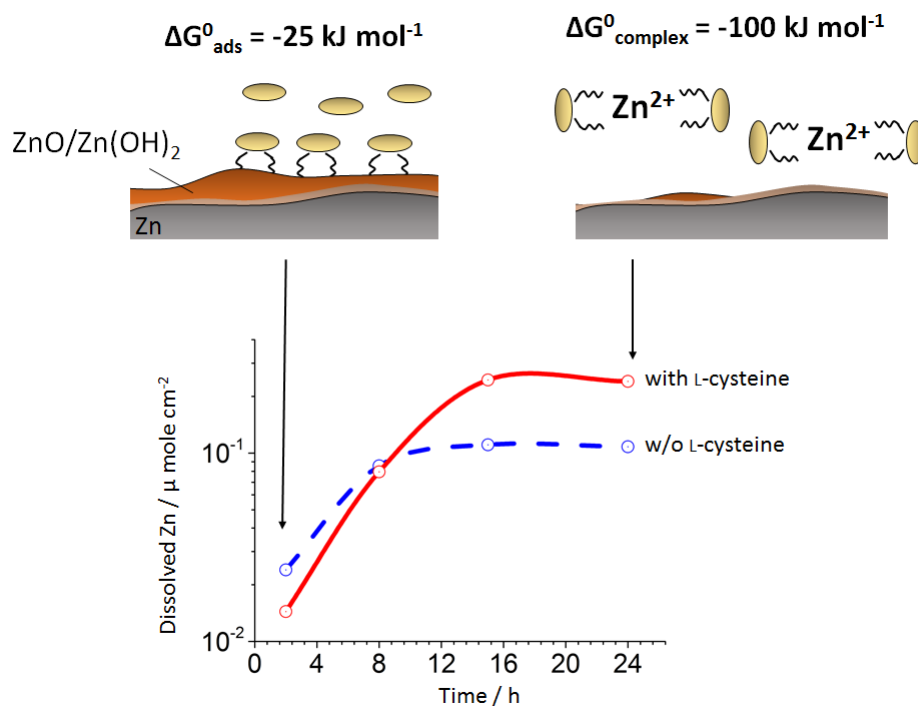


Figure 3: Action de  $10^{-4} - 10^{-3}$  M de L-cystéine sur Zn dissous à pH neutre: l'adsorption initiale de la L-cystéine sur les oxydes de Zn définit son effet inhibiteur. Cependant, la dissolution des oxydes de Zn au cours du temps est favorisée par la thermodynamique qui conduit à l'accélération de la dissolution de Zn.

spectroélectrochimie d'émission atomique (AESEC). Le **chapitre A** décrit les développements de cette technique proposés et utilisés pour améliorer les résultats décrits dans la partie C. La technique AESEC a été proposée pour le « screening » des inhibiteurs car elle compte un certain nombre d'avantages par rapport à d'autres techniques électrochimiques pour les études mécanistiques car elle permet d'accéder à des courants élémentaires la dissolution du métal et ceci, sans perturbation du système (à circuit ouvert) et elle ne nécessite pas une préparation de l'échantillon sophistiquée.

La 3ème partie de la thèse est la plus importante et elle est composée des chapitres techniques présentés sous la forme de quatre publications (tous déjà soumises ou publiés). Ces chapitres visent à répondre aux questions spécifiques posées dans l'introduction.

Le **chapitre 6** présente une action controversée de la L-cystéine sur le Zn à circuit ouvert. En premier lieu, dans les pH 2-13 à des concentrations intermédiaires ( $10^{-3}$  M) et à temps courts (exemple de la courbe 3 sur la Fig. 2) son action était inhibitrice. En second lieu, son action était accélératrice pour des concentrations plus élevées ou à temps longs en pH neutre (exemple Fig. 3), ce qui a été vérifié sous écoulement à temps courts par AESEC et pour immersion à des temps plus longs. L'action de la L-cystéine à haute concentration est définie par la formation de complexes solubles avec

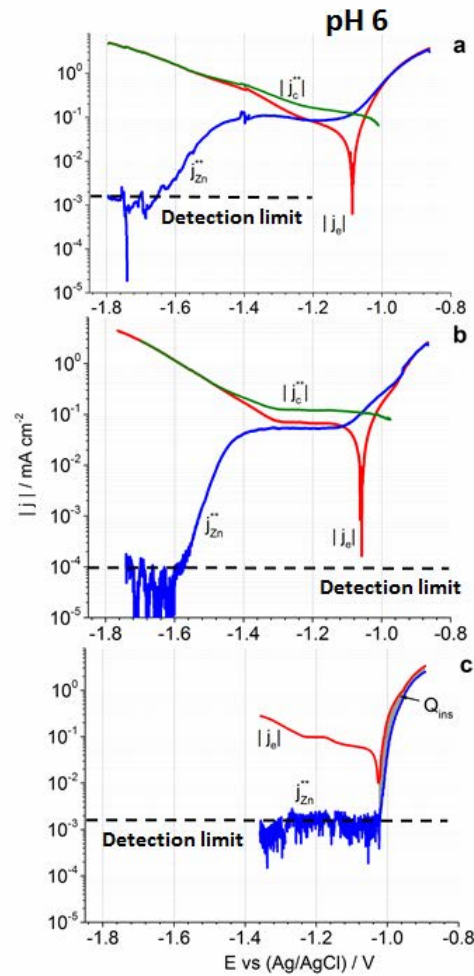


Figure 4: Courbes de polarisation AESEC pour Zn (acier galvanisé) dans (a)  $10^{-2}$  M L-cystéine, (b)  $10^{-3}$  M L-cystéine et (c) sans L-cystéine à pH 6. Le courant total ( $j_e$ ), courant déconvolué de Zn ( $j_{Zn}^{**}$ ) et le courant cathodique calculé ( $j_c$ ) sont montrés.

l'ion  $Zn^{2+}$ . Dans le cas d'inhibition, son efficacité a été inférieure à 70 % et l'évolution de l'efficacité d'inhibition en fonction du pH a été expliquée par la dimérisation sensible au pH de L-cystéine en L-cystine qui n'a pas de fonction inhibitrice sur Zn. L'action inhibitrice est corrélée avec une faible physisorption à la surface des oxydes de Zinc. La disparition de l'effet inhibiteur avec le temps dans les solutions neutres a été attribuée à la formation des complexes solubles entre  $Zn^{2+}$  et la L-cystéine adsorbé dont la formation est thermodynamiquement favorable. A pH 12, l'effet inhibiteur ne disparaît pas avec le temps d'immersion et même si certaines hypothèses ont été proposées, cet effet nécessite une étude plus approfondie.

Dans le **chapitre 5** quelques méthodes de mesure de vitesse de corrosion (basées sur

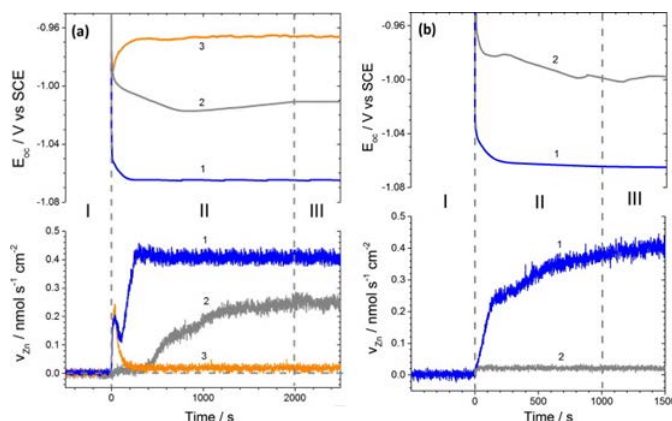


Figure 5: Exemples de l'évolution de la vitesse de dissolution de Zn ( $v_{Zn}$ ), et du potentiel de circuit ouvert (EOC) mesurés avec et sans inhibiteurs dans les expériences (a) sans masque et (b) avec un masque au pH initial 6. Courbes (1) - sans inhibiteur, (2) - avec addition de  $10^{-2}$  M  $\text{Na}_2\text{MoO}_4$  et (3) - avec addition de  $10^{-2}$  M  $\text{K}_2\text{CrO}_4$ .

les pentes de Tafel, les estimations de  $R_p$  à partir de EIS et la mesure du courant partiel du Zn par l'AESEC) sont comparées en application pour la réactivité de Zn en présence de cystéine. Généralement, il n'est pas possible de se fier à l'estimation du courant de corrosion à partir de l'extrapolation de Tafel étant donné la possible contribution du courant de dissolution anodique sur la valeur du courant total sous polarisation cathodique. Les courants de corrosion mesurés par AESEC ne comprennent pas les courants consommés par la formation d'intermédiaire Zn(II) légèrement soluble et donc peut sous-estimer leurs valeurs. Parmi les méthodes testées, l'AESEC a fourni les valeurs de courant de corrosion les plus appropriées et de plus, l'information la plus complète quant aux mécanismes de corrosion et ceci en une seule expérience électrochimique. Les courbes de polarisation réalisées par AESEC ont révélé la présence d'un plateau caché de dissolution de Zinc à pH neutre et légèrement alcalin (Fig. 4) probablement déterminé par la diffusion de la L-cystéine à la surface du métal. L'effet majeur de l'addition de la L-cystéine sur la dissolution du Zinc a été identifié, elle (i) induit un déplacement cathodique sur le début de la dissolution du Zn, et (ii) augmente le plateau de courant. Les deux effets ont été attribués à la complexation entre  $\text{Zn}^{2+}$  et la L-cystéine.

D'ailleurs, une tentative d'associer AESEC à la spectroscopie d'impédance électrochimique (SIE) a été faite pour la première fois pour avoir un nouvel aperçu de l'application de l'SIE. La nouvelle technique SIE/AESEC a permis de distinguer les deux mécanismes de dissolution du métal dans lesquels l'oxydation du métal conduit directement à la formation d'ions dissous ou passe à travers un film intermédiaire légèrement soluble (**Annexe F**).

Les propriétés mutuelles d'accélération/inhibition peuvent semer le doute concernant l'utilisation de la L-cystéine en tant qu'inhibiteur soluble pour le Zn. La L-phenylalaline a été aussi testée sur le Zn mais n'a pas révélé d'impact significatif sur la dissolution du Zn et n'a pas été étudiée en détail. Les résultats sont présentés en **Annexe B**.

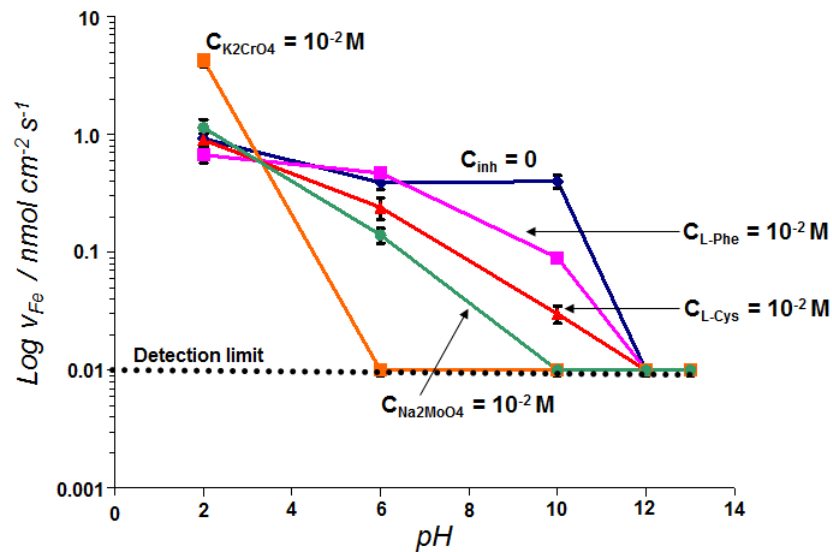


Figure 6: Les valeurs des vitesses de dissolution de Fe en fonction du pH à 0,5 M de NaCl dans une solution sans inhibiteur, à  $10^{-2}$  M  $\text{Na}_2\text{MoO}_4$ , à  $10^{-2}$  M L-cystéine, à  $10^{-2}$  M L-phénylalanine et à  $10^{-2}$  M  $\text{K}_2\text{CrO}_4$ .

Le Chapitre 7 présente l'étude de l'inhibiteur  $\text{MoO}_4^{2-}$ . L'effet inhibiteur de cet anion sur l'acier galvanisé a été associé à la formation d'un film riche en Mo dû à la réduction du Mo(VI). A pH très alcalin (pH 13), aucun film ne s'est formé, ceci étant corrélé à la faible capacité d'oxydation du Mo(VI) à ce pH. Aucun effet inhibiteur n'a été observé. Dans des milieux neutre et alcalins (pH 6 à 12) et avec un débit d'électrolyte homogène (obtenu par l'application d'un masque) des films riche en Mo(V) (détecté par XPS) se sont formés en moins de 2s au contact du Zn (Fig. 5). Le taux d'inhibition associé à ces films a été supérieur à 92 %.

L'hétérogénéité du débit de l'électrolyte lors des expériences réalisées sans le masque ont induit une diminution de l'effet inhibiteur après 500 s d'exposition et la formation locale de régions riches en Mo(IV) situées aux bords de la cellule. Ceci s'explique par la diminution locale du pH due à la stagnation des ions  $\text{Zn}^{2+}$  et leur hydrolyse. Cette hypothèse est corrélée avec les grandes proportions de Mo(IV) dans les films formés en solutions acides et leur faible taux d'inhibition. L'évolution de l'efficacité de l'inhibition sous l'écoulement non-homogène est présentée en exemple de la courbe 2 sur la Fig. 2. La comparaison de l'efficacité d'inhibition et la composition des films formés dans les conditions (écoulement, pH) différentes suggèrent que le Mo(V) est un composé important du film protecteur.

L'effet des trois inhibiteurs testée sur la dissolution du Zn et de l'acier sous l'écoulement inhomogène est résumé sur les Fig. 2 (Zn) et Fig. 6 (acier). Sur la base de l'ensemble des résultats présentés en Chapitres 6-7 et Annexes B et C, **le molybdate a été choisi pour être embarqué dans les HDL et pour les études sur les étapes 2 et 3.**

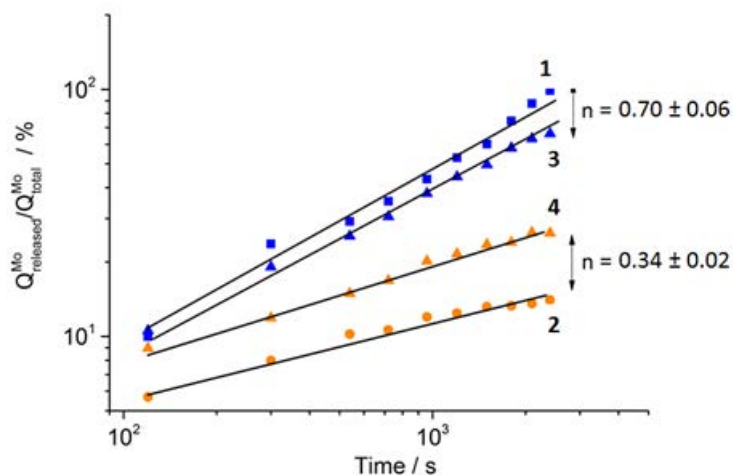


Figure 7: Evolution de taux de lixiviation (fraction de Mo soluble par rapport à la quantité totale de Mo dans la poudre, notée comme  $Q_{released}^{Mo}/Q_{total}^{Mo}$ ) pendant l'immersion dans les solutions de (1) 0.1 M  $\text{Na}_2\text{CO}_3$ , (2) 0.5 M  $\text{NaCl}$ , (3) 0.1 M  $\text{Na}_2\text{SO}_4$  at (4) 0.1 M  $\text{NaNO}_3$ .

Le **chapitre 8** montre l'étude de la lixiviation du  $\text{MoO}_4^{2-}$  intercalé dans  $\text{Zn}_2\text{Al}/\text{HDL}$  en premier temps, dans les solutions neutres en présence de  $\text{Cl}^-$ ,  $\text{NO}_3^-$ ,  $\text{SO}_4^{2-}$  ou  $\text{CO}_3^{2-}$ , et en second temps à pH fortement alcalins les HDL ont été détruits. Cette lixiviation a été étudiée par la combinaison de méthodes telles que ATR-IR, DRX et par l'analyse de la solution par ICP-AES. La vérification méthodologique de l'étude de lixiviation est présentée en **Annexe D**. La cinétique de l'échange anionique dépend fortement de la charge de l'anion externe qui s'intercale dans le HDL à la place du molybdate (Fig. 7). Il a été proposé sur la base de la valeur de l'ordre de réaction, que l'étape déterminante de la vitesse de l'échange avec des ions monovalents est la diffusion des ions à l'intérieur de l'HDL tandis que pour l'échange de  $\text{MoO}_4^{2-}$  avec les ions bivalents c'est la réaction à la surface. La quantité totale libérée en 24 h d'immersion et la vitesse de la libération de molybdate, ont été fortement diminuées quand l'échange se fait avec des anions monovalents. L'effet le plus spectaculaire pour libération du molybdate a été observé avec les ions  $\text{CO}_3^{2-}$ . Cet effet a été testé non seulement pour la lixiviation à partir de poudre des pigments hybrides  $\text{HDL-MoO}_4^{2-}$  mais aussi pour le système revêtu avec le polymère chargé des hybrides.

L'étude comparative de la quantité de  $\text{MoO}_4^{2-}$  libéré, de quantité du Zn dissous et la réponse du système revêtu avec et sans pigments hybrides en impédance électrochimique ont été comparés avec et sans présence du carbonates en solution afin du corrélérer l'effet de carbonate sur la lixiviation et le pouvoir protecteur de revêtement. L'action des ions présents dans l'électrolyte sur le pouvoir protecteur des  $\text{HDL-MoO}_4^{2-}$  incorporés dans un revêtement organique est schématiquement présentée sur la Fig. 8.

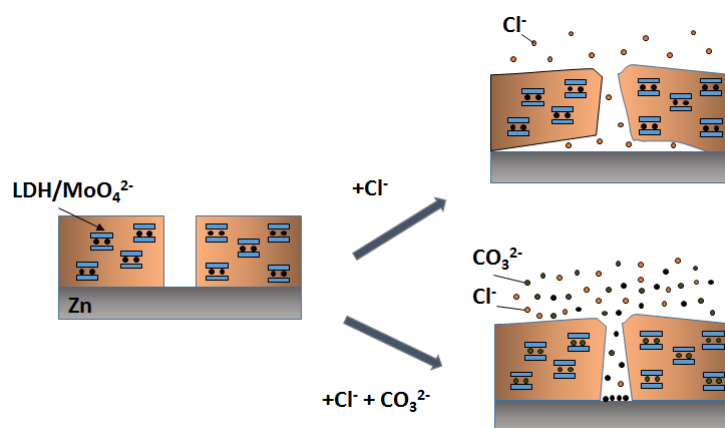


Figure 8: Représentation schématique de l'action du HDL-revêtement hybride sur Mo et Zn aux moyens de  $\text{Cl}^-$  et  $\text{Cl}^- + \text{HCO}_3^-$ : La perte de l'adhérence du revêtement en  $\text{Cl}^-$  grâce à corrosion de Zn et l'inhibition de la corrosion de Zn en  $\text{Cl}^- + \text{HCO}_3^-$  ont lieu grâce à la libération de l'inhibiteur soluble dans l'eau  $\text{MoO}_4^{2-}$

Le **Chapitre 9** (partie C de l'étude) présente la conclusion générale ainsi que les perspectives issues de ce travail.

---

## A. Introductory section

---

This part of the PhD thesis defines the context of the study and the scientific questions, which should be answered.



# Introduction

---

## 1.1 Origin and objectives of the PhD study

One of the common strategies used in the corrosion engineering to prevent the corrosion of metal substrates is an application of organic coatings, which serve a physical barrier between the metal and a corrosive media [1–6]. However, the coating can degrade because of UV radiation, temperature and mechanical damage (scratches or cracks) etc. [1, 2, 7–9]. This leads to opening of pores and crack propagation inside the coating through which aggressive species such as  $\text{Cl}^-$ ,  $\text{O}_2$  etc can diffuse and reach the metal interface, finally ending up in corrosion initiation [1, 3–5]. To prolong the protection after the coating failure, the water-soluble inhibiting agent can be added directly to the coating formulation. However, such modification can result in degradation of the mechanical properties of the coating and a spontaneous leaching of inhibiting agent in contact with an electrolyte [1, 3–5, 7]. To avoid this, an elegant solution consists to embed active species (i.e. water soluble inhibitors) into a reservoir of nanometric size prior to its incorporation into a protective film, which permits to control the inhibitor release and provide long term active protection of the substrate [7, 10–12]. Layered double hydroxides are intensively studied as host molecules for the corrosion inhibitors. Several works demonstrated their potential use for LDH-hybrid coatings on Al alloys [12–19]. However, the hybrid coatings for galvanized steel have been poorly studied and the fundamental mechanisms and elementary reactions acting in layered double hydroxides (LDH) – hybrid coatings on galvanized steel are not really understood. Moreover, the release kinetics from the host systems and its correlation with the inhibiting effect was never quantified even for Al alloys, which would require the development of a new methodology.

This work was focused on the fundamental mechanisms of the action of a LDH-inhibitor hybrid coated system for the corrosion protection of galvanized steel. The understanding of the inhibitor release mechanisms, the action of the inhibitor on the metallic substrate and on corrosion products are fundamental for the identification of effective anticorrosion systems. The intelligent screening of potential hybrid anticorrosion systems requires new methodologies.

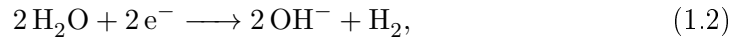
---

- ✓ The development of the methodology, which permits identification of a LDH-inhibitor system potentially interesting for application in hybrid coatings for galvanized steel and the fundamental understanding of the elementary reactions governing aqueous corrosion in such a system are the main objectives of this PhD work.

## 1.2 Milestones of the work

In general, the reactivity of LDH-hybrid coatings on galvanized steel in the case of a damage of an organic coating can be regarded as a series of simultaneous processes shown in Fig. 1.1:

1. electrochemical dissolution of the substrate in the presence of an inhibitor (process  $1_a$ ) accompanied by cathodic oxygen or/and water reduction (process  $1_b$ )



and the formation of insoluble films (processes  $1_c$ );

2. leaching of the inhibitor from LDHs and its action on metal substrate (process 2)

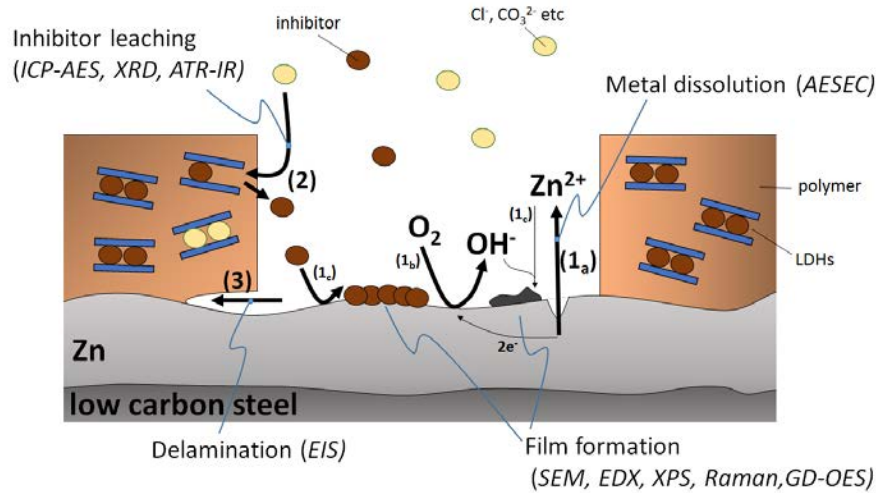


Figure 1.1: Schema of the corrosion inhibition of galvanized steel by LDH – inhibitor hybrids in the coating formulation. The main processes studied in this work are highlighted: ( $1_a$ ) electrochemical dissolution of the substrate accompanied by ( $1_b$ ) cathodic oxygen reduction and the formation of insoluble films (process  $1_c$ ), (2) leaching of the inhibitor from LDH samples and (3) delamination of the coating.

3. degradation of the complete system by the delamination process (process 3) driven by processes (1) and inhibited by process (2)

Previous studies of delamination of polymer coating from galvanized steel demonstrated strong alkalization in the confined zones under the polymer due to  $\text{OH}^-$  generation by reactions 1.1 and 1.2 [20–22]. Strong alkalization should impact Zn reactivity (process 1<sub>a</sub>), inhibitor release (process 2) and film formation (processes 1<sub>c</sub>). On the basis of this reactivity schema, the objectives of the work was achieved by the realization of three milestones:

1. To identify the effective water-soluble inhibitor on Zn and steel substrates, and to understand the mechanism of its action in a wide range of conditions defined by its potential use in a coating formulation. In particular, some specific requirements for the active inhibitor should be verified: rapid inhibiting kinetics and ability to work at high pH;
2. To understand the factors and mechanisms controlling the release of the selected water-soluble inhibitor from the selected host system in order to approach the release control;
3. To understand mechanisms of an active corrosion protection in model hybrid coated system (for the inhibitor selected at Step 1) and to quantify the release kinetics from hybrid coating in the relation with its inhibition efficiency. To specify the parameters controlling the release kinetics from the coating system via varying the parameters defined at Step 2.

### 1.3 Summary and structure of the PhD dissertation

This PhD work is organized into 4 main parts: **(A) Introductory section**, **(B) Experimental section**, **(C) Results section** and **(D) Concluding remarks**.

The Introductory section (**Part A**) defines the context and the scientific questions which should be answered. This part contains 3 chapters: this introduction (**Chapter 1**), the literature review of corrosion inhibitors and the mechanisms of their action on Zn (**Chapter 1**), and of approaches of the controlled release of inhibitor from different types of hybrid coatings (**Chapter 3**).

The most important works are listed and the proposed in the literature strategies and mechanisms towards Zn protection by water-soluble inhibitors and controlled inhibitor release from hybrid coatings are analyzed in **Chapters 2 and 3**. Based on the literature review, 2 groups of inhibitors were tested: organic (L-cysteine, L-phenialaline) and inorganic ( $\text{MoO}_4^{2-}$ ).  $\text{Zn}_2\text{Al}/\text{-LDH}$  host system was proposed for the hybrid coatings. It should be noted that in addition to **Chapters 2 and 3**, each chapter in **Part C** includes a bibliographic study.

**Part B** describes one of the main methodologies used in the work for the intelligent screening of water soluble inhibitors – atomic emission spectroelectrochemistry (AESEC)

technique (**Chapter 4**) and its development for such a study in term of the optimization of flow conditions (**Appendix A**) and elaboration of new methodology (**Appendix F**).

The Results section (**Part C**) present the most important results obtained during the work and their discussions. These results can be completed by some data presented in **Appendix**. **Part C** consists of four technical chapters presented in the form of 4 publications (2 of which was already accepted and 2 submitted). These chapters aim to answer the specific questions asked in the introduction. Only difference between the articles and associated with them chapters is an unification of the symbols, continuous numbering of the references, figures, tables and equations applied for the whole PhD work and presence of a small introduction in the beginning and a short summary in the end reminding the role of the chapter in the whole structure of the PhD thesis.

The screening of the selected inhibitors and understanding of the results is presented in **Chapters 5 - 7**. The L-cysteine action on Zn is presented in **Chapters 5** and **6**. **Chapter 6** presents the results of L-cysteine action on Zn at open circuit in the pH range of 2-13 done in short-term AESEC tests and longer immersion tests. At short exposures L-cysteine inhibited dissolution at intermediate concentrations. The initial inhibition decreased with pH because of pH-enhanced dimerization of L-cysteine confirmed by UV-vis spectroscopy. After long exposures at neutral pH the inhibition turned into acceleration. This was not observed in alkaline solutions. L-cysteine accelerated the dissolution at high concentrations ( $10^{-2}$  M). The effects were explained by a competition between strong complexation of L-cysteine with Zn-ions and its weak physisorption on the substrate. The hypothesis was confirmed by surface characterizations.

In **Chapter 5**, the effect of L-cysteine was verified in conventional polarization and EIS experiments, coupled with AESEC. A plateau of the Zn dissolution under the cathodic polarization was discovered. The effect of L-cysteine at all pH values and all concentrations was to increase the plateau current. The effect was more pronounced at high pH suggesting a synergy between hydroxide and L-cysteine. The three independent measurements of corrosion rates (Tafel extrapolation, measurement of  $R_p$  and spontaneous Zn dissolution) were compared and discussed in details.

Mutual inhibiting/accelerating properties may render dubious the use of L-cysteine as a practical water soluble inhibitor for Zn. L-phenialanine was also tested on Zn but it did not show any significant impact on Zn dissolution and was not investigated in detail. The results are presented in **Appendix B**.

**Chapter 7** presents the investigation of  $\text{MoO}_4^{2-}$  water-soluble inhibitor.  $\text{MoO}_4^{2-}$  anions showed the inhibition efficiency comparable to chromates (more than 92 %) in alkaline solutions and in neutral solutions under homogeneous flow achieved by the application of the mask. The protective properties of  $\text{MoO}_4^{2-}$  anions were assigned to the fast (in less than 2 s) formation of Mo(V)-rich film. The effect of the proposed inhibitors on the dissolution of low carbon steel (located underneath the Zn layer of galvanized steel) was also verified in order to exclude possible accelerating effect of the chosen species. The results are presented in **Appendix C** in comparison with a reference Cr(VI) inhibitor. All tested species acted as inhibitors for steel with the highest performance for  $\text{MoO}_4^{2-}$ .  $\text{MoO}_4^{2-}$  water soluble inhibitor was chosen for further investigation in the LDH hybrid

system (**Chapter 8**) system due to its excellent performance as water soluble inhibitor on Zn.

**Chapter 8** presents the results of leaching studies of  $\text{MoO}_4^{2-}$  from  $\text{Zn}_2\text{Al}/\text{-MoO}_4^{2-}$  LDHs in form of separated powders and from the  $\text{Zn}_2\text{Al}/\text{-MoO}_4^{2-}$  LDH hybrid coatings on galvanized steel during the immersion tests in different environments. The leaching tests showed that  $\text{MoO}_4^{2-}$  release was controlled by the nature of the exchanged ion from the media by ion-exchange mechanism at neutral pH or by the dissolution of the  $\text{Zn}_2\text{Al}/\text{-LDH}$  framework at alkaline pH. The presence of only  $\text{Cl}^-$  resulted in less than 40 % of  $\text{MoO}_4^{2-}$  release after 24 hours of the immersion while the additions of the carbonates resulted in complete 100 % release after 1 hour. The immersion tests showed slight inhibiting effect of coated system in  $\text{Cl}^-$  and high in  $\text{CO}_3^{2-}$  medias coherent with higher level of  $\text{MoO}_4^{2-}$  released. The ways to control the inhibitor release and hence, the inhibition performance of smart coatings were discussed in the vein of environment composition.

The **Part D** of the dissertation comprises the final Chapter 9, which presents the general conclusions and the perspectives brought by this PhD thesis.

## 1.4 List of publications

During the present PhD work following scientific papers were published or submitted:

### Full-text articles

1. V. Shkirskiy, P. Keil, H. Hintze-Bruening, F. Leroux, P. Volovitch, K. Ogle, "Observation of L-cysteine enhanced zinc dissolution during cathodic polarization and its consequences for corrosion rate measurements" (**Chapter 5**), *Electrochimica Acta*, in press, doi:10.1016/j.electacta.2015.09.009
2. V. Shkirskiy, P. Keil, H. Hintze-Bruening, F. Leroux, F. Brisset, K. Ogle, P. Volovitch, "The effect of L-cysteine on the inhibition and accelerated dissolution processes of zinc metal" (**Chapter 6**), *Corrosion Science*, 100 (2015) 101-112, doi:10.1016/j.corsci.2015.07.010
3. V. Shkirskiy, P. Keil, H. Hintze-Bruening, F. Leroux, T. Stimpfling, D. Dragoie, K. Ogle, P. Volovitch, "MoO<sub>4</sub><sup>2-</sup> as a soluble inhibitor for Zn in neutral and alkaline solutions" (**Chapter 7**), *Corrosion Science*, 99 (2015) 31-41, doi:10.1016/j.corsci.2015.05.005
4. V. Shkirskiy, P. Keil, H. Hintze-Bruening, F. Leroux, P. Vialta, G. Lefèvre, K. Ogle, P. Volovitch, "Factors affecting MoO<sub>4</sub><sup>2-</sup> inhibitor release from Zn<sub>2</sub>Al/-based layered double hydroxide and their implication in protecting hot dip galvanized steel by means of organic coatings" (**Chapter 8**), *Applied Materials and Interfaces*, in press, doi:10.1021/acsami.5b06702
5. V. Shkirskiy, K. Ogle, "A novel coupling of electrochemical impedance spectroscopy with atomic emission spectroelectrochemistry: Application to the open circuit dissolution of zinc" (**Appendix F**), *Electrochimica Acta*, 168 (2015) 167-172, doi:10.1016/j.electacta.2015.03.171
6. V. Shkirskiy, A.D. King, O. Gharbi, P. Volovitch, J.R. Scully, K. Ogle, N. Birbilis, "Revisiting the electrochemical impedance spectroscopy of magnesium with online inductively coupled plasma atomic emission spectroscopy", *ChemPhysChem*, 16 (2014) 536-9, doi: 10.1002/cphc.201402666

### Submitted article

1. V. Shkirskiy, P. Maciel, J. Deconinck, K. Ogle, "On time resolution of the atomic emission spectroelectrochemistry method" (**Appendix A**), submitted to *Journal of The Electrochemical Society*

### Oral presentations in international conferences

1. Presenting V. Shkirskiy, Co-authors P. Volovitch, K. Ogle, F. Leroux, T. Stimpfling, P. Keil, H. Hintze-Bruening, "Role of pH on the L-cysteine action on zinc in 3 w/w

- % NaCl“, European Corrosion Congress (Eurocorr), 8-12 September, 2014, Pisa, Italy, abstract N 121, CD-ROM.
2. Presenting V. Shkirskiy, Co-authors P. Volovitch, K. Ogle, F. Leroux, T. Stimpfling, D. Dragoe, P. Keil, H. Hintze-Bruening, "The reactivity of hot dip galvanized steel in the presence of  $\text{Na}_2\text{MoO}_4$  with pH“, Abstract book of 10th Coatings Science International conference COSI 2014, 22-26 Juin, Noordwijk, Netherlands, p. 118
  3. Presenting V. Shkirskiy, Co-authors K. Ogle, P. Volovitch, F. Leroux, P. Vialat, P. Keil, H. Hintze-Bruening, "A novel coupling of electrochemical impedance spectroscopy with on-line measurement of faradaic current“, 11<sup>th</sup> International symposium on electrochemical methods in corrosion research (EMCR) 2015, Troia, Portugal, 24-29 Mai 2015
  4. Presenting V. Shkirskiy, Co-authors P. Volovitch, K. Ogle, F. Leroux, P. Vialat, P. Keil, H. Hintze-Bruening, "Role of environment on release kinetics of intercalated  $\text{MoO}_4^{2-}$  inhibitor from  $\text{Zn}_2\text{Al}$ -layered double hydroxides“, European Corrosion Congress (Eurocorr) 2015, Graz, Austria, 6-10 September 2015



# Towards inhibition of Zn reactivity

---

Galvanized steels are widely used in numerous applications (roof, seats, parking brakes, oil pans, spring housings of cars, cornices and other wall ornaments, door and window hoods etc. [23–25]). They consist of low carbon steel covered with a protective layer of Zn based galvanized coating. Galvanized coating offers several protection mechanisms for the underlying steel:

1. from the first contact with the electrolyte it starts to corrode but it still serves as a barrier preventing penetration of aggressive species ( $O_2$ ,  $Cl^-$  etc) to the low carbon steel [23–27];
2. once both, steel and galvanized layer, are exposed, (due to scratch, cut-edge, advanced corrosion of galvanized layer etc.), Zn-based coating being anodic compared to steel, its corrosion offers a sacrificial protection preventing the degradation of the steel substrate [28–31];
3. finally, when the whole coating is consumed, steel starts to corrode. However the presence of low-soluble Zn corrosion products on the surface still decreases significantly the corrosion rate by a number of mechanisms discussed in the literature, such as barrier protection for aggressive species ( $O_2$ ,  $Cl^-$  etc), pH buffering etc [23, 29, 32].

The presence of a water soluble inhibitor effective for both zinc and steel substrates, which could be released from the organic coating “on demand”, when the coating is damaged, will reduce the rate of corrosion reactions operated by these mechanisms and hence, prolong the exploitation time of a metallic construction. In this PhD work we focused mainly on the inhibition of Zn as the first step of the corrosion of galvanized steel with some of the preliminary experimental data for the inhibition of the underlying low carbon steel (see Appendix B and C).

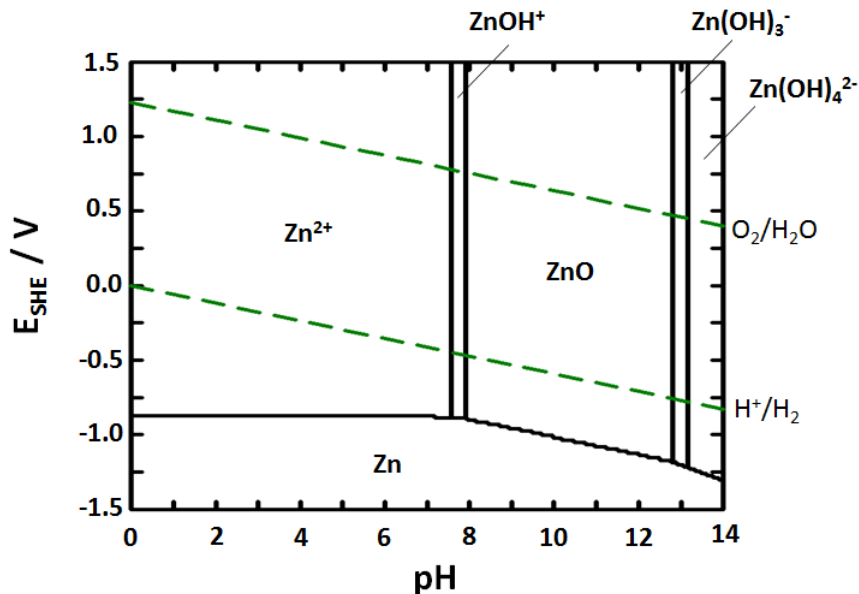


Figure 2.1: E-pH predominance diagram of Zn in aqueous additive free media plotted in Hydro Medusa software [33]. The species taken into account include:  $\text{Zn}^{2+}$ ,  $\text{Zn}(\text{OH})_2$ ,  $\text{Zn}(\text{OH})_3^-$ ,  $\text{Zn}(\text{OH})_4^{2-}$ ,  $\text{Zn}_2(\text{OH})_6^{2-}$ ,  $\text{Zn}_2(\text{OH})_3^+$ ,  $\text{Zn}_4(\text{OH})_4^{4+}$ ,  $\text{ZnOH}^+$ , a- $\text{Zn}(\text{OH})_2$ , e- $\text{Zn}(\text{OH})_2$ ,  $\text{ZnO}$  and  $\text{Zn}$  of standard database of Hydro-Medusa [33]. The region between the dashed green lines corresponds to the stability of  $\text{H}_2\text{O}$ .

The following chapter is based on a literature review and aims to reveal scientific problems in the field of Zn inhibition by a water soluble inhibitor. The additional bibliography is presented in the introduction for each chapter in Result section.

## 2.1 Origins of Zn protection in inhibitor free media

In this section, we will consider the corrosion of Zn in inhibitor free solutions in order to identify the strategies towards its protection.

Inspection of E-pH predominance diagram (Fig. 2.1) of Zn species in aqueous media shows that in the narrow pH range of 8.0 – 12.5 Zn oxidation results in the formation of Zn slightly soluble oxides/hydroxides (shown as ZnO) whereas at acid, neutral and alkaline pH soluble  $\text{Zn}^{2+}$ ,  $\text{ZnOH}^+$  and Zn hydrocomplexes ( $\text{Zn}(\text{OH})_3^-$ ,  $\text{Zn}(\text{OH})_4^{2-}$ ) are the dominant species. Based on the thermodynamics, E-pH diagram does not include kinetics of the species. Nevertheless, it can serve a basic guide helping to understand Zn dissolution. Once formed on the Zn surface, Zn slightly soluble oxides/hydroxides may block the electron transfer or/and the transport of aggressive species to the surface and prevent further corrosion propagation unlike the Zn soluble species. The role of Zn oxides/hydroxides in the possible Zn passivation will be considered in detail.

Powers and Breiter [34,35] showed that **the formed corrosion products on Zn consisted of two layers** by monitoring the change in the appearance of the surface of Zn

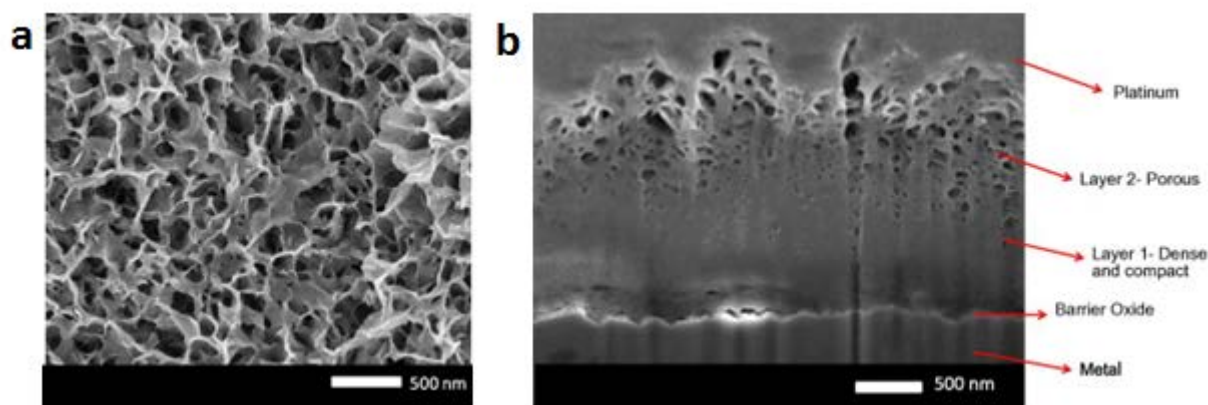


Figure 2.2: (a) - lateral view of oxides formed on Zn on exposure to 1  $\mu\text{L}$  seawater droplet after 6 hours of exposure, (b) - cross-sectional view of the oxides. Figure adapted from [41]

electrodes in 7 M KOH under a microscope during anodic polarization. The two layers were composed of the inner adherent layer of compact Zn oxides or Type II Zn oxides and outer precipitated layer or Type I Zn oxides. The recent study performed with the focused ion beam scanning electron microscopy (FIB-SEM) inspection of the Zn oxide/hydroxide layers after 6 hours of the exposure under the seawater droplet and carbonate containing solutions illustrated this bilayer structure of Zn oxides (Fig. 2.2) [36,37]. Macdonald et al [38] has been postulated that **the Type II Zn oxides was formed under direct Zn oxidation and been composed mainly of ZnO** however, the specific mechanism by which inner oxide is formed is a topic of some debate reviewed in [39]. **The Type II Zn oxides are formed by the hydrolysis of Zn(II) ions** ejected through ZnO with its composition strongly dependent on the local pH and the presence of foreign ions. Under anodic polarization at  $E > -1.15$  V vs Ag/AgCl and  $\text{pH} > 12$ , the passivation of Zn was observed related to the formation of Type II Zn oxides or modification of pre-formed Type II Zn oxides [38]. Recently Mokaddem et al [40] reported the formation of new Type III Zn oxides at potentials above  $-1.15$  V vs Ag/AgCl to which the passivation is attributed. The formation of Type III Zn oxides may be due to a potential induced phase transition of previously formed oxides, or it may be formed independently.

To approach the nature of Zn passive layer, one should focus on the properties of different types of experimentally observed Zn oxides. The inner ZnO oxide is a n-type semiconductor with a band gap of around 3.4 eV and the typical electrical conductivity ranging from  $10^1 \text{ Sm}^{-1}$  to  $10^3 \text{ Sm}^{-1}$  at 25  $^\circ\text{C}$  for oxides formed either on Zn under exposure to air or by the precipitation of  $\text{Zn}^{2+}$  from its saturated solution at room temperature [42]. High value of electrical conductivity (compare to  $10^6$ - $10^4 \text{ Sm}^{-1}$  typical for metals) is defined by the presence of numerous defects in the lattice structure of natively formed ZnO, which allows a charger transfer through its layer and supporting of cathodic reaction on Zn [23,36]. The investigation of oxygen reduction reaction (ORR)

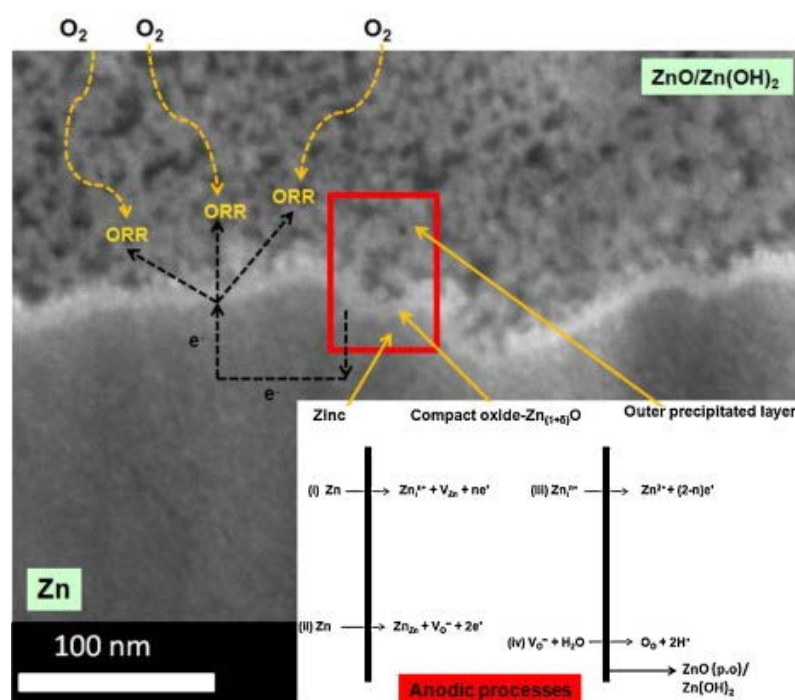


Figure 2.3: Representation of the cathodically driven solid-state mode of corrosion overlaid upon the FIB-SEM image of Zn oxides/hydroxides. As oxygen makes contact with the precipitated layer, ORR takes place on it driving anodic processes through the compact oxide. This results in the growth and development of the precipitated layer [36].

used a rotating disk electrode clearly illustrated it [43]. The Tafel slopes of ORR on compact ZnO electrodeposited on Pt was  $-139 \text{ mV dec}^{-1}$  what is close to the value of  $-133 \text{ mV dec}^{-1}$  obtained on pure Pt. Remarkably, in the presence of  $\text{Zn}^{2+}$  ions in the solution for the same experiment the Tafel slope decreased significantly till  $-282 \text{ mV dec}^{-1}$ . **The phenomenon was explained by the precipitation of Zn(II) intermediates. The data suggests that only inner ZnO oxides cannot limit Zn dissolution whereas the formation of Zn(II) precipitates defines the Zn dissolution.**

In this model, the overall process of Zn corrosion can be characterized as an oxygen penetration to compact oxides where ORR occurs, which drives Zn dissolution by a point defect mechanism through the compact oxide (Fig. 2.3) [36]. Modeling of the corrosion of a metal anode under a porous layer of its oxides shows that a large thickness, low porosity, low oxide electrical conductivity, poor oxygen reduction on the porous layer and high specific contact resistivity of the metal/oxide favor the inhibition of the dissolution of metal substrate [44]. One can control these parameters through the environment composition and thus, the nature of the precipitated oxide layer or so-called corrosion products.

A wide range of corrosion products can be formed on Zn (see Table 2.1) [31, 37, 45–51]. Odnevall and Leygraf [46] proposed a general reaction scheme for the formation and

the transformation of Zn corrosion products in atmospheric corrosion with the initial formation of  $\text{Zn}(\text{OH})_2$  and its following transformation as a function of  $\text{Cl}^-$  and  $\text{SO}_4^{2-}$  concentrations as shown in Fig. 2.4. The exposure of Zn under a sea water droplet at natural pH of 2.5  $\mu\text{L}$  showed the formation of gordaite and then simonkollite in the center droplet region with up to 2.5 days of the immersion [48]. After the evaporation, observed products included boyleite, Zn chlorate hydrate, Zn sulfate, sodium Zn chloride hydrate and Zn hydroxy carbonate. Systematic investigation of artificially synthesized ZHC, HZ, SZC and ZHS (see Table 2.1 for abbreviations) on ORR on cold rolled steel (CRS) showed a direct correlation between the nature of the corrosion products and the current intensity of ORR as follows  $\text{SZC} < \text{ZHC} < \text{ZHS} < \text{HX} < \text{CRS}$  at pH 7 [32]. From the possible origins of the barrier effects of Zn patinas, namely particle size of patinas, porosity considerations and hydrophobic interactions, only the morphological observations of patinas correlated well with the current intensity of ORR: **more compact layers form more efficient barriers** [32]. In the case of the formation of compact and non defective layer, the Zn patinas will serve as a physical barrier against  $\text{O}_2$  diffusion and being a semiconductor will control the electron flow from the metal to ORR taking place of the Zn patinas surface. A point-defect mechanism for ORR occurring on surface of Zn oxides was hypothesized by Pilbath and Sziraki [52]. However, there is still a distinct lack of knowledge about such as non-Faradaic processes. The distribution of the Zn patinas on metal surface can play an important role too.

Based on the investigation of Zn atmospheric corrosion, the lower corrosion rate on Zn in the presence of solid  $\text{NH}_4\text{Cl}$  on the Zn surface was attributed to the uniform layer of simonkollite on anodic and cathodic sites whereas in the presence of only solid  $\text{NaCl}$ , the formation of simonkollite was favored only on the cathodic sites [53]. Note, that due to a high saturation of the dissolved ions on the metal surface, the atmospheric corrosion differs significantly from the immersion tests where  $\text{NH}_4\text{Cl}$  accelerated Zn dissolution due to its complexation with Zn(II) and hence, the dissolution of Zn oxides. [54, 55].

**From the literature it seems that the outer precipitated layer of Zn cor-**

Table 2.1: Equivalence between the names of Zn corrosion products, its composition and the chosen abbreviation.

Common name	Chemical name	Abbreviation	Chemical formula
Zincite	Zinc oxide	ZnO	ZnO
	Zinc hydroxide	$\text{Zn}(\text{OH})_2$	$\text{Zn}(\text{OH})_2$
Simonkollite	Zinc hydroxy chloride	ZHC	$\text{Zn}_5(\text{OH})_8\text{Cl}_2 \cdot \text{H}_2\text{O}$
	Zinc hydroxysulfate	ZHS	$\text{Zn}_4(\text{OH})_6\text{SO}_4 \cdot n\text{H}_2\text{O}$ , $n = 3-5$
Hydrozincite	Zinc hydroxy carbonate	HZ	$\text{Zn}_5(\text{OH})_6(\text{CO}_3)_2 \cdot \text{H}_2\text{O}$
Gordaite	Sodium zinc chlorohydroxy sulfate	ZSC	$\text{NaZn}_4(\text{SO}_4)\text{Cl}(\text{OH})_6 \cdot 6\text{H}_2\text{O}$
	Sodium zinc carbonate	SZC	$\text{Na}_2\text{Zn}_3(\text{CO}_3)_4 \cdot 3\text{H}_2\text{O}$
	Zinc chlorohydroxysulfate		$\text{Zn}_4\text{Cl}_2(\text{OH})_4\text{SO}_4 \cdot 5\text{H}_2\text{O}$
Boyleite	Zinc magnesium sulfate		$(\text{Zn}, \text{Mg})\text{SO}_4 \cdot 4\text{H}_2\text{O}$
	Zinc chlorate hydrate		$\text{Zn}(\text{ClO}_3)_2 \cdot 6\text{H}_2\text{O}$

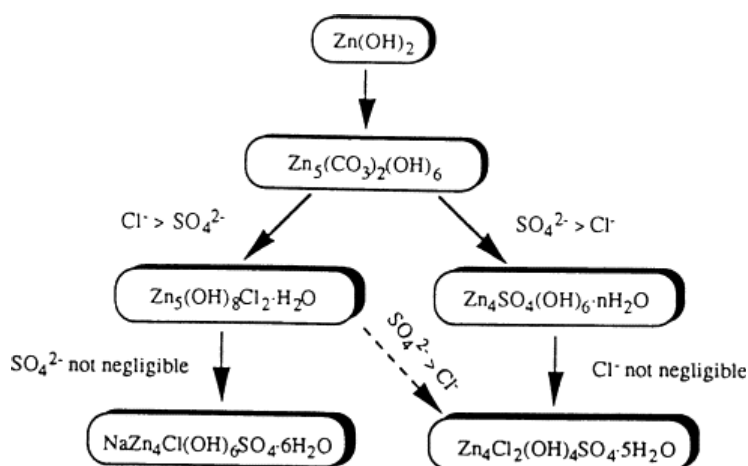


Figure 2.4: General reaction scheme of the formation of predominant Zn patinas under atmospheric corrosion [46].

**rosion products is responsible for the inhibition of Zn dissolution** serving the diffusion or/and electrical barrier to oxidation species such as oxygen. The performance of this protective layer is directly correlated with its compactness, uniformity and stability. As it was noted in the first paragraph, the Zn corrosion products formed in the inhibitor free aqueous solutions are stable only in the narrow pH range of 8.0 – 12.5 (Fig. 12.1). Moreover, even in this pH range they can be dissolved in the presence of excess of pollutants forming soluble complexes such as  $\text{Zn}(\text{NH}_3)_4^{2+}$ ,  $\text{ZnCl}_4^{2-}$  etc [23,31,33,46–49,55].

A common strategy for the improving the corrosion performance of the Zn substrate is the modification or/and the stabilization of the outer precipitated layer of Zn corrosion products by the addition of chemicals in the corrosive environment. Another strategy can be in the formation of a new precipitated layer by another species offering more stable protection than Zn patinas. Further focus will be addressed to the known inorganic and organic inhibitors and their action on Zn based substrates.

- ✓ Zn reactivity in additive free aqueous solutions is limited by the presence of outer precipitated layer of Zn(II) species.
- ✓ Performance of this layer is directly associated with its compactness, uniformity and stability.
- ✓ Potential water soluble inhibitors on Zn have to improve one or several of these parameters or/and form a new precipiated layer with better barrier properties in order to improve the corrosion performance of Zn substrates.

## 2.2 Zn reactivity in the presence of inhibitors

The literature on the inhibition of Zn based substrates can be classified into two main bodies depending on the application of the inhibitors:

- ✓ water soluble inhibitors, where the inhibitors are placed in aqueous solutions and the corrosion performance of dynamically formed precipitated layers is studied;
- ✓ conversion coatings, where on the first step the precipitated layers (or conversion coatings) are formed under specific conditions (usually acid pH, heat treatment) and then the studies of the corrosion performance of the coatings are performed.

The elemental steps of the interaction between an inhibitor and Zn are independent on the way of the application of the inhibitor. However, the kinetics of the formation of protective films, its morphology, composition and hence the corrosion performance within these two systems will be different due to the difference in the chemical composition, temperature and time scale. Mainly the water-soluble inhibitors will be considered below due to their application in hybrid anticorrosion coatings. The water-soluble inhibitors will be divided into several groups based on the mode of the action on Zn substrate: (i) reduction of anionic inhibitor with the formation of low soluble oxides, (ii) acid-base precipitation of external cations to oxides/hydroxides, (iii) acid-based co-precipitation of Zn(II) with exterior anions and (iv) adsorption of the inhibitor on the surface of Zn or/and Zn oxides. Note that the aspect of durability of the inhibitor action has not been considered in the literature and hence, it is not mentioned in the present literature review, but can be important for practical applications.

### 2.2.1 Reduction of anionic species to low soluble oxides

Several anions such as  $\text{CrO}_4^{2-}$ ,  $\text{MoO}_4^{2-}$ ,  $\text{TcO}_4^{2-}$ ,  $\text{NbO}_3^-$ ,  $\text{VO}_4^{3-}$ ,  $\text{TaO}_3^-$ ,  $\text{ReO}_4^-$ ,  $\text{ReO}_4^{2-}$  and  $\text{WO}_4^{2-}$  [56] can inhibit Zn dissolution through their reduction to lower oxidation state on Zn surface with their following acid-base precipitation on Zn surface. In this section only the most known  $\text{CrO}_4^{2-}$  and  $\text{MoO}_4^{2-}$  will be considered.

Cr(VI) species have widely been used for the decades as both the most effective water soluble inhibitor and the base of the conversion coatings [41]. However, due to its toxicity [57], its use is forbidden nowadays and alternative inhibitors are intensively investigated in order to achieve similar corrosion performance using environmentally friendly species. Being in contact with Zn metal, Cr(VI) immediately reduces to Cr(III) compounds mainly composed by  $\text{Cr}_2\text{O}_3$  oxide (reaction 2.1).



This oxide has a wide pH stability range of 4-14 with a solubility three order of magnitude less than for Zn(II) (Fig. 2.5), possesses hydrophobic properties, is p-type semiconductor with a large band gap of 4.7-5.0 eV [58] and thus could serve as a stable insoluble barrier to an electron flow on Zn. Moreover, Cr(VI) may adsorb into  $\text{Cr}_2\text{O}_3$  oxides due to its highly

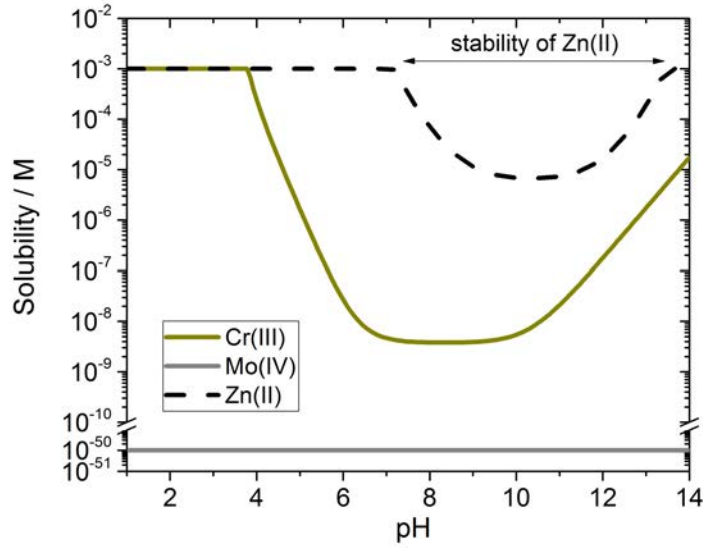


Figure 2.5: Solubility of 0.001 M Cr(III) (mainly  $\text{Cr}_2\text{O}_3$ ), 0.001 M Mo(IV) (mainly  $\text{MoO}_2$ ) and 0.001 M Zn(II) species as a function of pH in the aqueous solution. The diagram was calculated using Hydro Medusa software [33]. The species taken into account include for Zn(II) -  $\text{Zn}^{2+}$ ,  $\text{Zn}(\text{OH})_2$ ,  $\text{Zn}(\text{OH})_3^-$ ,  $\text{Zn}(\text{OH})_4^{2-}$ ,  $\text{Zn}_2(\text{OH})_6^{2-}$ ,  $\text{Zn}_2(\text{OH})_3^+$ ,  $\text{Zn}_4(\text{OH})_4^{4+}$ ,  $\text{ZnOH}^+$ , a- $\text{Zn}(\text{OH})_2$ , e- $\text{Zn}(\text{OH})_2$  and  $\text{ZnO}$ ; for Cr(III) -  $\text{Cr}^{3+}$ ,  $\text{Cr}(\text{OH})_2^+$ ,  $\text{Cr}(\text{OH})_3$ ,  $\text{Cr}(\text{OH})_4^-$ ,  $\text{Cr}_2(\text{OH})_2^{4+}$ ,  $\text{Cr}_3(\text{OH})_4^{5+}$ ,  $\text{CrOH}^{2+}$  and  $\text{Cr}_2\text{O}_3$ ; for Mo(IV) -  $\text{Mo}_2\text{O}_2^{4+}$ ,  $\text{Mo}(\text{OH})_4$ ,  $\text{MoO}_2$  of standard database of Hydro Medusa [33].

solubility and mobility. Thermodynamics and cyclic voltammograms predict reduction of Cr(VI) to Cr(III) taking place along with hydrogen evolution reaction (HER) and ORR [59]. Therefore, Cr(VI) can migrate to active cathodic sites on Zn and form  $\text{Cr}_2\text{O}_3$  providing an active healing effect.

The performance of inhibitors is usually described by the inhibition efficiency ( $\eta$ , %) defined as follows [60]

$$\eta = (1 - j_{corr}/j_{corr}^0)100\% \quad (2.2)$$

where  $j_{corr}$  and  $j_{corr}^0$  are the corrosion current with and without the additions of an inhibitor consequently. Cr(VI) species completely suppress Zn dissolution: in 0.05 M  $\text{K}_2\text{CrO}_4$  water soluble inhibitor in 0.01 M  $\text{H}_2\text{SO}_4$   $\eta$  equaled 99 % [61], in 0.2 mM  $\text{SrCrO}_4$  and 0.2 mM  $\text{Na}_2\text{CrO}_4$  in artificial acid rain water (pH 4.5)  $\eta$  equaled 92 % and 94 % correspondingly [62].

In order to mimic the action of Cr(VI) water soluble inhibitor, an alternative inhibitor should

1. possess high oxidizing properties to be able to be reduced in the presence of HER and ORR,

2. form a low soluble film of the reduced species, which is stable in a wide pH range
3. and possess high adsorption capacity and mobility to provide self-healing effect.

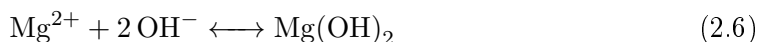
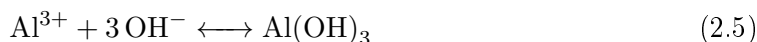
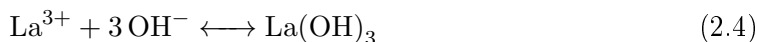
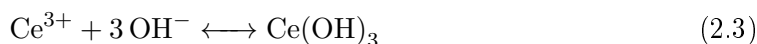
**First choice of an alternative inhibitor can be made for oxyanion analogues of Cr due to their close chemical properties, in particular to Mo(VI) compounds.**

The action of Mo(VI) compounds as a water soluble inhibitors on Zn is poorly documented. Aramaki [63] reported  $\eta = 64\%$  for 0.01 M  $\text{Na}_2\text{MoO}_4$  in neutral 0.5 M NaCl solution. Wang et al [61] showed  $\eta = 71\%$  for 0.05 M  $\text{Na}_2\text{MoO}_4$  in 0.01 M  $\text{H}_2\text{SO}_4$  solutions with a logarithmic rate law of protective film formation. In both works, the inhibition was attributed to the formation of Mo-rich insoluble film but the composition of the film was not reported. From the literature about Mo-rich conversion coatings, Mo(VI) is known to be reduced by Zn metal in acid solutions under air to Mo(V), Mo(IV), Mo(III) species with a lower oxidizing ability than Cr(VI) [33, 64–69]. In the presence of iron, Mo(VI) species were not reduced at all [70]. **Thermodynamic predictions show that Mo(IV) species are completely insoluble in aqueous solutions with the estimated solubility of  $10^{-50}$  M (Fig. 2.5) [33, 69] that makes Mo(VI) a promising candidate for the particular consideration for the corrosion inhibition of Zn.** The detailed literature review about the Mo(VI) interaction with Zn metal from the data obtained for application of  $\text{MoO}_4^{2-}$  in conversion coatings will be presented in Chapter 7 dedicated to Mo(VI) action on Zn.

- ✓ **Mo(VI) is poorly studied as a water soluble inhibitor on Zn while potentially it could provide a good protective protection due to the formation of hardly soluble Mo(IV) species. However, the oxidizing ability of Mo(VI) as a water soluble inhibitor on Zn needs to be verified. In the case of the encapsulation into hybrid coatings,  $\text{MoO}_4^{2-}$  will require the use of anionic nanocontainers.**

### 2.2.2 Acid-base precipitation of external cations to oxides/hydroxides

Other type of potential inhibitors consists of cations, which can precipitate forming low soluble oxides/hydroxides due to acid-base reactions (reactions 2.3-2.6) expanding the pH range of the stability of native Zn(II) oxides/hydroxides as emphasized in Fig. 2.7.



In this section we will consider the most studied and known species such as  $\text{Ce}^{3+}$ ,  $\text{La}^{3+}$ ,  $\text{Al}^{3+}$  and  $\text{Mg}^{2+}$ .

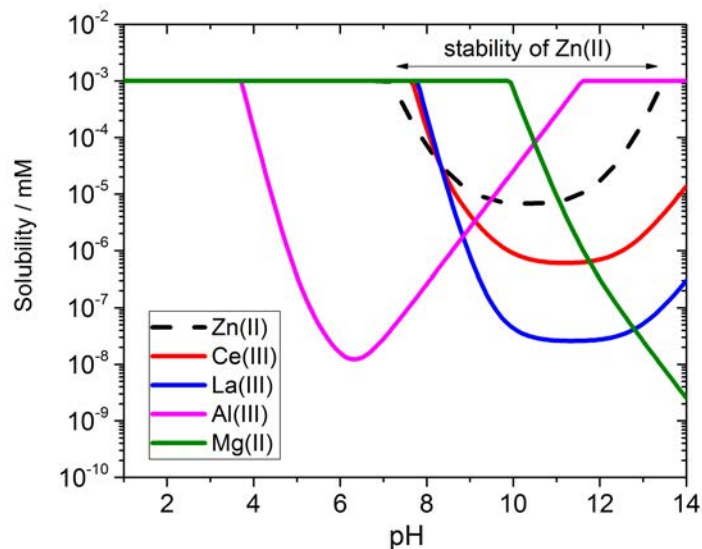


Figure 2.6: Solubility of 0.001 M Ce(III), 0.001 M La(III), 0.001 M Al(III), 0.001 M Mg(II) and 0.001 M Zn(II) species as a function of pH in the aqueous solution. The diagram was calculated using Hydro Medusa software [33]. The species taken into account include for Zn(II) -  $\text{Zn}^{2+}$ ,  $\text{Zn}(\text{OH})_2$ ,  $\text{Zn}(\text{OH})_3^-$ ,  $\text{Zn}(\text{OH})_4^{2-}$ ,  $\text{Zn}_2(\text{OH})_6^{2-}$ ,  $\text{Zn}_2(\text{OH})_3^+$ ,  $\text{Zn}_4(\text{OH})_4^{4+}$ ,  $\text{ZnOH}^+$ ,  $\alpha\text{-Zn}(\text{OH})_2$ ,  $\epsilon\text{-Zn}(\text{OH})_2$  and  $\text{ZnO}$ ; for Ce(III) -  $\text{Ce}^{3+}$ ,  $\text{Ce}(\text{OH})_2^+$ ,  $\text{Ce}(\text{OH})_3$ ,  $\text{Ce}(\text{OH})_4^-$  and  $\text{CeOH}^{2+}$ ; for La(III) -  $\text{La}^{3+}$ ,  $\text{La}(\text{OH})_2^+$ ,  $\text{La}(\text{OH})_3$ ,  $\text{La}(\text{OH})_4^-$ ,  $\text{La}_5(\text{OH})_9^{6+}$  and  $\text{LaOH}^{2+}$ ; for Al(III) -  $\text{Al}^{3+}$ ,  $\text{Al}(\text{OH})_2^+$ ,  $\text{Al}(\text{OH})_3$ ,  $\text{Al}(\text{OH})_4^-$ ,  $\text{Al}_3\text{O}_4(\text{OH})_2^{47+}$ ,  $\text{Al}_2(\text{OH})_2^{4+}$ ,  $\text{Al}_3(\text{OH})_4^{5+}$ ,  $\text{AlOH}^{2+}$  and  $\text{AlOOH}$ ; for Mg(II) -  $\text{Mg}^{2+}$ ,  $\text{Mg}_4(\text{OH})_4^{4+}$ ,  $\text{MgOH}^+$ ,  $\text{Mg}(\text{OH})_2$  and  $\text{MgO}$  of standard database of Hydro Medusa [33].

Rare earth based inhibitors such as Ce(III) and La(III) have been used as cationic inhibitors to protect Zn. These inhibitor systems were shown to form precipitated layers with high electrical resistivity [71] inhibiting ORR on Zn. Inspection of Fig. 2.7 confirms the precipitation of Ce(III) and La(III) compounds at  $\text{pH} > 8$  extending the formation of the outer precipitated layers in comparison to only Zn(II) species. In 0.6 M NaCl in the presence of 100 to 1000 ppm of  $\text{CeCl}_3 \cdot 7\text{H}_2\text{O}$ , Ce(III) cations were shown to immediately adsorb on Zn surface, which prevented penetration of  $\text{Cl}^-$  [72]. Afterwards, adsorbed Ce(III) served precursors to the Ce(III)-rich layer formation. The XPS analysis of the film after the immersion in 0.5 M NaCl with the additions of  $10^{-4}$  M  $\text{CeCl}_3$  revealed the presence of thick film of  $\text{Ce}(\text{OH})_3$  and  $\text{Ce}_2\text{O}_3$  and small amount of  $\text{ZnO}$  and  $\text{Zn}(\text{OH})_2$  [73]. Similarly to Ce(III), La(III) provided a fairly thick precipitated film of  $\text{La}(\text{OH})_3$ ,  $\text{La}_2\text{O}_3$  and small quantities of  $\text{Zn}(\text{OH})_2$  and  $\text{ZnO}$  [73]. Aramaki [73] reported the high inhibition efficiency of 91.2 % and 93.9 % of  $10^{-4}$  M La(III) and  $10^{-3}$  M Ce(III) respectively.

Al(III) and Mg(II) cations were also used to improve the corrosion performance of Zn substrate. Inspection of Fig. 2.7 confirms the precipitation of Al(III) in the pH

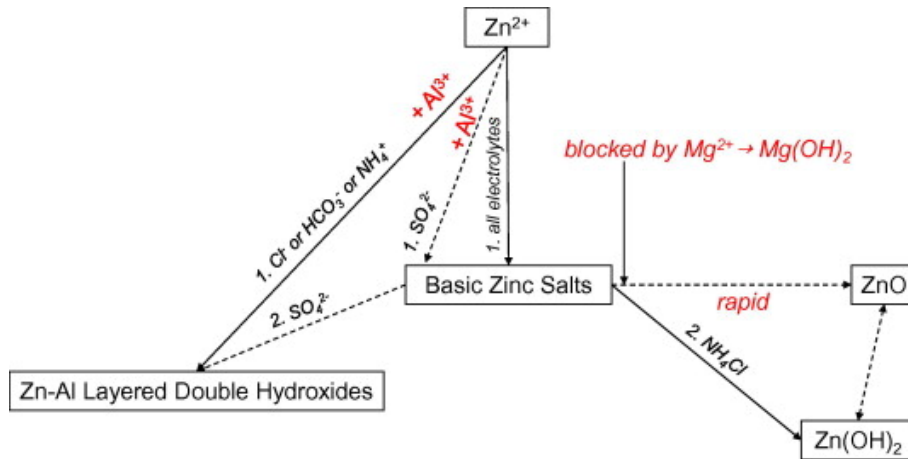


Figure 2.7: Schematic illustration of the formation and transformation of different corrosion products on Zn in the presence of different species in the electrolyte (as indicated) [75].

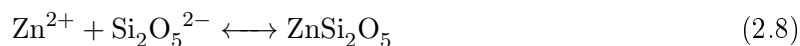
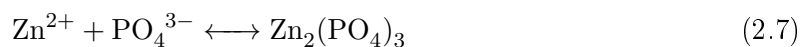
range of 4-11 and Mg (II) at pH > 10 that potentially permits to enhance the stability of Zn native protective layer. Indeed, the presence of Mg(II) cations in the solutions significantly decreased the rate of ORR on Zn [28, 50, 74–77]. The hypotheses proposed to explain the effect included: (i) the enhancing of the isolating properties of Zn(II) precipitates due to the doping of Mg(II) [28, 74, 76], (ii) pH buffering at pH 10.5 during Mg(OH)<sub>2</sub> precipitation [28, 74, 78–80] and (iii) stabilization protective corrosion products on Zn such as simonkolleite, hydroxysulfates against their transformation into soluble or less compact hydroxides, carbonates or sulfate complexes [75]. The most recent study conducted for Zn<sub>3</sub>Mg<sub>3.7</sub>Al alloy in synthetic rain water showed that the primordial role of Mg(II) cations consisted in the stabilization of more compact BZS, which prevents its transformation to less compact ZnO [75] (Fig. 2.7). The effect contradicts the thermodynamic predictions and hence was explained by the skin effect of the precipitated Mg(OH)<sub>2</sub>

influence of Mg(II) on the kinetics of BZS transformation [75]. The role of Al(III), consisted in the precipitation of Zn<sub>2</sub>Al/-LDH, which is considered by many authors as a good barrier for oxygen diffusion explained by their compact morphology, low electron density and layered structure with difficult ion-transfer through the layers [75, 78, 79, 81–83].

- ✓ **Ce(III), La(III) and other cations, which can form stable and low soluble oxides/hydroxides by acid-base reactions, can be considered as potential candidates for the intercalation into nanocontainers in hybrid coatings. Note that the potential application of mentioned cations in hybrid coatings will require the use cation nanocontainers such as oxide nanoparticules [84–86], zeolites [87], bentonites [88] etc.**

### 2.2.3 Anion enhanced precipitation of Zn(II) compounds

It was shown in section 2.1 that the dissolved Zn(II) species alone can inhibit Zn dissolution by the precipitation of Zn corrosion products and providing the barrier against both an electron flow and aggressive species. One of the strategy to improve the corrosion performance of Zn is the variation of the composition of Zn(II) precipitates and hence their compactness, uniformity and stability by the addition of inorganic anions (well known phosphates, silicates or carbonates - reaction 2.7-2.9) or chelating organic compounds (such as triazoles - reaction 2.10) forming slightly soluble Zn(II) compounds with a broader pH stability range than for Zn(II) in anionic free solution (Fig. 2.8).



Each of mentioned specie will be considered in details below.

#### Action of phosphates and silicates

Very little is known in the scientific literature about the  $\text{PO}_4^{3-}$  and  $\text{Si}_2\text{O}_5^{2-}$  action as water soluble inhibitors on Zn with an extensive amount of the literature available on the formation and the corrosion performance of the phosphate and silicate conversion coatings [89–94]. Aramaki [63] reported a high inhibition efficiency of 90 % for  $10^{-2}$  M  $\text{PO}_4^{3-}$  and  $10^{-4} - 10^{-2}$  M  $\text{Si}_2\text{O}_5^{2-}$  in aerated 0.5 M NaCl with adjusted pH values of 7. Relatively thin layers of corrosion products were mainly composed of  $\text{Zn}(\text{OH})_2$  with a small quantities of  $\text{ZnSi}_2\text{O}_5$  in the case of  $\text{Si}_2\text{O}_5^{2-}$  additions and of  $\text{Zn}_3(\text{PO}_4)_2$  in the case of  $\text{PO}_4^{3-}$  additions. The precipitates were mainly accumulated at spots on the corroded Zn surface, resulting in the inhibition of anodic process. Wang et al [61] reported the inhibition efficiency of 67 % for  $10^{-3}$  M  $\text{Na}_2\text{SiO}_3$  in 0.01 M  $\text{H}_2\text{SO}_4$ . The Si-rich film growth follows a mix-parabolic law, corresponding to a process controlled by both ion diffusion and surface reaction.

#### Action of carbonates

Always present in the atmosphere, contamination by carbonates constantly render the reactivity of Zn substrates exposed under air. The calculated total concentration of carbonates leading to the extension of the passivity domain of Zn was  $> 4$  mM [96–98] that about 10 times more than 0.3 mM of carbonates contained in aqueous solutions under air at 1 atm and 25 °C [99]. The extension of Zn passivation was attributed to the formation of slightly soluble  $\text{ZnCO}_3$  and/or  $\text{Zn}_5(\text{OH})_6(\text{CO}_3)_2$ . Recently, Salguero Azevedo et al. [55] showed for Zn3Mg3.7Al alloy that the presence of 0.01 M  $\text{NaHCO}_3$

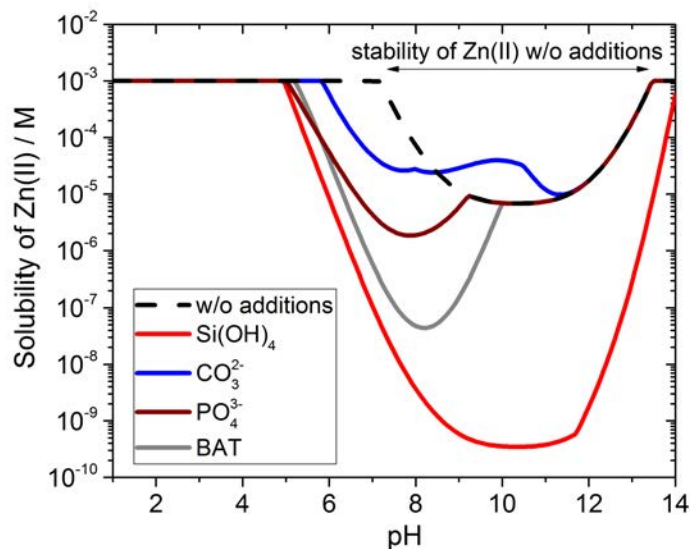


Figure 2.8: Solubility of 0.001 M Zn(II) species in the presence of 0.01 M  $\text{Si(OH)}_4$ , 0.01 M  $\text{CO}_3^{2-}$ , 0.01 M  $\text{PO}_4^{3-}$  or bisaminotriazole (BAT) as a function of pH in the aqueous solution. The diagram was calculated using Hydro Medusa software [33]. The species taken into account include  $\text{Zn}^{2+}$ ,  $\text{Zn(OH)}_2$ ,  $\text{Zn(OH)}_3^-$ ,  $\text{Zn(OH)}_4^{2-}$ ,  $\text{Zn}_2(\text{OH})_6^{2-}$ ,  $\text{Zn}_2(\text{OH})_6^{3+}$ ,  $\text{Zn}_4(\text{OH})_4^{4+}$ ,  $\text{ZnOH}^+$ ,  $\alpha\text{-Zn(OH)}_2$ ,  $\text{e-Zn(OH)}_2$ ,  $\text{ZnO}$ ,  $\text{CO}_3^{2-}$ ,  $\text{CO}_2$ ,  $\text{H}_2\text{CO}_3$ ,  $\text{PO}_4^{3-}$ ,  $\text{H}_2\text{PO}_4^-$ ,  $\text{H}_3\text{PO}_4$ ,  $\text{HCO}_3^-$ ,  $\text{HPO}_4^{2-}$ ,  $\text{Si}_2\text{O}_2(\text{OH})_5^-$ ,  $\text{Si}_2\text{O}_3(\text{OH})_4^{2-}$ ,  $\text{Si}_3\text{O}_6(\text{OH})_3^{3-}$ ,  $\text{Si}_3\text{O}_8(\text{OH})_5^{3-}$ ,  $\text{Si}_4\text{O}_7(\text{OH})_5^{3-}$ ,  $\text{Si}_4\text{O}_8(\text{OH})_4^{4-}$ ,  $\text{SiO(OH)}_3^-$ ,  $\text{SiO}_2(\text{OH})_2^{2-}$ ,  $\text{Zn(CO}_3)_2^{2-}$ ,  $\text{ZnCO}_3$ ,  $\text{ZnHCO}_3^+$ ,  $\text{SiO}_2$ ,  $\text{Zn}_2\text{SiO}_4$ ,  $\text{Zn}_3\text{PO}_4 \cdot 4\text{H}_2\text{O}$ ,  $\text{Zn}_5(\text{OH})_6(\text{CO}_3)_2$ ,  $\text{ZnCO}_3 \cdot \text{H}_2\text{O}$  and  $\text{ZnSiO}_3$  of standard database of Hydro Medusa [33]. The formation constant of  $\text{Zn(BAT)}_2$  were added manually as 13.9 with the the protonation constant of BAT as  $\text{pK}_1 = 1.0$  and  $\text{pK}_2 = 8.2$  [95].

in 0.1 M NaCl indeed results in the accumulation of slightly soluble Zn(II) species under anodic polarization. However, it did not decrease the total anodic current and hence, did not passivate Zn. The detailed investigation by Laska et al. [37] of the effect of  $\text{HCO}_3^-$  on Zn permitted to distinguish two situations: (i) for  $< 1 \text{ mM HCO}_3^-$ , the initial corrosion attack was slowed down due to pH buffering; (ii) for  $\geq 1 \text{ mM HCO}_3^-$  carbonate converted the native Zn oxide layer into Zn (hydroxy) carbonates resulting in a temporally increased corrosion however, while oxide layer was formed strong inhibition of cathodic reaction was observed. The cross section of the morphology of Zn patinas formed after 1 hour of the immersion show that the compactness of the layers increased with concentration of  $\text{HCO}_3^-$ , which correlated well with the decrease of the polarization resistance of the coatings (Fig. 2.9) [37].

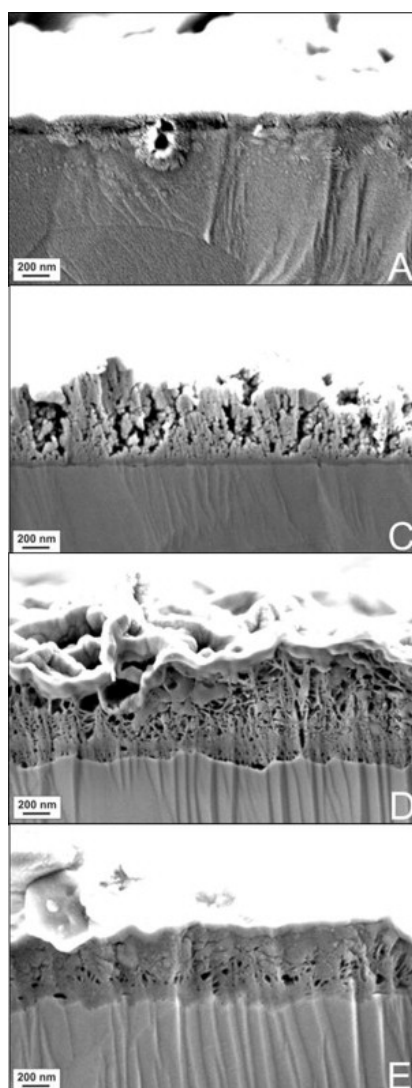


Figure 2.9: SEM images (cross sections) of corrosion precipitates on Zn formed after 1 hour at open circuit potential in solutions A, and C-E, A 0.1 M NaCl, C 0.1 mM NaHCO<sub>3</sub> + 0.1 M NaCl, D 1 mM NaHCO<sub>3</sub> + 0.1 M NaCl, and E 10 mM NaHCO<sub>3</sub> + 0.1 M NaCl [37].

### Action of organic chelating agents

Organic inhibitors are commonly separated from inorganic when classifying the corrosion inhibitors based on the specification of chemical species [41, 100–106]. However, this separation can be mislead when considering the inhibition mechanisms because a big part of organic inhibitors act similar to inorganic anion inhibitors with the formation of low soluble Zn(II) compounds [107–110, 110, 111, 111–114]. The organic inhibitors acting by this mechanism are briefly reviewed below.

As a typical example of chelating organic inhibitors, Fig. 2.8 shows the extent of stability of Zn(II) slightly soluble species in the presence of bisaminotriazole (BAT) from pH values of 7 – 13 in BAT free solutions to pH values of 5-13 with a lower solubility of formed Zn(II) species. Inhibiting effect on Zn was reported for 8-hydroxyquinoline and quinolone derivatives [108], phosphonium salts [115, 116], triazole and triazole derivatives [112, 113] and milk casein inhibiting effect [114] on Zn can be found. Leroy [110, 111] has been reported the most detailed review with the investigation of more than seventy compounds suitable to act as chelating agents on Zn. The observed corrosion protection of such inhibitors resulted from simultaneous actions of two mechanisms: (i) direct reaction with metal ions while they are still bound up in the lattice of metal surface or surface oxides and (ii) the formation of slightly soluble Zn(II) complexes with already dissolved  $Zn^{2+}$  ions [110, 111]. The inhibition efficiency ( $\eta$ ) of these compounds can be comparable to the inhibition efficiency of Cr(VI). Aramaki [117] reported  $\eta$  of  $10^{-6}$  M sodium S-octyl-3-thiopropionate equaled to 95 % after 3 hours of the immersion in aerated 0.5 M NaCl. 8-quinol, sodium benzoate showed similar  $\eta$  of 95 % at higher  $10^{-2}$  M concentrations. In all cases, the surface observation by XPS revealed the presence of  $Zn(OH)_2$  and ZnO and small quantity of Zn(II) chelate compounds [117].

---

- ✓ **The potential application of anionic inhibitors in hybrid coatings will require the use of anionic nanocontainers such as layered double hydroxides (LDH). Between the considered anionic species ( $PO_4^{3-}$ ,  $Si_2O_5^{2-}$ ,  $CO_3^{2-}$  and BAT, and Mo(IV) in section 2.2.1) Mo(IV) has the lowest solubility in a wide pH range (compare Fig. 2.8 and Fig. 2.5) leaving  $MoO_4^{2-}$  the best candidate for the intercalation into anionic nanocontainers.**
  - ✓ **A little is known about the action of phosphates and silicates on Zn as a water soluble inhibitor whereas the major part of the literature devoted to the investigation of conversion coatings.**
  - ✓ **Effects of carbonates, which are always present in the solution under air, on Zn reactivity cannot be neglected.**
  - ✓ **Chelating organic molecules can efficiently inhibit Zn corrosion through the formation of Zn(II) organo precipitates and the direct reaction with Zn or the corrosion products.**
- 

#### 2.2.4 Adsorption on Zn surface

The last class of inhibitors act through adsorption on Zn metal or/and into the surface oxides sealing the pores in Zn outer precipitated layer [41, 100–106]. Formed adsorbed layer may partially block the cathodic or/and anodic sites, increase the com-

compactness of the outer Zn(II) precipitated layer and being hydrophobic may repel the corrosive species from the surface and hence, improve the corrosion performance [41, 103]. Organic molecules are the typical and the most studied examples of this type of inhibitors [41, 100–106]. Beside the mentioned in the previous section, in this case organic molecules can form soluble complexes with  $Zn^{2+}$  and hence, does not form the Zn(II) precipitates.

As typical examples of these inhibitors on Zn, amino-pyrazole derivatives [118], substituted N-arylpyrroles [119], organic onium compounds [120], benzene thiols [121], C<sub>10</sub>-C<sub>12</sub> amines [122], non-aliphatic amino acids [103] were studied. Adsorption properties of the mentioned molecules are related to the presence of polar functional groups with S, O or N atoms in the molecule, heterocyclic compounds and pi electrons usually regarded as the reaction center for the establishment of the adsorption center [41, 100–106]. The surface coverage ( $\theta$ ) of adsorbed inhibitors was shown to follow Langmuir (Eq. 2.11), Temkin (Eq. 2.12) or Frumkin (Eq. 2.13) isotherms [60]

$$\theta = \frac{KC}{1 + KC} \quad (2.11)$$

$$\theta = K_1 \ln(K_2 C) \quad (2.12)$$

$$KC = \frac{\theta}{1 + \theta} e^{-2A_F \theta} \quad (2.13)$$

where  $C$  is the concentration of the inhibitor in the solution;  $K$ ,  $K_1$  and  $K_2$  - constants and  $A_F$  - parameter associated with the interaction of adsorbed molecules. It is often assumed that the adsorbed molecule block hydrogen reduction/recombination in a 1:1 manner without changing the mechanism of HER [60, 123]. Within the limits of this assumption,  $\theta$  can be defined from the corrosion rates as

$$\theta = \frac{v^0 - v_{corr}}{v^0 - v'} \quad (2.14)$$

where  $v_{corr}$  is the corrosion rate a given concentration of the inhibitor,  $v^0$  is the corrosion rate in inhibitor free solution and  $v'$  is the corrosion rate at the highest inhibitor concentration, i.e.  $\theta \rightarrow 1$ . Eq. 2.14 is often used to connect surface coverage and corrosion currents in the case of ORR as the empirical relation. The common parameter defined within the described mathematical model is standard Gibbs energy of adsorption ( $\Delta G^0$ ), which serves a criteria of how strong the adsorption and hence, protective properties of adsorbed layer, are. Empirically defined  $\Delta G^0 > -20$  kJ/mol corresponds to the physical adsorption whereas  $\Delta G^0 < -30$  kJ/mol corresponds to the chemisorption of the organic inhibitors [124]. **The major drawback of the considered model is that the complexation of organic molecule with metal ions into the solution bulk is ignored. In contrast to the formation of adsorbed layer, this phenomenon can enhance the metal dissolution. The latter hypothesis requires additional examination.**

The inhibition efficiency on Zn in the presence of adsorbent agents can be comparable to Cr(VI). For  $10^{-4} - 10^{-3}$  M organic onium compounds in 1 M  $H_3PO_4$   $\eta$  was about 99

% with  $\Delta G^0 = -60 - -40 \text{ kJ mol}^{-1}$  [120].  $5.0 \times 10^{-3} \text{ M}$  substituted N-arylpyrroles in  $0.5 \text{ M NaCl}$  inhibited Zn with  $\eta$  of about 95 % observed in polarization experiments, electrochemical impedance and weight loss measurements [119].  $10^{-6} \text{ M}$  n-decylamine for  $n = 3$  and 9 in  $0.1 \text{ M HClO}_4 + 0.01 \text{ M I}^-$  inhibited Zn dissolution with  $\eta$  of about 90 % and  $\Delta G^0 = -35 \text{ kJ mol}^{-1}$  [122].

In spite of the high inhibition efficiency of the mentioned compounds, they cannot be applied at industrial scale due to their biological toxicity and harmful characteristics [104, 106]. To overcome this problem, “green” organic inhibitors were proposed, which are non-toxic, biodegradable and do not accumulate into living cells [100, 102–104, 106]. As potential candidates organic molecules extracted from natural sources such as plants or animals, synthetic drugs and natural L-amino acids have been proposed. The amino acids are the most promising candidates due to their relatively low cost in comparison to synthetic drugs and higher stability than extracts from plants and animals [100, 102–104, 106].

The L-amino acids have been successfully tested for mild steel, carbon steel, stainless steel, iron, nickel, copper, aluminum, and its alloys and different alkaline and acid aggressive medias [104]. However, a little knowledge is accumulated about the effect of amino acids on Zn based substrates. Studied for Mg1Al1Zn alloy at pH 7 in phthalate buffer solution, amino acids at  $10^{-3} \text{ M}$  showed  $\eta$  of about 80-90 % with the highest inhibition efficiency for the L-cysteine and L-phenylalanine [125]. The inhibiting properties were correlated with the presence of –SH group responsible on the adsorption on Mg1Al1Zn alloy [125]. Further detail investigation is required to reveal the action of L-amino-acids on Zn.

- 
- ✓ **Action of natural amino acids on Zn as potential green inhibitors is poorly documented. Referring to the better adsorption of organic compounds with functional donor atoms such as S, N or O, some amino acids such as L-cysteine and L-phenylalanine can act as an inhibitor on Zn and hence, actions of amino acids on Zn are worth a detailed examination. The potential problem often neglected in the literature consists in the ignoring of the complexation of organic molecules with  $\text{Zn}^{2+}$ . Organic molecules can form soluble complexes that potentially can enhance the metal dissolution. To observe the possible effects of the complexation of organic molecules, the action of selected amino acids needs to be considered at different time scales and concentrations.**
-



---

# Controlled inhibition by hybrid anticorrosion coatings

---

This chapter is a continuation of the literature review on the protection methods for galvanized steel by hybrid anticorrosion coatings. In Chapter 2, the mechanisms of action of different water soluble inhibitors, which can be potentially used in hybrid coatings, was considered. In this chapter we will focus on the mechanisms of the release of a water soluble inhibitor from different coated systems.

The inhibitor embarked into a hybrid coating remains encapsulated in the nano/micro host systems until an external trigger is applied to the coating [7, 10]. It could be either a physical impact, like mechanical stress, temperature or UV light, or a chemical stimulus, like a change of pH value, or the exposure to other species like aggressive anions in aqueous solutions [7, 10]. The trigger of the inhibitor release as a function of the type of the nano/micro host systems is summarized in Table 3.1. The paramount role of the host systems consist in the local and fast release of the inhibitors in the regions where the corrosion occurs, often accompanied by the presence of aggressive ions such as  $\text{Cl}^-$ ,  $\text{HCO}_3^-/\text{CO}_3^{2-}$  and  $\text{OH}^-$ . The mechanisms of the release of entrapped chemicals from nanocontainers has been extensively studied for the drug release application [129–136]. Table 3.2 presents the summary of the kinetics models proposed in these studies. However, very little knowledge has been accumulated about the inhibitor release from hybrid

Table 3.1: Encapsulation systems and responsiveness towards specific stimuli.

System / Trigger	$\text{H}_2\text{O}$	$\text{Cl}^-$	pH decrease	pH increase	Reference
no host	X				[7, 84–87, 126–128]
oxide nanoparticles	X				[84–86]
polyelectrolyte shells				X	[126–128]
zeolites			X		[87]
layered double hydroxides		X	X	X	[12–19]

Table 3.2: Kinetic models used for the analysis of drug nanoparticle release.  $Q$  denotes the fraction of drug release,  $Z$  is the probit of fraction of drug release at any time,  $Z_0$  is  $Z$  at  $t = 0$  and  $k, t_d, n_r, m_r$  are the parameters of the models,  $t$  is the time. Adapted from [129, 130]

$N_o$	Model name	Model
1	Zero model	$Q = kt$
2	First order	$\ln(1 - Q) = -kt$
3	Higuchi	$Q = kt^{1/2}$
4	Power law	$\ln Q = \ln k + n_r \ln t$
5	Hixson-Crowell	$1 - (1 - Q)^{1/3} = kt$
6	Square root of mass	$1 - (1 - Q)^{1/2} = kt$
7	Three seconds root of mass	$1 - (1 - Q)^{2/3} = kt$
8	Weibull	$\ln(-\ln(1 - Q)) = -k \ln t_d + k \ln t$
9	Liner probability	$Z = Z_0 + kt$
10	Log - probability	$Z = Z_0 + k \ln t$
11	Non conventional order 1	$1 - (1 - Q)^{(1-n)} = (1 - n)kt$
12	Non conventional order 2	$(1 - Q)^{(1-n)} - 1 = (n - 1)k$
13	Reciprocal powered time	$(1/Q - 1) = m_r/t$

anticorrosion coatings. Below the controlled release from different hybrid anticorrosion coating will be considered on the basis of three release mechanisms:

1. desorption controlled release,
2. pH-controlled release
3. ion-exchange controlled release.

### 3.1 Desorption controlled release

The first example of smart coatings presented here will be model silica based hybrid sol-gel film (further sol-gel film). Sol-gel films combine flexibility, good mechanical properties and adhesion to the metallic substrate. They do not possess active corrosion protection, serving only as a mechanical barrier. These factors make sol-gel films an ideal model matrix to study the release and the inhibition by different encapsulated inhibitors [137, 138]. Herein, the summary of several works conducted by Zheludkevitch et al [84, 85] and Lamaka et al [86] with sol-gel films doped with oxide nanoparticle reservoirs on Al2024-T3 in 0.005 M and 0.05 M NaCl naturally aerated solutions will be presented.

On the first step, different inhibitors such as  $\text{Ce}(\text{NO}_3)_3$  [84, 85] ions and benzotriazole [86] were directly incorporated into sol-gel films. It resulted in a harmful effect on the stability and barrier properties of the films due to the promotion of the water uptake with the immersion time in the presence of inhibitors in the matrix and hence, the formation of fragile films. Moreover, the release of inhibitors in this case was spontaneous and fast. The stock of inhibitors ended after a relatively short time (100 h) of the immersion.

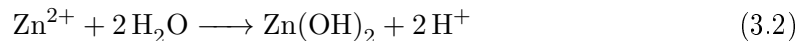
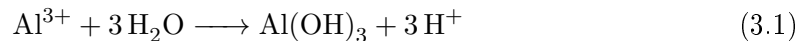
The incorporation of undoped TiO<sub>2</sub> [86] or ZrO<sub>2</sub> [84, 85] nanoparticles into sol-gel matrix already showed the reinforcement of the coating matrix against the water uptake that improved its mechanical stability during the immersions. Following addition of the TiO<sub>2</sub> doped with Ce(NO<sub>3</sub>)<sub>3</sub> and benzotriazole, and ZrO<sub>2</sub> doped with Ce(NO<sub>3</sub>)<sub>3</sub> provided the active corrosion protection by the slow release of the inhibitors and their inhibiting effect on the substrate. XPS analysis of ZrO<sub>2</sub> doped with Ce(NO<sub>3</sub>)<sub>3</sub> revealed that the presence of Ce(III) decreased of electron binding energy of Zr(IV) from 182.8 eV to 182.1 eV (corrected for C<sub>1s</sub> at 285.0 eV), indicating Ce(III) directly interacts with ZrO<sub>2</sub> nanoparticles by an adsorption or absorption [85].

The desorption of the inhibitors from doped TiO<sub>2</sub> or ZrO<sub>2</sub> occurs immediately after the contact of the nanoparticles with the electrolyte [84–86]. Its rate is defined by the nature of adsorbed/absorbed compounds and the temperature of the environment but not by the parameters accompanying the corrosion process (pH change, presence of aggressive species). Thus, the role of doped nanocontainers consists only in the prolongation of the inhibitor release and cannot provide the inhibitor release on demand triggered by the corrosion propagation.

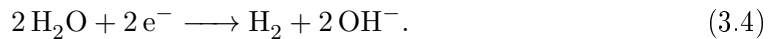
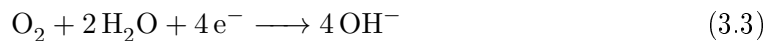
- 
- ✓ **Nanoparticles (ZrO<sub>2</sub>, TiO<sub>2</sub>) doped with the corrosion inhibitors can be used in hydride smart coatings to prolong the inhibitor release in comparison with the inhibitor release directly placed in the coating but they cannot provide the inhibitor release on demand triggered by the corrosion propagation.**
- 

## 3.2 pH-controlled release

The corrosion activity is always accompanied by the pH change on the local anodes due to hydrolysis of dissolved metal ions as an example for Al and Zn in reactions 3.1 and 3.2 [23, 33, 139, 140]



or/and the local cathodes due to oxygen/water reduction (reactions 3.3 and 3.4) [23, 30, 33, 139]



Therefore, the most relevant trigger of the release of the corrosion inhibitor is the pH change in the context of the corrosion protection in the smart coatings. This section is devoted to the application of the pH sensitive polyelectrolyte shells synthesized by Layer-by-Layer (LbL) assembly technique as potential reservoirs for the corrosion inhibitors in the hybrid coatings. The review is mainly based on the works of Shchukin et al [126–128]

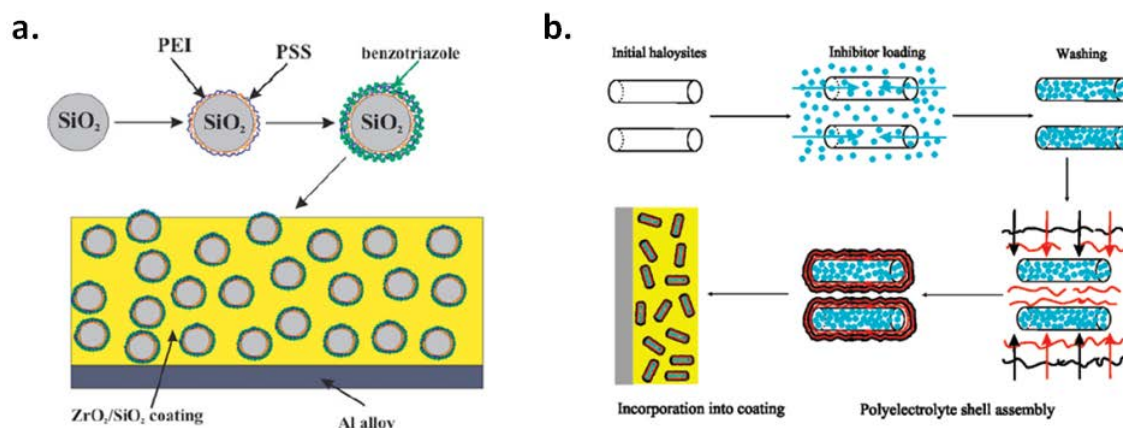


Figure 3.1: Schematic illustration of the fabrication of polyelectrolyte shells with entrapped inhibitors on (a)  $\text{SiO}_2$  and (b) halloysites hosts. Figures are adapted from [126, 128].

in 0.5 M, 0.05 M or 0.005 M NaCl naturally aerated solutions with modified  $\text{SiO}_2$  and hollow tubular aluminosilicate particles (halloysite), incorporated into  $\text{ZrO}_2$ - $\text{SiO}_2$  sol-gel coatings on Al2024-T3 alloy.

The LbL assembly technique consists in the alternate application of polyelectrolyte layers on a supporting host such as spherical  $\text{SiO}_2$  [127, 128] or tubular halloysite [126] (Fig. 3.1). To produce inhibitor loaded pH sensitive shell, the deposition of poly(ethylene imine)/poly(styrene sulfonate) (PEI/PSS) or poly(allylamine hydrochloride)(PAH)/PSS layers followed by benzotriazole or 2-mercaptobenzotriazole molecules was performed as shown in Fig. 3.1. The final reservoirs have a  $\text{SiO}_2$ /PEI/PSS/benzotriazole/PSS/benzotriazole and 2-mercaptobenzotriazole/halloysite/PAH/PSS layered structures. The inhibitor content for the final  $\text{SiO}_2$  based particles was 96 mg per 1 g of  $\text{SiO}_2$  nanoparticles [127, 128] and for the final halloysite based particles was 25 mg per 1 g of halloysite [126].

PEI/PSS and PAH/PSS layers do not permit the entrapped inhibitor to release at neutral pH but in alkaline pH the polyelectrolytes become porous that enables the inhibitor release. The study of leaching from 2-mercaptobenzotriazole/halloysite/PAH/PSS showed that approximately 30 days are required at pH 10 to release 90 % of the inhibitor whereas at pH 6 the inhibitor remained entrapped during up to 30 days of the experiment [126]. The inspection of the substrate coated with halloysite-containing sol-gel film showed higher impedance values with smaller corrosion activity and improved barrier properties compared to the blank sol-gel coatings.

The scanning vibrating electrode technique (SVET) inspection revealed the appearance of a high cathodic current density in the origin of the defect from the first minutes of the immersion of the blank sol-gel coating. For the sample with  $\text{SiO}_2$ -containing sol-gel film, only after the immersion for 24 hours the cathodic current was detected in the defect [127, 128]. However, after 26 hours, the onset of the suppression of corrosion current was observed whereas after 48 hours, the cathodic activity in the defects became

almost undetectable again. The active corrosion protection in the defect was related to the inhibitor release triggered by local pH increase due to oxygen reduction.

- 
- ✓ **SiO<sub>2</sub> or halloysite particles modified with pH sensitive polyelectrolytes can serve as a container for corrosion inhibitors and can be applied for the smart coatings. The advantage of these coatings consists in the release of the inhibitor on demand when the corrosion is triggered by local pH increase.**
- 

### 3.3 Ion-exchange controlled release

Increasing the complicity in term of the inhibitor release from the simple desorption and the pH triggered release, another type of nanoreservoirs based on the release by the ion-exchange was proposed. As in the previous section, pH can also trigger the release from ion-exchangeable reservoirs since the change of pH is determined by the excess of cations H<sup>+</sup> or anions OH<sup>-</sup> but the mechanism of release is totally different. First, the cation-exchanger will be considered.

Bentonite proposed as a cation exchanger consists of stacks of negatively charged aluminosilicate sheets, between which cation-inhibitors can be intercalated. Ca(II) and Ce(III) doped bentonites dispersed into polyester were applied to galvanized substrates in order to inhibit coating delamination from the cut edge of samples [88]. The corrosion performance was evaluated from the measurement of delamination rate under exposure to continuous salt spray test (SST) during 1000 hours. The results showed that the Ce(III) doped bentonites additions outperformed SrCrO<sub>4</sub> pigments during the whole SST test [88].

Zeolites or crystalline-aluminosilicates are another example of the cation exchangers, which consists of an array of corner-sharing SiO<sub>4</sub><sup>4-</sup> or AlO<sub>4</sub><sup>5-</sup> tetrahedrals [141]. These building blocks become arranged in a periodic way to form channels and cages with large specific surface areas, typically above 300 m<sup>2</sup> g<sup>-1</sup> with the volume of internal voids above 0.1 cm<sup>3</sup> g<sup>-1</sup>. The internal surface of voids is negatively charged that provides to zeolites adsorption, catalytic and cation-exchange properties [141]. Dias et al [87] reported a successful application of Ce(III) cations doped NaX zeolites (Na<sub>x</sub>Al<sub>58</sub>Si<sub>134</sub>O<sub>384</sub> × ZH<sub>2</sub>O) loaded in SiO<sub>2</sub> based sol-gel coating on Al2024-T3 alloy in 0.5 M NaCl. In the leaching tests, Ce(III) doped NaX zeolites were shown to exchange Ce(III) ions with H<sup>+</sup>: 69 % of Ce(III) were released at pH 2.6, while at pH 8.8 the release of Ce(III) was not observed in 0.5 M NaCl. Under the immersion of the coating with an artificial scratch, local acidification of the surface at cathodic sites due to hydrolysis of dissolved Al<sup>3+</sup> provoked the release of Ce(III). Further, the released Ce(III) cations precipitated at the cathodic areas where the local pH increased, inhibiting the cathodic reaction [87].

In spite of the successful application of cation-exchangers in several coated systems, the release of the inhibitor in this case can be triggered by the metal cations available in the surroundings. The presence of cations may not be directly associated with the

Table 3.3: Summary of tested LDH hybrid coatings.

Substrate	LDH	Media	Reference
Al2024-T3/bisphenol epoxy resin	$Zn_2Al/-V_{10}O_{28}^{6-}$	0.5 M NaCl	[13]
Al2024-T3/polyvinyl butyral	$Mg_2Al/-CrO_4^{2-}$ $Mg_2Al/-NO_3^-$ $Mg_2Al/-CO_3^{2-}$	0.5 M HCl	[14]
Al2024-T3/polyvinyl butyral	$Mg_2Al/-$ benzotriazole $Mg_2Al/-$ ethyl xanthate $Mg_2Al/-$ oxalate	0.5 M HCl	[15]
Al2024-T3/water-based epoxy resin	$Zn_2Al/-V_2O_7^{4-}$	0.5 M NaCl	[16]
Al2024-T3/sol-gel layer with water-based epoxy primer	$Zn_2Al/-$ 2-mercaptobenzothiazole $Zn_2Al/-VO_x$ $Zn_2Al/-H_xPO_4$ and their combination	0.5 M NaCl	[17]
Al2024-T3/mix of epoxy resin and polyamines	$Zn_2Al/-$ 4-aminobenzenesulfonic acid $Zn_2Al/-$ 3-aminobenzenesulfonic acid $Zn_2Al/-$ 3,4-dihydroxybenzoic acid	0.5 M NaCl	[12]
Al2024-T3/epoxy resin	$Zn_2Al/-$ 2-hydroxyethyl phosphate $Mg_2Al/-$ 2-hydroxyethyl phosphate	0.005 M NaCl	[18]
Carbon steel/bisphenol epoxy resin	$Mg_2Al/-$ 2-benzothiazolythio-succinic acid	0.1 M NaCl	[19]

corrosion process, which can lead to the loss of the inhibitor. Moreover, in the case of Zn based substrates, local acidification is less favorable than in the case of Al alloy due to weak hydrolysis of  $Zn^{2+}$  ions [23, 30, 33, 139, 140]. Therefore, there is a dubious use of  $H^+$  triggered zeolite doped particles for hydride coatings on Zn based substrates. Further, layered double hydroxides (LDH) will be considered as anion-exchangers for the application in the smart coatings.

The first compounds later classified to LDH type were discovered in Sweden around 1842 in a form of minerals that can be easily crushed into a white powder similar to talc after which it was named as hydrotalcite ( $Mg_6Al_2(OH)_{16}CO_3 \times 4H_2O$ ) [142]. After considerable time past, in 1941 Frondel [143] recognized the interrelations in the structure between the several hydrotalcite-minerals whereas already in 1942 Feiknecht [144, 145] decipher its complete structure. To understand the structure of these compounds it is necessary to start from the structure of brucite ( $Mg(OH)_2$ ) where octahedral Mg(II) (6-fold coordinated to OH-) share edges to form infinite sheets. These sheets are stacked on

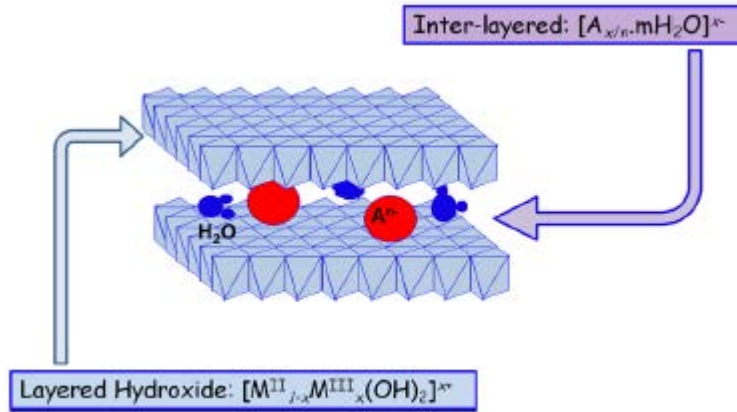
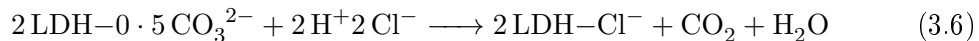
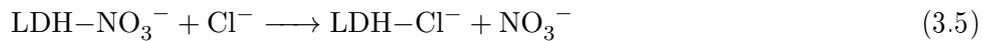


Figure 3.2: Structure of layered double hydroxide materials where M(II) and M(III) represents di and trivalent metal atoms and A - intercalated anions [7].

top of each other and are held together by hydrogen bonding (Fig. 3.2). When Mg(II) ion are substituted by a trivalent ion with a not very different radius (such as Fe(III), Al(III), Cr(III), Sc(III) etc) a positive charge is generated in the hydroxyl sheet. This net positive charge can be compensated by different anions such as  $\text{CO}_3^{2-}$ ,  $\text{NO}_3^-$ ,  $\text{Cl}^-$ ,  $\text{MoO}_4^{2-}$ ,  $\text{PO}_4^{2-}$ ,  $\text{CrO}_4^{2-}$  etc, which lie in the interlayer region between the two brucite like sheets [142, 146]. The water of the crystallization always is kept inside the free space of this interlayer too. The ability to exchange the intercalated anions permitted to use LDH in catalyst, as adsorbents, in medicine as drug delivery containers and open a potential use as nanocontainers for the anion inhibitor in smart coatings [142, 146].

In the context of corrosion protection, LDH nanocontainers can play a dual role providing (i) release of anionic inhibitors and (ii) entrapment of aggressive anionic species such as  $\text{Cl}^-$ . It has been known for some time that LDH compounds act as effective halogen scavengers in polymer systems and as halide getters in aqueous solutions. Williams et al [14] reported that  $\text{Mg}_2\text{Al}/\text{-LDH}$  intercalated with  $\text{NO}_3^-$  and  $\text{CO}_3^{2-}$  decreased the rate of the filiform corrosion on Al2024-T3 in 0.5 M HCl mainly due to entrapment of  $\text{Cl}^-$  anions and neutralizing of acid media by reactions:



In the recent work, Tedim et al [147] shown that the permeability of  $\text{Cl}^-$  from 0.5 M NaCl through a coating loaded with  $\text{Zn}_2\text{Al}/\text{-}2\text{NO}_3^-$  decreased dramatically in comparison to  $\text{Zn}_2\text{Al}/\text{-}2\text{Cl}^-$  LDHs: 2.5 mM  $\text{Cl}^-$  in  $\text{Zn}_2\text{Al}/\text{-}2\text{Cl}^-$  system and  $> 0.1$  mM  $\text{Cl}^-$  in  $\text{Zn}_2\text{Al}/\text{-}2\text{NO}_3^-$  system after 400 hours of the experiment. The entrapment effect can be understood as a promoter of coatings stability from corrosion standpoint, in the sense that it will delay diffusion of “aggressive” ions to the metal surface and, consequently, the initiation of corrosion process.

Since the pioneering work of Buchheit et al [148] several groups have focused on the anticorrosion properties of LDH as a reservoir for controlling release of inhibitor, including Buchheit's [13, 19, 148], Williams' [14, 15], Zheludkevich's [11, 16, 149] and Leroux's [12, 18, 150]. The summary of their works in term of used substrates, corrosive environment, type of LDH and inhibitor and coating composition are presented in Table 3.3 with the detailed review provided in Chapter 8. **All mentioned in Table 3.3 works focused on the intercalation of different inhibitors in various LDH systems and testing them mainly on Al2024 alloy only in  $\text{Cl}^-$  containing medias. However, the natural environment contains many other species such as  $\text{SO}_4^{2-}$  and  $\text{NO}_3^-$  available from the pollutants and  $\text{HCO}_3^-$  and  $\text{CO}_3^{2-}$  available from the dissolution of  $\text{CO}_2$  [151].** It is well known from the literature that the presence of each of these anions can change both the level of inhibitor release and kinetics of the release. For example, the studies of anion exchange with  $\text{Mg}_2\text{Al}/\text{-LDH}$  have shown that the affinity of monovalent anions decreases in the row  $\text{OH}^- > \text{F}^- > \text{Cl}^- > \text{Br}^- > \text{NO}_3^- > \text{I}^-$  and for the divalent anions  $\text{CO}_3^{2-} > \text{SO}_4^{2-}$  [152], implying that the anions with greater affinity can exchange the anions with lower affinity but not vice versa. Kinetics of the anion release obeyed either parabolic law or first order law kinetics with no specific relation between anions reported [129–132, 153].

---

- ✓ **LDH anion exchangers are promising candidates for the application as a hosting system for inhibitors in smart coatings due to (i) their ability to entrap aggressive anions present in corrosive environments and (ii) the release inhibitor on demand triggered by the pH change or the presence of aggressive anions such chlorides, carbonates etc.**
  - ✓ **Release of inhibitors from LDH was performed only in  $\text{Cl}^-$  medias in corrosion research for hydride coated systems on Al2024. The role of other anions such as  $\text{CO}_3^{2-}$  and  $\text{SO}_4^{2-}$  commonly present in corrosive environments in the performance of the inhibitor release are not investigated. However, several works dedicated to the anion exchange of LDH reported their high impact of the release process.**
- 

### 3.4 General conclusions from the literature review

LDH particles are excellent candidates for the use as nanocontainers in hybrid anticorrosion coatings due to their dual ability to release an inhibitor on demand when the corrosion occurs and to entrap the aggressive anions from the corrosive environment. LDHs are the anionic nanocontainers that imply the intercalation of anionic or organic water soluble water inhibitors in their framework. The important point for the study of these inhibitors is the identification of the factors controlling the release rate.

Between the considered anionic inhibitors, molybdate is the most promising candidate for the further investigation, since when being reduced it forms almost insoluble oxides stable in a wide pH range.

Among organic inhibitors, amino acids are the most attractive and poorly studied candidates for Zn inhibition due to their biocompatibility, stability and low cost. Amino acids with donor functional groups such as S should adsorb better on Zn and hence, are the first candidates to be studied as an inhibitor for Zn. However, the harmful effect could appear if the formation of soluble complexes is favored.

Several scientific questions, which still remain open regarding the mechanisms of the action of chosen system, will be answered during this work:

- ✓ **How does the competitive formation of soluble complexes affect the inhibiting effect of organic inhibitors? (Chapters 6)**
- ✓ **What is the action of  $\text{MoO}_4^{2-}$  as a water soluble inhibitor on galvanized steel at alkaline pH? What parameters define its action? (Chapter 7)**
- ✓ **How does the release kinetics from LDHs depend on the composition of corrosive environment? (Chapter 8)**
- ✓ **What is the relationship between the release kinetics of the inhibitor from LDH anticorrosion coatings, the inhibitor action and the protection offered by the coated system? Which species in the environment can affect it? (Chapter 8)**



---

## B. Experimental section

---

Different procedures are routinely used for the screening of corrosion inhibitors including climatic tests, immersion tests, measurements of polarization resistance and corrosion currents. The major drawbacks of these methods are that (i) they cannot explain the mechanisms of degradation and (ii) their conditions are still different from the service conditions, which does not allow to rely only on their results for prediction of the service life. In this work the conventional electrochemical methods (measurement of corrosion potential, potentiodynamic polarization, electrochemical impedance spectroscopy etc) conducted in a flow electrochemical cell were coupled with real time solution analysis by inductively coupled plasma atomic emission spectroscopy (ICP-AES) to gain the comprehensive picture of the elementary electrochemical processes. The basic principles of the method are reviewed in Chapter 4 with the description of deconvolution data treatment developed in this work.

Table 3.4: List of techniques applied for surface characterization.

Common name	Abbreviation	Studied parameters	Main limitations
Scanning electron microscopy	SEM	Surface morphology compositional distribution	Lateral resolution $\approx 10$ nm
Energy-dispersive X-ray spectroscopy	EDX	Elemental distribution	Spatial resolution $\approx 1 \mu\text{m}^3$ Detection limit $\approx 0.1$ at.%
X-ray photoelectron spectroscopy	XPS	Chemical specification oxidation state environment of atoms	Spatial resolution $\approx 5 \text{ nm}^3$ Detection limit $\approx 0.1$ at.%
Raman spectroscopy	-	Chemistry of functional groups sensible to metal-O	Spatial resolution $\approx 5 \mu\text{m}^3$ Detection limit $\approx 0.5$ at.%
Attenuated total reflectance infrared spectroscopy	ATR-IR	Chemistry of functional groups sensible to metal-OH	Spatial resolution $\approx 10 \mu\text{m}^3$ Detection limit $\approx 0.5$ at.%
Glow discharge optical emission spectrometry	GD-OES	Elemental depth distribution	Destructive Spatial resolution $\approx 1 \text{ nm}^3$ Detection limit $\approx 10^{-5}$ at.%

### 3. CONTROLLED INHIBITION BY HYBRID ANTICORROSION COATINGS

---

Along with the electrochemical methods, the post-mortem characterization of the reactive surface was done in order to correlate the features of the charge transfer across metal/oxide/electrolyte interfaces with its composition and structure. The used methods of surface characterization are listed in Table [3.4](#).

---

## AESEC technique

---

### 4.1 Introduction

Electrochemical methods are certainly the "workhorse" techniques for the research into the mechanisms of aqueous corrosion, corrosion inhibition and metal dissolution [60, 106, 154–158]. One of the major disadvantage of conventional electrochemical methods, it is a nonselectivity of the measured electrical current: we can count the number of electrons passing through the systems but in the general case, we cannot attribute them to the specific reactions of metal oxidation or oxygen reduction etc ongoing on the metal surface [60, 154, 155, 158]. In order to separate anodic and cathodic processes, the high over potentials needs to be applied that may alter the state of the system [60, 158]. The first method proposed to overcome this problem was rotating ring disk electrode (RRDE) [159]. In spite RRDE is able to separate the anodic and cathodic reactions, it is not possible to distinguish the partial metal currents in the case of alloy dissolution [159]. In the recent decades, the development of the experimental base allowed to couple flow electrochemical cells with different analytical techniques such as inductively coupled plasma atomic emission spectrometer (ICP-AES) [154, 160–162], inductively coupled plasma atomic mass spectrometer (ICP-MS) [163–165], Raman spectroscopy [166], quartz micro balance [61, 167] in order to access the partial metal currents. In this PhD thesis a coupling of flow electrochemical cell with ICP-AES, so-called atomic emission spectroelectrochemistry (AESEC) method, was applied to screen  $\text{MoO}_4^{2-}$ , L-cysteine and L-phenylalanine as a potential water soluble inhibitors on galvanized steel.

Fig. 4.1 shows a block diagram of the AESEC technique. It consists of (A) an electrochemical flow cell where a flat metal is exposed to a flowing electrolyte; (B) a downstream ICP-AES that is used to analyze the elemental composition of the electrolyte leaving the cell; and (C) a special that is used to collect the emission intensities and electrochemical data as a function of time. Description of each part of AESEC with the treatment of AESEC data are presented below.

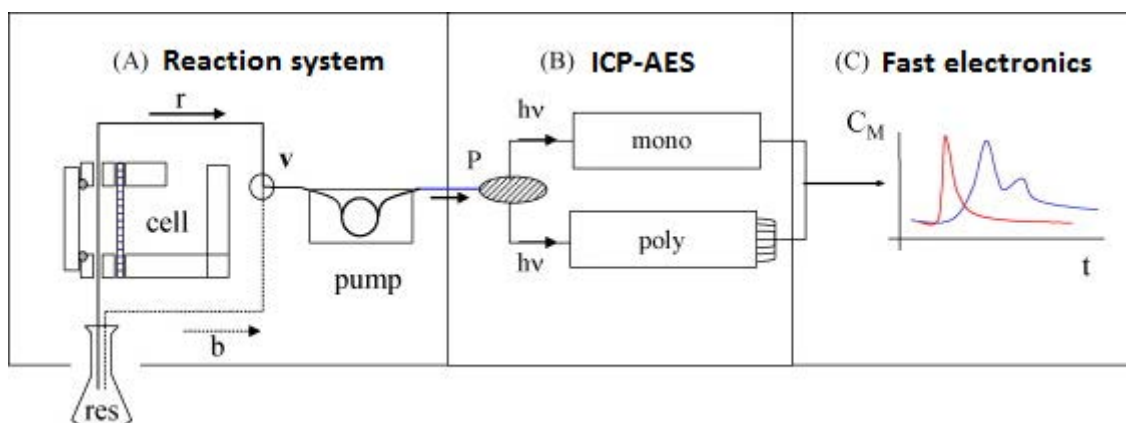


Figure 4.1: Schematic block diagram of the AESEC experiment. (A) Reaction cell with electrolyte reservoir (res) and peristaltic pump. Arrows indicate direction of the electrolyte flow during an experiment: (b) background experiment with cell bypass and (r) reaction experiment. The valve (v) is used to switch between a background and a reaction measurement. (B) ICP-AES spectrometer. (P) indicates the plasma. Photons ( $h\nu$ ) emitted from the plasma are collected in a monochromator (mono) and a polychromator (poly) unit. (C) Fast electronics allows real time monitoring the emission intensity of up to 31 wavelengths, 30 from the polychromator+1 from the monochromator as well as four analog signals for electrochemical measurements (not shown). The emission intensity is used to calculate the concentrations of specific elements ( $C_M$ ). Adapted from [161]

## 4.2 Electrochemical flow cell

Fig. 4.2 shows the schematic diagram of the flow electrochemical cell with a computer generated image. The cell is composed of two compartments: working electrode compartment with a small volume of 0.2 ml and a counter electrode compartment with a 10 ml volume. These two compartments are separated by a porous membrane, permitting the current transfer without bulk mixing of two electrolytes. Reference (Ag/AgCl saturated in this work) and counter (Pt plate in this work) electrodes are placed in the counter electrode compartment. Working electrode is placed in the working electrode compartment where it is exposed to a flowing electrolyte with a geometric surface area of  $0.51 \text{ cm}^2$  defined by the contour of the O-ring. A spring system was used in some experiments to homogenize the force of the sample against the O-ring.

The flow of the electrolyte is shown by a dashed arrow: it enters the working compartment from the bottom of the cell and leaves from the top of the cell. Hence, any gas generated during the experiment flows out of the cell. Conventionally,  $1 \text{ ml min}^{-1}$  or  $3 \text{ ml min}^{-1}$  flow rate are used in AESEC experiments. The detail description of the flow conditions of the cell along with its precise dimensions can be found in Appendix A devoted to the numerical simulation of the cell.

Gamry Reference 600<sup>TM</sup> potentiostat (Gamry Instrument, US) was used for all electrochemical experiments. The analog potential signal from potentiostat was routed into

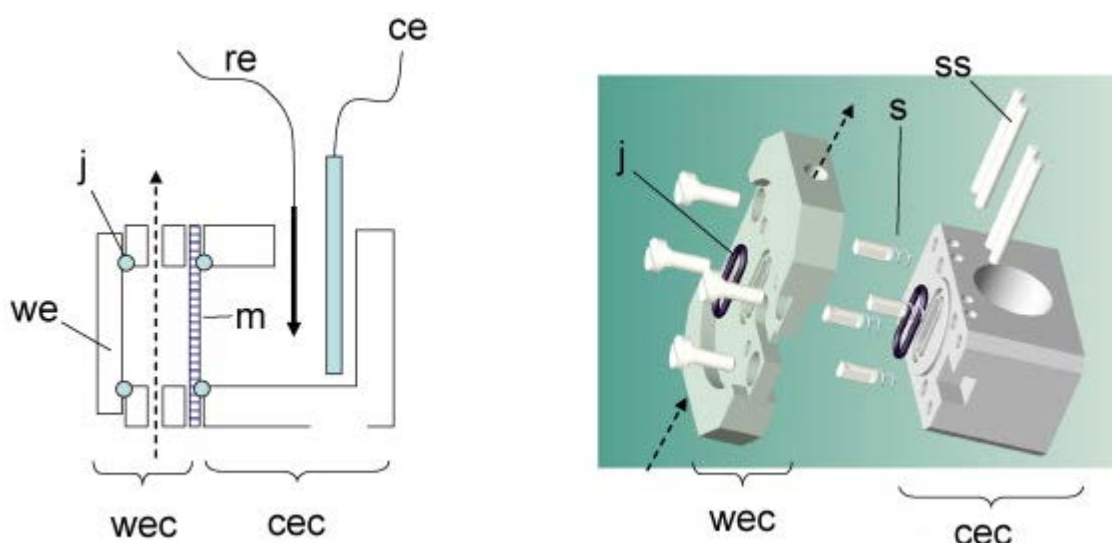


Figure 4.2: A functional diagram of the flow electrochemical cell (left) and a computer image of the cell as constructed (right). *wec* is working electrode compartment; *cec* is counter electrode compartment; *j* is O-ring; *m* is membrane; *we* is working electrode; *ce* is counter electrode; *re* is reference electrode; *s* is spring and *ss* is spring support. Dashed arrows indicate the direction of solution flow. Adapted from [161]

the measuring circuit of the ICP-AES to guarantee the same time scale for the both measurements.

### 4.3 Inductively coupled plasma atomic emission spectroscopy

Inductively coupled plasma atomic emission spectroscopy (ICP-AES) is the quantitative analytical technique, which permits to detect the most elements of the periodic table with low detection limits of  $\mu\text{g L}^{-1}$  or  $\text{mg L}^{-1}$  with the small matrix effect of the electrolyte [168, 169]. Sometimes it is referred as optical emission spectroscopy (OES) to distinguish it from Auger electron spectroscopy. In this work ICP-AES abbreviation will be used. ICP-AES was developed in XX century after the pioneering works of Stanley Greenfield in 1964 with the plasma induced in bows [170]. The general principle is based on the ionization or excitation of atoms by the energy source (plasma) leading to the emitting of the polychromatic radiation. The emitted radiation can be easily detected when it is in a vacuum ultraviolet (120-185 nm), ultraviolet (185-400 nm), visible (400-700 nm), and near infrared regions (700-850 nm) [168, 169].

#### Introduction system of ICP-AES

In this work a commercial ICP-AES from Horiba Jobin Yvon (Ultima 2C<sup>TM</sup>) was used to measure the composition of the electrolyte downstream from the working electrode compartment of the electrochemical cell. The peristaltic pump transferred the electrolyte

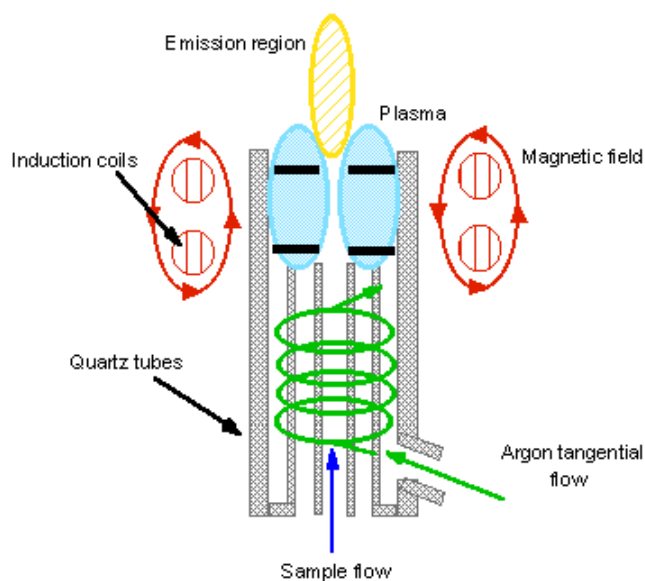


Figure 4.3: Scheme of the ICP torch. Adapted from [173].

into a concentric glass nebulizer and a cyclonic spray chamber. The Meinhard nebulizer (Model TR-30-K3) was used in this work, which has a bigger diameter than its alternative Conical nebulizer and hence, can operate at a higher flow rate of  $3 \text{ ml min}^{-1}$ . A higher flow rate yields to a better temporal resolution but lowers sensitivity due to dissolving of species into a larger volume per second of an electrolyte. However, with the bigger inner diameter, Meinhard nebulizer cannot be easily blocked by the solid particles, which can be formed easily during the metal corrosion at neutral pH in the flow cell [171,172].

### Excitation source of ICP-AES

Approximately 5 % of the electrolyte is transferred from the cyclonic spray chamber to torch with a laminar flow of  $0.1$  to  $1.0 \text{ L min}^{-1}$  and then ejected to the  $40.68 \text{ MHz}$  inductively coupled plasma, operating at  $1 \text{ kW}$ . Fig. 4.3 shows a schematic diagram of ICP torch. Besides gas inlet from the nebulizer, the circular quartz tube (with the outside diameter of  $12\text{-}30 \text{ mm}$ ) commonly has two more gas inlets: for argon and for the auxiliary gas. The Ar gas enters the plasma through the outer channel with a tangential flow pattern at a rate of  $8 - 20 \text{ L min}^{-1}$  aimed to maintain the Ar plasma. The auxiliary gas (not shown on Fig. 4.3) also has a tangential flow pattern with  $0.5 - 3.0 \text{ L min}^{-1}$  aimed to favor the transportation of analyzed solution to the analytical zone of the plasma for some specific applications. The auxiliary gas was not used in the present work.

The Ar plasma was used as it has a high ionization energy ( $15.6 \text{ eV}$ ) and a good capacity to atomize, ionize and excite most of the elements [168,169]. The analytical zone in the Ar plasma is approximately  $1 \text{ cm}$  above the coils, which offers the best optical viewing area for maximum sensitivity. The temperature of the plasma in analytical zone

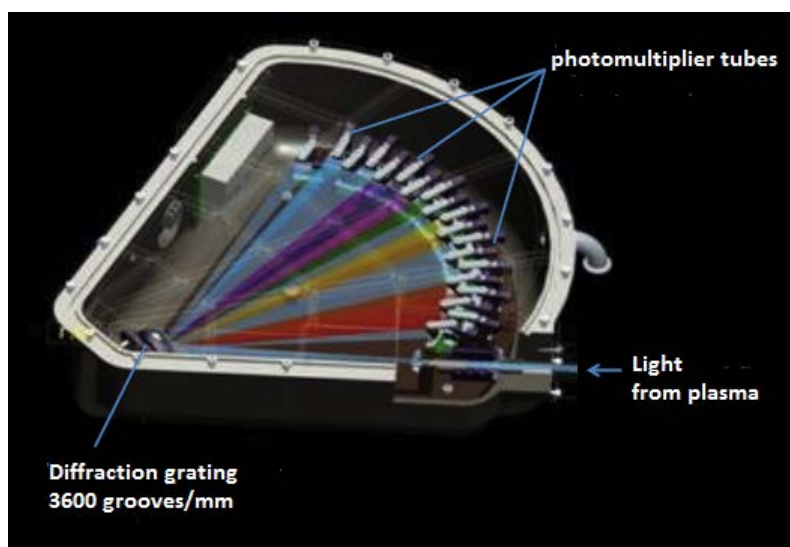


Figure 4.4: Scheme of Paschen–Runge polychromator showing the diffraction of light in Rowland circle. Adapted from [174]

ranges from 5000 - 8000 K (varies with the power, flow rates etc) [168, 169]. The high temperature assures that most samples are completely atomized determining the main features of ICP-AES: low matrix effect of the electrolyte on the detection of desired element and inability to access structural information about analyzed species.

### Dispersing system of ICP-AES

Radiation emitted from the plasma ( $h\nu$ ) was collected in the radial direction and split between a polychromator for the simultaneous detection of 30 predetermined wavelengths and a monochromator that could be used for the detection of any adjustable wavelength. The polychromator used a Paschen–Runge configuration with a 0.5 M focal plane and was equipped with a holographic grating of 3600 grooves/mm and 30 independent photomultiplier tubes (Fig. 4.4). The theoretical resolution of the polychromator was 0.025 nm in the first order and 0.015 nm in the second order covering a spectral range from 165 to 408 nm. The monochromator used Czerny–Turner configuration with a 1.0 m focal plane and was equipped with a holographic grating of 2400 grooves/mm with practical resolution of 0.005 nm in a spectral range from 120 to 320 nm and a resolution of 0.010 nm in a range from 320 to 800 nm (Fig. 4.5). Both polychromator and monochromator were nitrogen purged in order to eliminate oxygen from the system and access the excitation lines in ultraviolet region. In most of the experiments of this PhD thesis monochromator was used to detect concentration of Zn to archive better signal resolution and sensitivity.

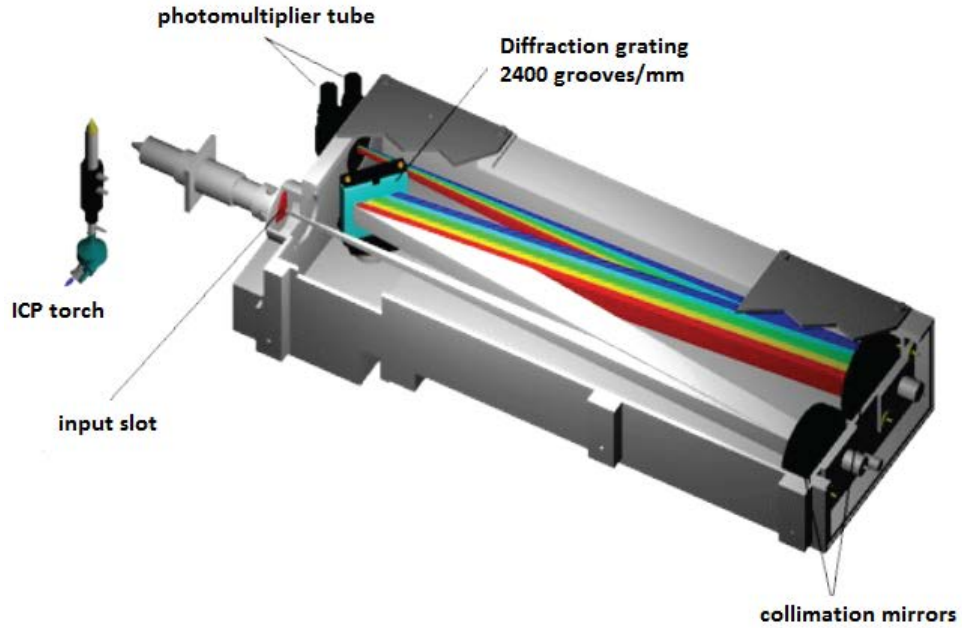


Figure 4.5: Scheme of Czerny-Turner monochromator with a 1.0 m focal plane. Adapted from [174]

### Principal of quantification of elements in ICP-AES

For a given excited atom in Ar plasma, the wavelength of an emitted ray between two energy levels  $E_n$  and  $E_m$  can be obtained by [168, 169, 174]:

$$\lambda = \frac{hc}{E_n - E_m}, \quad (4.1)$$

where  $c$  is the speed of light and  $h$  is the Planck constant ( $h = 3.336 \times 10^{-11}$  s cm<sup>-1</sup>). The intensity of this ray is given by

$$I = (E_n - E_m)n_n P \quad (4.2)$$

where  $n_n$  is the initial population of electrons and  $P$  is the probability of possible transitions per unite of time.

The Boltzmann law puts together the population  $n_n$  and the total population  $N$  of the considered ionization state:

$$\frac{n_n}{N} = \frac{g_n e^{-E_e/kT}}{Z} \quad (4.3)$$

where  $E^e$  is the excitation energy,  $g_n$  is statistical weight of the considered level,  $k$  is the Boltzmann constant ( $k = 1.3804 \times 10^{-23}$  J K<sup>-1</sup>) and  $Z$  is the partition function, i.e.

the sum of  $g_n e^{-E/kT}$  for all possible levels of the considered ionization state. From Eq. 4.1-4.3,  $I$  becomes

$$I = \frac{cg_n P N e^{-E_e/kT}}{Z\lambda} \quad (4.4)$$

This relation enables to re-connect the intensity of an emission ray with the concentration of an element in the solution by calibrating the spectrometer with the solutions of known concentrations. The obtained law is described by the equation [168, 169, 174]:

$$I_{\lambda,m} = SC_m + I_{\lambda,m}^0, \quad (4.5)$$

where  $I_{\lambda,m}$  is the intensities of different etalons,  $C_m$  is the concentration of these etalons and  $I_{\lambda,m}^0$  is the intensity of spectral background.  $S$  corresponds to the slope of the calibration curves, which gives the sensitivity of the chosen wavelength. For a solution with an unknown concentration ( $C$ ):

$$C = \frac{I_\lambda - I_{\lambda,m}^0}{S} \quad (4.6)$$

where  $I_\lambda$  is the intensity of the ICP-AES signal related to  $C$ .

#### 4.4 Fast electronics

The signals ( $I_\lambda$ ) from the phototubes (mono and poly) were monitored in real time using the Quantum<sup>TM</sup> software and data acquisition package developed by HORIBA Jobin Yvon, SAS for use with glow discharge spectroscopy. Briefly, three 16-bit A/D converters operating at a frequency of 250 kHz are used to continually monitor the output of the 31 photomultipliers. The data is transferred to the computer after averaging over a user defined integration period, in this PhD thesis set for 1 s. This means that each measured value of intensity corresponds to the average of 250000 data points. The result is that the dynamic range of the experiment is vastly increased over that of a single measurement with a 16-bit A/D converter and the data from the different channels may be considered as true simultaneous measurements.

The electronic system was further modified for the AESEC experiment to permit the introduction of four supplementary analog channels, two of which were used in this work to collect current and potential data from the Gamry potentiostat. These channels were amplified and offset to be consistent with the spectroscopic emission signals. Analysis of electronic noise demonstrated that potential measurements with this system were stable to approximately 0.05 mV. This modification ensured that the spectrometer and electrochemical data were collected with the same time base greatly simplifying the correlation of the transitory signals.

#### 4.5 AESEC data treatment

Coupling of the flow electrochemical cell with ICP-AES permits to quantify in real time the concentrations of dissolved metals in the solution by Eq. 4.6. Note, AESEC analysis shows only the soluble part of the dissolved metal cations, while the insoluble

products are not directly detected. For Zn dissolution, this soluble part can be expressed in term of the rate of metal dissolution ( $v_{Zn}$ ) [160, 161]

$$v_{Zn} = \frac{f_e C_{Zn}}{A} \quad (4.7)$$

where  $f_e$  is the flow rate of the electrolyte in the feed capillary,  $C_{Zn}$  is the instantaneous concentration of the Zn(II) species and  $A$  is the geometric surface area of the exposed metal. Normalization of  $v_{Zn}$  by  $A$  is done for the convenience and does not imply that the reactions are homogeneous on the surface. Using the Faraday's law it can be further expressed as the equivalent metal current ( $j_{Zn}$ ):

$$j_{Zn} = nFv_{Zn} \quad (4.8)$$

where  $n$  is the number of electrons ( $n = 2$  for Zn) and  $F$  is the Faraday constant (96500 s A mol<sup>-1</sup>).

The total electrical current passing through the working electrode can be expressed as a sum of the anodic and cathodic partial currents (denoted as  $j_e$ ,  $j_a$  and  $j_c$  respectively):

$$j_e = j_a + j_c \quad (4.9)$$

The AESEC technique measures the soluble component of the anodic current of metal dissolution. For Zn dissolution, the anodic current may be expressed as:

$$j_a = j_{Zn} + j_{Zn}^{ins} - 2Fv_{ZnO} \quad (4.10)$$

where  $j_{Zn}$  and  $j_{Zn}^{ins}$  correspond to the formation of the soluble Zn cations and insoluble Zn oxides respectively;  $v_{ZnO}$  represents the chemical dissolution of Zn oxides. If  $v_{ZnO}$  is negligibly small, the quantity of insoluble Zn corrosion products (denoted as  $Q_{ins}$ ) under the anodic polarization can be estimated as:

$$Q_{ins} = \int_0^t j_{Zn}^{ins} dt = \int_0^t (j_e - j_{Zn}) dt \quad (4.11)$$

where  $j_e$  is equal to  $j_a$  under the assumption of a negligible contribution of cathodic reaction to the overall current. If  $j_{Zn}^{ins}$  and  $v_{ZnO}$  are negligibly small,  $j_c$  can be estimated as

$$j_c = j_e - j_{Zn} \quad (4.12)$$

Eq. 4.11 and 4.12 can not be directly applied because the signals from the potentiostat ( $j_e$ ) and from the ICP-AES ( $j_{Zn}$ ) have very different time resolution:  $j_e$  is essentially instantaneous while  $j_{Zn}$  is broadened by the hydrodynamic influence of the flow cell. That might be corrected in two ways: either a numerical convolution of the  $j_e$  or a numerical deconvolution of  $j_{Zn}$ , in both ways using the transfer function ( $h(t)$ ).

The transfer function (or sometimes called the residence time distribution) of the flow electrochemical cell is merely the output signal of  $j_{Zn}$  after application of the input signal  $j_e$  per unit of time. 1 s time resolution was used in all AESEC experiments of

this work. In AESEC, experimental measurement of  $h(t)$  can be closely approximated by a simplified version of the log-normal function in which the pre-exponential factor is constant [160, 161]

$$h(t) = \begin{cases} \sqrt{\frac{\beta}{\pi\tau^2}} \cdot e^{-\frac{1}{4\beta}} \cdot e^{-\beta \ln^2 \frac{t}{\tau}} & \text{if } t > 0 \\ 0 & \text{if } t = 0 \end{cases} \quad (4.13)$$

where  $\tau$  is located at the peak maximum. The simplified version of the log-normal function is used only for the convenience of the approximation of the experimental data.

The application of the numerical convolution procedure of  $j_e$  was demonstrated previously in numerous publications [160, 161]. It is based on the numerical application of the convolution sum to  $j_e$ :

$$j_e^*(t) = \sum_{\zeta=0}^t j_e(\zeta)h(t - \zeta). \quad (4.14)$$

Along with its obvious simplicity, the convolution procedure has the disadvantage since that the convoluted signal  $j_e^*(t)$  includes the hydrodynamics of the flow cell, which are not related to the electrochemical processes. The numerical deconvolution of  $j_{Zn}$  would serve a better tool due to elimination of hydrodynamics of the flow cell and providing a  $j_{Zn}$  signal directly related to the electrochemical reaction at the interface.

In this work for the first time the algorithm of numerical deconvolution of  $j_{Zn}$  signal was developed and the deconvolution treatment of the AESEC data was performed.

#### 4.5.1 Development of deconvolution algorithm

The convolution of an input discrete signal  $i(t)$  in the time domain is given by the formula:

$$i^*(t) = \sum_{\zeta=0}^t i(\zeta)h(t - \zeta) \quad (4.15)$$

where  $i^*(t)$  is an output convoluted signal and  $h(t)$  is a transfer function. In term of AESEC data,  $i^*(t)$  presents the measured metal current influenced by cell hydrodynamics whereas  $i(t)$  is the true desired signal we would like to find. All considered functions will be assumed to be discrete with 1 point per second sampling rate, commonly used in AESEC analysis [160, 161].

For AESEC experiment the transfer function is usually described by an empirical function in a form of log-normal distribution [160] (Fig. 4.6 and Eq. 4.13)

Representing the Eq. 4.15 via the formulas below

$$\begin{aligned} i^*(0) &= i(0)h(0) \\ i^*(1) &= i(0)h(1) + i(1)h(0) \\ i^*(t) &= i(0)h(t) + i(1)h(t-1) + \dots + i(t)h(0) \end{aligned} \quad (4.16)$$

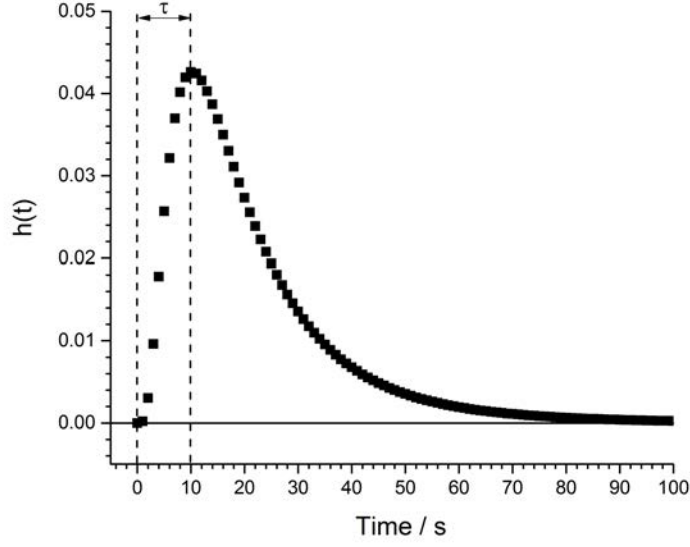


Figure 4.6: Transfer function  $h(t)$  of AESEC with the parameters  $\beta = 0.99$  and  $\tau = 10.2$  where  $\tau$  shows the position of the peak maximum.

we can express the original input signal  $i(t)$  as

$$\begin{aligned}
 i(0) &= \frac{i^*(0)}{h(0)} \\
 i(1) &= \frac{1}{h(0)} (i^*(1) - f(0)h(1)) \\
 i(t) &= \frac{1}{h(0)} (i^*(t) - i(t-1)h(1) - \dots - i(0)h(t))
 \end{aligned} \tag{4.17}$$

Further the signal  $i(t)$  obtained after the sequence of the convolution and the deconvolution procedures will be presented as  $i^{**}(t)$  in order to distinguish it from the original input signal  $i(t)$ .

The  $h(0)$  in Eq. 4.17 represents the first element of the transfer function. For our system (Fig. 4.6 and Eq. 4.13)  $h(0)$  equals to zero. Moreover, the elements at  $t = 1$  and  $2$  s ( $h(1)$  and  $h(2)$  correspondingly) are negligibly small and can be omitted (Fig. 4.6). The estimated error of the deconvolution procedure caused by the consideration of  $h(t)$  with  $t$  starting from  $3$  s would be less than  $0.4\%$ . The final formula to perform the numerical deconvolution of  $i^*(t)$  is

$$i^{**}(t) = \frac{1}{h(t_1)} \left( i^*(t + t_1) - \sum_{\zeta=1}^t i^{**}(t - \zeta)h(\zeta + t_1) \right) \tag{4.18}$$

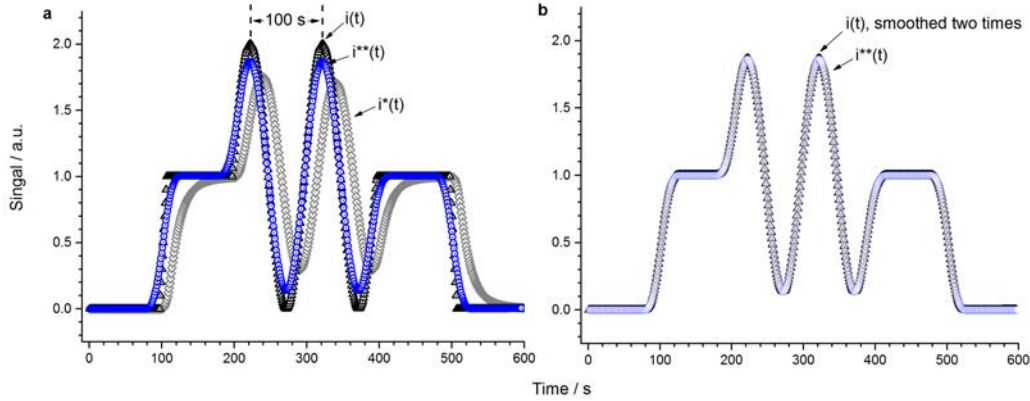


Figure 4.7: (a) - comparison of the synthetic input signal (denoted as  $i(t)$ ) after convolution (denoted as  $i^*(t)$ ) and deconvolution (denoted as  $i^{**}(t)$ ) numerical treatments. Since the “boxcar” average smoothing was applied twice during the deconvolution numerical treatment (b) represents two times smoothed  $i(t)$  and  $i^{**}(t)$  for an accurate estimation of error of deconvolution procedure. The original signal consists of 0.01 Hz wave to demonstrate the utility of deconvolution treatment for an alternative 0.01 Hz signals.

where  $t_1$  equals to 3 s.

Since  $i^{**}(t)$  is a recursive function, the deconvolution defined by Eq. 4.18 is extremely sensitive to a level of noise of  $i^*(t)$  signal and cannot be directly applied to the experimental data. In the present work a “boxcar” averaging procedure with 20 points of window was applied to the  $i^*(t)$  signal before and after the deconvolution in order to decrease the level of noise. The filtering procedure was chosen arbitrary. Due to the loss of the high frequency AESEC data during the filtering of  $j_{Zn}(t)$ , the deconvolution treatment can be used only for the data with a low frequency of an alternating signal of  $j_{Zn}(t)$ .

Fig. 4.7 presents the results of the numerical convolution and following deconvolution treatments of a synthetic discrete signal  $i(t)$ . A small difference between the original  $i(t)$  and obtained  $i^{**}(t)$  (Fig. 4.7a) is due to the smoothing procedures and is not defined by an error of choosing  $t_1$  value (Eq. 4.18). The convolution, deconvolution and “boxcar” average smoothing are linear operators. The latter fact permits to estimate an error of only deconvolution procedure by comparing  $i^{**}(t)$  with two times smoothed original  $i(t)$  signal. **Fig. 4.7b shows an excellent performance of deconvolution defined and justifies its use for the AESEC experimental data. Further, the focus on the development of the deconvolution treatment can be devoted to minimize an error caused by the smoothing procedure.**

The algorithms for the numerical convolution and deconvolution of the real AESEC data were realized in Python programming language. The source codes are presented in Appendix E.

## 4.6 Summary

In this chapter, the instrumentation and the principle of the treatment of the AESEC data have been introduced. The AESEC is the main technique used in this work for the intelligent screening of water soluble inhibitors on galvanized steel due to its advantage of recording the elemental dissolution currents. For the first time, the deconvolution algorithm was derived for the AESEC data. The numerical convolution of  $j_e$  and deconvolution of  $j_{Zn}$  of the AESEC data were performed depending on the specific measurements. **As a general rule,  $j_{Zn}$  was applied to analyze current transients if the alternating signal of  $j_{Zn}(t)$  changed less than 0.01 Hz, otherwise the numerical convolution of  $j_e$  was applied.**

---

## C. Results section

---

This section presents the most important results obtained during this work and their discussions. It consists of four technical chapters presented in the form of 4 publications (all of them are already accepted). These chapters aim to answer the specific questions raised in the Introductory section:

- ✓ **How does the competitive formation of soluble complexes affect the inhibiting effect of organic inhibitors? (Chapters 6)**
- ✓ **What is the action of  $\text{MoO}_4^{2-}$  as a water soluble inhibitor on galvanized steel at alkaline pH? What parameters define its action? (Chapter 7)**
- ✓ **How does the release kinetics from LDHs depend on the composition of corrosive environment? (Chapter 8)**
- ✓ **What is the relationship between the release kinetics of the inhibitor from LDH anticorrosion coatings, the inhibitor action and the protection offered by the coated system? Which species in the environment can affect it? (Chapter 8)**

The only difference between the articles and associated with them chapters is a unification of symbols, continuous numbering of references, figures, tables and equations applied for the whole PhD work and the linking introduction and summary sections, which would remind a reader the role of a chapter in the structure of the PhD thesis.

**Note**, no synthesis was made during this work. The synthesis of the LDH/Mo phase was made by Dr. Thomas Stimpfling and Prof. Fabrice Leroux in Université Blaise Pascal in Clermont-Ferrand. The complete coated systems were supplied by BASF.



# Observation of anodic zinc dissolution during cathodic polarization and it's consequencues for corrosion rate measurements

---

Before the intelligent screening of water soluble inhibitors, we proposed a comparative study of different methodologies used for the estimation of corrosion rates in the presence of inhibitors in order to understand their weak and strong points and to identify the most effective tool for the intelligent screening of water soluble inhibitors. This chapter presents the comparison of different methodologies on the example of galvanized steel/L-cysteine system.

The content of the chapter repeats the article: V. Shkirskiy, P. Keil, H. Hintze-Bruening, F. Leroux, P. Volovitch, K. Ogle, "Observation of anodic zinc dissolution during cathodic polarization and it's consequences for corrosion rate measurement", *Electrochimica Acta*, in press.

## Abstract

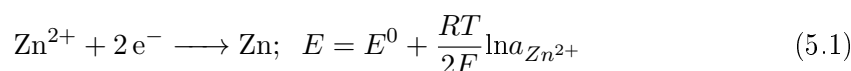
The corrosion inhibiting and accelerating effect of L-cysteine on Zn were correlated with the formation of Zn oxides by means of a novel coupling of impedance spectroscopy (EIS) with atomic emission spectroelectrochemistry (AESEC). A plateau of anodic Zn dissolution was discovered in the cathodic branch of the polarization curve, hidden by the large cathodic current. The effect of L-cysteine at all pH values and all concentrations was to increase the plateau current. The effect was most pronounced at high pH suggesting a synergy between hydroxide and L-cysteine. Due to the presence of Zn plateau current, Tafel extrapolation resulted in wrong estimation of corrosion currents. The contribution of the anodic Zn oxidation in plateau region to the total current was inversely proportional to the frequency of AC perturbation.

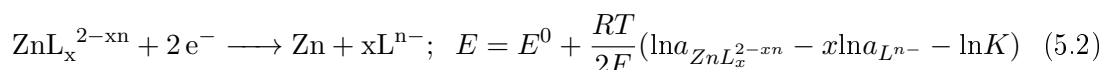
## 5.1 Introduction

The corrosion resistance of metal substrates is usually related to the structure and composition of the oxide layer on the metal surface [28, 31, 37, 38, 44, 48, 175–177]. The oxide layer on Zn in contact with aqueous electrolytes consists of an outer oxide/hydroxide film (known as Type I Zn oxide) and an inner compact layer (known as Type II Zn oxide) [23, 34–40, 140, 178]. The inner layer has been postulated to form by the direct oxidation of Zn to ZnO driven by the cathodic reaction such as oxygen reduction on the surface of the ZnO semiconductor [36, 38–40, 52, 178–180]. Zn<sup>2+</sup> ions may be ejected through the ZnO film and precipitate to Type I Zn porous oxides with a strong dependency of the film composition on the local pH [31, 36–38, 46, 48, 140]. The large thickness and compactness, low porosity, low electrical conductivity and high negative surface charge of Zn outer precipitated layer lower the dissolution of the metal substrate [31, 37, 41, 44, 48, 175, 176]. Enhancing these parameters of Type I Zn oxides through the addition of chemical species to corrosive environment, corrosion inhibitors, provide a tool to control the corrosion of Zn based substrates.

Organic ligands are often added to the environment to serve as corrosion inhibitors [41, 109, 117]. Inhibition may occur when the organic molecule seals the outer porous Zn oxides by adsorption on their surface enhancing the barrier between the metal and the environment [41, 60, 123]. However, organic ligands may also destabilize the oxide film by increasing the solubility of the metal cations, resulting in an activation of the surface, evidenced by an enhanced dissolution rate [117, 181, 182]. In recent work [183], we demonstrated that the molecule L-cysteine showed both a slight inhibiting effect at low concentrations and an accelerating effect at higher concentrations. Although this may render dubious the use of L-cysteine as a practical inhibitor for Zn, it represents an excellent system for a closer look at the mechanisms of inhibition and acceleration by organic molecules.

The presence of a complexing ligand (L) such as hydroxide or L-cysteine results in a cathodic shift of the equilibrium potential for Zn dissolution as given by [60, 123]





In the presence of small concentrations of the ligand the anodic dissolution of Zn may be limited by the concentration of the ligand. For a corroding system, it may prove difficult to discern the effect of a ligand on the anodic reaction as much of the anodic activity may be masked by the cathodic current. This makes the use of conventional electrochemical methods (polarization curves and/ or electrochemical impedance spectroscopy (EIS)) difficult to interpret since a significant anodic current may be “hidden” underneath the cathodic branch.

In this work we use the AESEC (atomic emission spectroelectrochemistry) methodology [161] to measure the Zn dissolution rate as a function of potential during polarization experiments. In this way, the hidden anodic dissolution of Zn, masked by a large cathodic current is revealed, and the influence of L-cysteine on the anodic dissolution of Zn may be brought to light. The experiments were performed with and without  $10^{-2}$  M and  $10^{-3}$  M L-cysteine additions to show either an inhibiting or an accelerating effect of the L-cysteine respectively. As the reaction also involves the formation of a slightly soluble oxide film, EIS/AESEC experiments were also conducted for the systems. The novel combination of conventional EIS with AESEC permits a direct monitoring of the effect of AC perturbations on the elemental dissolution rate (see Appendix F). The EIS/AESEC coupling gave access to the kinetic parameters of individual cathodic and anodic reactions but its utility was shown only for a limited number of systems with a diffusion limited cathodic reaction (Appendix F). In this work, a new system with a diffusion limited anodic reaction was studied using an EIS/AESEC coupling.

## 5.2 Experimental

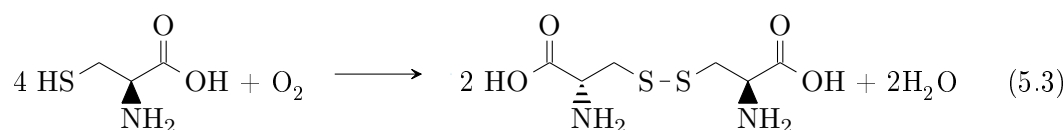
### 5.2.1 Materials

A commercial hot dip galvanized steel (HDG bonder plates (type: HDG/5) were supplied by “Chemetall”. The average thickness of the galvanization layer (approximately 0.1 % wt Al added to the Zn) amounts 20  $\mu\text{m}$ . The sample was cut into 2 cm  $\times$  4 cm coupons, cleaned with tetrahydrofuran, acetone and ethanol in ultrasonic bath for 10 min, dried under flowing nitrogen, then immersed in 1 M NaOH solution at 50  $^{\circ}\text{C}$  for 30 s, further rinsed with water and finally dried under flowing nitrogen again. The NaOH treatment was used to simulate the oxidizing effect of a conventional alkaline degreasing and to remove the residual oxides. The experiments were performed in 0.5 M NaCl (analytical grade, VWR Prolabo) containing solutions in purified water (Millipore<sup>TM</sup> system, 18  $\Omega$   $\text{cm}^2$ ) with additions of  $10^{-2}$  M and  $10^{-3}$  M L-cysteine (analytical grade, Sigma Aldrich) at pH values of 6 and 12. The pH of solutions was adjusted by the addition of 1 M NaOH.

### 5.2.2 Aeration of L-cysteine solutions

Prior to the pH adjustment the solutions containing L-cysteine were aerated for 20 min by an air pump in order to partially oxidize L-cysteine to its dimer L-cystine corresponding

to the quasi-equilibrium [183]:



In our previous publication [183] we showed that after 20 min of aeration 5 % of L-cysteine at pH 6 and 30 % of L-cysteine at pH 12 is converted to L-cystine independent of the L-cysteine concentration over the range of  $10^{-5}$  -  $10^{-3}$  M.

### 5.2.3 AESEC technique

#### Measurement principle

The on-line measurement of the Zn current during electrochemical impedance spectroscopy (EIS) and polarization experiments was performed by atomic emission spectroelectrochemistry (AESEC), described in detail elsewhere [161]. Briefly, it consists of an electrochemical flow cell coupled with an inductively coupled plasma atomic emission spectrometer (ICP-AES). In the flow cell, a reaction between the sample (hot dip galvanized steel) and an aggressive electrolyte occurs, leading to the production of dissolved ions and/or insoluble oxides. Then, the electrolyte is transported downstream to the ICP-AES, where its composition is continuously analyzed. The ICP-AES analysis shows only the soluble part of the released Zn cations, while the insoluble oxides are not directly detected. This soluble part of the released Zn is expressed as an equivalent Zn current ( $j_{Zn}$ ) and was calculated from the instantaneous Zn concentration ( $C_{Zn}$ ) using Faraday's law:

$$j_{Zn} = nFC_{Zn}f_e/A \quad (5.4)$$

where  $n = 2$  is the assumed charge of the Zn cations,  $F$  is the Faraday's constant,  $f_e$  is the flow rate and  $A$  is the geometric surface area. The normalization of  $j_{Zn}$  by the geometric surface area was done only for convenience and does not imply that electrochemical reactions were uniformly distributed on the surface.

#### AESEC parameters

The emission intensity for Zn was monitored at 213.856 nm. The detection limits in each solutions, defined as two times standard deviation of the blank solution, are shown in Table 5.1. The variations of detection limits for Zn were in a range of 0.1 - 1.7  $\mu\text{A cm}^{-2}$  and independent on the concentration of L-cysteine. Al was also monitored at 167.081 nm but the intensity of its signal was always below the detection limit of  $2.5 \pm 0.3 \mu\text{A cm}^{-2}$ .

The reactive surface area was  $0.51 \pm 0.01 \text{ cm}^2$ , the flow rate of the electrolyte was fixed at  $0.050 \pm 0.002 \text{ cm}^3 \text{ s}^{-1}$  and the temperature was  $25 \pm 1 \text{ }^\circ\text{C}$  ( $298 \pm 1 \text{ K}$ ). The time constant distribution or transfer function (denoted as  $h(t)$ ) of the electrochemical flow cell obeyed an empirical function in the form of a log-normal distribution [160] (see

Appendix).  $h(t)$  was measured by applying a galvanostatic pulse of 1.0 mA for 1 s to 99.9 % Cu in deaerated 2.0 M HCl and fitting the resulting concentration transient. In this work, the parameters for log-normal distribution were found to be  $\beta = 0.99 \pm 0.02$  and  $\tau = 10.2 \pm 0.2$  s. The time offset due to transport through the capillaries was  $\Delta t = 14.0 \pm 0.5$  s.

The electrochemical tests were performed with a Gamry Reference 600<sup>TM</sup> potentiostat with Ag/AgCl saturated reference electrode and a Pt sheet counter electrode. EIS was done at open circuit from 10 kHz to 0.01 Hz with 10 points per decade and 4 cycles per frequency with voltage amplitude of 5 mV rms. All presented EIS data satisfied the Kramers-Kronig (K-K) criteria with less than 2 % error. (The software for the K-K verification was provided with Gamry station). Polarization curves were recorded from the lowest cathodic potential with 0.5 mV/s sweep rate. The corrections for the ohmic drop was neglected herein due to a low resistance of electrolytes of  $30 \Omega \text{ cm}^{-2}$ . The analog potential and current signals were routed into the measuring circuit of the ICP-AES to guarantee the same time scale for the Zn current, total current and potential measurements. All data signals from ICP-AES were collected with 1 Hz sampling rate.

### Data analysis

The total electrical current passing through the working electrode can be expressed as a sum of the anodic and cathodic partial currents (denoted as  $j_e$ ,  $j_a$  and  $j_c$  respectively):

$$j_e = j_a + j_c \quad (5.5)$$

The AESEC technique measures the soluble component of the anodic current of metal dissolution. For Zn dissolution, the anodic current may be expressed as:

$$j_a = j_{Zn} + j_{Zn}^{ins} - 2Fv_{ZnO} \quad (5.6)$$

where  $j_{Zn}$  and  $j_{Zn}^{ins}$  correspond to the formation of the soluble Zn cations and insoluble Zn oxides respectively;  $v_{ZnO}$  represents the chemical dissolution of Zn oxides. If  $v_{ZnO}$  is

Table 5.1: Detection limits of Zn defined as two times standard deviation of the blank solutions in 0.5 M NaCl with the additions of L-cysteine (RSH).

		Detection limit of Zn, $\mu\text{A cm}^{-2}$
pH 6	$10^{-2}$ M RSH	1.7
	$10^{-3}$ M RSH	0.1
	0 M RSH	1.5
pH 12	$10^{-2}$ M RSH	0.8
	$10^{-3}$ M RSH	0.1
	0 M RSH	0.8

negligibly small, the quantity of insoluble Zn corrosion products (denoted as  $Q_{ins}$ ) under the anodic polarization can be estimated as:

$$Q_{ins} = \int_0^t j_{Zn}^{ins} dt = \int_0^t (j_e - j_{Zn}) dt \quad (5.7)$$

where  $j_e$  is equal to  $j_a$  under the assumption of a negligible contribution of cathodic reaction to the overall current. If  $j_{Zn}^{ins}$  and  $v_{ZnO}$  are negligibly small,  $j_c$  can be estimated as

$$j_c = j_e - j_{Zn} \quad (5.8)$$

Eq. 5.7 and 5.8 can not be directly applied because the signals from the potentiostat ( $j_e$ ) and from the ICP-AES ( $j_{Zn}$ ) have very different time resolution:  $j_e$  is essentially instantaneous while  $j_{Zn}$  is broadened by the hydrodynamic influence of the flow cell. That might be corrected in two ways: either a numerical convolution of the  $j_e$  or a numerical deconvolution of  $j_{Zn}$ , in both ways using the transfer function  $h(t)$  defined above.

The application of the numerical convolution procedure of  $j_e$  was demonstrated previously in numerous publications [160]. Along with its obvious simplicity, the convolution procedure has the disadvantage since that the convoluted signal  $j_e^*(t)$  includes the hydrodynamics of the flow cell. The deconvolution of  $j_{Zn}$  serves to eliminate hydrodynamics of the flow cell and provide a  $j_{Zn}$  signal directly related to the electrochemical reaction at the interface. In this work for the first time the numerical deconvolution of  $j_{Zn}$  signal was performed. Due to the loss of the high frequency EIS/AESEC data during the deconvolution treatment was used only for the lowest 0.01 Hz frequency of the AC perturbation. Details about the convolution and deconvolution algorithm used herein are presented in Chapter 4.

## 5.3 Results and Discussions

### 5.3.1 Equilibrium considerations

As this work presents some relatively complex kinetic experiments, it is of interest to consider the equilibrium chemistry of the Zn/ L-cysteine (RSH) system prior to looking at the experimental data. This will allow us to interpret some of the major trends of the kinetic data although caution must be exercised as to the precise nature of the different species formed, especially as concerns interfacial solid films.

Fig. 5.1 shows a predominance area diagram for the Zn/RSH system calculated for pH values of 6 and 12 and a formal concentration of L-cysteine of  $10^{-2}$  M. The calculation was made using the standard database of Hydra – Medusa [33] to which we have added the formation constants of  $Zn^{2+}$  with RSH species (Table 5.2) and the protonation constants of L-cysteine [184]:



Fig. 5.1 demonstrates that Zn dissolution may occur through three dissolution processes depending on the total interfacial  $Zn^{2+}$  concentration and pH. These dissolution processes are indicated with arrows in Fig. 5.1.

1. Dissolution  $A_1$ , occurs when the total  $Zn^{2+}$  concentration is less than the total RSH concentration. This is a stoichiometric reaction to form  $Zn(RS)H^+$  at pH 6 or  $Zn(RS)_2^{2-}$  at pH 12. The redox potential is around  $-1.1$  V vs SHE at pH 6 ( $-1.32$  V vs. Ag/AgCl) or  $-1.35$  V vs SHE at pH 12 ( $-1.57$  V vs. Ag/AgCl).
2. Dissolution  $A_2$  occurs at pH 6 when the total  $Zn^{2+}$  concentration is more than the total RSH concentration, and the excess of  $Zn^{2+}$  is present in the solution as the uncomplexed aqueous cation. This occurs with a potential shift to around  $-0.80$  V vs. SHE ( $-1.02$  V vs. Ag/AgCl).
3. Dissolution  $A_3$  occurs when the total  $Zn^{2+}$  concentration is quite large, the interfacial solution becomes saturated and an oxide precipitates as indicated by  $A_{3a}$  (here shown as ZnO). As only the interfacial region is saturated and the solution in the cell is continually renewed, the process will occur through a chemical dissolution as indicated by  $A_{3b}$ .

### 5.3.2 AESEC polarization experiments

To gain an overview of the chemistry of the Zn/electrolyte systems, AESEC polarization curves were obtained for Zn in the six electrolytes (Fig. 5.2 and 5.3). The curves consist of the total current ( $j_e$ ) and the elemental Zn dissolution current ( $j_{Zn}^{**}$ ) presented as a function of applied potential ( $E$ ). From the conventional polarization curve of  $j_e$  vs  $E$ , it is noted that all experiments yield  $E(j_e = 0)$  near  $-1.0$  V vs. Ag/AgCl electrode with the exception of Fig. 5.3a, obtained at pH = 12 with  $10^{-2}$  M L-cysteine. For this electrolyte the value of  $E(j_e = 0)$  was shifted to  $-1.46$  V vs. Ag/AgCl electrode consistent with the

Table 5.2: Stability constants of complexes formation between L-cysteine (RSH) and  $Zn^{2+}$  used in the equilibrium calculations for Fig. 5.1. The data were taken from the IUPAC database [184]. Either recommended values or the ones measured under conditions similar to the experiments in this paper were taken.

Formula of complex	$\log K$
$Zn(RS)_2^{2-}$	18.71
$Zn(RS)$	9.17
$Zn(RS)_3^{4-}$	21.64
$Zn(RS)_2H^-$	23.32
$Zn_3(RS)_4^{2-}$	43.5
$Zn_3(RS)_4H^-$	49.5
$Zn_3(RS)_4H_2$	29.03
$Zn(RS)_2H_2$	29.0
$Zn(RS)H^+$	19.5
$Zn_2(RS)_3^{2-}$	24.8
$Zn_2(RS)_3H^-$	36.39
$Zn_2(RS)_3H_2$	41.72

5. OBSERVATION OF ANODIC ZINC DISSOLUTION DURING CATHODIC POLARIZATION AND IT'S CONSEQUENCES FOR CORROSION RATE MEASUREMENTS

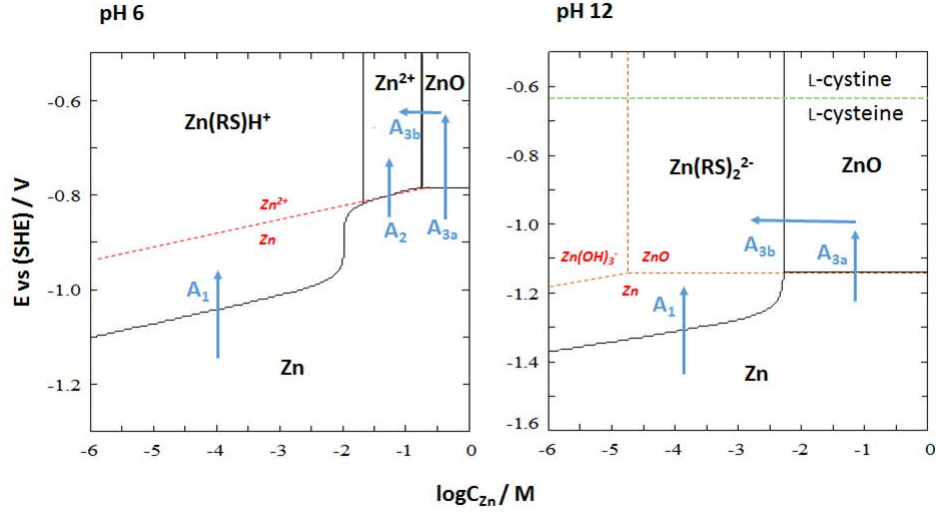


Figure 5.1: Predominance area diagrams for Zn in  $10^{-2}$  M L-cysteine (solid black lines) and L-cysteine free solutions (red dotted lines) at pH 6 and 12. The dotted green line corresponds to the L-cysteine/L-cysteine equilibrium at  $-0.28$  V vs SHE at pH 6 (not shown on the figure) and  $-0.64$  V vs SHE at pH 12 [184]. The Zn containing species taken into account include:  $\text{Zn}^{2+}$ ,  $\text{Zn}(\text{OH})_2$ ,  $\text{Zn}(\text{OH})_3^-$ ,  $\text{Zn}(\text{OH})_4^{2-}$ ,  $\text{Zn}_2(\text{OH})_6^{2-}$ ,  $\text{Zn}_2(\text{OH})_3^+$ ,  $\text{Zn}_4(\text{OH})_4^{4+}$ ,  $\text{ZnOH}^+$ ,  $\alpha\text{-Zn}(\text{OH})_2$ ,  $\text{e-Zn}(\text{OH})_2$ , ZnO, Zn of the standard database of Hydro-Medusa [33] and L-cysteine complexes with  $\text{Zn}^{2+}$  shown in Table 5.2. Arrows  $A_1$ ,  $A_2$  and  $A_3$  show different pathways of Zn dissolution discussed in this work.

strong complexing nature of this electrolyte. Inspection of the  $j_{Zn}^{**}$  vs.  $E$  curve for this system shows that the anodic dissolution of Zn begins at  $-1.60$  V vs. Ag/AgCl electrode, rises exponentially with an apparent Tafel slope of  $94 \pm 2$  mV  $\text{dec}^{-1}$ , and then reaches a steady plateau from  $-1.45$  V to  $-1.0$  V. This plateau resembles the plateau current observed at  $\text{pH} > 13$  in the similar potential range from  $-1.45$  V to  $-1.0$  V vs Ag/AgCl electrode [40]. At  $-1.3$  V vs. Ag/AgCl electrode and above,  $j_e$  equals  $j_{Zn}^{**}$  within the experimental error of 1 % (Fig. 5.3a), demonstrating the excellent agreement between the two completely independent measurements, thereby validating the mass balance between  $j_e$  and  $j_{Zn}^{**}$ .

The most important point to observe in Fig. 5.2 and 5.3 is that all of the Zn/electrolytes investigated here show a similar plateau current. The difference is that, for the other cases, this plateau is masked by the large cathodic current and may not be discerned from inspection of the  $j_e$  vs  $E$  polarization curve alone. For 0.5 M NaCl at pH 6.0 (Fig. 5.2c) the plateau is barely detectable rising only slightly above the detection limit. In all cases, except Zn/ $10^{-2}$  M L-cysteine at pH 12 of Fig. 5.3a where the anodic scan was not continued for a sufficiently long period, there is a sharp increase in the anodic current and the Zn dissolution rate around  $-1.0$  V. The presence of L-cysteine does not seem to affect the position or slope of this rapid onset of dissolution. It is of

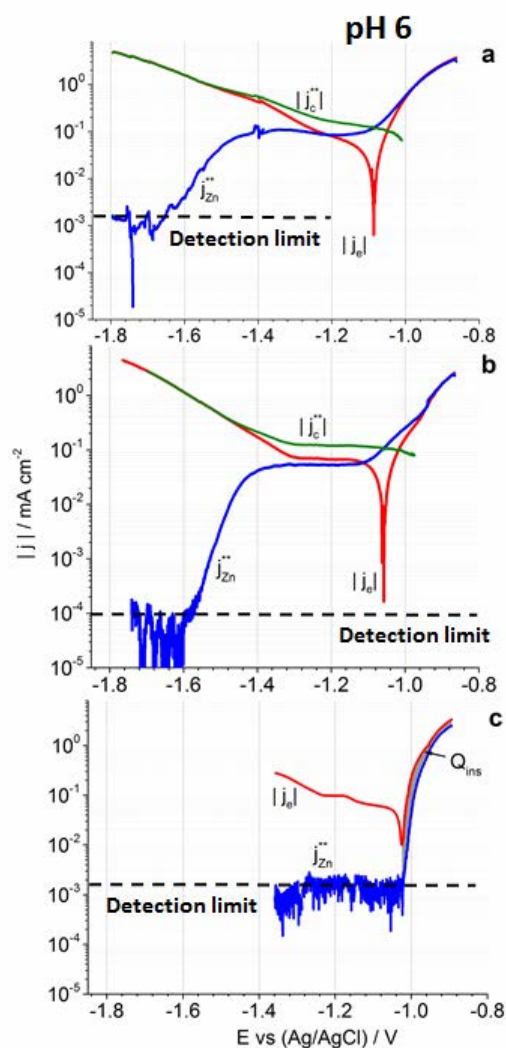


Figure 5.2: AESEC polarization curves for Zn (galvanized steel) at  $0.5 \text{ mV s}^{-1}$  and  $25^\circ\text{C}$  in (a)  $10^{-2} \text{ M}$  L-cysteine, (b)  $10^{-3} \text{ M}$  L-cysteine and (c) additive free  $0.5 \text{ M}$  NaCl aqueous solutions at pH 6. The total current ( $j_e$ ), deconvoluted Zn current ( $j_{Zn}^{**}$ ) and the calculated cathodic current ( $j_c^{**}$ ) are shown.

interest to note that for all situations except Zn/ $10^{-2} \text{ M}$  L-cysteine at pH 12 of Fig. 5.3a, the cathodic current intercepts the anodic dissolution curve in this region. For Fig. 5.3a, the current in the plateau region is larger than the cathodic current; as a consequence  $E(j_e = 0)$  shifts to  $-1.45 \text{ V}$  vs. Ag/AgCl electrode.

The addition of L-cysteine at pH = 6 and at pH = 12 increases the plateau current. The effect is illustrated in Fig. 5.4 which gives the plateau current at the three concentrations investigated in this work for the two pH values. Although this is shown as a

5. OBSERVATION OF ANODIC ZINC DISSOLUTION DURING CATHODIC POLARIZATION AND IT'S CONSEQUENCES FOR CORROSION RATE MEASUREMENTS

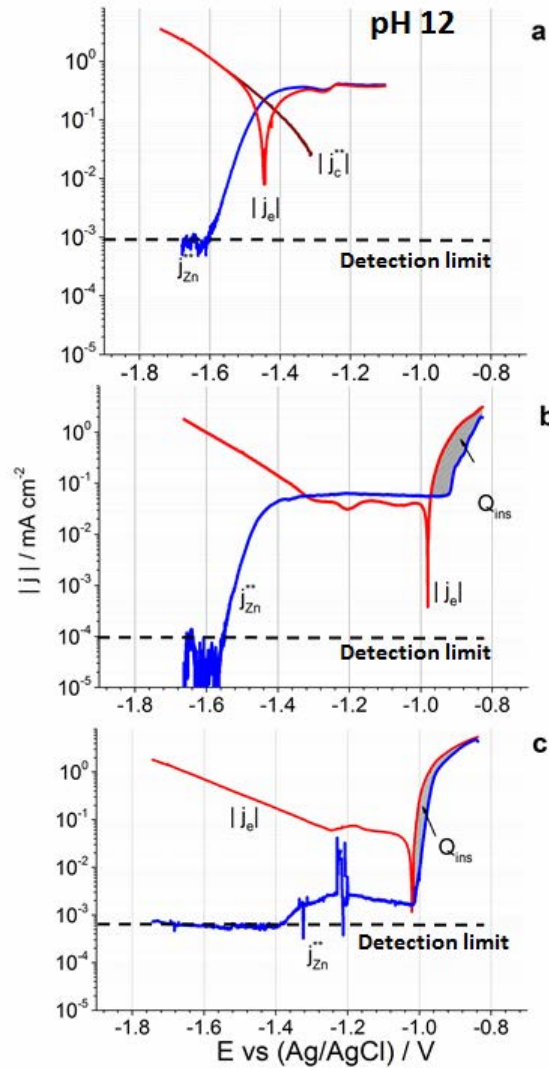


Figure 5.3: AESEC polarization curves for Zn (galvanized steel) at  $0.5 \text{ mV s}^{-1}$  and  $25 \text{ }^{\circ}\text{C}$  in (a)  $10^{-2} \text{ M}$  L-cysteine, (b)  $10^{-3} \text{ M}$  L-cysteine and (c) additive free  $0.5 \text{ M}$  NaCl aqueous solutions at pH 12. The total current ( $j_e$ ), deconvoluted Zn current ( $j_{Zn}^{**}$ ) and cathodic current ( $j_c$ ) are shown.

function of the formal L-cysteine concentration, it should be kept in mind that approximately 30% of the L-cysteine is dimerized to L-cystine at pH 12 [183]. Both L-cysteine and L-cystine form complexes with  $\text{Zn}^{2+}$  and probably contribute to the increase in the plateau current during the plateau potential domain. The above results demonstrate that the major effect of L-cysteine/L-cystine additions on Zn dissolution is (i) to induce a cathodic shift of the onset potential for Zn dissolution due to the complexation of  $\text{Zn}^{2+}$ , and (ii) to enhance the plateau current also most likely due to the complex formation.

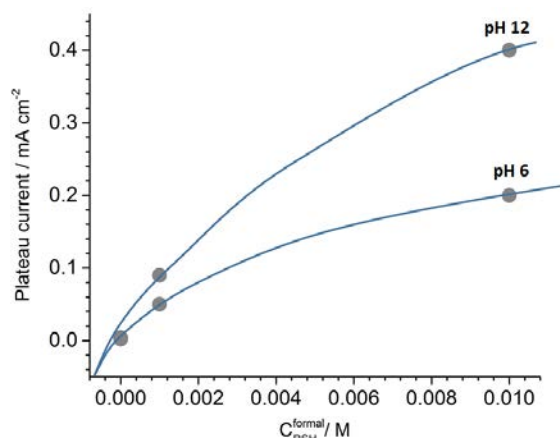


Figure 5.4: Plateau currents from Fig. 5.2 and 5.3 as a function of the formal L-cysteine concentration ( $C_{RSH}^{formal}$ ). The solid curves are presented only for the visual reference.

Further, L-cysteine / L-cystine additions have little to no effect on the Zn/Zn<sup>2+</sup> dissolution reaction occurring around -1.0 V vs Ag/AgCl electrode, which appears to be the dominant reaction at the open circuit potential with the exception of Fig. 5.3a.

### Cathodic reactions

As the kinetics of the Zn/Zn<sup>2+</sup> reaction seems to be independent of the L-cysteine concentration, the apparent inhibiting effect of L-cysteine at intermediate concentrations may be attributed primarily to its effect on the cathodic reaction. This effect is probably due to L-cysteine adsorption stabilizing the oxide films as discussed in our previous work [183]. If we assume that oxide formation makes a negligible contribution to  $j_{Zn}^{**}$  during the cathodic branch, it is possible to estimate the variation of  $j_c$  with potential as  $j_c^{**} = j_e \sim j_{Zn}^{**}$ . These curves are shown in Fig. 5.2 and 5.3.

The absence of the L-cystine reduction in the prepared L-cysteine solutions on the Zn electrode during the polarization experiments was verified as follows: a potential of -1.8 V vs Ag/AgCl was applied to HDG in 0.5 M NaCl flowing electrolyte. After 5 min, the solution was instantaneously switched to 0.5 M NaCl electrolyte with the addition of 10<sup>-2</sup> M L-cysteine. The total current was stable during the whole experiment at -4.8 mA cm<sup>-2</sup>. The Zn current was always below the detection limit of 1.5  $\mu A$  cm<sup>-2</sup>. The result excludes the influence of the possible L-cystine reduction on the total current under the cathodic polarization of HDG.

### Quantification of slightly soluble Zn intermediates

Analysis of the AESEC polarization curves yields an estimation of the amount of slightly soluble Zn intermediates formed during the anodic polarization. At pH 6, in the L-cysteine free solution (Fig. 5.2c)  $j_{Zn}^{**}$  is consistently less than  $j_e$  during the anodic polarization. This may be attributed to the formation of slightly soluble Zn oxides, which do

not contribute to the  $j_{Zn}^{**}$  value. The estimation of  $Q_{ins}$  (dashed area in Fig. 5.2c) yields 25 mC cm<sup>-2</sup>.

At pH 12, in 10<sup>-3</sup> M L-cysteine, the estimation of  $Q_{ins}$  yields 220 mC cm<sup>-2</sup> (Fig. 5.3b). In L-cysteine free solution  $Q_{ins}$  yields 206 mC cm<sup>-2</sup> Fig. 5.3c. The similar values of  $Q_{ins}$  at pH 12 are in accord with A<sub>3</sub> pathway in Fig. 5.1 for both systems.

### 5.3.3 EIS/AESEC experiments

In the previous section we demonstrated that the effect of L-cysteine on the corrosion of Zn occurs primarily through the cathodic reaction via the intermediate of Zn oxide/hydroxide films.

These films are presumed to exist even during the cathodic branch of the polarization curve. However, it is impossible to quantify oxide formation from a mass balance in the cathodic branch, since oxide formation and the cathodic reactions occur simultaneously with Zn dissolution. For this reason, we have used the EIS/AESEC methodology presented in [185, 186] to verify the existence of the oxide films.

The EIS/AESEC dissolution profiles, consisting of  $j_e$  and  $j_{Zn}$ , are divided into three periods (Fig. 5.5 and Fig. 5.6). The contact of solution with the Zn surface occurs at  $t = 0$  s giving rise to the initial transient peak for the  $j_{Zn}$  (onset of the period I). After approximately 900 s of stabilization of  $j_{Zn}$  under exposure at open circuit, the EIS experiment begins (period II). The conventional impedance data were collected during this period with the Gamry system. Period III shows the return of  $j_{Zn}$  to the open circuit value.

At pH 6 (Fig. 5.5),  $j_{Zn}$  shows a rapid onset in the 10<sup>-2</sup> M and 10<sup>-3</sup> M L-cysteine solutions suggesting a rapid chemical dissolution of residual Zn oxides at the initial stage. In contrast, the slow rise of the Zn dissolution during the initial 100 s in the L-cysteine free 0.5 M NaCl solution clearly indicates an incomplete dissolution of the residual film of Zn oxides. The important point in Fig. 5.5 is that the  $j_{Zn}$  oscillations during EIS application are observed only in the L-cysteine containing solutions where the formation of soluble Zn(II) species prevails (Fig. 5.2). No variations of  $j_{Zn}$  are detected in the L-cysteine free 0.5 M NaCl where the formation of slightly soluble Zn oxides was detected. The cathodic current estimated by Eq. 5.8 in the L-cysteine solutions did not show any significant dependence on the potential. This is consistent with the potential independent cathodic reaction due to a diffusion limited oxygen reduction as also suggested by the nearly potential independent  $j_c^{**}$  (Fig. 5.2).

At pH 12 (Fig. 5.6), the oscillations of  $j_e^*$  for the Zn/10<sup>-2</sup> M L-cysteine system appears in both  $j_{Zn}$  and  $j_c$  as predicted from the polarization curves (Fig. 5.3). Unlike Zn/10<sup>-3</sup> M L-cysteine at pH 6, no oscillations of  $j_e^*$  appear in  $j_{Zn}$  at pH 12. This observation suggests a preferential formation of slightly soluble intermediates under these conditions.

In the L-cysteine free solution the AC perturbation at low frequencies affects the Zn dissolution by increasing  $j_{Zn}$ . At lower frequencies of  $j_e$  the spikes of  $j_{Zn}$  are clearly observed. Previously reported spikes in the AESEC signal were associated with presence of particles in the solution detached from the surface [171, 172]. Apparently the application

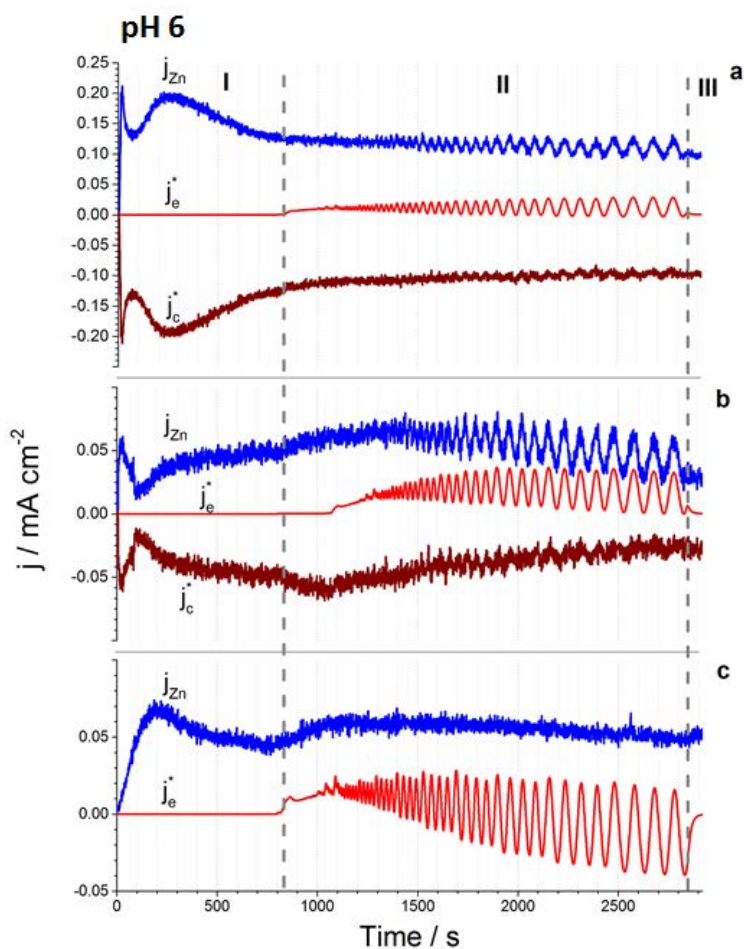


Figure 5.5: EIS/AESEC experiment showing the comparison of the convoluted total current, Zn current and cathodic current ( $j_e^*$ ,  $j_{Zn}$  and  $j_c^*$  respectively) in (a)  $10^{-2}$  M L-cysteine, (b)  $10^{-3}$  M L-cysteine and (c) additive free 0.5 M NaCl aqueous solutions at pH 6. I and III correspond to dissolution at open circuit before and after the EIS application during II period.

of AC perturbation decreases the adhesion between the surface and solid Zn oxides that results in a release of solid Zn oxide particles into the solution.

Fig. 5.7 and 5.8 present the impedance spectra in Nyquist format for the three systems measured during the experiments of Fig. 5.5 and 5.6 at pH values of 6 and 12. Two time constants are clearly observed for each spectra. However, a marked instability is indicated in Fig. 5.5 and 5.6 despite an error of less than 2 % for the Kramers-Kronig transformation. The instability is indicated by (i) the difference in  $j_{Zn}$  values before and after EIS applications, (ii) the variation of the central value of the AC current and (iii) a disturbance of the impedance values at low frequencies presented in Fig. 5.7 and 5.8 for

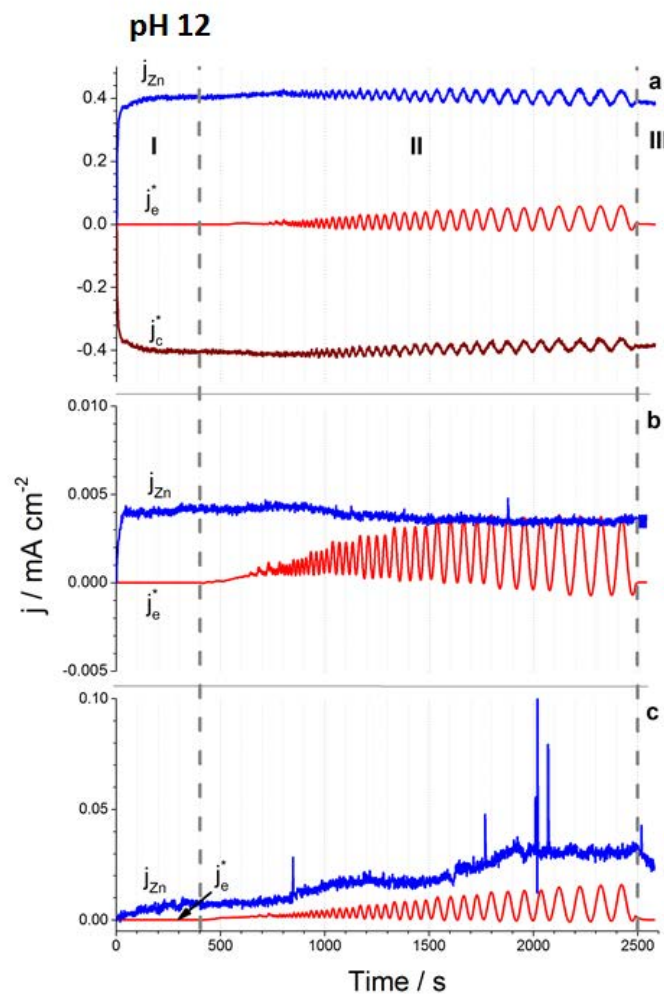


Figure 5.6: EIS/AESEC experiment showing the comparison of the convoluted total current, Zn current and cathodic current ( $j_e^*$ ,  $j_{Zn}$  and  $j_c^*$  respectively) in (a)  $10^{-2}$  M L-cysteine, (b)  $10^{-3}$  M L-cysteine and (c) additive free 0.5 M NaCl aqueous solutions at pH 12. I and III correspond to dissolution at open circuit before and after the EIS application during II period.

Zn/0.5 M NaCl (c curves) and Zn/ $10^{-3}$  M L-cysteine (b curves) systems at both pH. An instability of Zn/0.5 M NaCl system was previously explained by a possible continuous precipitation of Zn oxides [187]. The fitting parameters of the EIS spectra are presented in Table 5.3.

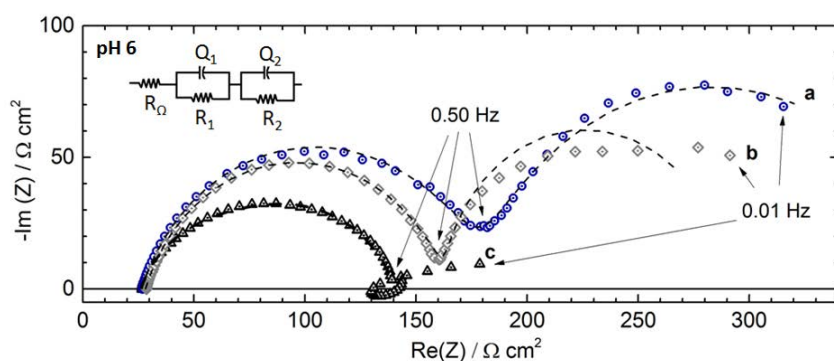


Figure 5.7: Impedance spectra in Nyquist format for Zn (galvanized steel) dissolution in (a)  $10^{-2}$  M L-cysteine, (b)  $10^{-3}$  M L-cysteine and (c) additive free 0.5 M NaCl aqueous solutions at pH 6 from 10 kHz to 0.01 Hz from the experiment in Fig. 5.5. The two time constant equivalent circuit used to simulate the impedance response is shown in the inset.

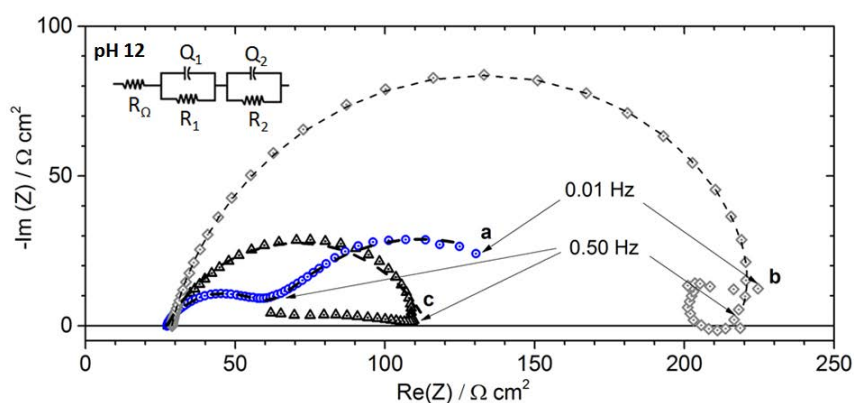


Figure 5.8: Impedance spectra in Nyquist format for Zn (galvanized steel) dissolution in (a)  $10^{-2}$  M L-cysteine, (b)  $10^{-3}$  M L-cysteine and (c) additive free 0.5 M NaCl containing solutions at pH 12 from 10 kHz to 0.01 Hz from the experiment in Fig. 5.6. The two time constant equivalent circuit used to simulate the impedance response is shown in the inset.

### Contributions of anodic and cathodic currents to the total current during EIS

The contribution of anodic and cathodic currents to the total electrical current as a function of AC perturbation frequency for Zn/ $10^{-2}$  M L-cysteine deserves a particular consideration. At pH 6 (Fig. 5.9a), no significant variation of the ratio between the anodic dissolution to total current ( $\Delta j_{Zn}/\Delta j_e^*$ ) was observed. The variation of the total

5. OBSERVATION OF ANODIC ZINC DISSOLUTION DURING CATHODIC POLARIZATION AND ITS CONSEQUENCES FOR CORROSION RATE MEASUREMENTS

Table 5.3: Fitting parameters for EIS spectra of Zn dissolution in 0.5 M NaCl containing solutions with additions of L-cysteine (RSH) presented in Fig. 5.7 and 5.8

		$R_1, \Omega \text{ cm}^2$	$Q_1, \text{F cm}^{-2} \text{ s}^{\alpha-1}$	$\alpha_1$	$R_2, \Omega \text{ cm}^2$	$Q_2, \text{F cm}^{-2} \text{ s}^{\alpha-1}$	$\alpha_2$
pH 6	$10^{-2}$ M RSH	$153 \pm 2$	$22.2 \pm 0.9 \times 10^{-5}$	0.77	$211 \pm 5$	$26 \pm 3 \times 10^{-5}$	0.79
	$10^{-3}$ M RSH	$136 \pm 1$	$15.0 \pm 1.0 \times 10^{-5}$	0.78	-	-	-
	0 M RSH	$117 \pm 1$	$18.2 \pm 0.8 \times 10^{-5}$	0.75	-	-	-
pH 12	$10^{-2}$ M RSH	$34 \pm 2$	$97.4 \pm 5.2 \times 10^{-5}$	0.67	$102 \pm 2$	$37 \pm 2 \times 10^{-5}$	0.65
	$10^{-3}$ M RSH	$201 \pm 2$	$7.2 \pm 0.8 \times 10^{-5}$	0.86	-	-	-
	0 M RSH	$87 \pm 1$	$22.1 \pm 0.8 \times 10^{-5}$	0.72	-	-	-

current is exclusively related to Zn dissolution ( $\Delta j_{Zn}/\Delta j_e^* \approx 1$  within the experimental error), in agreement with the idea of a diffusion limited cathodic reaction under these conditions.

In contrast, from AESEC polarization curve at pH 12  $j_{Zn}^{**}$  was observed to be independent of potential under anodic polarization (Fig 5.3a). As a consequence, a contribution of the cathodic current to the total current is clearly observed ( $\Delta j_c/\Delta j_e^* \neq 0$ ). Moreover,  $\Delta j_c/\Delta j_e^*$  decreases with the increase of the AC frequency (Fig. 5.9b). As possible explanations, diffusion limitation of anodic current, precipitation of Zn(II) intermediates and/or autocatalysis driven by the adsorption of L-cysteine intermediates may be mentioned.

Independent of the precise physical nature of the phenomenon, the time constant ( $t_c$ ) of the process can be defined as a measure of the time it takes the system's response to

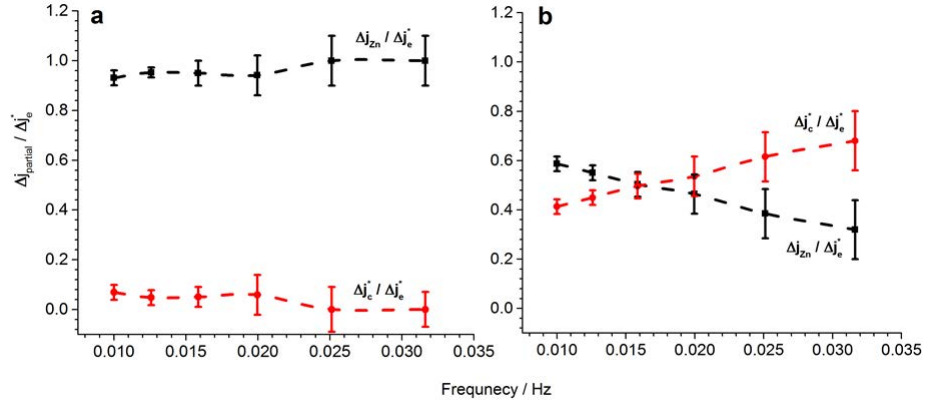


Figure 5.9: The ratio of the partial Zn current and cathodic current amplitudes to the total convoluted current (denoted as  $\Delta j_{Zn}/\Delta j_e^*$  and  $\Delta j_c/\Delta j_e^*$  respectively) as a function of the frequency perturbations in  $10^{-2}$  M L-cysteine solution (a) at pH 6 and (b) at pH 12.

reach  $(1 - 1/e)$  or 63.2 % of its steady state value valid for any liner system [188].  $t_c$  is defined as

$$t_c = 1/w_c \quad (5.10)$$

where  $w_c$  satisfies the condition

$$\Delta j_{Zn}(w_c)/\Delta j_{Zn}(w \rightarrow 0) = 0.63 \quad (5.11)$$

$\Delta j_{Zn}(w \rightarrow 0)$  was defined at 0.01 Hz. From Eq. 5.11,  $t_c = 40$  s is determined implying that at least 40 s of an external perturbation are required to observe significant contribution of the anodic dissolution to the total current.

### 5.3.4 Corrosion rate measurements

The direct measurement of  $j_{Zn}^{**}$  from AESEC polarization curves leads us to reconsider the standard methods of the corrosion rate estimation from the conventional polarization experiments [156, 157, 189–194]. This work provides three unique ways of estimating the corrosion rates: from the polarization experiments ( $j_{corr}^E$  or  $j_{corr}^{E_T}$ ), Zn dissolution at open circuit ( $j_{corr}^{AESEC}$ ) and from the EIS data ( $j_{corr}^{SG}$ ).

1.  $j_{corr}^{E_T}$  was estimated from the conventional Tafel extrapolation of  $j_e$  under anodic and cathodic polarizations to  $E(j_e = 0)$  [157, 189, 190].  $j_{corr}^E$  was estimated from the intersection of  $j_{Zn}^{**}$  and  $j_c^{**}$  from AESEC polarization curves (Fig. 5.2 and 5.3).
2.  $j_{corr}^{AESEC}$  were estimated from the values of the Zn spontaneous dissolution after the EIS experiments (period III in Fig. 5.5 and 5.6).
3.  $j_{corr}^{SG}$  was estimated from EIS data applying the Stern Geary relation [156, 191–194]:

$$j_{corr}^{SG} = \frac{b_a b_c}{2.3(b_a + b_c)} \cdot \frac{1}{R_p} \quad (5.12)$$

Table 5.4: Values of corrosion currents for Zn (galvanized steel) in the presence of L-cysteine (RSH) defined from the polarization curves by Tafel extrapolation ( $j_{corr}^{E_T}$ ) and by the direct measurement of Zn current at  $E(j_e = 0)$  ( $j_{corr}^E$ ), measurement of Zn dissolution under open circuit ( $j_{corr}^{AESEC}$ ) and Stern Geary relation ( $j_{corr}^{SG}$ )

		$j_{corr}^E, \mu\text{A cm}^{-2}$	$j_{corr}^{E_T}, \mu\text{A cm}^{-2}$	$j_{corr}^{AESEC}, \mu\text{A cm}^{-2}$	$j_{corr}^{SG}, \mu\text{A cm}^{-2}$
pH 6	$10^{-2}$ M RSH	$109 \pm 4$	$45 \pm 3$	$95 \pm 5$	$112 \pm 4$
	$10^{-3}$ M RSH	$102 \pm 3$	$61 \pm 4$	$31 \pm 4$	-
	0 M RSH	-	$56 \pm 17$	$52 \pm 4$	-
pH 12	$10^{-2}$ M RSH	$230 \pm 4$	$190 \pm 10$	$386 \pm 7$	$150 \pm 8$
	$10^{-3}$ M RSH	-	$39 \pm 12$	$4 \pm 1$	-
	0 M RSH	-	$49 \pm 14$	$18 \pm 2$	-

where  $R_p$  values were defined from the EIS spectra of the most stable Zn/10<sup>-2</sup> M L-cysteine systems.  $b_a$  and  $b_c$  was estimated from  $j_c^{**}$  and  $b_a$  was estimated from  $j_{Zn}^{**}$  in a potential region of -1.6 V to -1.4 V.

The values of the corrosion rates are presented in Table 6.2.

### Comparison of $j_{corr}^{E_T}$ and $j_{corr}^E$

In the cases where the formation of slightly soluble Zn(II) products can be neglected,  $j_{Zn}^{**}$  should equal the partial anodic current and hence, provide a direct measurement of the corrosion current. This is the case for Zn/10<sup>-2</sup> M L-cysteine at pH values of 6 and 12 (Fig. 5.2a and 5.3a) and Zn/10<sup>-3</sup> M L-cysteine at pH 6 (Fig. 5.2b). For the three examined systems,  $j_{corr}^E$  values are regularly higher than the  $j_{corr}^{E_T}$  values. The presence of significant hidden anodic currents increases the total current under the cathodic polarization, which results in a wrong estimation of Tafel slope of cathodic reactions. Actual values of the cathodic currents ( $j_c^{**}$  in Fig. 5.2a and 5.2b) are lower than the total currents under cathodic polarizations, which leads to a significant error in the conventional Tafel extrapolation method.

It is of interest to consider the determination of Tafel slopes for Zn oxidation for the mentioned systems with the hidden anodic plateau currents (Fig. 5.2a, Fig. 5.2b and Fig. 5.3b). The true value of  $b_a$  corresponding to Zn/Zn(II) oxidation has to be defined from the onset of Zn dissolution at -1.6 to -1.4 V vs Ag/AgCl before the plateau current indicating the formation of a barrier to electrochemical Zn dissolution. The origin of a barrier could be a diffusion limited mass transport of the L-cysteine complexation agent to the metal surface commonly observed in similar potential range but under anodic polarization for the diffusion of OH<sup>-</sup> at alkaline pH > 12 [38, 39, 179, 180, 195]. Slopes of  $j_e$  vs  $E$  conventionally determined from the anodic branch of polarization curves at  $E > -1.0$  vs Ag/AgCl in neutral and slightly alkaline medias are related to breakdown of the barrier and hence, do not reflect the electrochemical Zn oxidation.

### Comparison of $j_{corr}^{E_T}$ and $j_{corr}^{AESEC}$

As discussed in previous section,  $j_{corr}^{E_T}$  underestimated the true values of the corrosion currents  $j_{corr}^E$ . The values of  $j_{corr}^{AESEC}$  are even lower for Zn/10<sup>-3</sup> M L-cysteine and Zn/0.5 M NaCl at pH 12 where the formation of slightly soluble Zn(II) products were observed. The  $j_{corr}^{AESEC}$  values show only the soluble part of corroded Zn and do not include the Zn cations which stay on the surface in the form of precipitates. In contrast,  $j_{corr}^{E_T}$  value includes the current consumed by the formation of precipitates. Evidently, the formation of insoluble Zn<sup>2+</sup> species at pH 12 lowers  $j_{corr}^{AESEC}$  value from  $j_{corr}^{E_T}$ .

### Comparison of $j_{corr}^E$ and $j_{corr}^{SG}$

The comparison of  $j_{corr}^E$  and  $j_{corr}^{SG}$  for Zn/10<sup>-2</sup> M L-cysteine at pH 6 shows an excellent correlation whereas at pH 12, the values vary significantly,  $j_{corr}^E = 230 \mu\text{A cm}^{-2}$  and  $j_{corr}^{SG} = 150 \mu\text{A cm}^{-2}$ . This is probably due to the effect of the cathodic sweep alternating

the state of the system at  $E(j_e = 0)$  for polarization curves and the state at open circuit potential.

Interestingly, the simple interpretation of the disturbed impedance spectra from Fig. 5.7 results in a wrong estimation of effects of the L-cysteine additions. Consideration of  $R_p$  values at the lowest 0.01 Hz (Fig. 5.7) for all curves would suggest a significant inhibiting effect of  $10^{-2}$  M L-cysteine additions that is in direct contradiction to the observed accelerating effect at  $10^{-2}$  M L-cysteine estimated from AESEC polarization curves and Zn dissolution under open circuit. This example demonstrates the importance of system stability when interpreting EIS data, despite it's satisfying Kramers-Kronig criteria.

To summarize the data of Table 6.2, the true values of corrosion currents can be estimated only from the direct measurements of Zn dissolution at  $E(j_e = 0)$  when the formation of soluble Zn(II) species prevails. In general, Tafel extrapolation to  $E(j_e = 0)$  cannot be used without additional verification of possible contributions of anodic dissolution to total current under cathodic polarization as shown for Zn/ $10^{-2}$  M L-cysteine and Zn/ $10^{-3}$  M L-cysteine at pH 6 (Fig. 5.2a and Fig. 5.2b).

## 5.4 Conclusions

A novel EIS/AESEC coupling was applied to investigate the effect of L-cysteine on the formation of the precipitated layer of Zn oxides. Based on the experimental EIS/AESEC data and their numerical treatment, several conclusions can be drawn:

1. The resolution of the total current into elemental Zn and cathodic currents under cathodic polarizations at pH values of 6 and 12 revealed the presence of a "hidden" plateau current of Zn dissolution presumably determined by the diffusion of L-cysteine species to the metal surface.
2. The results demonstrated that the major effect of L-cysteine additions on Zn dissolution is (i) to induce a cathodic shift of the onset potential for Zn dissolution, and (ii) to enhance the plateau current. Both effects may be attributed to the complexation of  $Zn^{2+}$  with L-cysteine.
3. The additions of  $10^{-3}$  M L-cysteine dissolved Zn oxides at pH 6, as indicated by the excellent correlation of the total current ( $j_e$ ) and the Zn dissolution current ( $j_{Zn}$ ) during the anodic polarization, and during the AC application around the open circuit potential. At pH 12 in  $10^{-3}$  M L-cysteine, the formation of slightly soluble Zn(II) intermediates were observed.
4. The analysis of the partial currents for the Zn/ $10^{-2}$  M L-cysteine system during EIS experiments at pH values of 6 and 12 in the frequency range of 0.032 Hz - 0.010 Hz revealed the contribution of the individual cathodic and anodic rates to the total current. Only the anodic current contributed to the total current in the whole frequency range at pH 6 consistent with a diffusion limited cathodic reaction. At pH 12, the dominance of the cathodic current was observed. The time constant of the anodic

process equaled 40 s implying that at least 40 s of an external perturbation were required to observe significant contribution of the Zn dissolution to the total current.

5. The values of corrosion currents can be measured by AESEC from Zn dissolution at  $E(j_e = 0)$  when the formation of soluble Zn(II) species prevails. In a general case, one cannot rely on the estimation of the corrosion current from the conventional Tafel extrapolation of the total current to  $E(j_e = 0)$  due to possible contribution of the anodic dissolution to the total current under cathodic polarization.
6. For the first time the numerical deconvolution of the AESEC data was applied to the elemental currents. The performance of the deconvolution was demonstrated on the model examples. The factor limiting the application of the deconvolution treatment is a noise reduction, which can affect the high frequency variations of the input signal. Further development of the deconvolution treatment will be addressed to the optimization of the noise reduction procedure.

## Summary

---

- ✓ In a general case, one cannot rely on the estimation of the corrosion current from the conventional Tafel extrapolation due to a possible contribution of the anodic dissolution to the total current under cathodic polarization. A valid estimation of the corrosion rates from  $R_p$  values essentially required a system stability, which was difficult to achieve during the corrosion of the studied systems. Among the tested electrochemical methods, AESEC provided the most appropriate values of corrosion currents. However, open circuit corrosion currents measured by AESEC did not include the oxidation processes resulting in the formation of low soluble Zn(II) intermediates and hence, can underestimate corrosion rates.
  - ✓ Obviously, the time and flow conditions in the AESEC experiments differ significantly from the conditions of the immersion tests and atmospheric corrosion. AESEC disfavors the accumulation of corrosion products and their ageing, but it has a major advantage in the investigation of the elementary steps of the corrosion mechanisms giving the access to the kinetic data about the metal dissolution. Thus, AESEC method will be applied for the intelligent screening of potential water soluble inhibitors.
-

# The effects of L-cysteine on the inhibition and accelerated dissolution processes of zinc metal

---

In the previous chapter (Chapter 5) we concluded that AESEC can be very efficient method for the intelligent screening of water soluble inhibitors on the example of galvanized steel/L-cysteine system at short exposure times and pH values of 6 and 12. In this chapter AESEC was applied for the mechanistic study of the action of L-cysteine on galvanized steel in a wide range of pH values and exposure times in order to answer the scientific question raised from the literature review:

- ✓ **How does the competitive formation of soluble complexes affect the action of L-cysteine on Zn?**

The content of the chapter repeats the article: V. Shkirskiy, P. Keil, H. Hintze-Bruening, F. Leroux, F. Brisset, K. Ogle, P. Volovitch, Effect of L-cysteine on Zn reactivity: spontaneous dissolution, *Corrosion Science*, 100 (2015) 101-112.

## Abstract

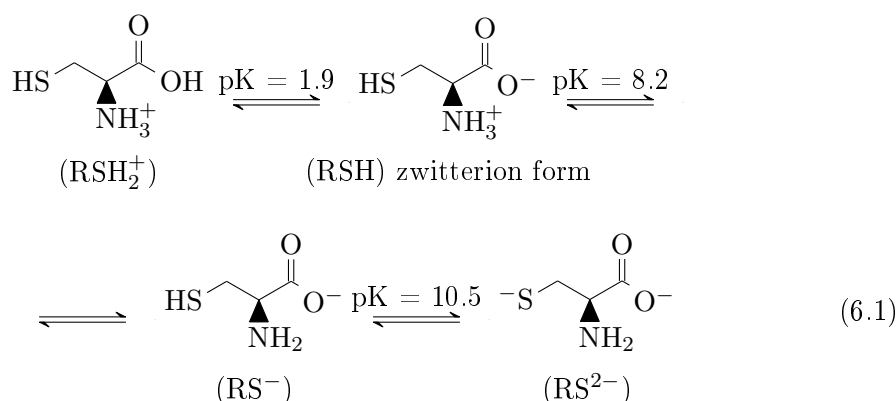
Effect of L-cysteine on the Zn dissolution in 0.5 M NaCl with initial pH of 4-12 was measured in continuously renewed electrolyte and in immersion tests. At short exposures 1 mM L-cysteine inhibited dissolution. The initial inhibition decreased with pH because of pH-enhanced dimerization of L-cysteine, confirmed by UV-vis spectroscopy. In long exposures at pH=6-8 the inhibition turned into the acceleration. This was not observed at pH=12. 10 mM L-cysteine accelerated Zn dissolution. The effects were explained by a competition between strong complexation of L-cysteine with Zn-ions and its weak physisorption on the substrate. The hypothesis was confirmed by surface characterizations.

## 6.1 Introduction

Amino acids are considered as one of the most promising candidates to replace chromium as a soluble inhibitor in aqueous environments [100, 103, 104, 106, 125, 181, 196] because they are non-toxic, relatively cheap and easy to produce. The action of various organic inhibitors on the corrosion of Zn and galvanized steel was extensively studied in neutral, weak acid and weak alkaline solutions [41, 109, 117, 197]. Most of the studied in these works inhibitors suppressed Zn corrosion by a simultaneously formed protective films [109, 117, 197] preventing anodic and/or cathodic processes on the surface. These protective films were formed either by insoluble complexes like in the case of Zn-benzotriazole [117] or, that was very often observed for Zn based substrates, by sealing an inner oxide and outer porous hydroxide layers with a small quantity of complexes or adsorbed molecules [41, 117].

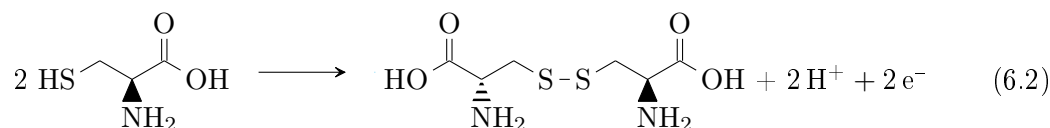
This work focuses on the understanding of the action of L-cysteine on Zn from hot dip galvanized (HDG) steel. L-cysteine is an alpha-amino acid, which contains not only carboxyl and amino functional groups but also a thiol group [184]. The thiol group is known to form strong bonding with some d-elements like Zn [184], which could explain the interest of this molecule as a potential inhibitor for HDG.

The chemistry of L-cysteine is complex. Depending on the solution pH, L-cysteine is present in different forms [184]



In aerated solutions L-cysteine is oxidized by the dissolved oxygen forming a dimer (L-cystine). The reaction rate increases in the presence of Fe(III), Cu(II) or other catalysts

[184, 198, 199]. The half reaction can be written as



It is clear from reaction (6.2) that the pH increase should enhance the dimerization. This makes necessary to distinguish the formal or primarily prepared (PP) concentration of the L-cysteine from the residual concentration of non-oxidized L-cysteine after its partial dimerization in aerated solutions.

The action of these two sulfur containing amino acids was previously studied on several metallic substrates. The dimer (L-cystine) accelerated corrosion of Ni in acid solutions [200]. L-cysteine accelerated corrosion of 304L stainless steel in 1 M H<sub>2</sub>SO<sub>4</sub> [201]. The effect was explained by the dissolution of the passive film due to the formation of soluble complexes between L-cysteine and Fe(III) species present in the passive film.

In contrast, L-cysteine inhibited corrosion of copper and copper alloys in acid and neutral solutions [181, 196, 202–206], mild steel in phosphoric acid [207, 208] and Al alloys in neutral NaCl solutions [150, 209]. The inhibiting effect of L-cysteine on Cu corrosion was attributed to the formation of an insoluble complex between the Cu(I) species present in the oxide film and the L-cysteine via the mercapto group. The L-cysteine molecules were reported not to interact with Cu(II) species [181, 203, 204].

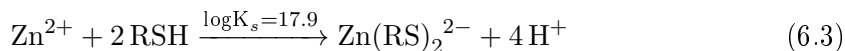
The inhibition action is often quantified using the inhibition efficiency, defined as the ratio between the corrosion rates with and without the inhibitor [100, 103, 104, 106, 125, 181, 196]. For 10 mM L-cysteine on copper substrates the inhibition efficiency was reported to be 70 % in neutral and 80-90 % in alkaline and acid solutions [181, 196, 202–204]. Higher inhibition efficiency in alkaline and acid solutions was attributed to stronger interactions of Cu(I) with the charged forms of L-cysteine (forms RSH<sub>2</sub><sup>+</sup>, RS<sup>-</sup> and RS<sup>2-</sup> in reaction 6.1) than with the zwitterion form (form RSH).

The inhibition efficiency usually increases with the inhibitor concentration [100, 103, 104, 106, 125, 181, 196]. The quantitative relation is made assuming a linear proportionality between the metal dissolution rate and the surface coverage of the metal by the adsorbed inhibitor [181, 196, 202–205, 210, 211] where the surface coverage is defined by Langmuir, Temkin or Frumkin adsorption isotherms [181, 196, 202–205]. However, the inhibition efficiency of L-cysteine for Cu substrates decreased at high concentrations in neutral and acid solutions [181]. The author explained the phenomenon by the dissolution of the adsorbed film at high concentrations of L-cysteine. The existence of an optimum concentration of corrosion inhibitor is known for several other systems [117, 182], however, for the best of our knowledge, there is no other mention in the literature about a non linear behavior of the inhibition efficiency of L-cysteine as a function of its concentration.

Despite the potential interest of L-cysteine as a water soluble inhibitor for HDG, we have found only one publication about the action of L-cysteine on Zn substrate [212]. 10 - 50 mM L-cysteine in 0.1 M HCl solution was reported to inhibit Zn corrosion with inhibition efficiency of 87 % at the highest concentration.

Considering the action of L-cysteine (RSH) and L-cystine (RSSR) on Zn based sub-

strates, as in the case of stainless steel, it could not only adsorb on the surface but also dissolve Zn oxides due to the formation of soluble complexes, for example [184]:



The logarithm of the stability constant ( $\log K_s$  in reactions (6.3) and (6.4)) of the most stable in aqueous solutions complex  $\text{Zn}(\text{RS})_2^{2-}$  is close to 17.9. For  $\text{Zn}(\text{RSSR})$ , the most stable L-cystine complex with  $\text{Zn}^{2+}$ , the reported value of  $\log K_s$  is 12.8 [184]. The effect of the solution pH on the values of  $K_s$  for L-cysteine and L-cystine was insignificant [184]. However, the structure and the stability of the surface oxides on Zn are strongly pH dependent [23, 36, 40, 41], which could result in significantly different interactions of the surface with the PP solutions of L-cysteine.

This brief review demonstrates that L-cysteine can play a dual role for the metal reactivity: it can (i) inhibit the metal dissolution absorbing on the surface and blocking active corrosion sites and (ii) accelerate the dissolution of the oxide film through the soluble complexes formation. The action of the L-cysteine on the corrosion performance of Zn is poorly documented and it cannot be easily predicted. Therefore, the objective of the current work is to verify if any inhibiting or accelerating effect of L-cysteine on Zn aqueous corrosion is present in a broad pH range and try to understand the effects of the solution concentration and pH.

The work consists of two parts. In the first part the immediate action of L-cysteine and L-cystine on the spontaneous Zn dissolution in 0.5 M NaCl was studied by in-situ measurements of Zn dissolution rate using atomic emission spectroelectrochemistry (AESEC) technique [161]. Briefly, AESEC consists in a coupling of an electrochemical flow cell with inductively coupled plasma atomic emission spectrometer permitting the quantification of metal dissolution during electrochemical tests. The results of the in-situ AESEC measurements were compared with the results of longer immersion tests and correlated with the surface characterizations. The effect of pH on the inhibition efficiency of L-cysteine for Zn corrosion was studied and the first mechanistic model was proposed explaining the evolution of the inhibition efficiency with pH and concentration of L-cysteine. This publication is followed by the second part of this work [213] where we present the results of the coupling the electrochemical impedance spectroscopy (EIS) and potentiodynamic polarization techniques with the AESEC measurements in order to study in detail the anodic and cathodic reactivity of polarized Zn in the presence of L-cysteine.

## 6.2 Experimental

### 6.2.1 Materials

The sheets of hot dip galvanized steel (HDG) bonder plates (type: HDG/5) supplied by “Chemetal” with an average thickness of galvanized layer of 20  $\mu\text{m}$  were used. The skin pass rolling was applied to HDG samples resulted in the initial surface roughness

[187]. The sheets were cut into 2 cm × 4 cm coupons, cleaned in ultrasonic bath with tetrahydrofuran, acetone and ethanol for 10 min each consequentially and dried under a nitrogen flow. Immediately prior to the experiments the samples were alkaline degreased in 1 M NaOH solution at 50 °C for 30 s, then rinsed with deionized water and dried under nitrogen flow. This treatment removed natural oxides [187] and resulted in more reproducible surface state.

All experiments were performed in 0.5 M NaCl solution (analytical grade, VWR Prolabo) prepared in purified water (Millipore™ system with the water resistivity of 18.2 MΩ cm) with and without the addition of the necessary quantities of the L-cysteine (analytical grade, Sigma Aldrich) and the L-cystine (analytical grade, Sigma Aldrich). The experiments were performed in additive free solutions, in 10 mM, 1 mM, 0.1 mM and 10 μM primarily prepared (PP) L-cysteine solutions and in 0.5 mM L-cystine.

Before the dissolution experiments, the L-cysteine solutions were aerated for 20 min by an air pump in order to reach the quasi equilibrium between the L-cysteine and L-cystine (reaction (6.2)) expected during the first 10 min [199]. Then the initial pH values were adjusted to the values of 2 and 4 by 1 M HCl, to the values of 6, 8 and 10 by 0.1 M NaOH and to the values of 12 and 13 by 4 M NaOH.

### 6.2.2 AESEC technique

#### Zn spontaneous dissolution

The online measurements of the Zn spontaneous dissolution were carried out using AESEC technique, described in detail elsewhere [161]. The setup consists of an electrochemical flow cell coupled with an inductively coupled plasma atomic emission spectrometer (ICP-AES) Ultima 2C™ produced by HORIBA Jobin Yvon. In the flow cell, the reaction between the sample and the aggressive electrolyte occurs, leading to the production of dissolved ions and insoluble oxides. Then, the electrolyte is transported to the ICP-AES, where its composition is continuously analyzed. The ICP-AES shows only the soluble part of the corroded Zn, while the insoluble oxides are not directly detected. The Zn dissolution rate ( $v_{Zn}$ ) was calculated from the instantaneous Zn concentration ( $C_{Zn}$ ):

$$v_{Zn} = \frac{f_e C_{Zn}}{A} \quad (6.5)$$

where  $A$  is the surface area and  $f_e$  is the flow rate of the electrolyte in the feed capillary. During the spontaneous reactivity of Zn, the corrosion of the substrate and the dissolution of the oxide film can occur simultaneously, resulting in the fact that the  $v_{Zn}$  detected by ICP-AES is composed of two terms: (i) the dissolution rate of ions, leached from the metallic surface due to the electrochemical oxidation and (ii) the chemical dissolution of Zn oxides.

#### AESEC parameters

Taking into account the composition of HDG, the dissolution of Zn and Al was surveyed by monitoring the emission intensities of Zn and Al at 213.856 nm and 167.081 nm

consequently. The detection limits, defined as the two times standard deviation of the signal of blank solution, were  $6.2 \pm 0.8 \mu\text{g/L}$  for Zn and  $1.8 \pm 0.2 \mu\text{g/L}$  for Al under the conditions of the experiments. In all experiments the Al concentration was below the detection limit .

The reactive surface area ( $A$ ) was  $0.51 \pm 0.01 \text{ cm}^2$ . The flow rate of the electrolyte ( $f$ ) was fixed to  $3.0 \pm 0.1 \text{ ml min}^{-1}$  and the temperature was  $24 \pm 1 \text{ }^\circ\text{C}$ .

The measurement of the open circuit potential was performed using Gamry Reference 600<sup>TM</sup> potentiostat (Gamry Instrument, US) with a saturated calomel reference electrode (SCE). The analog potential signal was routed into the measuring circuit of the ICP-AES to guarantee the same time scale for the both measurements.

Each measurement was repeated three times to estimate the standard deviation and the mean values.

### 6.2.3 UV/Vis spectroscopy

UV/Vis analysis was realized using a SPECTRONIC 200 UV/Vis spectrophotometer (Thermo Scientific<sup>TM</sup>, US). The absorption spectra of the L-cystine and the L-cysteine were monitored in the range of 200–320 nm in 0.5 M NaCl solutions at its natural pH of 6.2. The calibration curve for the pristine L-cystine was obtained using solutions with the concentrations of the L-cystine of 5, 10, 20, 30, 40, 50 and 60 ppm (equivalent to 21  $\mu\text{M}$  - 250  $\mu\text{M}$ ) for the absorbance values recorded at 238 nm [214]. The absorption spectra for the PP L-cysteine were recorded for the solutions with the initial pH values of 4, 6 and 12 using solutions with the concentrations of the L-cysteine of 10, 20, 40, 60, 80, 100 and 120 ppm (equivalent to 83  $\mu\text{M}$  - 990  $\mu\text{M}$ ).

### 6.2.4 Immersion tests

The immersion tests were done in a home made cell [215] with  $10.2 \pm 0.1 \text{ cm}^2$  ( $A$ ) of the top HDG surface exposed to 30 ml ( $V_0$ ) of 0.5 M NaCl solutions with the initial pH values of 6 and 12 with and without additions of L-cysteine or L-cystine. A plastic paraffin film (Parafilm<sup>TM</sup>) covered the cell during the immersion tests to reduce the evaporation of the electrolyte and the uptake of  $\text{CO}_2$  gas from the atmosphere. The effect of the 0.68 mM residual concentrations of L-cysteine and of the 0.5 mM L-cystine were tested. The concentration of L-cystine corresponded to its saturated solution and was limited by its solubility. The tests were performed under the controlled room temperature of  $24 \pm 1 \text{ }^\circ\text{C}$ . The samples were weighted before the immersion tests. After 2, 8, 15 and 24 hours of the exposure, the solutions in the cell were mixed and 2 ml aliquots ( $V_{al}$ ) were sampled. The concentrations of dissolved Zn ( $C_{Zn}$ ) were analyzed by ICP-AES and were used to calculate the total quantity of the dissolved Zn ( $Q_{Zn}$ ) using the formula:

$$Q_{Zn} = \frac{C_{Zn}(V_0 - MV_{al})}{A} \quad (6.6)$$

where  $M$  is the number of the aliquots taken before the last measurement. After 24 hours of the exposure, the samples were dried under nitrogen flow and weighted. Precipitated

corrosion products were removed from the dried sample surface by a razor blade and dissolved in 10 ml of 2 M HCl. The Zn and Al concentrations were measured using the ICP-AES. Two measurements under each conditions were performed to estimate the standard deviation and the mean values. The concentration of Al was below the detection limit in all experiments and only the Zn concentrations will be presented below.

It should be noted that the measurement of the Zn corrosion rate from the immersion tests in a stagnant electrolyte and in a flowing electrolyte in the AESEC measurements cannot be directly compared because of the difference in the flow conditions. Due to the flow of the electrolyte, the sedimentation of corrosion products is disfavored in AESEC tests compared with the immersion tests in the motionless electrolyte, which obviously influences the Zn reactivity.

### 6.2.5 Surface characterization

After the immersion tests, the surface morphology was observed using scanning electron microscope with field emission gun source (SEM-FEG) Gemini 1530. The high resolution secondary electron (SE) images of the top surface were obtained using the detector in a standard detection mode (SE) and positioned in lens (InLens mode). The accelerating voltage was 5 kV. The detection of sulfur was tempted using the coupled energy dispersive spectroscopy (EDS) with Si(Li) detector using QUANTAX software.

The surface was also characterized by Raman spectroscopy using Renishaw InVia confocal raman microscope with excitation by a Co Diode Pumped Solid State (DPSS) blue laser (532 nm, power 20 mW) with edge filter  $> 100 \text{ cm}^{-1}$ . The acquisition was piloted by WiRE spectral acquisition wizard. The lenses with magnification factors of x 5, x 20 and x 50 were used. The accumulation time for individual spectra was 120 s. The mapping of the area of  $180 \mu\text{m} \times 450 \mu\text{m}$  (48233 acquisitions of 2 s each) was made for the samples immersed in the solutions with the initial pH 12.

## 6.3 Results

### 6.3.1 Dimerization of L-cysteine to L-cystine in aerated aqueous solutions

Fig. 6.1a illustrates the determination of the amount of the L-cystine (RSSR) formed in the primarily prepared (PP) and then aerated L-cysteine (RSH) solutions at pH 6. Similar experiments were made at pH 4 and 12. The spectra were collected after 5 and 20 min of the solution aeration. After the different aeration times they varied less than 1 % implying that a major part of the L-cysteine corresponding to quasi equilibrium oxidized in the first 5 min of the aeration.

According to the stoichiometry of the dimerization (reaction(6.2)), the residual concentration of the non-dimerized L-cysteine ( $C_{RSH}^r$ ) can be determined as

$$C_{RSH}^r = C_{RSH}^f - 2C_{RSSR}^f \quad (6.7)$$

where  $C_{RSH}^f$  is the formal concentration of the L-cysteine and  $C_{RSSR}^f$  is the concentration of the formed L-cystine. The conversion ( $\varepsilon$ ) of the L-cysteine after the aeration procedure

6. THE EFFECTS OF L-CYSTEINE ON THE INHIBITION AND ACCELERATED DISSOLUTION PROCESSES OF ZINC METAL

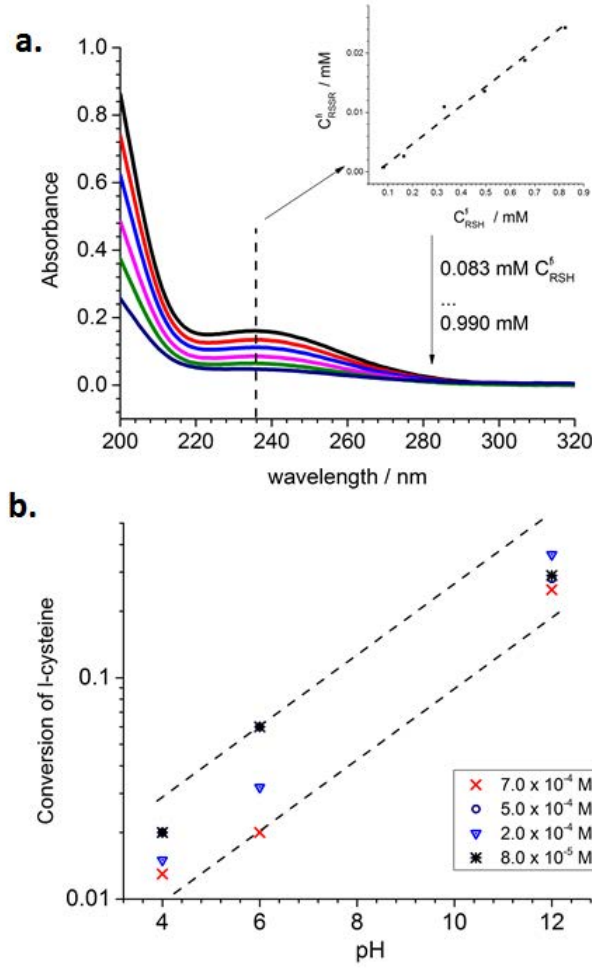


Figure 6.1: Examples of (a) UV/Vis determination of L-cystine ( $C_{RSSR}^f$ ) in L-cysteine containing solutions at pH 6 after 20 min of air bubbling where  $C_{RSH}^f$  is the formal and  $C_{RSH}^r$  is the residual concentrations of L-cysteine, and (b) conversion ( $\varepsilon$ ) of L-cysteine to L-cystine at different pH and  $C_{RSH}^f$  as indicated.

can be defined as

$$\varepsilon = (C_{RSH}^f - C_{RSH}^r) / C_{RSH}^f \quad (6.8)$$

The values of  $\varepsilon$ , measured for different  $C_{RSH}^f$  and pH values, are summarized in Fig. 6.1b. This data can be described by an empirical relation:

$$\log \varepsilon = (0.16 \pm 0.01)\text{pH} - (2.5 \pm 0.1). \quad (6.9)$$

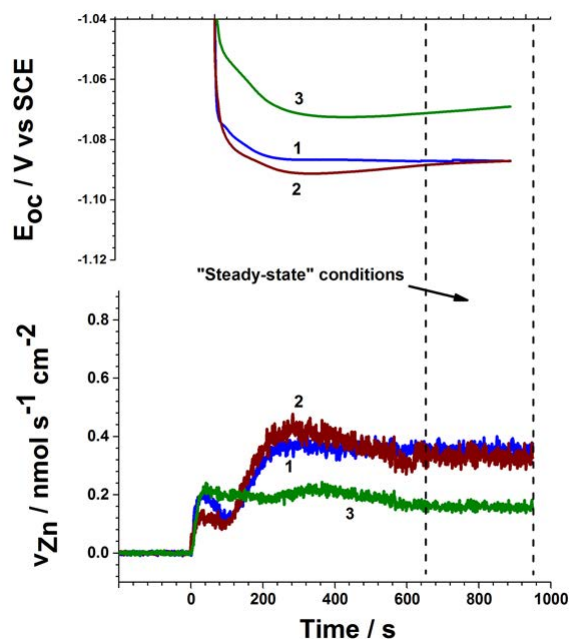


Figure 6.2: Evolution of Zn dissolution rate ( $v_{Zn}$ ) and open circuit potential ( $E_{OC}$ ) in (1) additive free, (2) 0.5 mM primarily prepared (PP) L-cystine and (3) 1 mM PP L-cystine solutions in 0.5 M NaCl at initial pH 6.

### 6.3.2 Real time dissolution measurement

#### Effect of L-cystine on Zn reactivity

Fig. 6.2 displays the typical Zn dissolution profiles recorded during the open circuit (OC) exposure of HDG to different solutions. Before the dissolution measurement the electrolyte goes directly to the ICP-AES without contacting the sample to measure the background signal for approximately 200 s. At  $t = 0$  s the solution contacts the surface resulting in the immediate increase of the Zn dissolution rate ( $v_{Zn}$ ) and the decrease of the open circuit potential ( $E_{OC}$ ). Afterwards, the values of  $v_{Zn}$  and  $E_{OC}$  tend to a “steady-state”, considered where  $v_{Zn}$  and  $E_{OC}$  variations do not exceed their standard deviation values for at least 200 s.

It is clear from Fig. 6.2 that the addition of 0.5 mM L-cystine (concentration of L-cystine corresponded to its saturated solution [216]) to 0.5 M NaCl solution does not affect the Zn reactivity at the initial pH value of 6. The experimentally observed solubility of the L-cystine did not vary significantly in the pH range of 2-13 (logarithm of the solubility was  $-3.30 \pm 0.04$  M). The experiments at lower concentrations were not performed because of the absence of any effect even at the maximal possible concentration of L-cystine.

The results were similar in the pH range of 2-13: the addition of 0.5 mM L-cystine to 0.5 M NaCl did not affect the Zn dissolution.

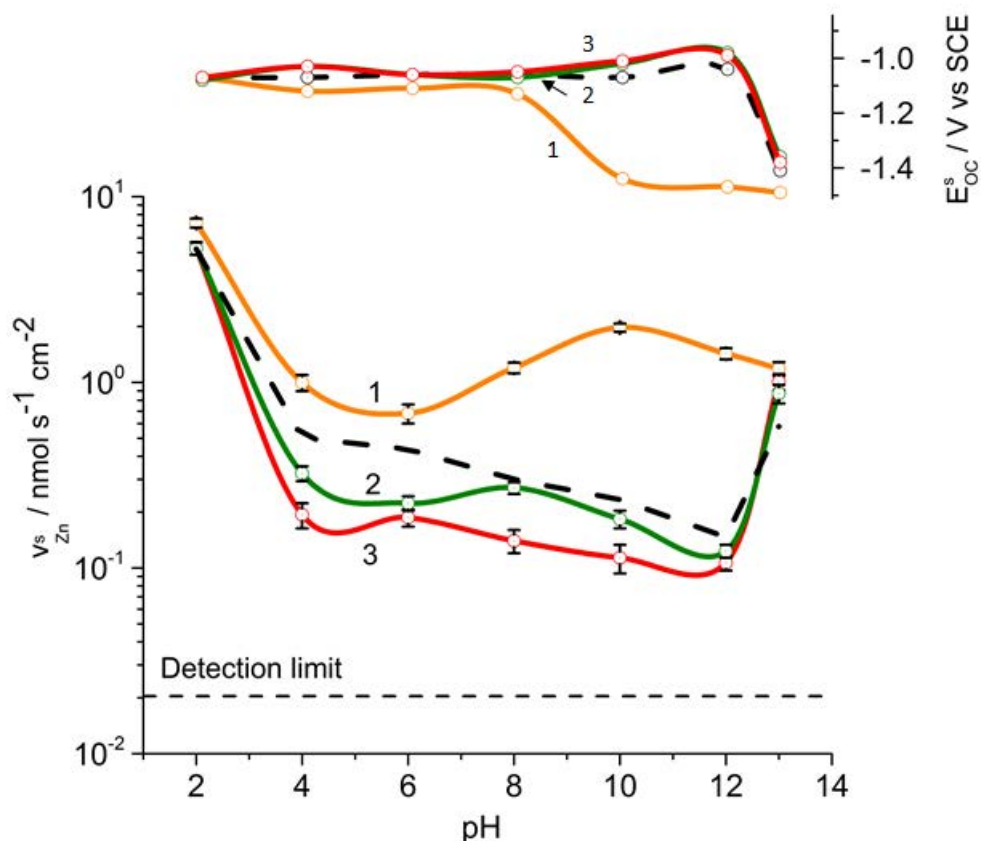


Figure 6.3: “Steady-state” values of Zn dissolution rate ( $v_{Zn}^s$ ) and open circuit potential ( $E_{OC}^s$ ) as function of pH in (1) 10 mM primarily prepared (PP) L-cysteine, (2) 1 mM PP L-cysteine, (3) 0.1 mM PP L-cysteine solutions in 0.5 M NaCl. Dot line corresponds to the additive free solution [187]

### Effect of L-cysteine on Zn reactivity

The evolution of  $v_{Zn}$  and  $E_{OC}$  was recorded in the PP L-cysteine containing solutions of different pH and L-cysteine concentrations. Typical dissolution profile is presented in Fig. 6.2 curve 3. The “steady-state”  $v_{Zn}$  and  $E_{OC}$  values ( $v_{Zn}^s$  and  $E_{OC}^s$  correspondingly) obtained from these measurements are presented in Fig. 6.3.

As shown in Fig. 6.3, in the solutions containing 1 mM and 0.1 mM PP L-cysteine, the  $v_{Zn}^s$  is slowed down at the initial pH values of 4-12. However, the addition of the  $10^{-2}$  M PP L-cysteine accelerates the dissolution. The accelerating effect is enhanced in the solution with the initial pH of 10-12 and is accompanied by the the  $E_{OC}^s$  drop down till -1.44 V vs SCE. In Fig. 6.4 the evolution of the potential in the 10 mM L-cysteine is superimposed with the E-pH diagram of Zn in 0.5 M NaCl and 10 mM residual L-cysteine calculated by Hydra Meduza Software [33]. The evolution of the experimental values of

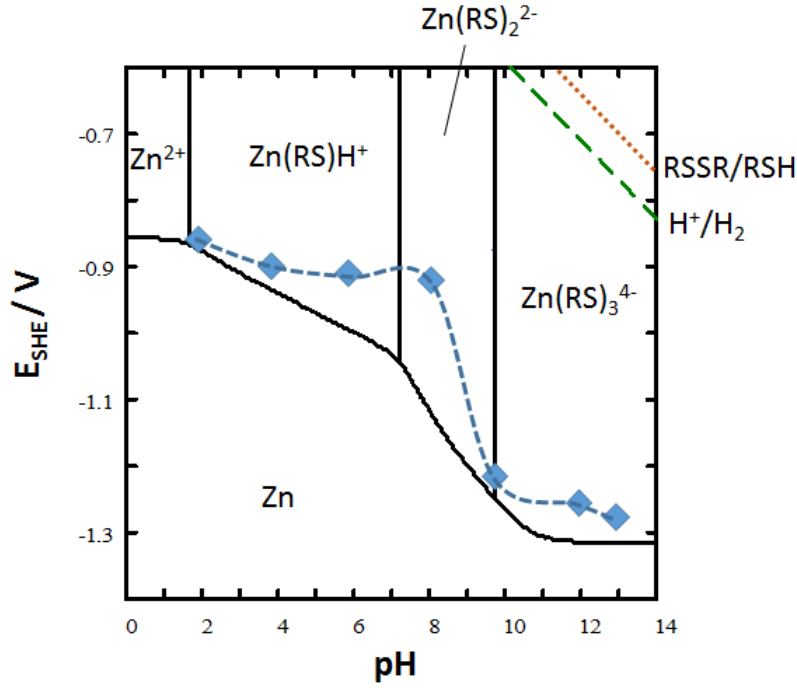


Figure 6.4: E-pH diagrams for Zn in 10 mM L-cysteine(RSH) in 0.5 M NaCl solution at 25 °C calculated by HydraMeduza software (version 2015) considering 0.5 mM Zn species and equilibrium between different species listed below. Dashed blue line corresponds to the “steady-state” measured values of open circuit potential during Zn dissolution in the presence of 10 mM L-cysteine (Fig. 6.3). Green and orange dash lines correspond to hydrogen and L-cystine (RSSR) reduction to RSH [184]. The species taken into account with the standard constant ( $K$ ) of species formation (presented as  $\log K$ ) from  $\text{Zn}^{2+}$  taken from the standard Hydro Meduza database (consulted 07/05/2015) [33] include:  $\text{Zn}(\text{OH})_2$  (-16.4),  $\text{Zn}(\text{OH})_3^-$  (-28.2),  $\text{Zn}(\text{OH})_4^{2-}$  (-41.3),  $\text{Zn}_2(\text{OH})_6^{2-}$  (-54.3),  $\text{Zn}_2(\text{OH})_3^{3+}$  (-9.0),  $\text{Zn}_4(\text{OH})_4^{4+}$  (-27.0),  $\text{ZnCl}^+$  (0.43),  $\text{ZnCl}_2$  (0.45),  $\text{ZnCl}_3^-$  (0.5),  $\text{ZnCl}_4^{2-}$  (0.2),  $\text{ZnClOH}$  (-7.48),  $\text{ZnOH}^+$  (-7.5),  $\alpha\text{-Zn}(\text{OH})_2$  (-12.45),  $\varepsilon\text{-Zn}(\text{OH})_2$  (-11.5),  $\text{Zn}_2(\text{OH})_3\text{Cl}$  (-15.2),  $\text{Zn}_5(\text{OH})_8\text{Cl}_2$  (-38.5),  $\text{ZnCl}_2$  (-7.03),  $\text{ZnO}$  (-11.2) and  $\text{Zn}$  (-25.757).  $\text{Zn}^{2+}$  complexes with RSH were added manually with  $K$  values taken from the IUPAC database [184] (listed in Table 6.1)

$E_{OC}^s$  and the potential of Zn oxidation to  $\text{Zn}^{2+}$  complexes with L-cysteine demonstrates similar trends (Fig. 6.4).

The inhibition efficiency ( $\eta$ ) of L-cysteine on the Zn dissolution can be expressed according to the formula below

$$\eta, \% = \frac{v_{\text{Zn}}^s(\text{without L-cysteine}) - v_{\text{Zn}}^s(\text{with L-cysteine})}{v_{\text{Zn}}^s(\text{without L-cysteine})} \times 100\% \quad (6.10)$$

6. THE EFFECTS OF L-CYSTEINE ON THE INHIBITION AND ACCELERATED DISSOLUTION PROCESSES OF ZINC METAL

---

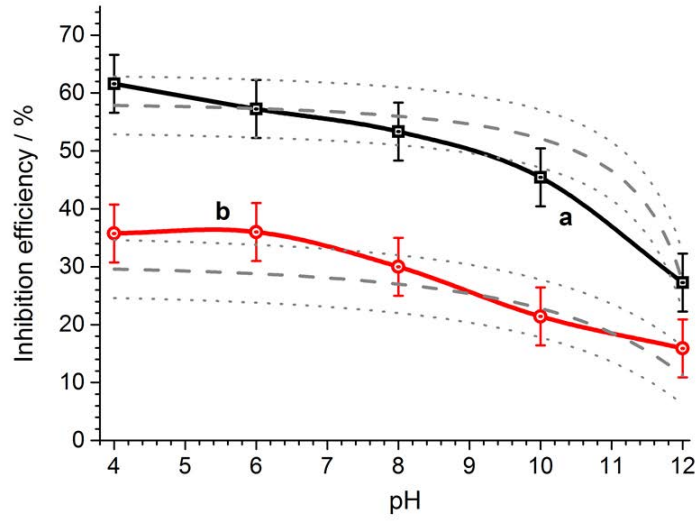


Figure 6.5: Inhibition efficiency of (a) 1 mM and (b) 0.1 mM primarily prepared (PP) L-cysteine solutions. The dot lines show the evolution of the inhibition efficiency calculated from the concentrations of non-dimerized L-cysteine in the solutions with given pH and PP concentrations using Eq. (6.7) and (6.9). See text for details.

Table 6.1: Stability constants of complexes formation ( $K_s$ ) between L-cysteine (RSH) and  $Zn^{2+}$  used in the equilibrium calculations for Fig. 6.4. The data were taken from the IUPAC database [184]. Either recommended values or the ones measured under conditions similar to the experiments in this paper were taken.

Formula of complex	$\log K_s$
$Zn(RS)_2^{2-}$	18.71
$Zn(RS)$	9.17
$Zn(RS)_3^{4-}$	21.64
$Zn(RS)_2H^-$	23.32
$Zn_3(RS)_4^{2-}$	43.5
$Zn_3(RS)_4H^-$	49.5
$Zn_3(RS)_4H_2$	29.03
$Zn(RS)_2H_2$	29.0
$Zn(RS)H^+$	19.5
$Zn_2(RS)_3^{2-}$	24.8
$Zn_2(RS)_3H^-$	36.39
$Zn_2(RS)_3H_2$	41.72

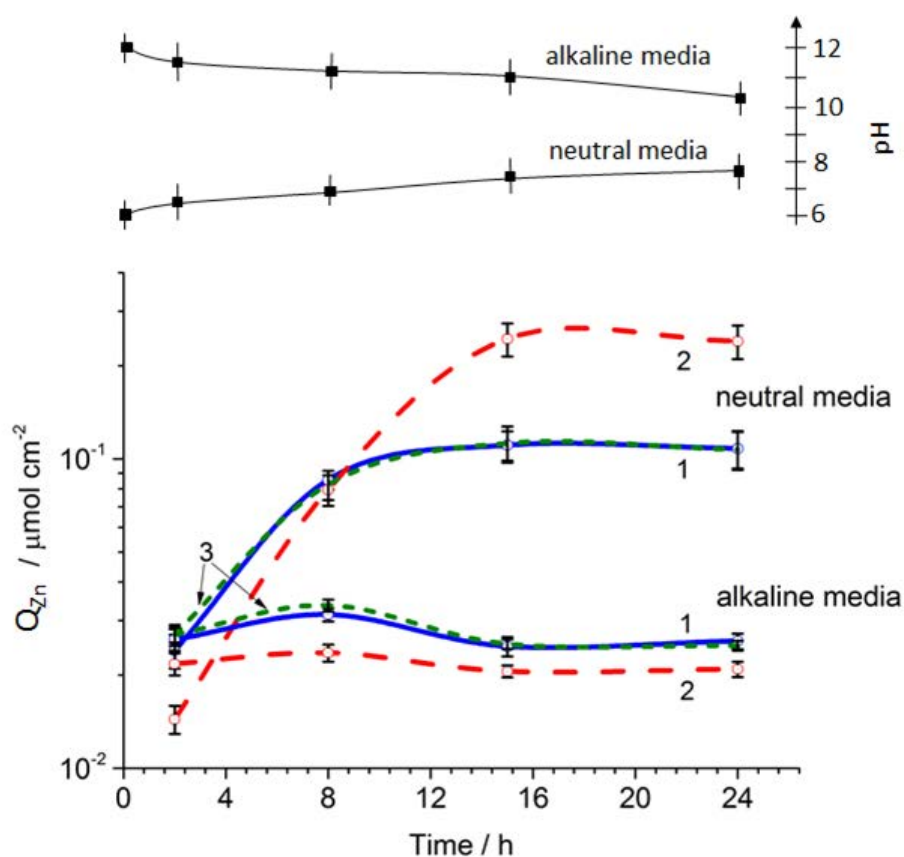


Figure 6.6: Amount of Zn ( $Q_{Zn}$ ) dissolved during immersion tests in 0.5 M NaCl at the initial pH 6 (neutral media) and 12 (alkaline media) in (1) additive free solutions, (2) 0.68 mM L-cysteine containing solutions and (3) 0.5 mM L-cystine containing solutions. The pH evolution for the solutions with the initial pH of 6 and 12 is also shown.

$\eta$  values, calculated from the data of Fig. 6.3, are presented in Fig. 6.5. From Fig. 6.5,  $\eta$  is maximal at the initial pH 4 ( $62 \pm 5$  % in 1 mM and  $36 \pm 5$  % in 0.1 mM PP L-cysteine solutions).  $\eta$  uniformly decreases with pH reaching  $27 \pm 5$  % in 1 mM and  $16 \pm 5$  % in 0.1 mM L-cysteine solutions.

In the presence of 10  $\mu\text{M}$  PP L-cysteine, no changes in Zn reactivity in 0.5 M NaCl solution were detected neither for  $v_{Zn}$  nor for  $E_{OC}$  evolution for all pH. Several supplementary experiments with intermediate PP L-cysteine concentrations in the solution at pH 6 were performed but the results are not shown in the Fig. 6.3.

Table 6.2: Solutions with the additions of L-cysteine used in the immersion tests. The formal and residual concentrations of L-cysteine along with the concentration of formed L-cystine are noted.

№	pH	L-cysteine, mM		L-cystine, mM	
		formal	residual	formal	formed
1	6	0.7	0.68	0	0.01
2	12	1	0.68	0	0.16

### 6.3.3 Zn reactivity in immersion tests

#### Common features in immersion tests with and without L-cysteine

The difference between the weights of HDG samples before and after the immersion tests in different solutions was less than the error of the measurement of 0.1 mg. The detected by ICP-AES quantity of Zn(II) in the precipitated Zn corrosion products after 24 hours of the exposure was about 10 nmol per  $\text{cm}^{-2}$  of the exposed surface in all experiments. Fig. 6.6 displays the pH evolution and the evolution of the quantity of the soluble Zn over 24 hours of the immersion in the different solutions as indicated in the figure and the figure caption. Comparing the quantity of Zn(II) in the soluble and insoluble corrosion products, it can be concluded that less than 0.5 % of oxidized Zn stays on the surface in the insoluble form. This fact permits to quantify the corrosion rates on the basis of the data presented in Fig. 6.6 discarding the contribution of the insoluble products in the mass balance.

For the solutions with or without L-cysteine with the initial pH 6 and 12, the final pH after 24 hours of the immersion is about 8 and 10 respectively (Fig. 6.6), which can be related to the accumulation of carbon dioxide present in the atmosphere as well as to the precipitation of corrosion products.

The fact that in the additive free solutions (curves 1) the Zn ions after 1 hour of the immersion is the same at pH 6 and 12 but it increases with time in neutral media and remains stable in alkaline media is coherent with the previously reported destabilization of native Zn oxides at neutral pH and the stabilization of native Zn oxides in slightly alkaline media [140].

#### Effects of L-cystine and L-cysteine additions

Fig. 6.6, curves 3 shows that as in the AESEC experiments the 0.5 mM L-cystine containing solutions do not show any effect on the Zn dissolution over 24 h of the immersion.

In order to work with the identical equilibrium concentrations of the L-cysteine present in the solution in non-dimerized form at different pH, the residual concentrations of the L-cysteine were calculated using Eq. 6.9. Used PP concentrations of L-cysteine, which corresponded to 0.68 mM of the residual concentration are presented in Table 6.2.

The comparison of the quantities of the dissolved Zn(II) with and without the inhibitor, presented in Fig. 6.6, demonstrates that at neutral pH, the initially observed

inhibiting effect of the L-cysteine turns into an accelerating effect ( $\eta < 0$ ) after approximately 8 hours of the immersion. In alkaline solution the inhibition is still present after 24 hours of the immersion.

#### 6.3.4 Surface characterization after immersion tests

##### Effect of 10 mM L-cysteine addition on structure and composition of oxide layers on Zn

Fig. 6.7a and 6.7b present the typical surface morphology of the HDG before and after the immersion tests. Strong initial surface roughness is caused by the skin pass process.

After the immersion of HDG in 10 mM PP L-cysteine for 24 hours, the cavities are homogeneously attacked whereas some pits are visible on the upper part of the surface (Fig. 6.7c and 6.7d). The porous oxide/hydroxide layer typically present on Zn surface in neutral and alkaline solutions [23, 36, 140] is not visible. No signal of sulfur was visible in the EDS spectra (the spectra are not shown here). A small oxygen signal was detected, which can indicate a thin and compact layer of Zn oxides/hydroxides. No signal of sulfur was visible. Trace quantities of impurities (Si, P) were detected. The absence of visible porous oxides correlates with the highest between the all samples corrosion rate (Fig. 6.3).

The Raman spectra (not shown here) of the surface after the immersion in 0.5 M NaCl at pH 6 confirmed the presence of ZnO (wurtzite crystal structure) by the peaks at 330, 435 and 570 nm and 1070 nm [217] and some  $Zn_5(OH)_8Cl_2$  by the peak at 3480 nm and a shoulder around 400 nm on the peak at 435 nm of ZnO [217]. Some zinc carbonate was also detected, which could be accumulated during the storage of the samples after the exposure.

In the presence of L-cysteine the signals were weak and the main difference with the sample immersed in the L-cysteine free solution was that only the peak at 570 nm was detected for ZnO, which was previously described as the defective black oxide  $Zn_{1+x}O$  containing an excess of the metallic zinc [51, 218]. All spectra presented large background increase around 800 nm, which could be related to the presence of the badly structured hydroxides  $\beta$ -Zn(OH)<sub>2</sub>. No characteristic peak for the C-S bond of the L-cysteine was observed at 685 nm or near.

##### Effect of 0.68 mM L-cysteine addition on structure and composition of oxide layers on Zn

After 1 hour of the immersion in neutral NaCl solutions, conditions in which the addition of 0.68 mM L-cysteine inhibits Zn dissolution (Fig. 6.6), the surface is covered by a great number of crystallites (Fig. 6.8). Their quantity in the porous layer and their size seem to be higher in the L-cysteine free solution (Fig. 6.8a versus 6.8b). The EDS reveals traces of sulfur on the sample immersed in the presence of the L-cysteine (inset in Fig. 6.8b versus 6.8a).

The morphology of the oxide layer shown in high resolution images (Fig. 6.8c and

## 6. THE EFFECTS OF L-CYSTEINE ON THE INHIBITION AND ACCELERATED DISSOLUTION PROCESSES OF ZINC METAL

---

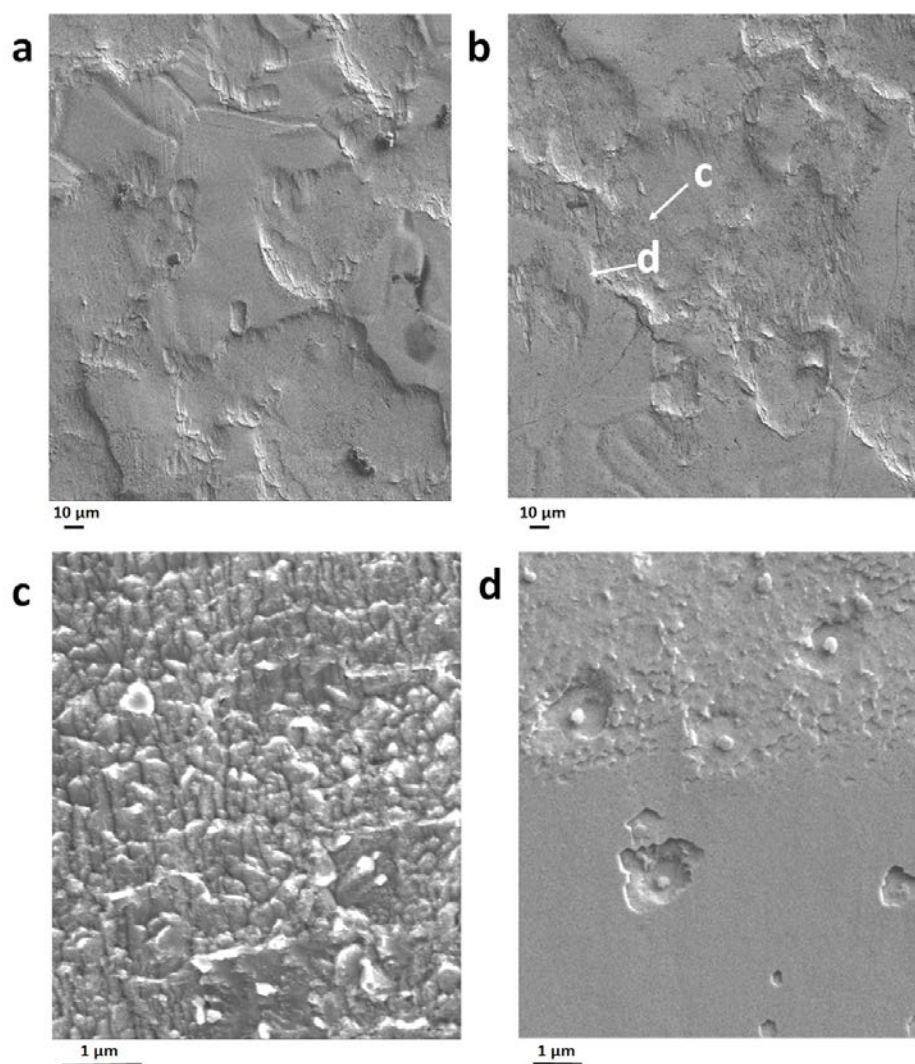


Figure 6.7: SEM images of HDG surface (a) before and (b) after 24 hours of immersion in 0.5 M NaCl solution with 10 mM PP L-cysteine at initial pH 6. Secondary electron contrast, accelerating voltage of 5 kV. Fig. (c) and (d) show high resolution images of areas denoted in Fig. 6.7b obtained InLens mode.

6.8d) is also different: numerous spherical agglomerates precipitated on the porous layer and isolated holes in the dense layer formed in additive free solution (Fig. 6.8c) and hexagonal columns present in smaller quantity on the compact layer, which seems to suffer the intergranular corrosion after the immersion in the presence of the L-cysteine (Fig. 6.8d).

On the samples immersed for 1 hour in the absence of L-cysteine the main product detected by the raman spectroscopy was a mixture of ZnO and defect  $Zn_{1+x}O$  with

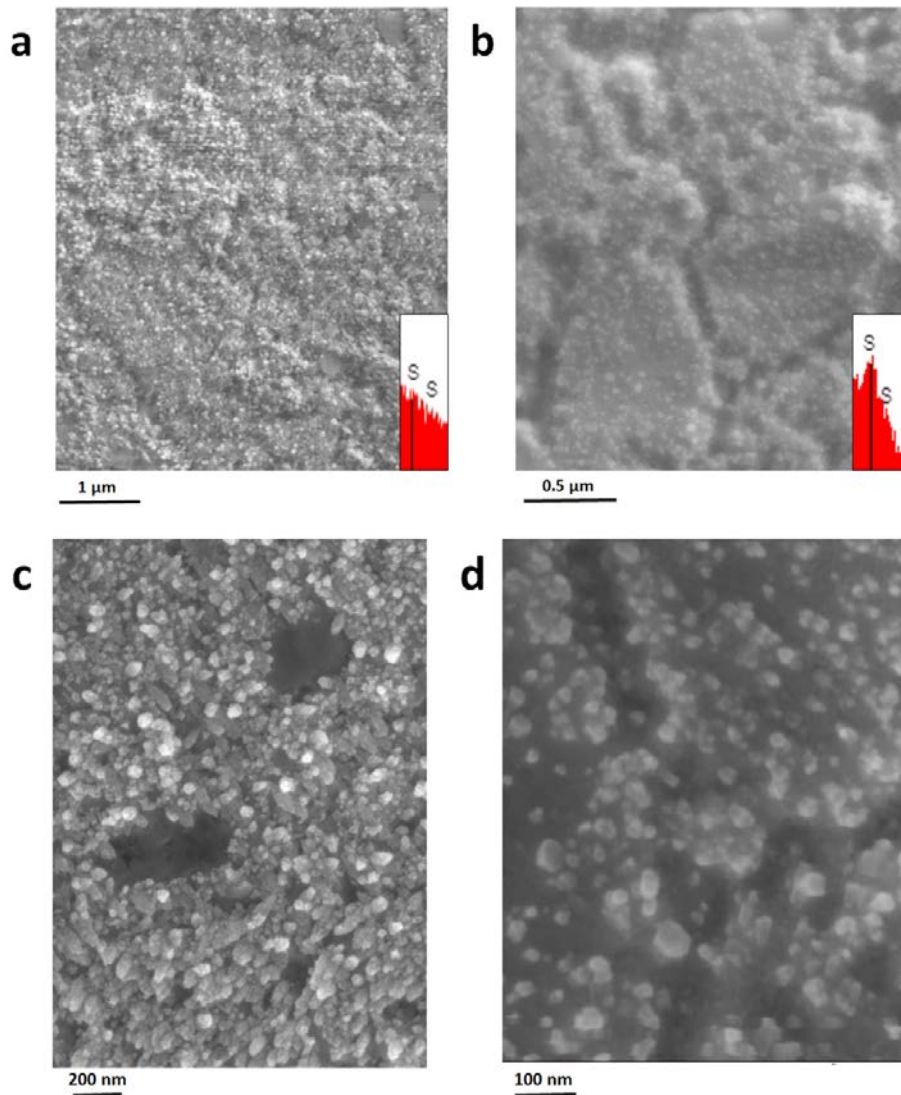


Figure 6.8: SEM images of HDG surface after 1 hour of immersion at initial pH 6 in (a, c) 0.5 M NaCl and (b, d) 0.5 M NaCl + 0.68 mM L-cysteine. Inset in (a, b) shows the sulfur peak in EDS spectrum. Characteristic spherical agglomerates (c) and hexagonal columns (d) are marked. Secondary electron contrast, accelerating voltage of 5 kV. High resolution images (c, d) are made InLens mode.

small quantities of  $\epsilon$ -Zn(OH)<sub>2</sub>. The intensity of the peak at 570 nm (defect Zn<sub>1+x</sub>O) oxide in the presence of L-cysteine did not vary significantly (the spectra are not shown here). However, the signal at 435 nm was significantly lower and the signal at 330 nm disappeared, which is coherent with a high fraction of the defective oxide. The signal of the  $\epsilon$ -Zn(OH)<sub>2</sub> (260 nm, 400 nm, large band between 103 and 1100 nm with a maximum

near 1080 nm) increased. As in the case of more concentrated solutions, no peak was detected at 685 nm or near, which is characteristic for the C-S bond of the L-cysteine.

After 24 hours of the immersion at neutral pH, when the L-cysteine action turned into the acceleration, the porous layer formed in L-cysteine free solution consists of amorphous particles with an irregular shape (Fig. 6.9a) while the surface immersed in 0.68 mM L-cysteine solution is covered with a “needle-like” oriented columns (Fig. 6.9b). In this case the signal of sulfur was not detected by EDS.

After 24 h of the immersion in alkaline solutions both, porous and dense layers are visible (Fig. 6.10a and 6.10b). Significant quantity of precipitated spherical agglomerates and hexagonal columns form the porous layer in the L-cysteine free solution. The layer seems to be more compact and contained quantity of the precipitated particles in the presence of 0.68 mM L-cysteine. The signal of sulfur was not detected by EDS.

The Raman spectroscopy shows the same tendencies for the film composition as after the immersion in the neutral solutions (Fig. 6.10 c and d): high fraction of ZnO in the L-cysteine free solution and mainly defective  $Zn_{1+x}O$  oxide and  $\epsilon$ -Zn(OH)<sub>2</sub> in the presence of L-cysteine.

## 6.4 Discussion

### 6.4.1 Effect of dimerization of L-cysteine on initial Zn reactivity

The absence of any effect of the pristine L-cystine suggests a low adsorption capacity of the L-cystine molecules on the Zn surface and a weak ability to form complexes with Zn cations. Indeed, the reported value of the stability of Zn complex with L-cystine ( $\log K_s = 12.8$ ) is much lower than with L-cysteine ( $\log K_s = 17.9$ ) (reactions (6.3) and (6.4)) [184].

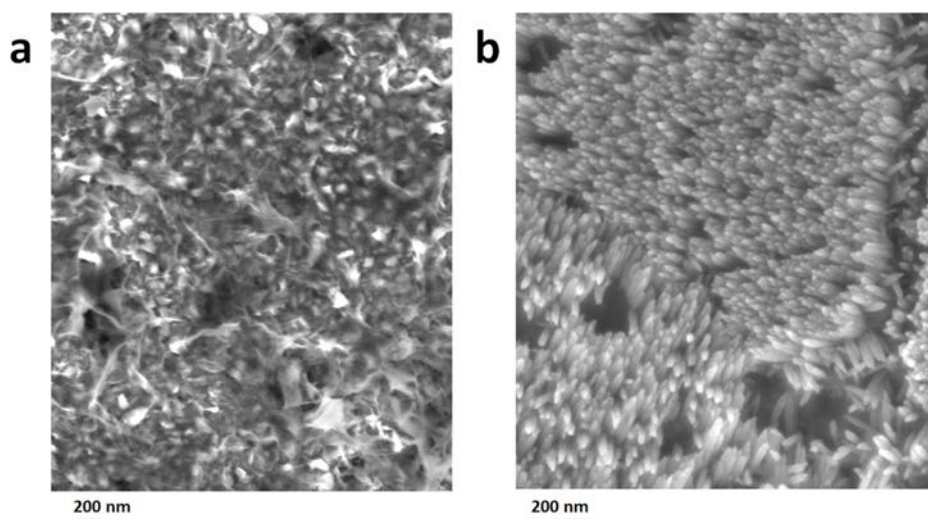


Figure 6.9: SEM images of HDG surface after 24 hours of immersion at initial pH 6 in (a) 0.5 M NaCl and (b) 0.5 M NaCl + 0.68 mM L-cysteine. InLens mode, accelerating voltage of 5 kV.

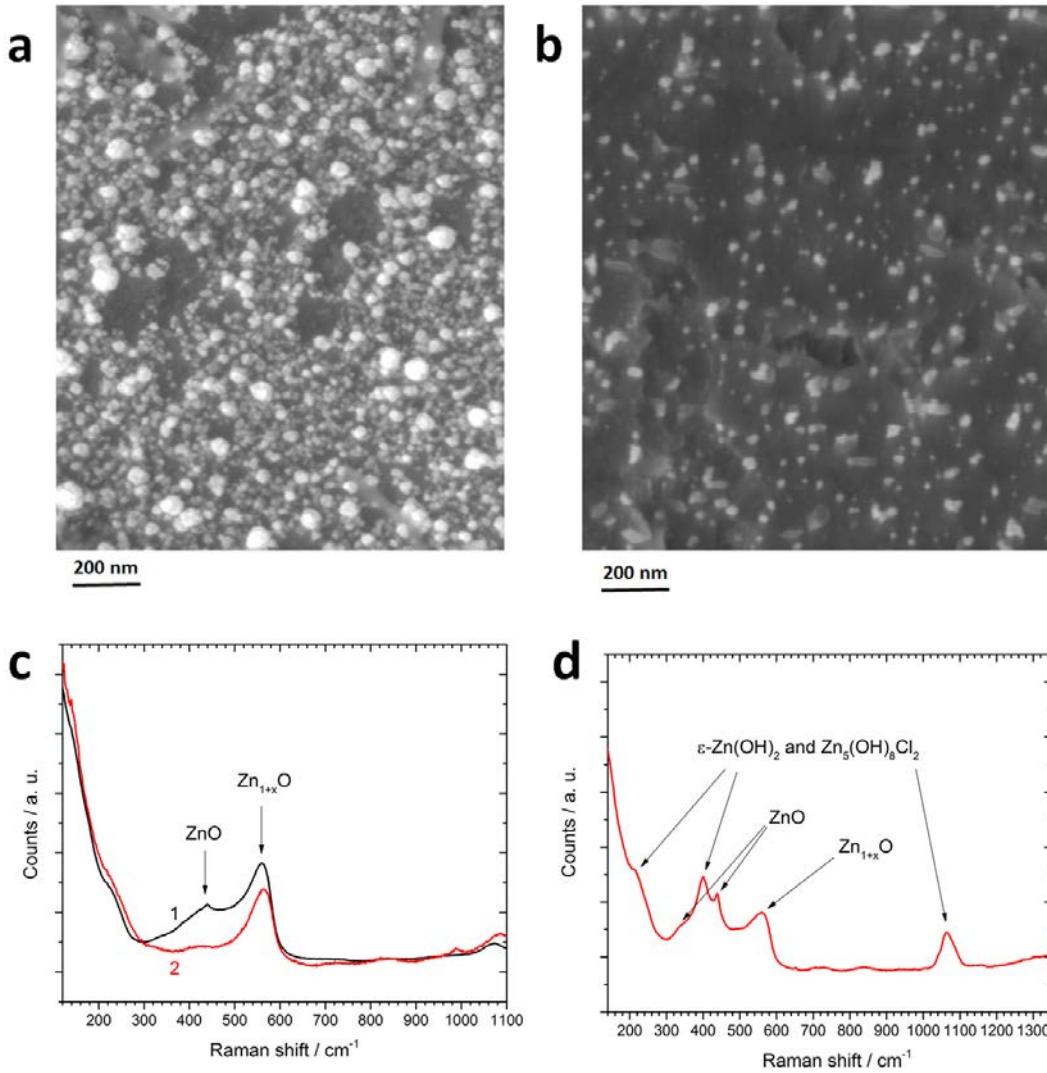


Figure 6.10: SEM images (a, b) and Raman spectra (c,d) of HDG surface after 24 hours of immersion at pH 12 in (a, c curve 1) 0.5 M NaCl and (b, c curve 2) 0.5 M NaCl + 0.68 mM L-cysteine. SEM images were made in lens mode, accelerating voltage of 5 kV. Spectrum (d) was made at grain boundaries of figure a

L-cysteine inhibited Zn dissolution in concentration range of 0.1–1 mM. Using the common approach for metal–organic inhibitor systems in which the organic molecules are assumed to adsorb on active centers of the surface, the surface reactivity decreases linearly with the surface coverage ( $\theta$ ), given with the relation [210,211]

$$\theta = \frac{v_{Zn}^0 - v_{Zn}^s}{v_{Zn}^0 - v_{Zn}^i} \quad (6.11)$$

where  $v_{Zn}^0$  is the Zn dissolution in the inhibitor free solution and  $v'_{Zn}$  is the Zn dissolution when the surface is saturated with the adsorbed inhibitor molecules, that is to say  $\theta \approx 1$ , which in our experiments corresponded to 0.1 mM PP L-cysteine.

Assuming the simplest Langmuir adsorption isotherm for the residual concentrations of L-cysteine on Zn at pH 6, the plot of  $C_{RSH}^r/\theta$  as a function of  $C_{RSH}^r$  (Fig. 6.11) permits to estimate the adsorption/desorption equilibrium constant  $K_{ads}$ :

$$\frac{C_{RSH}^r}{\theta} = C_{RSH}^r + \frac{1}{K_{ads}} \quad (6.12)$$

and to calculate the standard Gibbs free energy ( $\Delta G_{ads}^0$ ). For the data presented in Fig. 6.11, the  $\Delta G_{ads}^0$  is about  $-25 \text{ kJ mol}^{-1}$ , which corresponds to the strong physisorption [124] of L-cysteine.

Taking into account the absence of any significant effect of the L-cystine on Zn reactivity, one can expect that only non-dimerized L-cysteine can act as an inhibitor. In this hypothesis the decrease of the inhibition efficiency with pH can correlate with the increase of the fraction of the dimerized L-cysteine with pH (Eq. (6.9)). Calculated in this way residual concentrations of L-cysteine at different pH and the value of  $K_{ads}$ , obtained for pH 6 can be used to estimate the decrease of the inhibition efficiency ( $\eta$ ) with pH with help of Eqs. (6.11) and (6.12):

$$\eta, \% = \frac{C_{RSH}^r K_{ads}}{1 + C_{RSH}^r K_{ads}} \left( 1 - \frac{v'_{Zn}}{v_{Zn}^0} \right) 100\% \quad (6.13)$$

where  $C_{RSH}^r$  is calculated according to Eqs. (6.7) and (6.9):

$$C_{RSH}^r = C_{RSH}^f (1 - 10^{(0.16 \pm 0.01)\text{pH} - (2.5 \pm 0.1)}) \quad (6.14)$$

It is clear that the tendency obtained from such an estimation is in a good agreement with the experimental values. Therefore, the observed decrease of the inhibition efficiency in the PP L-cysteine solutions can be directly associated with the lowering of the PP L-cysteine concentration due to its dimerization into L-cystine. The result implies that the initial inhibition efficiency of the L-cysteine on Zn dissolution is determined by the residual (non-dimerized) L-cysteine concentration and that for 1 mM of non-dimerized L-cysteine inhibition efficiency is about 60 % in the pH range of 4-12.

#### 6.4.2 Competitive actions of L-cysteine on Zn dissolution

Our results demonstrated the initial inhibiting action of 0.1–1 mM PP L-cysteine on the Zn dissolution. At the same time, 10 mM L-cysteine at all pH acted as an accelerator. Moreover, 0.68 mM non-dimerized L-cysteine at pH 6 demonstrated the reverse from the inhibiting to the accelerating effect in the immersion tests after 8 hours of the exposure. In this section we will discuss possible reasons of such a complex behavior.

It is generally accepted that the oxide/hydroxide films are permanently present on Zn in contact with aqueous electrolytes and the dissolution reactions pass through these

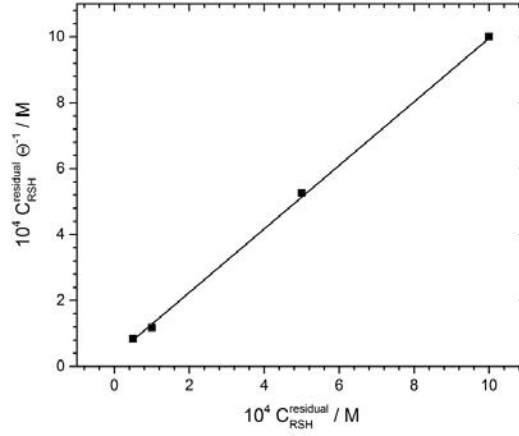
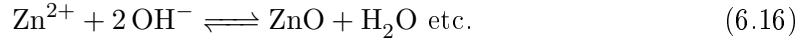
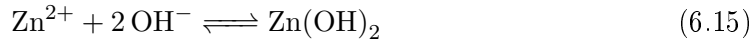


Figure 6.11: Adsorption isotherm of primarily prepared solutions of 50  $\mu\text{M}$  - 1 mM L-cysteine at pH 6. Defined values of  $K_{ads} = 30 \text{ mM}^{-1}$  and  $\Delta G_{ads}^0 = -25 \text{ kJ mol}^{-1}$ .

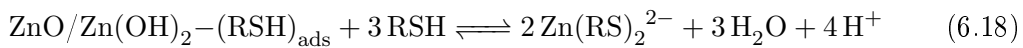
oxide/hydroxide layers [36, 38, 40, 178, 180, 219]. The corrosion product films on Zn consist of an inner defective compact oxide layer and outer porous oxides/hydroxides ( $\text{ZnO}/\text{Zn}(\text{OH})_2$ ). The formation of the porous layer is considered to be due to the precipitation of Zn cations ejected through the compact layer:



Oxygen diffusion through the outer Zn porous oxides is considered as the rate determining step for the atmospheric corrosion of Zn [23, 36, 38].

It is known from the surface analysis of Zn/organic inhibitor systems [41, 117] that the organic molecules rarely penetrate till the interface between the porous and the compact oxides but either replace or incorporate into the porous layer. The incorporation of the adsorbed molecules of the inhibitor in the oxide-hydroxide film is considered as one of the probable mechanisms of the improvement of corrosion resistance but their exact role is still unclear [41, 117]. Therefore, the introduction of the L-cysteine molecules can:

1. enhance the barrier properties of the porous layer of Zn oxides and hydroxides by adsorption in the defects (reaction (6.17)) contributing to the improvement of the film compactness
2. dissolve the already formed oxide layers (reactions (6.17) and (6.18))



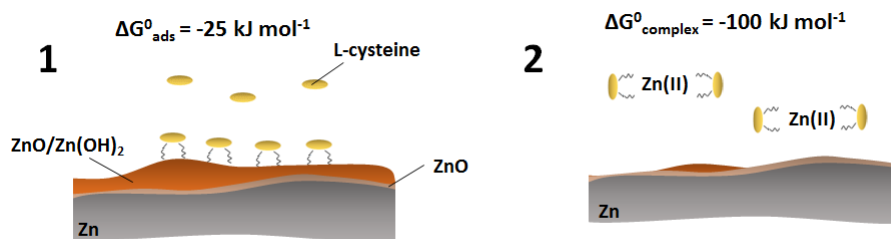


Figure 6.12: Schematic representation of steps of L-cysteine (RSH) action on Zn: (1) adsorption on Zn oxide/hydroxide surface and (2) dissolution of Zn oxide/hydroxide by complexation of L-cysteine with Zn(II).

3. stabilize soluble Zn(II) species by the complexation reaction (reaction (6.3)).

The value of the Gibbs free energy of the complex formation calculated as  $\Delta G^0 = -2.3RT \log K_s$ , where  $\log K_s$  equals to 18 [184], is  $-100 \text{ kJ mol}^{-1}$ . This high energy gain makes the complex formation more favorable than the adsorption (calculated in section 6.4.1,  $\Delta G^0$  was about  $-25 \text{ kJ mol}^{-1}$ ). Hence, at long exposure times one can expect that at the equilibrium, L-cysteine molecules are exclusively present in the form of the soluble  $\text{Zn}(\text{RS})_2^{2-}$  complex and L-cysteine dissolves Zn oxides and accelerates Zn dissolution (Fig. 6.12).

Such a model can explain some of the observed effects. Considering the rate law of the reaction 6.18 as proportional to the concentrations of the components, the rate of the  $\text{Zn}(\text{RS})_2^{2-}$  complex formation (reaction 6.18) should be proportional to  $C_{RSH}^r$ . Hence, one can expect that the rate of the complex formation increases with the concentration of the L-cysteine that can explain the immediate accelerating effect of 10 mM L-cysteine (Fig. 6.12). The absence of the precipitated porous oxides and no signal of sulfur in the EDS spectra under these conditions are coherent with such a hypothesis.

The initial inhibiting effect of 0.68 mM L-cysteine solution at pH 6 can be associated with the initial adsorption of L-cysteine by reaction (6.17) (Fig. 6.12). The weak sulfur signal detected on the surface after 1 hour of the immersion test is in accordance with this hypothesis. In Fig. 6.8b and 6.8d one can observe grain boundary (GB) corrosion in the presence of L-cysteine, which could be related to the presence of some impurities in the GBs decreasing the adsorption of L-cysteine. The shape of the precipitated crystals is coherent with the shape of observed by Feitknecht [47] and by Bernard et al. [217] the less soluble  $\epsilon\text{-Zn}(\text{OH})_2$ .

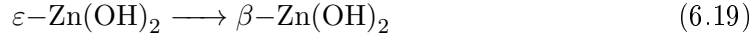
The loss of the inhibiting and the presence of the accelerating effect in the same solution after 8 hours of the immersion should be due to the accumulation of the adsorbed L-cysteine at the interface, which finally dissolves the oxide layers and increases the reaction rate. The absence of the sulfur signal after 24 hours of the immersion and the presence of the columnar co-oriented oxide/hydroxide film similar to the shape of more soluble  $\beta\text{-Zn}(\text{OH})_2$  [47,217] can be due to the excess of  $\text{Zn}^{2+}$  in the solution and the crystal growth in the presence of the surface active agent, which is in dynamic equilibrium

through the continuous re-dissolution and re-precipitation of the oxides/hydroxides. (For comparison, the external surface of the film in L-cysteine free solution was less regular and there was no definite crystal shape without additions of L-cysteine.)

Surprisingly, no acceleration was observed in 0.68 mM L-cysteine solution at pH 12. High resolution SEM observation revealed subtle differences in the surface morphology after 24 hours of immersion with and without L-cysteine with higher amount of the precipitated Zn oxide/hydroxides in the L-cysteine free solution. Although the amount of the precipitated on the surface of Zn oxides/hydroxides in the L-cysteine free solution was higher, underlying film could be more compact because the addition of L-cysteine could decrease the average particle size as previously reported in [220]. Some authors consider that small particles are able to form more compact layers [221,222].

The interesting observation is the prevalence of the defect form of zinc oxide  $Zn_{1+x}O$  in the films formed in the solutions containing L-cysteine in place of ZnO in the L-cysteine free solutions. Previously, the formation of highly defected films was demonstrated to be due to the partial reduction of ZnO films [218]. This suggests that in the presence of L-cysteine the oxide film could be partly reduced by the adsorbed L-cysteine molecules. This hypothesis needs further verification. However, if the reaction can take place, constant inhibition action of L-cysteine at pH 12 could be related to its higher capacity as a reducing agent at alkaline pH.

The replacement of ZnO by zinc hydroxides in the presence of L-cysteine, revealed by Raman spectroscopy, can be explained taking into account the solubility of different Zn oxides/hydroxides. After Feitknecht [47], the transformation of initially precipitated  $\epsilon$ -Zn(OH)<sub>2</sub> is described as:



where the ZnO formation is kinetically less favorable. In the presence of L-cysteine, due to the complex formation, the initially precipitated low soluble  $\epsilon$ -Zn(OH)<sub>2</sub> is continuously dissolved and re-precipitated and has no sufficient time to be transformed into the ZnO. Similar effect, namely the formation of Zn(OH)<sub>2</sub> in the titration of Zn<sup>2+</sup> ions in the presence of NH<sub>4</sub>Cl complex agent and the formation of ZnO in NaCl was previously communicated [75].

## 6.5 Conclusions

1. 10 mM primarily prepared (PP) L-cysteine solutions accelerated Zn spontaneous dissolution in pH range of 2-13, which was explained by the formation of soluble complexes between Zn<sup>2+</sup> and L-cysteine. The surface morphology and EDS analysis of the surface after the immersion tests confirmed the absence of precipitated Zn corrosion products or adsorbed L-cysteine.
2. 0.1 and 1 mM PP L-cysteine inhibited Zn dissolution in pH range of 4–12 at short time scales. EDS analysis revealed the traces of the L-cysteine on the HDG surface after 1 hour of the immersion at pH 6 implying the initial adsorption of the L-cysteine on Zn corrosion products.

## 6. THE EFFECTS OF L-CYSTEINE ON THE INHIBITION AND ACCELERATED DISSOLUTION PROCESSES OF ZINC METAL

---

3. The initial inhibiting effect of 0.68 mM non-dimerized L-cysteine turned into the accelerating effect after 8 hours of the immersion at pH 6. EDS did not detect the signal of sulfur, which was coherent with the idea that the initially absorbed L-cysteine contributes to the following dissolution of the oxide layer forming soluble complexes.
4. The inhibiting effect of 0.68 mM non-dimerized L-cysteine did not disappear with time at pH 12. SEM observations of the surface after 24 hours of the immersion revealed more precipitated oxides in the L-cysteine free solution and higher fraction of hydroxide species in the presence of L-cysteine. The reasons of the inhibition under these conditions need to be further studied
5. Additions of the pristine L-cystine did not affect Zn dissolution. The dimerization of L-cysteine into L-cystine in the PP L-cysteine solutions increased with pH. Therefore, the residual concentrations of L-cysteine in its PP solutions decreased. The estimated in this way decrease of the inhibition efficiency of L-cysteine correlated well with the measured inhibition efficiency. The result implied that the initial inhibition efficiency of 1 mM non-dimerized L-cysteine solution is pH independent in the pH range of 4-12 and is close to 60 %.

## Summary

---

- ✓ **The action of L-cysteine on galvanized steel as both the accelerator at high concentrations and long exposure times, and the inhibitor at low concentrations and short exposure times render dubious its practical use in hybrid coatings on galvanized steel.**
-

# $\text{MoO}_4^{2-}$ as a soluble inhibitor for Zn in neutral and alkaline solutions

---

This chapter presents the investigation of  $\text{MoO}_4^{2-}$  water soluble inhibitor as a potential candidate for the intercalation into LDH hybrid coatings. It aims to answer the specific question raised from the literature review:

- ✓ **What is the action of  $\text{MoO}_4^{2-}$  as a water soluble inhibitor on galvanized steel at alkaline pH? What parameters define its action?**

The content of this chapter repeats the article: V. Shkirskiy, P. Keil, H. Hintze-Bruening, F. Leroux, T. Stimpfling, D. Dragoe, K. Ogle, P. Volovitch, "MoO<sub>4</sub><sup>2-</sup> as a soluble inhibitor for Zn in neutral and alkaline solutions", *Corrosion Science*, 99 (2015) 31-41.

## Abstract

The inhibitive action of soluble  $\text{Na}_2\text{MoO}_4$  on the spontaneous reactivity of hot dip galvanized steel in 0.5 M NaCl was studied at pH 4-13 by a direct measurement of Zn dissolution rate in the flowing electrolyte and postmortem surface analysis. The stability and the composition of Mo-rich films depended on the solution pH and flow conditions. The inhibition efficiency of soluble Mo(VI) correlated with the composition of the films: Mo(V)-rich films were immediately formed under uniform flow at pH 6-12, and the inhibition efficiency of Mo(VI) in these conditions (>92 %) was comparable with the efficiency of Cr(VI).

## 7.1 Introduction

An application of protective organic coatings containing inhibiting pigments is one of the most common strategies used in corrosion engineering to prevent degradation processes and improve the corrosion resistance of galvanized steel [7]. Inhibitors can be placed directly into a polymer matrix or intercalated into nano/micro hosting systems (the so-called “smart” coatings [7, 10, 223]) which have an obvious advantage providing an instrument to control the release of inhibitors from the host system. An inhibiting pigment in painted systems should satisfy at least two requirements. First of all, its paramount role consists in the immediate hindering of the corrosion half reactions preventing cathodic and anodic delamination of the coating [20, 224] and protecting the substrate. Secondly, the inhibitor should not lose its efficiency with time in very different environments, which can occur in the confined zone under the paint. The corrosion of galvanized steel is usually associated with the pH increase [30] due to the cathodic reaction [225]:



Particularly high pH values are expected for the coated system where the diffusion of  $\text{OH}^-$  is limited [226]; the pH values greater than 13 were measured at the interface steel / polymer [227]. To summarize, rapid kinetics and stable effect in alkaline solutions are primordial attributes of the active inhibitors for coated galvanized steel.

Cr(VI) species were traditionally used in both, conversion coatings and as active inhibitors in different coated systems [41, 167, 228]. However, their use is undesirable for environmental and health reasons [57]. Because chromate and molybdate ions are the oxyanion analogues, Mo(VI) species have been widely studied as a possible alternative [64, 65, 229–234]. For Zn based substrates the inhibitive performance of Mo(VI) was mainly evaluated as a component of conversion coatings [64–68] and not as a soluble inhibitor. The conversion coating differs in that the film is formed at low pH usually in the presence of oxidizing agents ( $\text{NO}_3^-$  etc.) and other components which are able to modify the reactivity of the substrate by themselves (phosphates, silicates, etc.). The kinetics of the film formation is not the most important factor for the ingredient of the bath. In contrast, the pigments form the film at neutral or alkaline pH in less controlled solutions and the kinetics is one of the most important criteria for the choice of the pigment.

Little knowledge has been accumulated about the action of dissolved  $\text{MoO}_4^{2-}$  on Zn based substrates. . Defining the inhibition efficiency ( $\eta$ , %) as:

$$\eta = (1 - j_{corr}/j_{corr}^0) \cdot 100 \quad (7.2)$$

where  $j_{corr}$  and  $j_{corr}^0$  are the corrosion current densities with and without the inhibitor respectively. Aramaki [73] reported the  $\eta$  value of 64% for 0.01 M  $\text{MoO}_4^{2-}$  in neutral 0.5 M NaCl solution. Wang et al [61] reported the inhibition efficiency of 71% for 0.05 M  $\text{MoO}_4^{2-}$  additions in 0.01 M  $\text{H}_2\text{SO}_4$  solutions. In both these works, the action of  $\text{MoO}_4^{2-}$  ions was attributed to the formation of Mo-rich protective layer; its composition was not reported.

The composition of the molybdate films was mainly studied in relation to conversion coatings. Numerous works were dedicated to molybdate conversion coatings focusing on the growth [61, 64, 68], morphology [65, 66, 229] and anticorrosive properties of the film [229, 231, 235]. Molybdate conversion coatings on Zn were shown to consisted of Mo(III), Mo(IV), Mo(V) and Mo(VI) species and no Mo(0) [64, 65, 231, 235]. Such a composition is in disagreement with the thermodynamic predictions [33, 69] stating that in aqueous solutions metallic Zn should reduce Mo(VI) to the metallic state (Fig. 7.1). These results suggest a kinetic limitation of the multistep Mo(VI) reduction that in certain conditions stabilizes metastable compounds of Mo(III) and Mo(V) [33]. The evolution of the composition of molybdate conversion coatings formed at pH 5 and exposed to the neutral salt spray demonstrated that the transformation of the initial film containing Mo(V) and Mo(VI) species into the film consisting of Mo(IV) or Mo(III) resulted in the activation of Zn [231]. Magalhaes et al. [65] showed a high impact of phosphates in the bath on the morphology and the performance of the molybdate conversion coatings formed in acidic bath: phosphates improved the film performance in electrochemical tests and made it comparable with the performance of chromate conversion coatings.

The kinetics of molybdate – phosphate conversion process at pH 3 and 5 was pH-dependent: the reaction rate was faster at pH 3.0 than at pH 5.0 [64]. In both cases the coating was formed during about first 200 s of immersion. Inhibiting properties were associated with the formation of Mo(V)-rich film. According to Wang et al [61], the thickness of molybdate conversion coating formed after 1000 s of immersion in 0.05 M  $\text{Na}_2\text{MoO}_4$  (pH 6) was about 80 nm. Conversion coatings being usually prepared in acid solutions (pH 1-5) and in the presence of phosphates (and often silicates and/or titanates) [64, 65, 236], very little is known about the molybdate conversion processes in neutral or alkaline additive-free solutions. According to the literature, in alkaline conversion process either no film was formed at all or the film performance in corrosion tests was poor [65, 229]. As a consequence, no data concerning the kinetics and mechanisms of formation of these films are available.

The mechanisms of molybdate action proposed for various substrates generally stated that Mo(VI) is a weak oxidizing agent and acts as an anodic inhibitor through the formation of Mo-rich protective layers [41, 70, 231]. Molybdate was reported to be an efficient active agent to control the passivation of Al and Fe [73]. The films formed during potentiodynamic polarization of an Al alloy in the molybdate containing solutions

7.  $\text{MoO}_4^{2-}$  AS A SOLUBLE INHIBITOR FOR ZN IN NEUTRAL AND ALKALINE SOLUTIONS

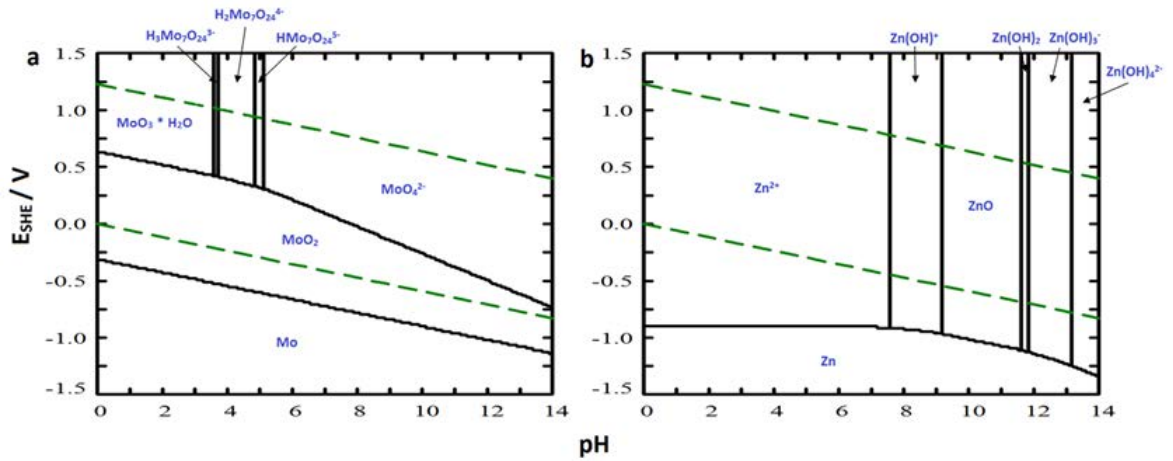


Figure 7.1: E-pH diagrams for Mo (a) and Zn (a) in aqueous media at 25° C calculated by Hydra Medusa software [33] considering  $10^{-2}$  M initial concentration of soluble  $\text{Mo}^{6+}$  or  $\text{Zn}^{2+}$  species and the equilibrium between different species listed below. Green dash lines correspond to hydrogen and oxygen reduction. The species taken into account include: for Zn:  $\text{Zn(OH)}_2$ ,  $\text{Zn(OH)}_3^-$ ,  $\text{Zn(OH)}_4^{2-}$ ,  $\text{Zn}_2(\text{OH})_6^{2-}$ ,  $\text{Zn}_2\text{OH}_3^+$ ,  $\text{Zn}_4(\text{OH})_4^{4+}$ ,  $\text{ZnOH}^+$ , a- $\text{Zn(OH)}_2$ , e- $\text{Zn(OH)}_2$ , ZnO and Zn; and for Mo [69] -  $\text{H}_2\text{Mo}_7\text{O}_{24}^{4-}$ ,  $\text{H}_2\text{MoO}_4$ ,  $\text{H}_3\text{Mo}_7\text{O}_{24}^{3-}$ ,  $\text{HMo}_7\text{O}_{24}^{5-}$ ,  $\text{HMoO}_4^{4-}$ ,  $\text{Mo}_{19}\text{O}_{59}^{4-}$ ,  $\text{Mo}_2\text{O}_4^{2+}$ ,  $\text{Mo}_7\text{O}_{24}^{6-}$ ,  $\text{MoO}_2(\text{OH})_{1.5}$ ,  $\text{Mo}_2\text{O}_2^{4+}$ ,  $\text{Mo}_2(\text{OH})_4^{4+}$ ,  $\text{Mo}^{3+}$ ,  $\text{H}_2\text{MoO}_4$  (or  $\text{MoO}_3 \times \text{H}_2\text{O}$ ),  $\text{Mo}_4\text{O}_{11}$ ,  $\text{Mo(OH)}_4$ ,  $\text{MoO}_2$  and Mo.

with the pH of 3-10 demonstrated a duplex structure: inner aluminum oxides and an outer Mo(IV), Mo(VI) oxide film; the oxidizing capacity of Mo(VI) decreased with pH [237]. The Mo-rich layer was proposed to serve a barrier for  $\text{Cl}^-$  species preventing their penetration to the aluminum oxides and preventing pitting events [237–239]. The morphology of the formed film was considered as a key factor for reactivity; no direct correlation between the Mo oxidation states in the film and its performance was proposed.  $\text{MoO}_4^{2-}$  ions were shown to passivate Fe based substrates in acid in presence of oxygen, however, the additions of  $\text{MoO}_4^{2-}$  did not prevent the corrosion in deaerated solutions despite the fact that potential/time and polarization curves indicated slow film formation [240, 241]. The authors suggested that Mo oxides precipitated in pores of the  $\gamma\text{-Fe}_2\text{O}_3$  passive layer formed in the presence of oxygen improving its inhibiting capacity.

To summarize, Mo(VI) as a soluble inhibitor or as a part of conversion coating was reported to have a performance comparable to Cr(VI) on Al and Fe based substrates and its performance on Zn based substrates in neutral and acid electrolytes was lower than the performance of Cr(VI). Mechanism of molybdate action at neutral and acid pH included a formation of Mo-rich protective film. The films with good performance were formed in the presence of phosphates which are known to affect the reactivity of Zn themselves. Some works associated the inhibiting properties of conversion layers with Mo(III) and Mo(IV) species while others associated it with Mo(V). This knowledge, even if useful, cannot predict the effect of soluble Mo(VI) species on the reactivity of Zn substrates in

the alkaline media and without other soluble species which can participate in the film formation.

To our knowledge, no literature is available about the mechanisms of  $\text{MoO}_4^{2-}$  action on Zn based substrates at alkaline pH and very little was reported even concerning the kinetics of formation of the composition of the film formed under these conditions. This publication presents the kinetics of the initial reactivity of  $\text{MoO}_4^{2-}$  ions as a soluble inhibiting pigment in neutral and alkaline conditions on Zn based substrates in the absence of common conversion process additives. This differs from the considerations of conversion coatings for Zn in which the common additives are present and the initial reactivity is not a key point. The results are compared with the reactivity of the substrate without the inhibitor and in the presence of Cr(VI) species in similar conditions. This work is centered on the Mo(VI) as an active inhibitor and doesn't test the performance of a preliminary formed film in solutions with various pH, as it could be in application for conversion coatings. We are looking forward the understanding film formation in alkaline solutions (up to pH 13) and tries to give a comprehensive picture of the effects of a pH inhomogeneity and flow conditions on its formation and stability.

## 7.2 Experimental

### 7.2.1 Materials

Alkaline degreased hot dip galvanized steel (HDG) bonder plates (type: HDG/5) were supplied by "Chemetal". The average thickness of the galvanization layer amounts 20  $\mu\text{m}$ . The plates were cut into 2 cm  $\times$  4 cm coupons, cleaned with tetrahydrofuran, acetone and ethanol in ultrasonic bath (10 minutes for each solvent), dried under nitrogen-flow then immersed in 1 M NaOH solution at 50  $^\circ\text{C}$  for 30 s then rinsed with water and dried under nitrogen-flow again. This treatment was used to simulate the oxidizing effect of a conventional alkaline degreasing and to remove air-formed corrosion products to give a more reproducible surface state consistent with the industrial practice.

SEM observation of the surface before and after alkaline treatment revealed very similar surface morphologies (Fig. 7.2). Considering the elemental composition (Table 7.1), the alkaline treatment removed the impurities (Ca, P and Mg), which originated from the technical degreasing process. The amount of Al significantly decreased after the alkaline treatment.

The dissolution experiments were performed in 0.5 M NaCl solution (analytical grade, VWR Prolabo) in the purified water (Millipore<sup>TM</sup> system, 18 M $\Omega$  cm) with and without the inhibitors:  $10^{-2}$  M  $\text{Na}_2\text{MoO}_4$  (analytical grade, VWR Prolabo) and  $10^{-2}$  M  $\text{K}_2\text{CrO}_4$

Table 7.1: Surface composition before and after alkaline treatment (from XPS analysis).

At, %	Zn	Al	O	C	N	Ca	P	Mg
<b>Before treatment</b>	7.8	18.6	51.3	17.0	1.2	1.6	2.4	traces
<b>After treatment</b>	32.4	0.3	39.6	24.8	2.9	-	-	-

## 7. $\text{MoO}_4^{2-}$ AS A SOLUBLE INHIBITOR FOR ZN IN NEUTRAL AND ALKALINE SOLUTIONS

---

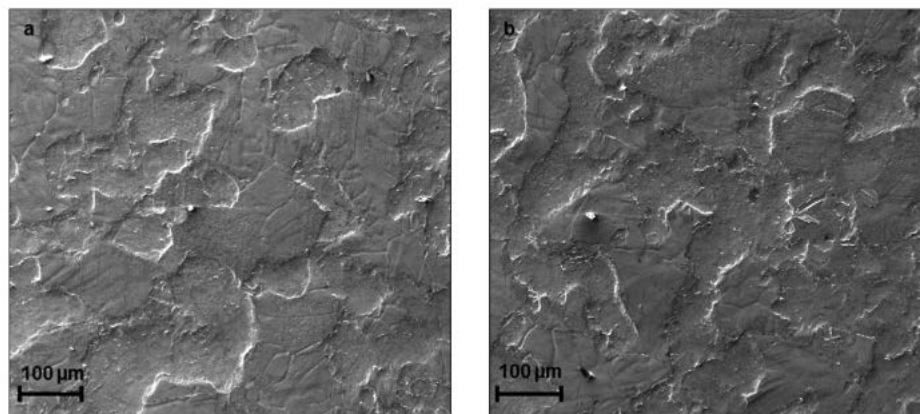


Figure 7.2: SEM images of HDG surface (a) before and (b) after alkaline treatment, secondary electron contrast, accelerating voltage 15 kV.

(analytical grade, Acros Organics). The initial pH values were adjusted by  $10^{-1}$  M HCl or  $10^{-1}$  M NaOH.

### 7.2.2 AESEC technique

#### Zn spontaneous dissolution, measurement principle

To estimate the corrosion behavior in  $10^{-2}$  M  $\text{Na}_2\text{MoO}_4$  and  $10^{-2}$  M  $\text{K}_2\text{CrO}_4$ , the spontaneous Zn dissolution at open circuit was measured by atomic emission spectroelectrochemistry (AESEC), as described in detail elsewhere [161]. Briefly, it consists of an electrochemical flow cell coupled with an inductively coupled plasma atomic emission spectrometer (ICP-AES). In the flow cell, the reaction between the sample (hot dip galvanized steel) and an aggressive electrolyte occurs, leading to the production of dissolved ions and insoluble oxides. Then, the electrolyte is transported to the ICP-AES, where its composition is continuously analyzed. The AESEC detects only the soluble part of the corroded Zn, while the insoluble oxides are not directly measured. The soluble part of the corroded Zn was defined as the Zn dissolution rate,  $v_{Zn}$ , and was calculated from the instantaneous Zn concentration,  $C_{Zn}$ :

$$v_{Zn} = f_e C_{Zn} / A \quad (7.3)$$

where  $A$  is the surface area and  $f_e$  is the flow rate of the electrolyte in the feed capillary. When the system reacts at open circuit, the corrosion of the substrate and the dissolution of the oxide film occur simultaneously resulting in the fact that  $v_{Zn}$  detected by ICP-AES consists of two terms: (i) dissolution rate of ions leached from the metallic surface due to electrochemical oxidation and (ii) the chemical dissolution of previously formed surface oxides.

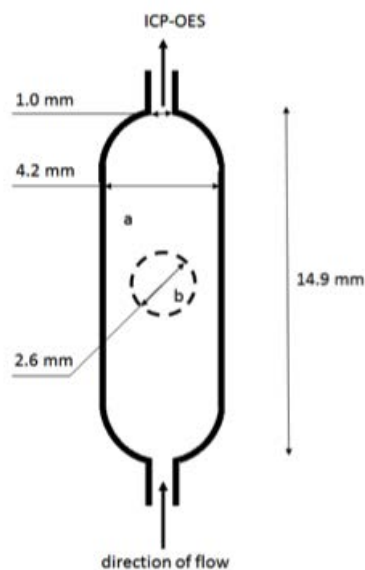


Figure 7.3: Schematic representation of active surface exposed to electrolyte flow in experiments (a) without mask and (b) with mask.

### Flow conditions of AESEC cell

AESEC was previously applied to study the inhibiting mechanisms in pickling solution [210] and for the measurement of the effect of solution pH on Zn reactivity [26]. In these works the whole surface limited by an O-ring was exposed to the electrolyte (Fig. 7.3, area a). However, the cell design implies a non homogeneous electrolyte flow and in particular a difference in the solution renewal between the center and the periphery of the cell. This could result in the non-uniform exposure conditions favoring localized corrosion. The simulation of the flow in the cell confirmed this hypothesis (Appendix A). In order to estimate the contribution of these effects, the exposure of Zn was made in two geometries. Firstly, as in the previous works, the whole surface limited by O-ring was exposed to the electrolyte. Secondly, the experiments were repeated with a mask: an insulating and impermeable adhesive tape covering the periphery of the cell but allowing the contact with the electrolyte in the central part where the flow conditions are presumably the most homogeneous (Fig. 7.3, area b). The second configuration is expected to decrease the variations in the exposure conditions in the same experiment. Further works are in progress to describe the electrolyte flow in the AESEC cell. The results with and without the mask were compared in order to verify the importance of the flow conditions on the formation kinetics and composition of the protective Mo-rich films.

### AESEC parameters

The emission intensities for Zn and Al were monitored at 213.856 nm and 167.081 nm respectively. The double standard deviation of the background signal associated to the detection limit was  $2.2 \pm 0.2 \mu\text{g/L}$  for Zn and  $2.7 \pm 0.3 \mu\text{g/L}$  for Al in the conditions of the experiments.

The reactive surface area was  $0.51 \pm 0.01 \text{ cm}^2$  for the experiments without the mask (Fig. 7.3, area a) and  $0.053 \pm 0.005 \text{ cm}^2$  for the experiments with the mask (Fig. 7.3, area b). The mask was made from the electroplating tape 3M 470 (1 mm thick) supplied by Gamry Instruments. The flow rate of the electrolyte was fixed at  $3.0 \pm 0.1 \text{ ml min}^{-1}$  and the temperature was  $25 \pm 1 \text{ }^\circ\text{C}$ .

The pH of the solution after the contact with the sample was periodically controlled. This was possible because only 5 vol. % of the solution is aspirated into the plasma; the remaining solution is collected for further analysis.

In order to analyze a transient region of the dissolution profile, the transfer function was determined and fit to a log-normal distribution [160]. In this work the parameters for the log-normal distribution were found to be  $\beta = 0.99 \pm 0.02$  and  $\tau = 10.23 \pm 0.10 \text{ s}$ . The time offset because of the transport into capillaries was  $\Delta t = 14 \pm 0.5 \text{ s}$ .

The open circuit potential (OCP) evolution was monitored by Gamry Reference 600<sup>TM</sup> potentiostat with a saturated calomel reference electrode (SCE). The analog potential signal was routed into the measuring circuit of the ICP-AES to guarantee the same time scale for the measurements of the OCP and the dissolution rates.

### Dissolution of Cr-rich layer

After the measurements of Zn spontaneous dissolution in  $10^{-2} \text{ M K}_2\text{CrO}_4$  containing solutions, the surface of sample was rinsed with water and dried under nitrogen. The sample was mounted in the cell and the formed layer was dissolved in 2 M HCl using AESEC measurement of the quantity of formerly deposited Cr.

### 7.2.3 Surface characterization

#### X-ray photon spectroscopy

The sample surface, before and after alkaline degreasing, was investigated by ESCALAB 250 from Thermo VG Scientific, using Mg  $K\alpha$ -anode (1253.4 eV) as an X-ray source. The

Table 7.2: Binding energies (eV) of Mo 3d used for the XPS data treatment

	Mo 3d <sub>3/2</sub>	Mo 3d <sub>5/2</sub>
Mo(IV)	229.9	233.2
Mo(V)	230.9	234.3
Mo(VI)	232.5	235.7

Table 7.3: Half-width at half-maximum (eV) of Mo 3d used for the XPS data treatment

	Mo 3d <sub>5/2</sub>
Mo(IV)	0.8
Mo(V)	1.0
Mo(VI)	0.8

survey spectra were collected with a pass energy of 80 eV and the detail spectra with a pass energy of 30 eV.

After AESEC measurements in Na<sub>2</sub>MoO<sub>4</sub> containing solutions the samples were characterized by X-ray photon spectroscopy (XPS) using a Thermo Fisher Scientific (UK), model K-Alpha controlled by “Avantage” acquisition software. An Al K $\alpha$  (1486.6 eV) source was used. The analyzer was calibrated on a silver sample (3d<sub>5/2</sub>, 368.6 eV). The binding energies were calibrated with respect to the C1s electron peak at 284.6 eV. The used binding energies and half-width values at half-maximum [242,243] are presented in Table 7.2 and 7.3.

### Scanning electron microscopy

The surface characterization before and after alkaline treatment was performed by scanning electron microscopy (SEM) using a Gemini 1530 microscope with a field emission gun source at 15 kV and QUANTAX software.

### Glow discharge optical emission spectroscopy (GD-OES)

Depth profiles of Cr-containing layers were measured using GD-OES (GD-Profiler 2<sup>TM</sup>, Horiba Jobin-Yvon) after the dissolution of the Cr rich layer. The radio frequency power was 3000 Hz. The pulsed glow discharge was applied with 35 W electric power and 650 Pa gas pressure.

## 7.3 Results

### 7.3.1 AESEC measurement of Zn spontaneous dissolution

In all AESEC experiments the Al dissolution was below the detection limit of  $2.7 \pm 0.3$  ug/L and only Zn dissolution profiles will be discussed. This was probably due to the removal of Al species from the surface by the alkaline pretreatment as indicated by the XPS data (Table 1).

#### AESEC experiments without mask

Fig. 7.4 shows the typical evolution of  $vZn$ , as a function of time (dissolution profile) and the evolution of open circuit potential,  $E_{oc}$ , for the sample without the mask in neutral (initial pH 6) and alkaline (initial pH 12) solutions without the inhibitors (curves 1), and in presence of  $10^{-2}$  M Na<sub>2</sub>MoO<sub>4</sub> (curves 2) or  $10^{-2}$  M K<sub>2</sub>CrO<sub>4</sub> (curves 3). Dissolution

## 7. $\text{MoO}_4^{2-}$ AS A SOLUBLE INHIBITOR FOR ZN IN NEUTRAL AND ALKALINE SOLUTIONS

profiles in solutions with different pH exhibited similar trends. The only exception was the absence of the effect of molybdate on the dissolution profile at pH=13. Three periods could be distinguished in dissolution profiles presented in Fig. 7.4:

1. Period I corresponds to the background measurement of the signal from the electrolyte prior to the contact with the sample. The signal variations around zero are due to an instrumental noise.
2. Period II is a transient dissolution. It starts when the solution contacts the sample ( $t = 0$ ) and continues until the dissolution rate reaches a "steady-state" value, defined here as a state in which  $v_{\text{Zn}}$  varies less than the standard deviation of the background signal and  $E_{oc}$  does not change more than 5 mV during at least 500 s.
3. Period III corresponds to the "steady-state" conditions.

### *Transient reactivity*

The Zn dissolution profiles in  $10^{-2}$  M  $\text{K}_2\text{CrO}_4$  at both, neutral and alkaline pH (Fig. 7.4 curves 3), show an early transient peak followed by a passive "steady-state" period. The duration of the transient peak can result from the nucleation and growth of the inhibitive film, and can be further increased by the electrolyte flow. The time before the passivation in chromate containing solutions was estimated by deconvoluting  $v_{\text{Zn}}$  signal as described in [161] as  $6 \pm 2$  s independantly of pH.

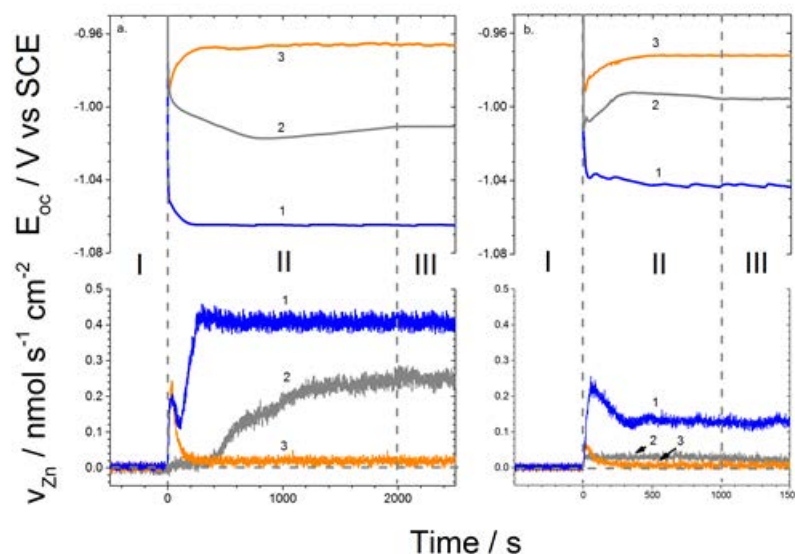


Figure 7.4: Examples of Zn dissolution rate,  $v_{\text{Zn}}$ , and open circuit potential,  $E_{oc}$ , evolution measured with and without inhibitors in experiments without mask at (a) initial pH 6 and (b) initial pH 12. Curves (1) - without inhibitor, (2) - with addition of  $10^{-2}$  M  $\text{Na}_2\text{MoO}_4$  and (3) - with addition of  $10^{-2}$  M  $\text{K}_2\text{CrO}_4$ .

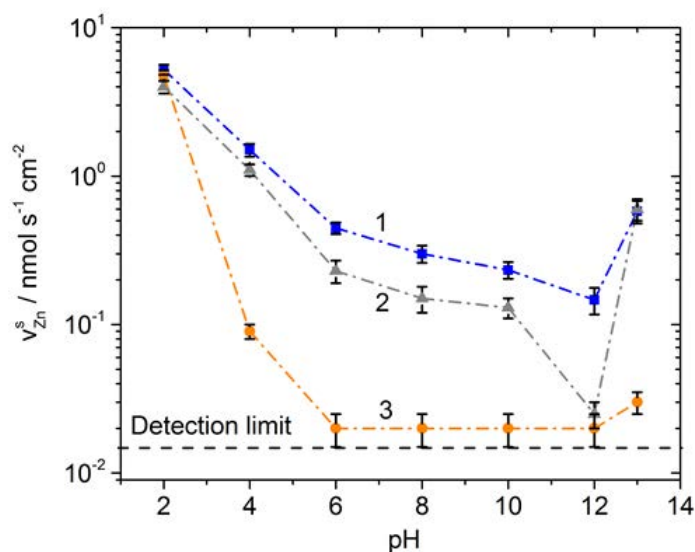


Figure 7.5: Mean values and standard deviations of “steady-state” Zn dissolution rates (denoted as  $v_{Zn}^s$ ) in 0.5 M NaCl as a function of initial pH: (1) - without inhibitor; (2) - in the presence of  $10^{-2}$  M  $\text{Na}_2\text{MoO}_4$  and (3) - in the presence of  $10^{-2}$  M  $\text{K}_2\text{CrO}_4$ .

No active transient was observed in  $10^{-2}$  M  $\text{Na}_2\text{MoO}_4$  (Fig. 7.4, curve 2). On the contrary, at neutral and slightly alkaline pH (pH values of 6 - 10) the initially passivated surface becomes active however the dissolution rate in the presence of Mo(VI) (an example for pH 6 in Fig. 7.4a, curves 2) is still lower than without the inhibitor (an example for pH 6 in Fig. 7.4a, curves 1). At pH=12 in  $10^{-2}$  M  $\text{Na}_2\text{MoO}_4$  the activation period was not observed (Fig. 7.4b, curves 2). At pH 13 the dissolution profiles with and without the inhibitor were the same.

*“Steady-state” period.*

In the “steady-state” period, the solution pH after the contact with the sample increased up to 6.8 for the solutions with the initial pH 6 without the inhibitor or in the presence of  $10^{-2}$  M  $\text{Na}_2\text{MoO}_4$ . This pH increase can be explained in the absence of the inhibitor by the intensive cathodic reaction on the Zn surface (reaction (7.1)) [225]. The effect was visible in molybdate containing solutions because the cathodic inhibition of Mo(VI) is weak [70, 73]. The pH change was not detected in the presence of chromate

Table 7.4: Inhibition efficiency (%) as a function of initial pH in experiment without mask. 5 % error for each experiment.

pH	2	4	6	8	10	12	13
$10^{-2}$ M $\text{Na}_2\text{MoO}_4$	13	26	48	50	44	83	0
$10^{-2}$ M $\text{K}_2\text{CrO}_4$	9	92	95	94	91	93	94

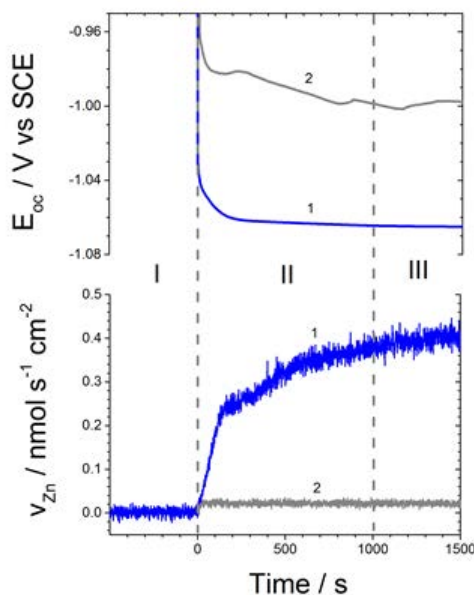


Figure 7.6: Examples of Zn dissolution rate,  $v_{Zn}$ , and open circuit potential,  $E_{oc}$ , evolution measured in experiments with mask at initial pH 6. Curves (1) - without inhibitor and (2) - in the presence of  $10^{-2}$  M  $\text{Na}_2\text{MoO}_4$

because of the strong cathodic inhibition in Cr(VI) containing solutions [27,244]. In the other experiments the solution pH was not affected by the reaction.

Three experiments were made in pH range of 2-13 and the average values of the Zn dissolution rate during the last 500 s of period III (denoted as  $v_{Zn}^s$ ) were calculated (Fig. 7.5). The “U”- like shape of  $v_{Zn}^s$  evolution with pH in 0.5 M NaCl without the inhibitors (curve 1) is in accordance to the previously published works [26,49,140]. Similar “U”-like shape was observed in the presence of  $10^{-2}$  M  $\text{Na}_2\text{MoO}_4$  or  $10^{-2}$  M  $\text{K}_2\text{CrO}_4$  (curves 2 and 3).

The dissolution rates presented in Fig. 7.5 were recalculated as an inhibition efficiency (IE) calculated as  $\eta \times 100$  %, where:

$$\eta = (v_{Zn}^s(\text{without inhibitor}) - v_{Zn}^s(\text{with inhibitor}))/v_{Zn}^s(\text{without inhibitor}). \quad (7.4)$$

The results are summarized in Table 7.4. The IE of chromate was more than 90% in all solutions except at pH 2. The low IE of Cr(VI) in acid solutions was previously explained by a porous or gel-like structure of the film formed under these conditions [167,245]. The molybdate containing solution showed a maximum IE of  $83 \pm 5\%$  at the initial pH 12.

### AESEC experiments with mask

Fig. 7.6 shows the dissolution profiles obtained in the experiments with the mask in 0.5 M NaCl at the initial pH 6 without (curves 1) and with the additions of  $10^{-2}$  M

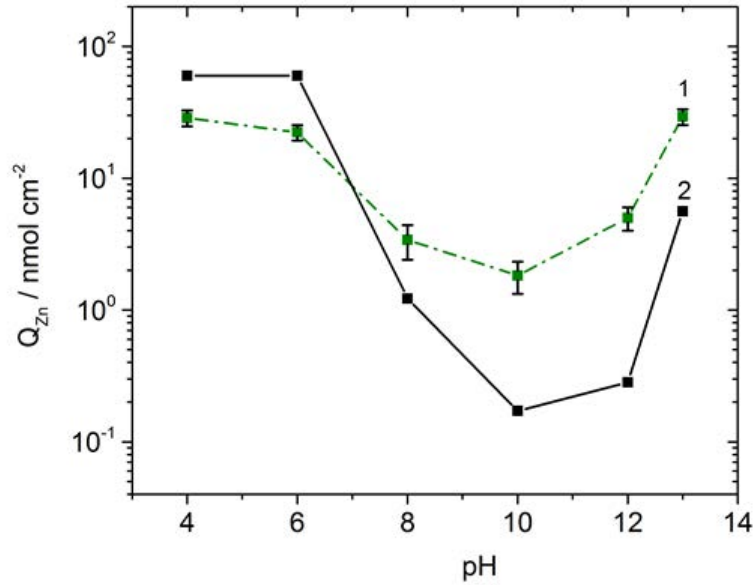


Figure 7.7: Amount of soluble  $Zn^{2+}$ ,  $Q_{Zn}$ , formed during passivation of hot dip galvanized steel in  $10^{-2}$  M  $K_2CrO_4$ : (1) – from AESEC measurement during formation of Cr-rich protective layer and (2) – from thermodynamic calculations by Hydra Medusa software [33] for 0.6 mM  $Zn^{2+}$  in 0.5 M NaCl.

$Na_2MoO_4$  (curves 2). Without the inhibitor, the dissolution profiles with and without the mask are similar (compare curve 1 in Fig. 7.6 and curve 1 in Fig. 7.4). In solutions containing  $10^{-2}$  M  $Na_2MoO_4$ , the Zn dissolution rate with the mask rises rapidly to a “steady-state” value (Fig. 7.6 curve 2). Contrary to the experiments without the mask, no characteristic transient period is observed. Similar differences in the dissolution profiles in the experiments with and without  $10^{-2}$  M  $Na_2MoO_4$  were observed for the solutions with the initial pH values of 6-10.

In the experiments with the mask the IE of  $10^{-2}$  M  $Na_2MoO_4$  solutions ( $> 90\%$ ) was comparable with the IE of  $10^{-2}$  M  $K_2CrO_4$  solutions (Table 7.5).

Table 7.5: Inhibition efficiency (%) as a function of initial pH in experiment with mask. 5 % error for each experiment.

pH	6	8	10
$10^{-2}$ M $Na_2MoO_4$	95	93	87

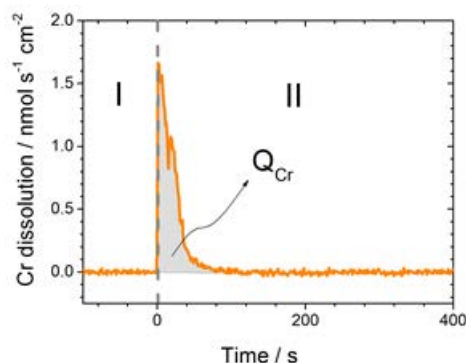


Figure 7.8: Example of quantification of Cr-rich layer by AESEC dissolution in 2 M HCl. Period I – the background measurement and period II – the dissolution of Cr-rich layer.  $Q_{Cr}$  – total amount of the dissolved Cr.

### 7.3.2 Film characterization

#### Quantification of Cr

The amount of Zn,  $Q_{Zn}$ , dissolved during the transient period II (see Fig. 7.4 curves 3 as an example) was calculated by integration of the Zn dissolution profiles in Cr(VI) containing solutions. Each measurement was repeated 3 times. The evolution of  $Q_{Zn}$  as a function of pH is presented in Fig. 7.7; it follows a "U"-like curve with a minimum at the pH around 10.

The quantities of Cr accumulated in the film by the reaction of Zn with 0.5 M NaCl containing  $10^{-2}$  M  $\text{K}_2\text{CrO}_4$  at different pH (pH 4 - 13) and different reaction times (8, 100 and 500 s) were obtained by the AESEC dissolution of the layer in 2 M HCl. Fig. 7.8 shows a typical Cr dissolution profile for such a quantification. Very similar results  $Q_{Cr} = 40 \pm 3$  nmol  $\text{cm}^{-2}$  (Table 7.6) were obtained independently of the solution pH and the activation time. Assuming the composition of the film to fall between  $\text{Zn}(\text{OH})_2$  (density  $\rho = 3.05$  g  $\text{cm}^{-3}$ ),  $\text{Cr}_2\text{O}_3$  ( $\rho = 5.22$  g  $\text{cm}^{-3}$ ) and  $\text{Cr}(\text{OH})_3$  ( $\rho = 3.11$  g  $\text{cm}^{-3}$ ), the passive film thickness can be estimated as 1.2 - 1.3 nm.

In order to confirm the reliability of the quantification using this procedure, GD-OES depth profiles before (Fig. 7.9a) and after the film dissolution in 2 M HCl (Fig. 7.9b) were compared. The signal of Cr after the dissolution in Fig. 7.9b is systematically below the detection limit for all films formed in the pH range from 4 to 13 confirming that the deposited Cr was totally dissolved.

The position of the end of the Cr rich layer erosion (Fig. 7.9a) is depicted only for a visual illustration and does not show the exact layer thickness. It might not be found for so small film thickness because of either redeposition of discharged elements or selective sputtering [246]. The top layer mainly includes C, H and O probably coming from adsorbed water and carbon dioxide.

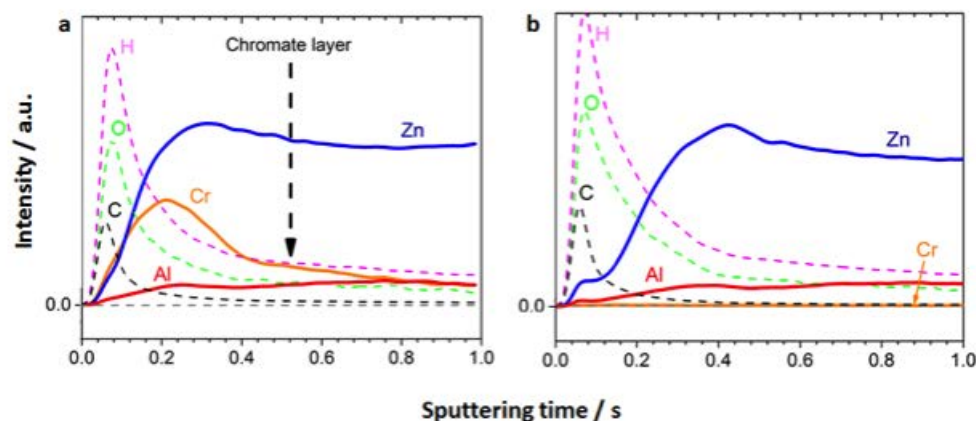


Figure 7.9: GD-OES depth profile of the Cr-rich film layer formed at initial pH 6 (a) and depth profile of the same surface after expose to 2 M HCl (b).

### Mo oxidation states

Microscopic observations of the Zn surface after the experiments in  $10^{-2}$  M  $\text{Na}_2\text{MoO}_4$  containing solutions (Fig. 7.10) reveal some heterogeneity of the reacted surface visible as the dark or the light stains which will be named later as “black” and “white” regions respectively. At the initial pH values of 2-4 only the “black” regions while at initial pH 12-13 only the “white” regions were observed. After the experiments without the mask in neutral and slightly alkaline solutions (the initial pH 6–10), the “white” and “black” regions may be distinguished simultaneously (Fig. 7.10, the regions labelled 1 and 2). Homogenous “white” films were formed in the experiments with the mask in the same solutions (Fig. 7.11).

To determine the oxidation states of Mo, different points were chosen on the “black” and “white” regions and analyzed by XPS. The distribution of the oxidation states within

Table 7.6: Amount of Cr in Cr-rich layer formed on hot dip galvanized steel after exposure in  $10^{-2}$  M  $\text{K}_2\text{CrO}_4$  with different solution pH and exposure times as indicated.

Initial pH	$Q_{\text{Cr}} / \text{nmol cm}^{-2}$		
	8 s of exposure	100 s of exposure	500 s of exposure
5	40	39	42
6	39	40	38
8	42	39	42
10	38	41	40
12	40	41	40
13	42	40	38

## 7. $\text{MoO}_4^{2-}$ AS A SOLUBLE INHIBITOR FOR ZN IN NEUTRAL AND ALKALINE SOLUTIONS

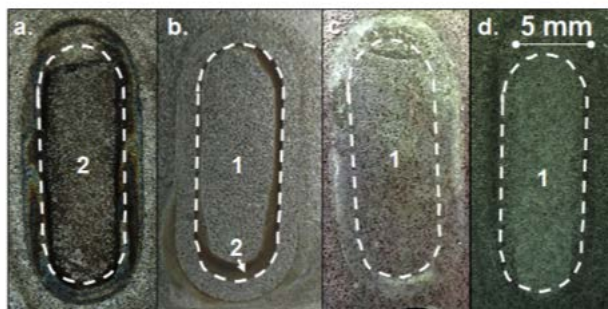


Figure 7.10: General view of samples after AESEC experiments without mask in 0.5 M NaCl in the presence of  $10^{-2}$  M  $\text{Na}_2\text{MoO}_4$  at (a) pH 2-4, (b) pH 6-10, (c) pH 12 and (d) pH 13. Dash line shows the exposed area. Zones (1) and (2) indicate “white” and “black” regions consequently.

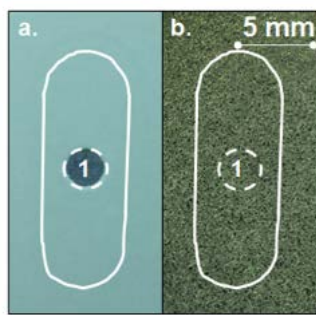


Figure 7.11: Example of surface appearance of hot dip galvanized steel after AESEC experiment in 0.5 M NaCl with  $10^{-2}$  M  $\text{Na}_2\text{MoO}_4$  at neutral pH with mask after the mask removal. The solid line limits the surface of the cell and the dash line shows the effective exposed area. Only “white” region (1) was observed.

each region was similar for the chosen pH. The typical XPS spectra for each film and each region is presented in Fig. 7.12. It clearly demonstrates the increase of the Mo oxidation state with pH increase in the experiment without the mask.

The composition of the different Mo-rich films is summarized in Table 7.7 and Table 7.8. The mixture of Mo(VI), Mo(V) and Mo(IV) species at pH 2-4 is consistent with the literature on the Mo conversion layers [64,67,229]. Mo(IV) was detected only in the “black” regions while Mo(V) and Mo(VI) were detected in the “white” regions at initial pH 6-10 in the experiments without and with the mask and at the initial pH 12. At the initial pH 13, only Mo(VI) was observed.

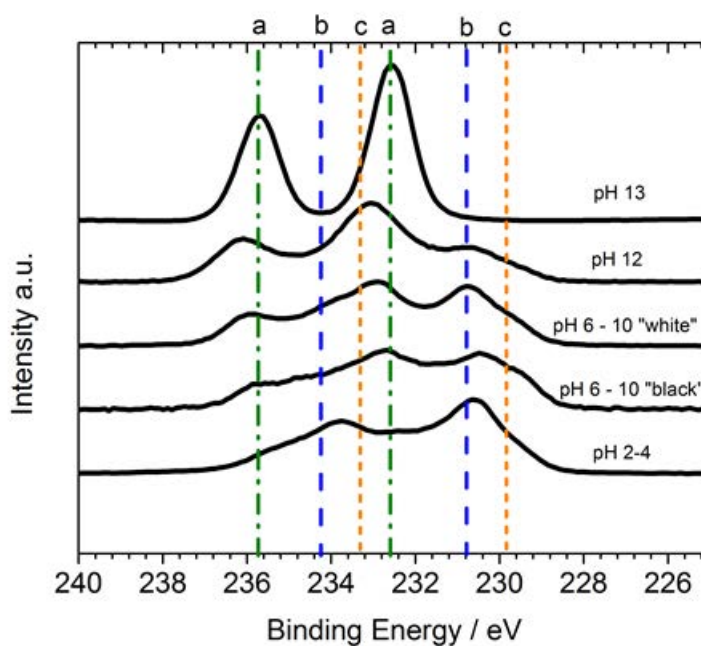


Figure 7.12: XPS spectra of Mo-rich layers formed in different conditions: (1) – pH 13 without mask, (2) – pH 12 without mask, (3) – pH 6-10 with mask, (4) – pH 6-10 “white” region without mask, (5) – pH 6-10 “black” region without mask and (6) – pH 2-4 without mask. Peak assignment: (a) – Mo(VI)<sub>3d</sub>, (b) – Mo(V)<sub>3d</sub> and (c) – Mo(IV)<sub>3d</sub>

Table 7.7: Quantitative analysis of Mo rich layer in experiment without mask.

Regions	pH 2-4	pH 6-10	pH 12	pH 13
“black”	Mo(IV) - 64 %	Mo(IV) - 63 %		
	Mo(V) - 11 %	Mo(V) - 8 %	-	-
	Mo(VI) - 25 %	Mo(VI) - 29 %		
“white”	-	Mo(V) - 73 % Mo(VI) - 27 %	Mo(V) - 38 % Mo(VI) - 62 %	Mo(VI) - 100 %

Table 7.8: Quantitative analysis of Mo rich layer in experiment with mask.

Regions	pH 6	pH 8	pH 10
“white”	Mo(V) - 51 %	Mo(V) - 69 %	Mo(V) - 42 %
	Mo(VI) - 49 %	Mo(VI) - 31 %	Mo(VI) - 58 %

## 7.4 Discussion

### 7.4.1 Inhibition efficiency of molybdate and the composition of the film

The inhibition efficiency of  $10^{-2}$  M  $\text{Na}_2\text{MoO}_4$  in the solution at the initial pH 12 without the mask and in the solutions in the pH range 6-12 in the experiments with the mask was identical to that of  $10^{-2}$  M  $\text{K}_2\text{CrO}_4$  under the similar conditions. The increased inhibition efficiency correlated with the formation of Mo(V)-rich protective film, which is coherent with the results previously reported for molybdate conversion coatings on Zn formed at pH 3 and 5 in  $\text{H}_3\text{PO}_4$  solutions [64]. It should be noted that the high inhibition efficiency of Mo(VI) for Zn substrate in alkaline conditions is observed for the first time.

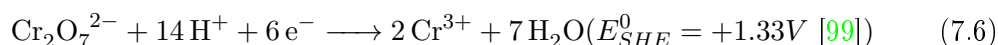
In solutions with acid or strong alkaline pH with or without the mask, the molybdate containing solution did not show very good performance. At the pH 13 it can be explained by a low oxidizing capacity of Mo(VI) [33, 69] resulting in the impossibility of  $\text{MoO}_4^{2-}$  reduction by Zn at open circuit and no protective film. In the acidic conditions, the reduction of  $\text{MoO}_4^{2-}$  ions resulted in the formation of a Mo(IV)-rich layer. One can conclude that the Mo(IV)-rich layer provided a low protection. The formation of colored Mo-rich layer in acid media is in agreement with the formation of colored molybdate conversion coatings in bath pH [67]; however a light brown color in the present work was attributed to the presence of Mo(IV) differing from the previously reported Mo(V) species [64, 67].

The interpretation of the observed effects of the molybdate and chromate additions on the Zn dissolution in neutral and alkaline media with a particular emphasis on the role of the flow conditions in case of molybdate additions are discussed below.

### 7.4.2 Universality of Cr(VI) action on Zn at pH 4 -13

From the literature, Cr(III) species should be formed by the reaction of Cr(VI) with metallic Zn [167, 196, 245]. The low solubility of Cr(III) in the pH range from 4 to 13 [33] is consistent with the formation of an effective Cr(III) protective layer against Zn dissolution. In our experiments in this region, the estimated thickness of Cr-rich films (equivalent of 1.2-1.3 nm of  $\text{Cr}_2\text{O}_3$ ) and their inhibition efficiency ( $92 \pm 2$  %) were pH independent.

The quantity of Zn that must be oxidized to form the protective film can be estimated under the assumption, that during the immersion of Zn in Cr(VI) containing solution the Zn oxidation (reaction (7.5)), the oxygen reduction (reaction (7.1)) and the Cr(VI) reduction (reaction (7.6)) will occur simultaneously [140, 244, 247]:



and that at high concentration of chromate ( $10^{-2}$  M in the experiment compared to  $10^{-7}$  M of oxygen at 25 °C and 1 bar) and strong cathodic inhibition of Cr(VI) [27, 244], the oxygen reduction (reaction (7.1)) will be suppressed. The last hypothesis is coherent

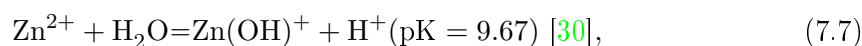
with the absence of a measurable pH increase during the AESEC experiments at the initial pH 6.

In such an approach, if all reduced Cr(VI) (reaction (7.6)) forms the Cr-rich layer, and by charge balance determines the amount of the oxidized Zn (reaction (7.5)), the amount of Zn dissolved during this period should be equal to  $Q_{Zn}=60 \text{ nmol cm}^{-2}$  for all solutions. Zn dissolution should be hence pH independent which is in contradiction with the experimental results presented in Fig. 7.7: in the experiments,  $Q_{Zn}$ , follows the "U"-like curve as a function of pH with a minimum at pH around 10 and all values lower than  $60 \text{ nmol cm}^{-2}$ . This result indicates that other factors control Zn dissolution. The most probable parameter is the solubility.

Indeed, assuming the local saturation of the oxidized Zn in a 0.01 mm interface with a "well mixed solution / diffusion controlled layer" [248] and the maximal Zn quantity at the interface as  $60 \text{ nmol cm}^{-2}$ , the maximal concentration of accumulated  $\text{Zn}^{2+}$  at the interface should be 0.6 mM. This value was used as a total concentration of  $\text{Zn}^{2+}$  species in Hydra Medusa chemical equilibrium software [33] in order to calculate the quantity of soluble  $\text{Zn}^{2+}$  species <sup>1</sup>. The evolution of the calculated amount of soluble Zn as a function of pH (Fig. 7.7, curve 2) shows the same trend as the experimental data (Fig. 7.7, curve 1). The difference between the absolute values could be related to the chemical dissolution of native Zn oxides. Therefore, the initial Zn dissolution was governed by the Zn solubility as a function of pH and not by the redox reactions (7.1), (7.5), (7.6).

### 7.4.3 Role of flow conditions for Zn reactivity in $10^{-2} \text{ M Na}_2\text{MoO}_4$ solutions

The appearance of the "black" Mo(IV) rich region on the edge of the cell and the "white" Mo(V) rich region at the initial pH values of 6-10 in the measurements without the mask (Fig. 7.10, Table 7.7) suggests significant differences in the local reactivity. Indeed, due to a lower solution renewal at the edge of the cell than in the center, from one side,  $\text{Zn}^{2+}$  ions could be accumulated in these regions, and from the other side, the oxygen concentration in these regions may decrease. Due to the hydrolysis reaction



one can expect a pH decrease in these regions. From the thermodynamic prediction, the rate of the  $\text{H}^+$  generation in these regions,  $v_{\text{H}^+}$ , with the interphase thickness,  $\delta$ , equals:

$$v_{\text{H}^+} = \frac{1}{2} \left( -K + \sqrt{K^2 + 4Kv_{\text{Zn}}/\delta} \right). \quad (7.8)$$

For a "well mixed solution / diffusion controlled layer" interface [248]  $\delta$  is often assumed as 0.01 mm. Applying Eq. 8 to the solution with the initial pH 10 and the

<sup>1</sup> $\text{Zn}^{2+}$ -species taken into account for the calculation were:  $\text{Zn}(\text{CO}_3)_2^{2-}$ ,  $\text{Zn}(\text{OH})_2$ ,  $\text{Zn}(\text{OH})^{3-}$ ,  $\text{Zn}(\text{OH})_4^{2-}$ ,  $\text{Zn}_2(\text{OH})_6^{2-}$ ,  $\text{Zn}_2\text{OH}^{3+}$ ,  $\text{Zn}_4(\text{OH})_4^{4+}$ ,  $\text{ZnCl}^+$ ,  $\text{ZnCl}_2$ ,  $\text{ZnCl}_3$ ,  $\text{ZnCl}_4^{2-}$ ,  $\text{ZnClOH}$ ,  $\text{ZnCO}_3$ ,  $\text{ZnHCO}_3^+$ ,  $\text{ZnOH}^+$ , a- $\text{Zn}(\text{OH})_2$ , e- $\text{Zn}(\text{OH})_2$ ,  $\text{Zn}_2(\text{OH})_3\text{Cl}$ ,  $\text{Zn}_5(\text{OH})_6(\text{CO}_3)_2$ ,  $\text{ZnO}$ . 30 mM amount of carbonate was taken into account because of carbon dioxide dissolution into water at 25°C, pH 6 and 1 atm conditions [99]

## 7. $\text{MoO}_4^{2-}$ AS A SOLUBLE INHIBITOR FOR ZN IN NEUTRAL AND ALKALINE SOLUTIONS

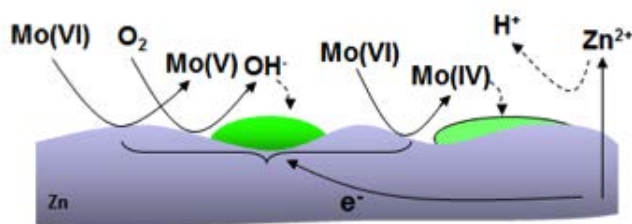


Figure 7.13: Schema of Mo-rich protective film formation on hot dip galvanized steel: preferential  $\text{Mo}^{5+}$  species precipitation on cathodic sites because of a local alkalinization and preferential  $\text{Mo}^{4+}$  species precipitation on anodic sites because of a local acidification in presence of  $\text{Mo}^{6+}$  at initial pH values of 6-10.

experimental value of Zn dissolution rate at this pH ( $v_{\text{Zn}} = 0.1 \text{ nmol s}^{-1} \text{ cm}^{-2}$ ; Fig. 7.4), one can expect the pH decrease so low as pH 4 in these regions after 500 s of the reaction. At this pH the Zn reactivity should increase. This value is in the same order of magnitude as the experimentally observed time period necessary to break down the initial passivity and activate Zn surface in  $10^{-2} \text{ M Na}_2\text{MoO}_4$  (curves 2 in Fig. 7.4a).

In the center of the cell, due to the continuous solution renewal,  $\text{Zn}^{2+}$  ions accumulation is smaller but the oxygen concentration is higher. As a result, with time, these regions become more alkaline.

With time, the inhomogeneous pH distribution on the surface may result in the formation of local cathodes in alkaline regions and local anodes in acid regions. Similar effects were previously communicated for Zn corrosion under seawater droplets [48,175]. Local acidification favors the formation of  $\text{Mo(IV)}$  (Fig. 7.1) detected in the “black” regions in the absence of the mask and explains the activation in these experiments. The  $\text{OH}^-$  generation on the cathodic sites (reaction (7.1)) may cause the pH increase (Fig. 7.13) and may reduce the redox capacity of  $\text{Mo(VI)}$  [33,65], resulting in the accumulation of the metastable  $\text{Mo(V)}$  in these areas, which was detected in the “white” regions, mainly situated in the center in the experiments without the mask. Indeed, when the surface inhomogeneities were eliminated by placing the mask and allowing the reaction only in the central part of the surface, activation was not observed (Fig. 7.6, curves 2). In these conditions both, the oxygen transport and the  $\text{Zn}^{2+}$  evacuation were improved. From the stoichiometry of reactions (7.1) and (7.5), the  $\text{OH}^-$  generation (reaction (7.1)) can be even twice quicker than  $\text{Zn}^{2+}$  ions accumulation. It results in the preferential surface alkalinization, which promotes the formation of the  $\text{Mo(V)}$ -rich protective layer associated with a good performance. The inhibition efficiency in these conditions was comparable with the inhibition efficiency of Cr-rich protective layer (Tables 7.5 and Table 7.4). The absence of the effect of the mask in the experiments without the inhibitor was presumably determined by the poor protective properties of formed Zn oxide/hydroxide

layer. As it was reported earlier [140], the domination of the  $\text{OH}^-$  generation is not enough to suppress the local acidification that results in the breakdown of the Zn native protective layer in neutral and moderate alkaline conditions.

The reactivity of hot dip galvanized steel without the inhibitor was not affected by the presence or the absence of the mask. The results suggest that the mask does not play a significant role when a poor protective layer is formed, as in the case of Zn oxide / hydroxide. Similar, in the case of strong cathodic inhibition by chromate the flow effect was negligible. It played however a critical role for the studied anodic inhibitor when the diffusion process disfavored the formation of the protective Mo(V)-rich films.

The strong effect of the flow conditions resulting in a very inhomogenous pH distribution in confined zone once more reveal the weakness of the direct transfer of the results of electrochemical or corrosion tests for the comparison of inhibitors and prediction of the relative performance of the coated systems containing this inhibitors. The variations of the flow conditions in the confined zone may create the behavior which will differ significantly from the results communicated for the same inhibitor present in the solution and directly reacting with the substrate or from the results known for different type of the coated system even if it is applied on the same substrate.

## 7.5 Conclusions

In the present work, for the first time the effect of molybdate on the kinetics of initial Zn dissolution from hot dip galvanized steel in neutral and alkaline NaCl solutions has been studied and compared with the effect of chromate in the similar conditions. The kinetic data were correlated with the composition of Mo-rich layers. Based on the experimental results and their numerical treatment, several conclusions can be drawn:

For the reference  $10^{-2}$  M  $\text{K}_2\text{CrO}_4$  inhibitor:

1. In flowing solution at initial pH values of 4-13, the uniform Cr-rich protective film is formed in approximately  $6 \pm 2$  s. The amount of Cr in the film (equivalent to 1.2-1.3 nm thick layer of  $\text{Cr}_2\text{O}_3$ ) and the inhibition efficiency associated with it ( $92 \pm 5$  %) were the same in the whole pH range. The amount of the initially dissolved Zn correlated with the evolution of  $\text{Zn}^{2+}$  solubility with pH.

For the  $10^{-2}$  M  $\text{Na}_2\text{MoO}_4$  inhibitor:

2. The formation kinetics and the composition and the inhibition efficiency of the molybdate film were sensitive to the electrolyte flow conditions (with or without the mask) and pH.
3. In strong alkaline electrolyte (pH 13) no film was formed which correlates with low oxidizing capacity of Mo(VI) at this pH. In acid solutions (pH 4 and lower), the formed films were rich in Mo(IV) and their inhibition efficiencies were less than 30 %.
4. In the experiments with the mask (homogenous electrolyte flow on the exposed surface) at the initial pH values of 6-12, homogenous Mo-rich films were formed within

## 7. $\text{MoO}_4^{2-}$ AS A SOLUBLE INHIBITOR FOR ZN IN NEUTRAL AND ALKALINE SOLUTIONS

---

2 s time period. The inhibition efficiency associated with the films was higher than 92 %. So high inhibition efficiency for molybdate in neutral and alkaline conditions were not previously communicated. These films contained Mo(V) and Mo(VI) but no Mo(IV). These results suggest that Mo(V) is an important component of the protective films.

5. In the experiments without the mask (the flow conditions varied from one surface location to another) at the initial pH values of 6-10, the initial inhibiting effect significantly decreased after about 500 s of the exposure; the film consisted of the “black” and “white” regions and a significant fraction of Mo(IV) was detected in the “black” regions. The inhibition efficiency in these conditions did not exceed 50 %.
6. The formation of the “black” regions and the high fraction of Mo(IV) (64 % of the total Mo) in these regions can be explained by the local pH decrease due to  $\text{Zn}^{2+}$  hydrolysis. This hypothesis correlated with the high Mo(IV) fraction in the films formed in acid solutions and their low inhibition efficiency.

Comparing the behavior of different systems with and without mask an interesting observation is that:

7. The difference in the flow conditions in the confined zone did not affect significantly the reactivity of Zn in the presence of chromate (strong cathodic inhibitor) or without inhibitor (weak inhibiting oxides). In the presence of molybdate (anodic inhibitor) the variations in the flow conditions can play a critical role for the reactivity of Zn substrate and the physicochemical properties of the Mo-rich film.

## Summary

---

- ✓ **In addition to the highest (among the chosen inhibitors) inhibiting effect on galvanized steel,  $\text{MoO}_4^{2-}$  showed the highest inhibiting performance for low carbon steel (see Appendix C). Therefore,  $\text{MoO}_4^{2-}$  inhibitor was chosen for the further intercalation into LDH anticorrosion coating on galvanized steel.**
-

# Factors affecting $\text{MoO}_4^{2-}$ inhibitor release from a $\text{Zn}_2\text{Al}/$ -based LDH and their implication in protecting HDG by means of organic coatings.

---

The delamination and degradation of the final coated system is controlled by both the action of the released inhibitor on galvanized steel and by the inhibitor release from the LDH hybrid coating. The immediate action of water soluble  $\text{MoO}_4^{2-}$  on Zn was demonstrated in Chapter 7. This chapter is focused on the release rates of the inhibitor from the LDH hosts. The first part of this chapter aims to answer the question raised in the literature review:

- ✓ **How does the release kinetics from LDHs depend on the composition of corrosive environment?**

In this part, the mechanism of  $\text{MoO}_4^{2-}$  release from  $\text{Zn}_2\text{Al}/\text{-MoO}_4^{2-}$  fillers was studied by the measurement of the release kinetics in different environments.

Then, a full coated system (low carbon steel/galvanization layer/primer with LDH- $\text{MoO}_4^{2-}$  fillers/topcoat) was immersed in different environments and the Zn dissolution, the Mo release and the evolution of the EIS response of the coated system were monitored as a function of time in order to answer the following question from the literature review:

- ✓ **What is the relationship between the release kinetics of the inhibitor from the LDH anticorrosion coating, the inhibitor action and the protection offered by the coated system? Which species in the environment can affect it?**

8. FACTORS AFFECTING  $\text{MoO}_4^{2-}$  INHIBITOR RELEASE FROM A  $\text{Zn}_2\text{Al}/$ -BASED LDH AND THEIR IMPLICATION IN PROTECTING HDG BY MEANS OF ORGANIC COATINGS.

---

**Note**, no synthesis was made during this work. The synthesis of the LDH/Mo phase was made by Dr. Thomas Stimpfling and Prof. Fabrice Leroux in Université Blaise Pascal in Clermont-Ferrand. The complete coated systems were supported by BASF.

The content of this chapter repeats the article: V. Shkirskiy, P. Keil, H. Hintze-Bruening, F. Leroux, P. Vialta, G. Lefèvre, K. Ogle, P. Volovitch, "Factors affecting  $\text{MoO}_4^{2-}$  inhibitor release from  $\text{Zn}_2\text{Al}/$ -based layered double hydroxide and their implication in protecting hot dip galvanized steel by means of organic coatings", *Applied Materials and Interfaces*, in press.

## Abstract

Zn<sub>2</sub>Al/-layered double hydroxide (LDH) materials with intercalated MoO<sub>4</sub><sup>2-</sup> were investigated as potential sources of soluble molybdate inhibitor in anticorrosion coatings for hot dip galvanized steel (HDG). The effect of pH, chlorides and carbonates on the release kinetics of the interleaved MoO<sub>4</sub><sup>2-</sup> ions from the LDH powder during the immersion in solutions containing different anions was studied by X-ray diffraction (XRD), in situ attenuated total reflectance infrared spectroscopy (ATR-IR) spectroscopy and inductively coupled plasma atomic emission spectroscopy (ICP-AES). Both the total release and the release kinetics have been shown to depend on the solution composition. Less than 30% of the total amount of the intercalated MoO<sub>4</sub><sup>2-</sup> was released after 24h of the immersion in neutral 0.005, 0.05 M and 0.5 M NaCl and 0.1 M NaNO<sub>3</sub> solutions whereas the complete release of MoO<sub>4</sub><sup>2-</sup> was observed after 1h in 0.1 M NaHCO<sub>3</sub> and in alkaline solutions. The in-situ ATR-IR experiments and quantification of the released soluble species by ICP-AES demonstrated that the release from neutral solutions passed through the anion exchange mechanism and the release from alkaline solutions passed through the dissolution of Zn<sub>2</sub>Al/-LDH. The release kinetics demonstrated that the anion exchange with monovalent anions (Cl<sup>-</sup> and NO<sub>3</sub><sup>-</sup>) could be described by the reaction order of  $n=0.35 \pm 0.05$  suggesting the diffusion control of the process whereas for the exchange with divalent anions (SO<sub>4</sub><sup>2-</sup> and CO<sub>3</sub><sup>2-</sup>),  $n$  was  $0.70 \pm 0.05$  suggesting the surface controlled reaction. Dissolution of Zn from HDG coated by a primer coating with and without Zn<sub>2</sub>Al/-MoO<sub>4</sub><sup>2-</sup> fillers, leaching of MoO<sub>4</sub><sup>2-</sup> from the coating along with the electrochemical impedance spectroscopy response of the coated systems were measured in NaCl solutions with and without 0.1 M NaHCO<sub>3</sub>. During the immersion in 0.5 M NaCl solutions, the release of soluble MoO<sub>4</sub><sup>2-</sup> was delayed for 24 h with no inhibiting effect whereas the immediate release in the presence of 0.1 M NaHCO<sub>3</sub> was accompanied by the immediate and strong inhibiting effect on Zn dissolution. The concept of controlling the inhibition performance of LDH hybrid coatings by means of the environment composition is discussed.

## 8.1 Introduction

One of the most common strategies used in corrosion engineering to prevent degradation processes and improve the corrosion resistance is an application of protective organic coatings [3–5, 7, 10]. Generally employed to act as a barrier towards electrolyte species and cathodic reactants, the conventional organic coatings additionally contain inhibiting pigments decreasing the extent of corrosion attack by the environment [3, 4, 7]. However, a direct addition of corrosion inhibitor agents into coatings can result in a harmful effect of the destabilization of the film structure and finally in the degradation of its barrier properties [7, 10]. A novel strategy that has attracted considerable interest among corrosion scientists and materials engineers is the intercalation or encapsulation of corrosion inhibitors in micro/nanostructured hosting systems such as hyperbranched polymers [249],  $\beta$ -cyclodextrin [250], oxide nanoparticles (porous oxide layers, core-shell and hollow spheres) [86, 251, 252], zeolites [87], halloysite nanotubes [253] and layer double hydroxide (LDH) capsules [12–14, 149]. This strategy has an obvious supplemental

## 8. FACTORS AFFECTING $\text{MoO}_4^{2-}$ INHIBITOR RELEASE FROM A $\text{Zn}_2\text{Al}/$ -BASED LDH AND THEIR IMPLICATION IN PROTECTING HDG BY MEANS OF ORGANIC COATINGS.

advantage as it provides an instrument for controlling the release of inhibitors from the host system. The LDH inorganic reservoirs has gained considerable attention as polymer fillers in nanocomposites (e.g. mechanical reinforcement, antistatic and barrier properties or fire retardation), drugs and genes delivery and pesticides absorbent and from that point of view LDHs appear the most promising reservoirs to host a corrosion inhibition agent [136,223,254]. In the present work, we focus on the application of LDH materials as a potential hosting system for  $\text{MoO}_4^{2-}$  ions as a corrosion inhibitor for hot dip galvanized steel.

LDHs, also known as anionic clays or hydrotalcite-like compounds with a general chemical formula of  $[\text{M}_{1-x}^{2+}\text{M}_x^{3+}(\text{OH})_2]\text{A}_{x/n}^{n-} \cdot x \text{mH}_2\text{O}$  where  $\text{M}^{2+}$  and  $\text{M}^{3+}$  are bi-valent and tri-valent metals, are built from a brucite ( $\text{Mg}(\text{OH})_2$ )-like layer with anions ( $\text{A}^{n-}$ ) as well as water molecules in the gallery space [142,146,254]. The stacking of the layers can be different resulting in two polymorph forms: the rhombohedral form where the lattice parameter ( $c$ ) is equal to three times of the interlayer distance (3R symmetry), while in the hexagonal form  $c$  is equal to twice of the interlayer distance (2H symmetry). The partial substitution of divalent cation by a trivalent into the brucite layer produces an excess of positive charge resulting in the presence of interleaved anions, [254] some of which could be active corrosion inhibitors. Entrapped anions can be released from an LDH due to a dissolution of the LDH framework at extreme pH values [153,255] or due to an anion exchange within the LDH framework [131,132,256]. The ion exchange rate depends on the ion charge [131,257,258]. Monovalent ions such as  $\text{Cl}^-$  and  $\text{NO}_3^-$  into  $\text{Mg}_2\text{Al}/$ -LDH can be easily replaced by divalent ions such as  $\text{CrO}_4^{2-}$ ,  $\text{SO}_4^{2-}$  and  $\text{CO}_3^{2-}$  [258]. However, this approximation should be applied with caution because of possible steric effects. Experimentally observed affinity of different anions to  $\text{Zn}_2\text{Al}/$ -LDH decreases in the order of  $\text{Mo}_7\text{O}_{24}^{6-} > \text{CO}_3^{2-} > \text{MoO}_4^{2-} > \text{SO}_4^{2-}$  [259]. For  $\text{Mg}_2\text{Al}/$ -LDH the affinity based on the calculated equilibrium constants of various exchange reactions, decreases in the order  $\text{CO}_3^{2-} > \text{C}_{10}\text{H}_4\text{N}_2\text{O}_8\text{S}^{2-} > \text{SO}_4^{2-} > \text{F}^- > \text{HPO}_4^{2-} > \text{Cl}^- > \text{B}(\text{OH})_4^- > \text{NO}_3^-$  [254,260] implying that an anion from this list could be easily replaced in the LDH structure by an anion staying on the left from it but not vice versa. Therefore, the control of the solution chemistry could provide a tool for the release control.

The carbonate ions were widely investigated for a drug delivery control in pharmaceutical applications [129,131,132,134,136]. Their role was clearly illustrated on the examples of the release of vitamin C from  $\text{Mg}_2\text{Al}/$ - and  $\text{Mg}_2\text{Fe}/$ -LDHs [134,135]. The presence of carbonates increased the release from 20-30% in deionized water to 50-60% in 0.1 M and to 60-70% in 0.01 M of  $\text{CO}_3^{2-}$ . At the same time the release kinetics changed from a second order to first order reaction [134]. High affinity of carbonates to LDH framework implies that even trace amounts of carbonates already present in LDH can affect the release behavior [254,261]. The exchange capacity of  $\text{Mg}_2\text{Al}/$ - $\text{NO}_3$  with  $\text{Cl}^-$  ions dropped each time by a factor of 1.5 with the increase of the residual carbonate concentration into LDH from 0.5 ppm to 84 ppm and then 130 ppm [261]. The high impact of carbonates on the release behavior could be used to control the release of the inhibitors from hydride LDH/inhibitor anticorrosion coatings.

Many research groups tested LDH as a potential reservoir for inhibitors in anticorro-

sion coatings on different substrates [12–14, 16–19, 148, 149]. Buchheit and colleagues [13] are among the pioneers, who used the LDHs in corrosion research.  $\text{Zn}_2\text{Al}/\text{-V}_{10}\text{O}_{28}^{6-}$  dispersed into amide-cured bisphenol epoxy resin on Al2024-T3 alloy showed a prolonged inhibiting effect with up to 200 hours in 0.5 M NaCl media associated with a rapid release of  $\text{V}_{10}\text{O}_{28}^{6-}$  from LDH. XRD spectra revealed that the release is determined by a partial substitution of  $\text{V}_{10}\text{O}_{28}^{6-}$  ions with  $\text{Cl}^-$  [13]. Various organic inhibitors such as benzotriazole, ethyl xantate, and oxalate were intercalated into  $\text{Mg}_2\text{Al}/\text{-LDH}$  matrix and tested as possible inhibitors for coated Al2024-T3 in HCl solution [14]. Several works of Zheludkevitch et al. [16, 149] reported the inhibition action of  $\text{Zn}_2\text{Al}/\text{-}$  and  $\text{Mg}_2\text{Al}/\text{-LDHs}$  loaded with vanadates, 2-mercaptobenzothiazole and quinaldic acid on Al2024 in the presence of  $\text{Cl}^-$  ions. Kinetic studies showed that the inhibitor release passed through a fast anion-exchange, driven by a dynamic chemical equilibrium [16, 149]. Interestingly, even in the cases when inhibitors cannot be exchanged with other ions due to their high affinity to LDH, the release can be possible due to the dissolution of LDH plates [10, 12]. Thus, 3- and 4-acetamidobenzenesulfonyl acids (ABSA) loaded into  $\text{Zn}_2\text{Al}/\text{-LDH}$  did not exchange in 0.5 M NaCl solution at neutral pH [12]. Nevertheless,  $\text{Zn}_2\text{Al}/\text{-3-}$  and 4-ABSA showed an inhibiting effect on Al2024 in the same solutions presumably defined by the local acidification of the surface during immersion tests [12].

pH is an universal trigger for the inhibitor release in coated systems due to a string pH modification in the confined zones which can occurs by the local acidification due to the hydrolysis of dissolved cations or by the local alkalinization due to water or oxygen reduction on the metal/solution interface. Such systems as  $\text{SiO}_2$  and halloysite modified with pH sensitive polyelectrolytes [127, 128], pH-sensitive polymer microcapsules [262], Eudragit particles [263] and zeolites [87] were successfully tested as the nanocontainers for pH-triggered release of inhibitors from anticorrosion coatings. However, very little is known about the role of pH for the release from LDH hybrid coatings.

Up to now the research in corrosion science has been focused on the intercalation of new inhibitors into different LDH frameworks and testing them on the Al based substrates in the presence of  $\text{Cl}^-$  ions. Despite well-known affinity of carbonates for LDH compounds and their presence in aerobic corrosion environments, the effect of carbon dioxide and dissolved carbonates on the inhibitor release and hence, on the final inhibiting properties of the hybrid coatings containing LDH/inhibitor fillers are poorly documented. The present work demonstrates the effect of carbonates on the release of intercalated molybdate from the  $\text{Zn}_2\text{Al}/\text{-MoO}_4^{2-}$  fillers and on the anticorrosion performance of coating containing such fillers for hot dip galvanized (HDG) steel. The choice of the inhibitor was motivated by the reported earlier high inhibiting efficiency of soluble  $\text{MoO}_4^{2-}$  comparable in some conditions with the efficiency of  $\text{CrO}_4^{2-}$  [187]. The first part of the work presents the effect of the solution composition ( $\text{Cl}^-$ ,  $\text{CO}_3^{2-}$ ,  $\text{NO}_3^-$ ,  $\text{SO}_4^{2-}$  and pH) on the mechanisms and kinetics of the release of intercalated  $\text{MoO}_4^{2-}$  from  $\text{Zn}_2\text{Al}/\text{-LDH}$  powders during the immersion in aqueous solutions. Then, the effect of the environment is verified for the coated systems by simultaneous measurement of the  $\text{MoO}_4^{2-}$  release, Zn dissolution from the underneath HDG and the response of the coated system on electrochemical impedance spectroscopy.

## 8.2 Experimental

### 8.2.1 Preparation of $\text{Zn}_2\text{Al}/$ - $\text{MoO}_4^{2-}$ LDH phase

All chemicals used for synthesis are listed in Table 8.1. LDH samples were prepared using the conventional co-precipitation method to form a  $\text{Zn}_2\text{Al}/$ -LDH phase with  $\text{MoO}_4^{2-}$  as the intercalated ions. To proceed, a solution of Zn and Al nitrate salts with a total cationic concentration of 0.1 M and a Zn/Al ratio of 2 was added dropwise to deionized water under nitrogen atmosphere to avoid the carbonate contamination from air. The pH was kept constant at  $9.5 \pm 0.1$  by the addition of 0.2 M NaOH. The volume of salt solution was adjusted to obtain 2 g of final LDH product (5.32 mmol). Before the addition of the solutions, a 4-fold molar excess of  $\text{MoO}_4^{2-}$  (21.3 mmol) was introduced into the reactor to achieve the intercalation of  $\text{MoO}_4^{2-}$ . The flow rate of the peristaltic pump was calculated for a total addition time of 3 hours. The LDH suspension was stirred for 3 hours more for ageing after the complete addition. The obtained solid phase was collected by centrifugation, washed 3 times with deionized water and finally dried overnight in an oven at 30 °C.

### 8.2.2 Coating preparation

The surface of hot dip galvanized steel (supplied by “Chemetall” GmbH) was alkaline degreased by spraying 2.5 % wt. solution of Gardoclean S5160 (supplied by “Chemetall” GmbH) at 60 °C for 12 s and then rinsed in deionized water. After degreasing, a 5  $\mu\text{m}$  thick model primer with or without 5 % wt. LDH hybrids in a powder form was applied on HDG surface with the following curing at 216 °C PMT. The primer was based on water-polyurethane binder dispersion and melamine – formaldehyde cross linker. The formulations of the primer with and without LDH hybrids were adjusted to ensure a similar solid content of the primer. After Primer application and curing, a 20  $\mu\text{m}$  thick, solvent borne polyester based top-coat (pigmented) was applied. Afterwards the whole system (Primer+Top coat) was cured at 243 °C PMT. The SEM cross section images of the final coatings with and without LDH/ $\text{MoO}_4^{2-}$  fillers are presented in Fig. 8.1.

Table 8.1: List of used chemicals

Chemical formula	Supplier	Purity
$\text{Zn}(\text{NO}_3)_2 \times 6\text{H}_2\text{O}$	Acros	98 %
$\text{Al}(\text{NO}_3)_3 \times 9\text{H}_2\text{O}$	Acros	99 %
$\text{Na}_2\text{MoO}_4 \times 2\text{H}_2\text{O}$	Acros	99 %
NaCl	Acros	99 %
$\text{NaHCO}_3$	Sigma-Aldrich	98 %
HCl	WVR Prolabo	36.5 % solution
$\text{ZnCl}_2$	WVR Prolabo	98 %
$\text{AlCl}_3$	WVR Prolabo	99.9 %

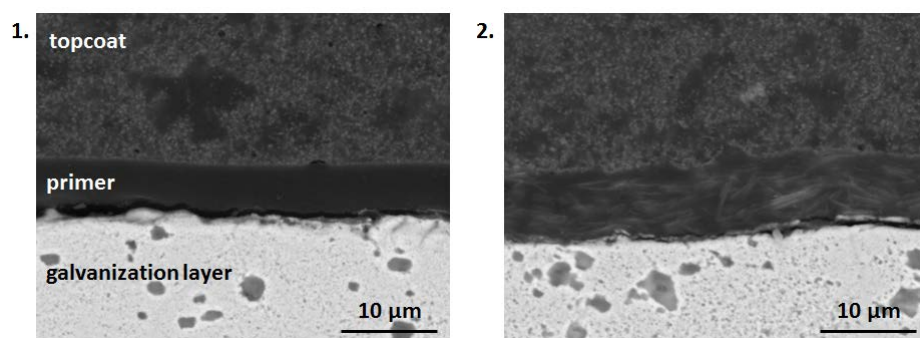


Figure 8.1: SEM images for the cross section of hot dip galvanized steel coated with the model epoxy-primer layer with (1) and without (2) loaded 5 wt. % LDH/Mo particles followed by the topcoat layer. The back-scattered electron contrast was used, accelerating voltage was 20 kV. The elemental analysis of the primer layer with charged LDH/Mo patterns revealed presence of Zn: Al : Mo as 2 : 1 : 0.4 in atomic ratios that confirms presence of  $\text{Zn}_2\text{Al}/\text{-MoO}_4^{2-}$  fillers.

### 8.2.3 Release studies from LDH powder

The evolution of the  $\text{Zn}_2\text{Al}/\text{-LDH}$  structure during the immersion of LDH powders in different solutions was studied by X-ray diffraction (XRD) in order to access the interlayer structure and by infrared spectroscopy for the chemical specification of the exchanged anions. The release of soluble molybdate from the LDH powder and from coated HDG samples was quantified from the solution analysis by inductively coupled plasma atomic emission spectroscopy (ICP-AES). Dissolution of Zn from the underneath HDG coating (in coated samples) was also accessed from the solution analysis by ICP-AES.

All solutions were prepared in deionized water (Millipore system,  $18 \Omega \text{ cm}^{-2}$ ) with addition of required quantities of solid NaCl,  $\text{NaHCO}_3$ ,  $\text{NaNO}_3$  and  $\text{Na}_2\text{SO}_4$  (see Table 1 for purities).

#### Leaching from LDH powder: XRD investigation

$\text{Zn}_2\text{Al}/\text{-MoO}_4^{2-}$  LDH powder ( $6 \cdot 10^{-4}$  moles) was dispersed in 30 ml of 0.005 M NaCl or 0.5 M NaCl solutions under air atmosphere. A small fraction of the suspension was recovered and centrifuged after the immersion times of 15 and 60 min. The solid phase was washed with deionized water to remove any non-intercalated anion and finally dried overnight at  $30^\circ\text{C}$  in an oven and analysed by XRD to detect  $\text{Cl}^-$  uptake in the presence of fixed concentration of carbonates from the air and molybdate release by modifications of the interlayer distance in the crystalline LDH phase.

XRD measurements were performed using a Philips X-Pert Pro diffractometer in Bragg-Brentano geometry equipped with an X-Celerator detector with  $\text{Cu-K}\alpha$   $1/\alpha$  2 radiation. Data were collected between  $5.0$  and  $70.0 \Theta(^{\circ})$ , with a step size of  $0.08 \Theta(^{\circ})$  and a counting time of 0.5 s step.

### **Leaching from LDH powder: In situ Attenuated Total Reflectance Fourier-transform infrared spectroscopy (ATR-FTIR)**

The exchange mechanism between molybdate and chloride or carbonate in the LDH present in both, crystalline and amorphous forms, was verified using infrared spectroscopy in the attenuated total reflection (ATR) mode. The LDH film was prepared directly on the surface of the ATR crystal as described elsewhere [259,264]. Shortly, an aliquot of 1  $\mu\text{L}$  of the LDH suspension (4.5 g/L) in purged with nitrogen solution was pipetted onto the crystal and dried under a flow of nitrogen. The background was recorded after the addition of a drop of water over the LDH layer. A Pike flow cell [264] was used to deliver the solutions from the reservoir to the LDH film. 50 ml of solution continuously circulated with a constant flow rate of 2 ml/min at room temperature. The pH of this solution was continuously monitored. To control the carbonate content, all solutions were deaerated with nitrogen for 30 min prior to the experiments (final solution pH was 7.0) and kept under a continuous stream of nitrogen at room temperature. After stabilizing for at least 30 min, a background spectrum was recorded and then 4 mM of NaCl was added to a circulating electrolyte. The evolution of the anion exchange into the LDH film was followed by the acquisition of spectra each 3 minutes until the steady state, considered when spectra intensity did not vary more than 5% since the last measurement. Then, to verify the effect of carbonate ions, 2 mM of  $\text{NaHCO}_3$  was added in the electrolyte and the spectra were recorded each 3 minutes until the steady state. Twice less concentration of  $\text{HCO}_3^-$  than  $\text{Cl}^-$  was added to guarantee identical charge balance in the LDH framework assuming the  $\text{CO}_3^{2-}$  intercalation. This assumption was confirmed experimentally by ATR-FTIR spectroscopy (see Results section).

Infrared spectra were measured with Thermo Scientific Nicolet 6700 FTIR spectrometer equipped with a mercury cadmium telluride detector cooled at 77 K by liquid nitrogen. Spectral resolution was  $4\text{ cm}^{-1}$ , and spectra were averaged from 256 scans. The ATR accessory was a horizontal ZnSe crystal coated with diamond ( $A = 2.54\text{ mm}^2$ ) with single reflection and an angle of incidence of  $45^\circ$  (Smart Miracle from PIKE). OMNIC software was used for the data collection and treatment.

### **Leaching from LDH powder: quantification by solution analysis by ICP-AES**

Leaching experiments were performed at controlled temperature of  $24 \pm 1^\circ\text{C}$  in preliminary aerated (30 min) or in Ar deaerated solutions to vary the content of carbonate ions. For deaerated conditions, Ar flow passed through the solutions for 30 min before the experiment and continuously lasted until the end of the experiment. Before the leaching tests, the initial pH of all solutions was adjusted to the value of 6 by 0.1 M HCl or 0.1 M NaOH. According to the predominance diagram, at neutral pH carbonate ions are mainly present in the form of  $\text{HCO}_3^-$  [33] and therefore,  $\text{HCO}_3^-$  species are mainly present in the solution.

Preliminary to experiments, LDH powders were manually ground to guarantee a homogenous size distribution in the leaching tests. The leaching experiments were per-

formed in 250 ml Teflon beaker containing 50 ml of continuously stirred solution. The experiment began when 0.1 g of LDH/Mo powder were added to the solution ( $t = 0$  s). After approximately 10s after the addition of LDH/Mo powder, 2 ml of suspension were sampled for the 1st point and then the measurements were repeated each 250 s during the first hour and finally after 24 hours of the experiment. The sampled solutions passed through three succeeding 0.22  $\mu\text{m}$  Nylon filters to separate the solid phase from the solution and then, the amounts of soluble Mo ( $Q_{released}^{Mo}$ ), Al ( $Q_{dissolved}^{Al}$ ) and Zn ( $Q_{dissolved}^{Zn}$ ) were determined by ICP-AES. The 202.03 nm, 213.86 nm and 167.08 nm emission lines were used to quantify the concentrations of Mo, Zn and Al respectively. The detection limits of ICP-AES measurements for Mo, Zn and Al ions were  $6.0 \pm 1.0 \mu\text{g/L}$ ,  $4.1 \pm 0.9 \mu\text{g/L}$  and  $2.1 \pm 0.8 \mu\text{g/L}$  consequently.

Independently, before the experiment 2 ml of the suspension were sampled and dissolved in 20 ml of 2 M HCl and the total amounts of Mo ( $Q_{total}^{Mo}$ ), Al ( $Q_{total}^{Al}$ ) and Zn ( $Q_{total}^{Zn}$ ) in 2 ml of suspension were determined by ICP-AES. The ratio of Zn : Al : Mo was 2 : 1 : 0.5 in all experiments, which corresponds to the solid  $\text{Zn}_2\text{Al}(\text{OH})_6[\text{MoO}_4]_{0.5} \times 2\text{H}_2\text{O}$  LDH phase. Further all results from the leaching tests were normalized by these total amounts and are presented as the release fractions (the ratios of  $Q_{released}^{Mo}/Q_{total}^{Mo}$ ,  $Q_{dissolved}^{Zn}/Q_{total}^{Zn}$  and  $Q_{dissolved}^{Al}/Q_{total}^{Al}$  multiplied by 100%).

The verification of the absence of any adsorption or precipitation of Mo, Zn and Al ions on the walls of the beaker and the efficiency of the filtering procedure used for separation of the solid LDH/Mo phase from the aqueous solution is presented in Appendix D.

#### 8.2.4 Tests of coated HDG samples

Before immersion, coated panels with and without LDH fillers in the primer were scratched until galvanization layer with a knife to obtain a scratch of 0.5 mm in width and 20 mm in length which corresponds to the exposed Zn surface of 10 mm<sup>2</sup>. The scratched panels were fixed as a bottom border of a cylindrical plexiglass home made electrochemical cell [215] in such a way that the scratch was disposed in the middle of the cell. 30 ml of the tested electrolyte was added to the cell resulting in the immersion of the tested side of the coated sample with the total exposed area of  $10.2 \pm 0.1 \text{ cm}^2$ . The coated HDG sample was connected to the potentiostat in a way that the electrochemical tests could be made during immersion using three electrode geometry. A plastic paraffin film covered the cell during the tests to reduce evaporation of electrolyte. The tests were performed at controlled room temperature of  $24 \pm 1^\circ\text{C}$  in 0.5 M NaCl electrolyte with and without additions of 0.1 M NaHCO<sub>3</sub>. The tests in 0.1 M NaHCO<sub>3</sub> were repeated two times to have a statistical reinforcement of the data. The initial pH values were adjusted to 6 by 0.1 M HCl.

During 120 hours of immersion EIS tests were performed and 1 ml aliquots were sampled with the interval of approximately 20 hours. The quantities of soluble Mo (202.031 nm), Zn (213.856 nm), Al (167.081 nm) and Fe (259.940 nm) were analysed by ICP-AES. The concentrations of Al and Fe were below the detection limits of 2.1

## 8. FACTORS AFFECTING $\text{MoO}_4^{2-}$ INHIBITOR RELEASE FROM A $\text{Zn}_2\text{Al}/$ -BASED LDH AND THEIR IMPLICATION IN PROTECTING HDG BY MEANS OF ORGANIC COATINGS.

$\pm 0.8 \mu\text{g/L}$  and  $4.4 \pm 0.9 \mu\text{g/L}$  respectively in all experiments. Only the Zn and Mo concentrations will be presented below.

EIS tests were performed using a three-electrode configuration with a platinum wire as a counter electrode, Ag/AgCl in saturated KCl as a reference electrode and scratched HDG coated panels as a working electrode. Impedance measurements were recorded at open circuit potentials with a 20 mV rms amplitude from 10000 Hz to 0.005 Hz at 10 points per decade and 4 cycles for each frequency.

### 8.3 Results

#### 8.3.1 $\text{MoO}_4^{2-}$ release from LDH powders

##### Survey of the $\text{Zn}_2\text{Al}/$ - $\text{MoO}_4^{2-}$ LDH modification in the presence of $\text{Cl}^-$ and $\text{HCO}_3^-$

###### *XRD results*

XRD patterns of the as-prepared LDH/Mo phase, and then after 15 min and 60 min of the immersion in 0.005 M NaCl and 0.5 M NaCl solutions are shown in Fig. 8.2. Generally described in  $R\bar{3}m$  rhombohedral symmetry, the LDH/Mo materials exhibit the presence of harmonic peaks (001) at low  $2\Theta$  values that provides the interlayer information and (110) diffraction line close to  $600 / 2\Theta$  that provides the intralayer information. A shift of the (003) diffraction peak to higher  $2\Theta$  values is commonly interpreted by the replacement of  $\text{MoO}_4^{2-}$  anions by the  $\text{Cl}^-$  or  $\text{CO}_3^{2-}$  anions in the LDH framework leading to the decrease of the basal spacing from 9.9-9.5 Å (for  $\text{MoO}_4^{2-}$ ) to 7.9-8.0 Å (for  $\text{Cl}^-$ ) and 7.7-7.5 Å (for  $\text{CO}_3^{2-}$ ) [254].

From Fig. 8.2, the 9.6 Å interlayer distance for the pristine LDH/Mo phase ( $t = 0$  min) is coherent with the presence of intercalated  $\text{MoO}_4^{2-}$  anions into the  $\text{Zn}_2\text{Al}/$ -LDH host. In 0.005 M NaCl, the position of the (003) diffraction peak does not change up to 60 min of the immersion implying a minor  $\text{MoO}_4^{2-}$  exchange with  $\text{Cl}^-$ . In 0.5 M NaCl, the interlamellar distance defined from the position of (003) plane decreased to about 7.5 - 8.0 Å evidencing a partial replacement of  $\text{MoO}_4^{2-}$  ions by  $\text{Cl}^-$  or/and  $\text{CO}_3^{2-}$ . After 60 min of the immersion the release was still incomplete, since the peak at about 9.5 Å corresponding to the interlayer distance of the pristine LDH/Mo was still present. The incomplete release of  $\text{MoO}_4^{2-}$  ions in  $\text{Cl}^-$  media was in the agreement with higher affinity of  $\text{MoO}_4^{2-}$  anions for  $\text{Zn}_2\text{Al}/$ -LDH framework than  $\text{Cl}^-$  anions [259]. The interlayer distances for LDHs with intercalated chloride or carbonate anions being not very different and the peaks being large, the XRD results could not permit to distinguish between the two species or to establish if only one or both of them were intercalated. In order to specify the chemical nature of the anion exchanged in both, well-crystallized and badly crystallized, LDH phase, in situ ATR-IR spectroscopy was done.

The presence of several peaks close to  $20^\circ$  in Fig. 8.2b can be associated with the simultaneous intercalation of several species:  $\text{Mo}_7\text{O}_{24}^{6-}$  ( $20^\circ$  - (006) plane and  $24^\circ$  - (012) plane [259]) and  $\text{Cl}^-/\text{CO}_3^{2-}$  ( $24^\circ$  - (006) plane [146]). The presence of  $\text{Mo}_7\text{O}_{24}^{6-}$  can be suspected from a small peak at  $7^\circ$  associated with (003) plane [259]. The intercalation of polymolybdates from  $\text{MoO}_4^{2-}$  solutions was confirmed by ATR-FTIR (see next section).

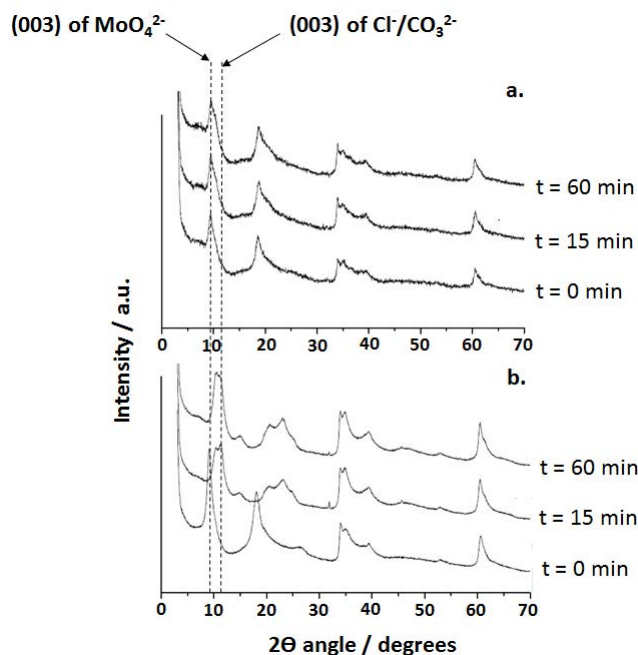


Figure 8.2: XRD spectra of the  $\text{Zn}_2\text{Al}/\text{-MoO}_4^{2-}$  phase after different immersion times as indicated in (a) 0.005 M NaCl and (b) 0.5 M NaCl solutions.

#### *ATR-FTIR survey and specification of the anion exchange*

The ATR-IR spectrum of pristine  $\text{Zn}_2\text{Al}/\text{-MoO}_4^{2-}$  showed the presence of characteristic bands at  $808\text{ cm}^{-1}$  for  $\text{MoO}_4^{2-}$  and at  $1360\text{ cm}^{-1}$  for  $\text{CO}_3^{2-}$  (Fig. 8.3a) intercalated into the LDH framework [259, 265]. The small peak of  $\text{CO}_3^{2-}$  can be explained by the adsorption of  $\text{CO}_2$  from air during LDH deposition on the crystal. The peak of  $\text{Zn}_2\text{Al}/\text{-LDH}$  structure is present as a shoulder at  $776\text{ cm}^{-1}$ . Fig. 8.3b presents the spectrum of the LDH film after the end of all leaching experiments. The structural band of the  $\text{Zn}_2\text{Al}/\text{-LDH}$  at  $776\text{ cm}^{-1}$  is now well visible. FTIR did not allow to quantify the level of  $\text{MoO}_4^{2-}$  release but the absence of an apparent shoulder at  $808\text{ cm}^{-1}$  in Fig. 8.3b may indicate that the amount of residual  $\text{MoO}_4^{2-}$  is small enough. The spectrum of pristine LDH was defined as a background and further spectra were recorded with its subtraction.

Fig. 8.4a represents the spectra recorded at different times after the addition of 4 mM of NaCl anions in the electrolyte (with background correction). The progressive increase of the negative peak at  $815\text{ cm}^{-1}$  (the position of  $\text{MoO}_4^{2-}$  peak) demonstrates the release of the intercalated  $\text{MoO}_4^{2-}$ . The exchange of  $\text{Cl}^-$  to  $\text{MoO}_4^{2-}$  reached a steady state after 15 min. At the end of this experiment the background was recorded once more, 2 mM of  $\text{NaHCO}_3$  was added to the electrolyte and the spectra were recorded until the steady state. The re-appearance and gradual increase of the negative peak of  $\text{MoO}_4^{2-}$  after the addition of bicarbonate (Fig. 8.4b) indicates further release driven by added bicarbonate ions. The presence of the band at  $1360\text{ cm}^{-1}$  can be interpreted as the intercalation of

8. FACTORS AFFECTING  $\text{MoO}_4^{2-}$  INHIBITOR RELEASE FROM A  $\text{Zn}_2\text{Al}/$ -BASED LDH AND THEIR IMPLICATION IN PROTECTING HDG BY MEANS OF ORGANIC COATINGS.

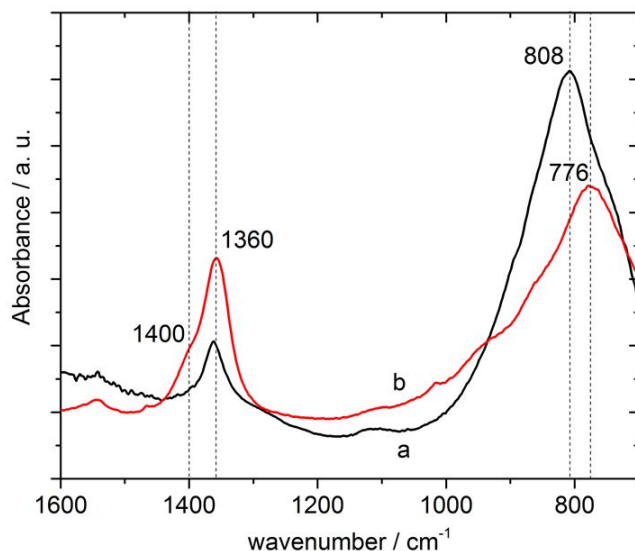


Figure 8.3: ATR-IR spectra of (a) pristine  $\text{Zn}_2\text{Al}/\text{MoO}_4^{2-}$  LDH phase and (b) LDH phase after leaching by 4 mM  $\text{Cl}^-$  and 2 mM  $\text{HCO}_3^-$  (see Fig. 8.4).

$\text{CO}_3^{2-}$  and not  $\text{HCO}_3^-$  as a major species. Expected bands for  $\text{HCO}_3^-$  are at  $1605\text{ cm}^{-1}$  and  $1010\text{ cm}^{-1}$  [266]. The shoulder at  $1400\text{ cm}^{-1}$  results from the lower symmetry of the carbonate in LDH [267]. It is of interest to emphasize that even the expected from thermodynamics fraction of  $\text{CO}_3^{2-}$  is less than 0.5 % in carbonate solutions at pH 6 [33], it is  $\text{CO}_3^{2-}$  and not  $\text{HCO}_3^-$ , which is exchanged with  $\text{MoO}_4^{2-}$  into  $\text{Zn}_2\text{Al}/\text{LDH}$ .

The small negative peak at  $1113\text{ cm}^{-1}$  can be explained by the release of  $\text{SO}_4^{2-}$  [259] presumably present in trace quantities in the pristine LDH. Moreover, the small peak at  $1113\text{ cm}^{-1}$  can be observed in the pristine LDH (Fig. 8.3a).

The small positive peak at  $926\text{ cm}^{-1}$  can be explained by the sorption of polymolybdate cations such as  $\text{Mo}_7\text{O}_{24}^{6-}$ . Davantes et al. [259] showed that for the  $\text{Zn}_2\text{Al}/\text{LDH}$  incorporation of  $\text{Mo}_7\text{O}_{24}^{6-}$  was realized from the  $\text{MoO}_4^{2-}$  solution at pH 5.8 due to its high affinity despite the fraction of  $\text{Mo}_7\text{O}_{24}^{6-}$  less than 0.5 % should be expected to be from thermodynamic prediction [33].

To summarize the XRD and ATR-FTIR results clearly indicated the anion exchange mechanism of the release in neutral solutions and higher release rate in the presence of carbonates  $\text{Zn}_2\text{Al}/\text{MoO}_4^{2-}$  LDHs. Detailed analysis of the IR spectra demonstrated the intercalation of  $\text{CO}_3^{2-}$  and not  $\text{HCO}_3^-$  in carbonate containing solutions at neutral pH. Further, kinetic investigation of  $\text{MoO}_4^{2-}$  release was conducted using quantification of the released  $\text{MoO}_4^{2-}$  by ICP-AES.

#### Quantification of $\text{MoO}_4^{2-}$ release in neutral electrolytes

Fig. 8.5 shows the evolution of the  $\text{MoO}_4^{2-}$  release with time during immersion in 0.5 M NaCl solutions with the different carbonate content at the initial pH 6. The steady

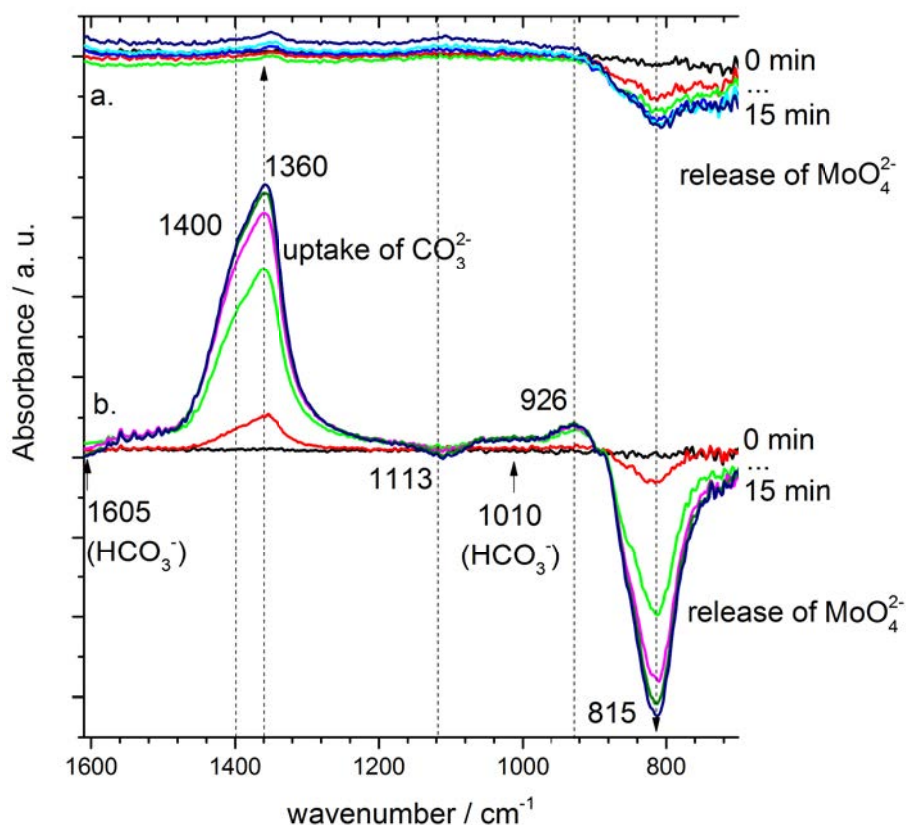


Figure 8.4: ATR-IR spectra of  $\text{MoO}_4^{2-}$  exchange in  $\text{Zn}_2\text{Al}/-\text{MoO}_4^{2-}$  with (a) 4 mM  $\text{Cl}^-$  and (b) with 2 mM  $\text{HCO}_3^-$  directly added in the solution after tests with  $\text{Cl}^-$  anions.

state, defined when the fraction of the released Mo normalized by the total quantity of the intercalated molybdate ( $Q_{\text{released}}^{\text{Mo}}/Q_{\text{total}}^{\text{Mo}}$ , %) varied less than 2%, was reached after approximately 1 h of the immersion. It is clearly seen from the figure that the additions of carbonate increases the steady state fraction of the released  $\text{MoO}_4^{2-}$ . Under argon deaeration, less than 30% of the the total amount of the intercalated  $\text{MoO}_4^{2-}$  is released; aeration procedure (which was equivalent to injection of approximately 30 mM of  $\text{HCO}_3^-$  [99]) increases the released fraction of  $Q_{\text{released}}^{\text{Mo}}/Q_{\text{total}}^{\text{Mo}}$  up to 65% whereas the additions of 0.1 M  $\text{NaHCO}_3$  results in the complete (100%) release of the intercalated  $\text{MoO}_4^{2-}$ .

To understand the initially high release it should be remembered that the first point on all curves in Fig. 8.5 does not correspond to the time  $t=0$  but to 10 seconds of the reaction. Strong initial release can be described as a “burst effect” initiated by the rapid exchange with species adsorbed from the air on LDH such as carbonates or by the release of  $\text{MoO}_4^{2-}$  adsorbed on the external surface of LDH crystallites [132, 268]. After the initially rapid release, all curves reach a plateau. In the presence of 0.1 M  $\text{NaHCO}_3$  the release rate increases near linearly up to 100%; in  $\text{NaCl}$  the shape is different. This

8. FACTORS AFFECTING  $\text{MoO}_4^{2-}$  INHIBITOR RELEASE FROM A  $\text{Zn}_2\text{Al}/$ -BASED LDH AND THEIR IMPLICATION IN PROTECTING HDG BY MEANS OF ORGANIC COATINGS.

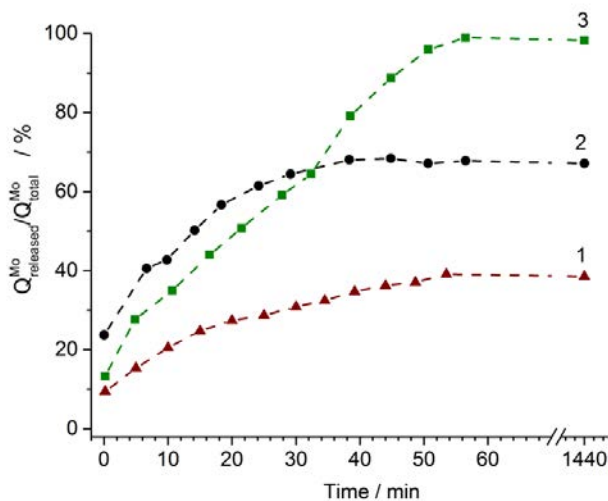


Figure 8.5: Evolution of released Mo (denoted as  $Q_{released}^{Mo}$ ) from the 5.3 mM LDH/Mo slurry divided by the total amounts of available Mo (determined by the complete dissolution of the LDH in 1 M HCl and denoted as  $Q_{dissolved}^{Mo}$ ) for the leaching tests in (1) 0.5 M NaCl under Ar, (2) primarily aerated 0.5 M NaCl and (3) 0.5 M NaCl + 0.1 M  $\text{NaHCO}_3$  solutions at initial pH 6.

can indicate the modification of a release mechanism in the presence of carbonate. The pH of the solutions did not vary significantly and at the end of the experiments equaled to  $6.5 \pm 0.2$ . The fractions of soluble Zn and Al normalized by the total available Zn and Al ( $Q_{dissolved}^{Zn}/Q_{total}^{Zn}$ , % and  $Q_{dissolved}^{Al}/Q_{total}^{Al}$ , %) were regularly below 1% even after 24 hours of the experiments confirming the observed by XRD and ATR-FTIR stability of the  $\text{Zn}_2\text{Al}/$ -LDH framework in neutral solutions and the anion exchange mechanism of the release.

To access the kinetic laws, the profiles of the  $\text{MoO}_4^{2-}$  release in the presence of the individual  $\text{Cl}^-$  and  $\text{HCO}_3^-$  ions were re-plotted in a double logarithmic scale ( $\log(Q_{released}^{Mo}/Q_{total}^{Mo}, \%)$  vs  $\log(t)$ , Fig. 8.6a). All curves demonstrate a linear behavior and the slope ( $n$ ) characteristic for each type of the exchanged ion is equal to 0.70  $Q_{total}^{Mo}$  0.05 in the case of the exchange with  $\text{HCO}_3^-$  and 0.35  $Q_{total}^{Mo}$  0.05 in the case of  $\text{Cl}^-$ .

The slope of the  $\text{MoO}_4^{2-}$  release profiles in double logarithmic scale in the presence of 0.1 M  $\text{NaNO}_3$  and 0.1 M  $\text{Na}_2\text{SO}_4$  correlated well with the  $n$  values for  $\text{Cl}^-$  in the case of  $\text{NO}_3^-$  and  $\text{HCO}_3^-$  (or  $\text{CO}_3^{2-}$  intercalated) in the case of  $\text{SO}_4^{2-}$  (Fig. 8.6b). In spite of the fact that in neutral solution carbonate is mainly present in the  $\text{HCO}_3^-$  form, numerous researches [254] showed the intercalation of only double charged  $\text{CO}_3^{2-}$ . The intercalation of  $\text{CO}_3^{2-}$  in neutral carbonate solutions can be explained by the higher affinity of  $\text{CO}_3^{2-}$  than  $\text{HCO}_3^-$  or/and by the additional transformation of  $\text{HCO}_3^-$  to  $\text{CO}_3^{2-}$  due to the local pH increase in the vicinity of the LDH crystallites [254]. The intercalation of only  $\text{CO}_3^{2-}$  was also confirmed in our experiments by the observed increase of the peak in IR spectrum

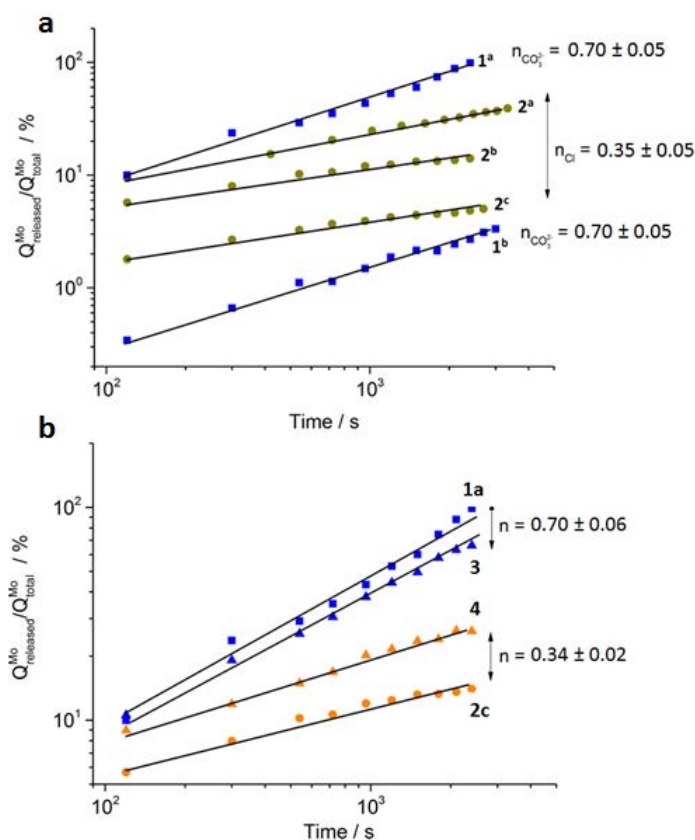


Figure 8.6: Evolution of released Mo (denoted as  $Q_{\text{released}}^{\text{Mo}}$ ) from the 5.3 mM LDH/Mo patterns divided by the total amounts of available Mo (determined by the complete dissolution of the LDH in 1 M HCl and denoted as  $Q_{\text{dissolved}}^{\text{Mo}}$ ) during the leaching tests in (1a) 0.1 M NaHCO<sub>3</sub>, (1b) primarily aerated water solution (equivalent to 30 mM of HCO<sub>3</sub><sup>-</sup> [99]), and deaerated (2a) 0.5 M, (2b) 0.05 M and (2c) 0.005 M NaCl, and (3) 0.1 M Na<sub>2</sub>SO<sub>4</sub> and (4) 0.1 M NaNO<sub>3</sub> solutions at initial pH 6. The slope of each curve (denoted as  $n$ ) is shown.

at 1360 cm<sup>-1</sup> during the anion exchange.

Therefore, the release kinetics can be associated with the charge of the intercalated anions replacing MoO<sub>4</sub><sup>2-</sup> ions and the values of  $n$  close to 0.35 are characteristic for the exchange of molybdate with monovalent ions and close to 0.70 for the exchange with divalent ions.

### MoO<sub>4</sub><sup>2-</sup> release in alkaline solutions

Fig. 8.7 shows the profiles of the MoO<sub>4</sub><sup>2-</sup> release along with the Zn and Al dissolution in the NaCl solutions under argon at the initial pH of 10 and 12. After 24 hours of the

8. FACTORS AFFECTING  $\text{MoO}_4^{2-}$  INHIBITOR RELEASE FROM A  $\text{Zn}_2\text{Al}/$ -BASED LDH AND THEIR IMPLICATION IN PROTECTING HDG BY MEANS OF ORGANIC COATINGS.

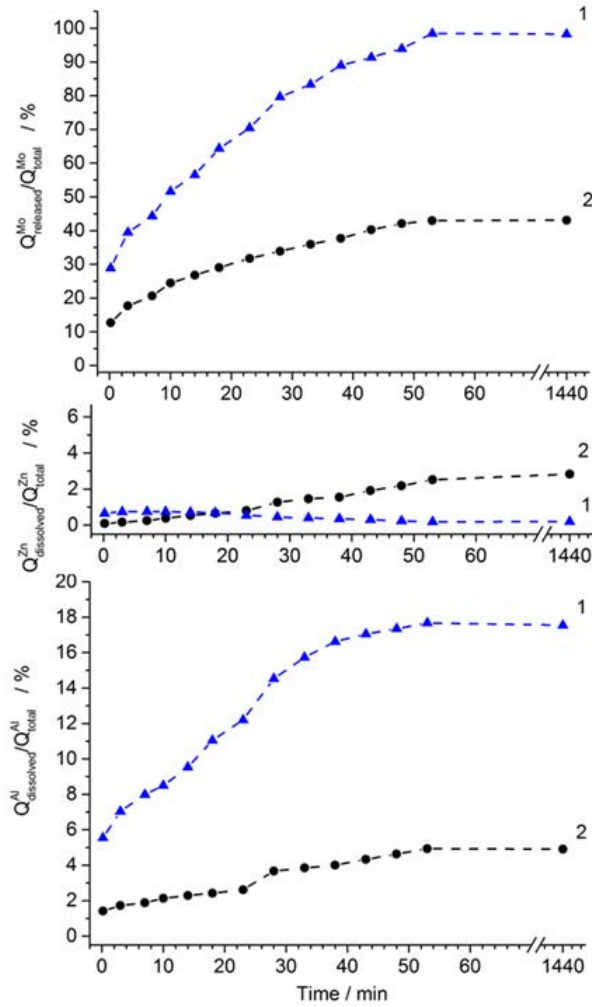


Figure 8.7: Evolution of released Mo ( $Q_{released}^{Mo}$ ) and dissolved Zn and Al ( $Q_{dissolved}^{Zn}$  and  $Q_{dissolved}^{Al}$ ) from the 5.3 mM LDH/Mo slurry normalized by the total amounts of Mo, Zn and Al ( $Q_{total}^{Mo}$ ,  $Q_{total}^{Zn}$  and  $Q_{total}^{Al}$ ) during the leaching tests in deaerated solutions at pH values of (1) 12 and (2) 10.

leaching tests, the solution pH did not vary more than 0.1 unit from the initial value.

Unlike the leaching tests in neutral solutions, the partial dissolution of  $\text{Zn}_2\text{Al}/$ -LDH framework was observed. At pH 10, the dissolution of both Zn and Al is visible (curves 2 in Fig. 8.7) with the fraction of the dissolved Zn and Al as  $Q_{dissolved}^{Zn}/Q_{total}^{Zn}, \% = 2.5\%$  and  $Q_{dissolved}^{Al}/Q_{total}^{Al}, \% = 4.5\%$  after 24 hours of the leaching tests. At pH 12 (curves 1 in Fig. 8.7), only the dissolution of Al is detected with  $Q_{dissolved}^{Al}/Q_{total}^{Al}, \% = 18\%$  after 24 hours of the test. The preferential dissolution of Al at alkaline pH correlated with higher solubility of Al than Zn ions in alkaline solutions [33].

Evidently, the release of  $\text{MoO}_4^{2-}$  ions at alkaline pH is determined not only by the

affinity of  $\text{OH}^-$  ions to  $\text{Zn}_2\text{Al}/\text{-LDH}$  framework but also by the partial dissolution of the  $\text{Zn}_2\text{Al}/\text{-LDH}$  framework. At pH 10, 40% of  $\text{MoO}_4^{2-}$  is released and 3 % of Al(III) is dissolved. Such relatively high fraction of released  $\text{MoO}_4^{2-}$  can be due to combined ion exchange with  $\text{OH}^-$  and partial dissolution of  $\text{Zn}_2\text{Al}/\text{-LDH}$  framework mechanisms. At pH 12 a complete 100% release of  $\text{MoO}_4^{2-}$  is observed after 1 hour of the immersion test where at least 18 % of the  $\text{Zn}_2\text{Al}/\text{-LDH}$  framework were disrupted. Note the pathways of  $\text{MoO}_4^{2-}$  release cannot be gained in this case from the determination of slopes of the release profiles in a double logarithmic scale due to the combined contribution of ion exchange and weathering mechanisms [130].

### 8.3.2 Molybdate release and effect of $\text{Zn}_2\text{Al}/\text{-MoO}_4^{2-}$ LDH fillers on the corrosion of coated samples

The EIS spectra of the coated HDG samples with and without LDH/Mo fillers during the immersion in 0.5 M NaCl with and without additions of 0.1 M  $\text{NaHCO}_3$  are shown in Fig. 8.8. Because of the presence of the defect in the polymer layer (an artificial scratch), EIS spectra are referring to the corrosion behavior of the metal substrate in the defect and beneath the coating and do not refer to the organic coating, its resistive part would be several orders of magnitude higher [1, 9, 269–272]. Moreover, the observed low frequency impedance values are somehow typical for Zn exposed to electrolytes containing a high level of salinity [23].

One distinct time constant of the RC element is visible by the U-like shape of the phase angle evolution in the frequency range of  $10^0 - 10^5$  Hz. This is commonly attributed to the faradaic discharge of at the solution/oxide/metal interfaces occurring through the film of corrosion products typical for Zn substrate in salty solutions [23, 180, 273]. The second time constant seems to appear at lower  $10^{-2} - 10^0$  Hz frequency range visible by the decrease of the value of phase angle that can attributed to the capacitive behavior of formed corrosion products [23, 180, 273]. Probably more time constants could be suspected not clearly distinguished. Therefore, the equivalent circuit only with the two time constants was used to fit the EIS spectra, which is shown in inset in Fig. 8.8.  $R_e$  is the electrolyte resistance,  $R_{ct}$  is the faradaic charge transfer resistance,  $R_{ox}$  electrical resistance of the corrosion products,  $C$  is the capacitance of electrode double layer and constant phase element (CPE) presents the capacitance of the layer of the corrosion products (inset in Fig. 8.8). CPE element better fitted the EIS spectra than an ideal capacitor, which is commonly attributed to the presence of inhomogeneities on the metal/oxide/electrolyte interfaces such as the surface roughness, non-uniform current distribution etc [156, 274]. All values of  $R_{ct}$  and  $C$  were determined from the fitting of EIS spectra.

The value of  $R_{ct}$  is usually used for the monitoring the protective properties of the coating since it is directly related to the value of the corrosion current of the substrate through Stern-Geary relation [194].

The evolution of the  $R_{ct}$  values along with the amounts of Zn dissolved from the underneath HDG ( $Q_{dissolved}^{Zn}$ ) and the released Mo ( $Q_{released}^{Mo}$ ) are shown in Fig. 8.9. In

8. FACTORS AFFECTING  $\text{MoO}_4^{2-}$  INHIBITOR RELEASE FROM A  $\text{Zn}_2\text{Al}/$ -BASED LDH AND THEIR IMPLICATION IN PROTECTING HDG BY MEANS OF ORGANIC COATINGS.

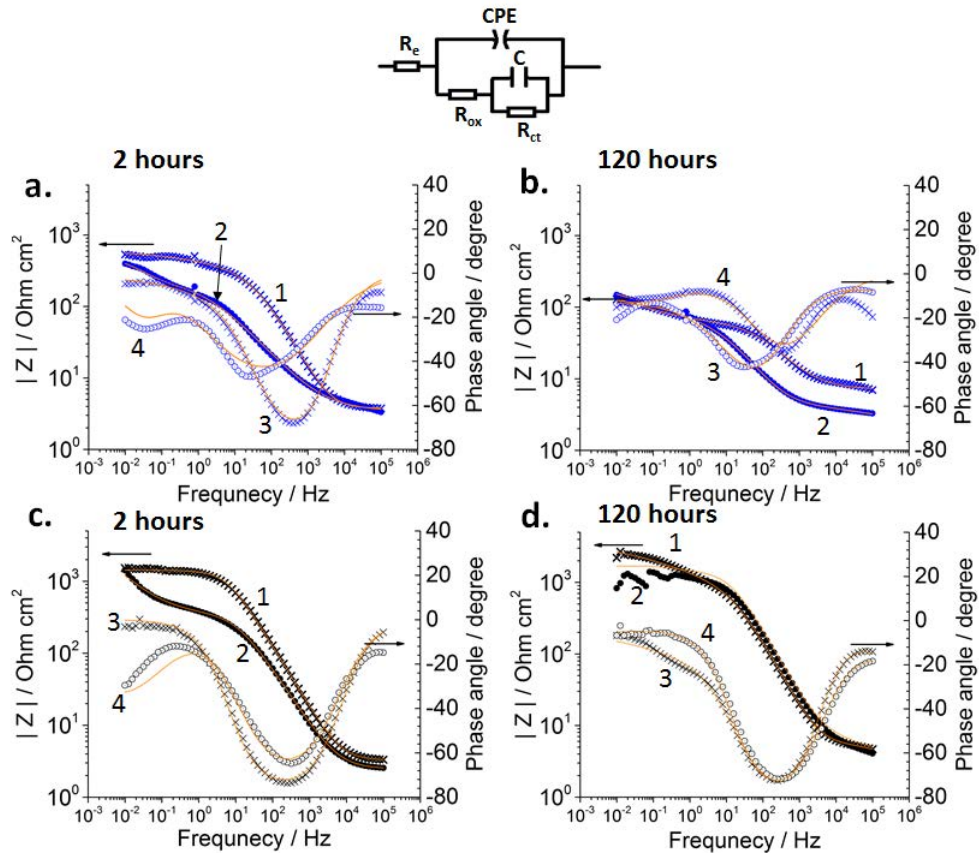


Figure 8.8: EIS spectra obtained on the coated HDG with a scratch after 2 hours and 120 hours of the immersion (a, b) in 0.5 M NaCl solution and (c, d) in 0.5 M + 0.1 M  $\text{NaHCO}_3$  solution. Curves 1 and 3 represent the evolution of the total impedance and the phase shift respectively for coatings with  $\text{Zn}_2\text{Al}/\text{-MoO}_4^{2-}$  fillers, and curves 2 and 4 - the evolution of the total impedance and the phase shift respectively for coatings without  $\text{Zn}_2\text{Al}/\text{-MoO}_4^{2-}$ . The inset shows the equivalent electrical circuit used to fit the EIS data. Solid curves show the fits.  $R_e$  is the uncompensated electrolyte resistance,  $R_{ct}$  - the faradaic charge transfer resistance,  $R_{ox}$  - electrical resistance of the corrosion products,  $C$  is the capacitance of the double layer and CPE is capacitance expressed as a constant phase element for the layer of corrosion products.

both, 0.5 M NaCl and 0.5 M NaCl + 0.1 M  $\text{NaHCO}_3$  solutions, the pH after 120 hours of the immersion changed from 6 to about 7-8. The inhibiting effect of the additions of the carbonates on the barrier properties of the coatings without the additions of the LDH fillers should be noted since the  $Q_{dissolved}^{Zn}$  values were regularly less and the  $R_{ct}$  values were regularly higher in the  $\text{NaHCO}_3$  solutions. The inhibiting properties of the carbonates were previously reported for both, uncoated [37,55,275] and polymer coated Zn substrates [20-22] and were explained by the formation of low soluble Zn corrosion

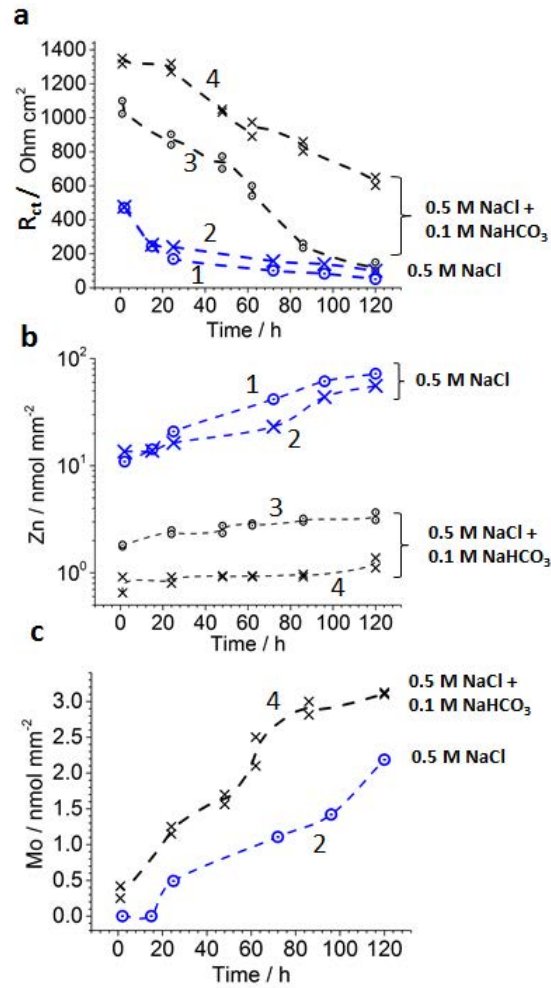


Figure 8.9: Evolution of (a) the value of charge transfer resistance  $R_{ct}$ , (b) Zn dissolution and (c) Mo release during immersion of coated HDG samples in 0.5 M NaCl and 0.5 M NaCl + 0.1 M NaHCO<sub>3</sub> solutions. The curves 1 and 3 are for the coating without LDH/MoO<sub>4</sub><sup>2-</sup> whereas the curves 2 and 4 are for the coating with LDH/MoO<sub>4</sub><sup>2-</sup> fillers.

products and the local pH buffering in the intact zones.

In 0.5 M NaCl the comparison of the values of  $R_{ct}$  and  $Q_{dissolved}^{Zn}$  measured for the samples with and without LDH/Mo fillers in the coating (curves 1 and 2 in Fig. 8.9a and Fig. 8.9b) demonstrates a slight if any inhibiting effect of LDH/Mo fillers: after 24 hours of the immersion  $Q_{dissolved}^{Zn}$  becomes slightly lower and  $R_{ct}$  becomes higher for samples in with LDH/Mo. Note, only one experiment for each coating system was made. The absence of statistical significance does not permit to interpret the small difference in  $Q_{dissolved}^{Zn}$  and  $R_{ct}$  for curves 1 and 2 in Fig. 8.9a and Fig. 8.9b as an inhibiting effect of LDH/Mo fillers. The release of MoO<sub>4</sub><sup>2-</sup> becomes visible only after 24 hours of the

8. FACTORS AFFECTING  $\text{MoO}_4^{2-}$  INHIBITOR RELEASE FROM A  $\text{Zn}_2\text{Al}$ -BASED LDH AND THEIR IMPLICATION IN PROTECTING HDG BY MEANS OF ORGANIC COATINGS.

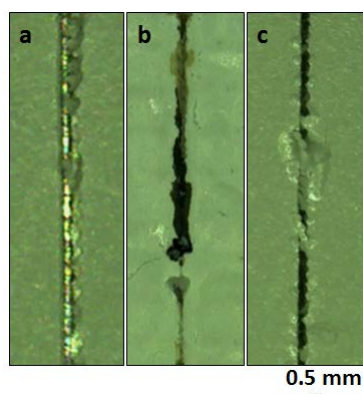


Figure 8.10: General view of the scratched area prior to the immersion tests (a) and after 120 hours of immersion in (b) 0.5 M NaCl and (c) 0.5 M NaCl + 0.1 M  $\text{NaHCO}_3$ .

immersion (curve 2 in Fig. 8.9c).

Well-pronounced inhibiting effect of LDH/Mo phase on Zn dissolution was observed when 0.1 M  $\text{NaHCO}_3$  was added in 0.5 M NaCl due to higher values of  $R_{ct}$  and lower values of  $Q_{dissolved}^{Zn}$  in 0.1 M  $\text{NaHCO}_3$  (compare curves 3 and 4 in Fig. 8.9a and Fig. 8.9b). These experiments were repeated two times in order to have statistical reinforcement of the carbonate effect. The data of two experiments are overlaid in Fig. 8.9.

The inhibiting effect is immediate and continues during the whole immersion tests, which can be associated with the continuous release of  $\text{MoO}_4^{2-}$  observed from the first moment of the experiments (curve 4 in Fig. 8.9c). At all times of the experiment, the addition of 0.1 M  $\text{NaHCO}_3$  in the solution results in the factor of two increase of the amounts of the released Mo ( $Q_{released}^{Mo}$ ) (compare curves 2 and 4 in Fig. 8.9c).

The macroscopic observation of the polymer around the scratch in Fig. 8.10 shows the swelling of the polymer in the area of a scratch after the immersions presumably caused by the water uptake.

The evolution of the double layer capacitance ( $C$ ) values permits the qualitative comparison of the active areas where the metal dissolution occurs. Active surface area can be restricted by the presence of insoluble oxides/hydroxides on the metal surface and the delaminated zone of the polymer [1, 272, 276, 277]. In the present work, contribution of the surface oxides to the change of double layer capacitance can be neglected since the capacitance of double layer can be described as an ideal capacitor. The satisfactory fit of double layer as  $C$  implies the homogeneous active surface during all immersion tests. Therefore, the increase of  $C$  values can be associated only with the increase of the disbonded areas of metal/polymer interface. Note that the quantitative estimation of disbonded area is generally impossible due to very different local environment in the confined zones of the defect.

Fig. 8.11 shows the evolution of the double layer capacitance ( $C$ ) normalized to  $C(t=0)$  for each EIS spectrum. Inspection of Fig. 8.11 evidences indetical behavior of  $C(t)/C(t=0)$  in 0.5 M NaCl for coated samples with LDH/ $\text{MoO}_4^{2-}$  (curve 2) and without

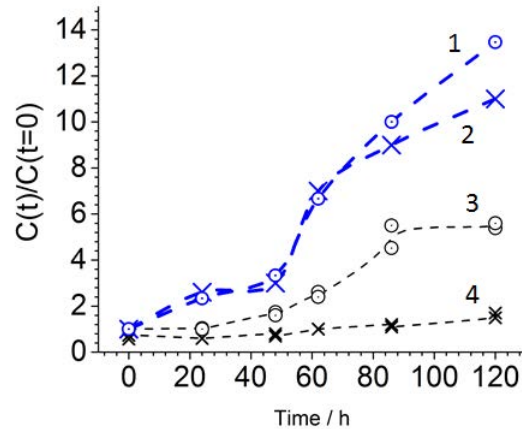


Figure 8.11: Evolution of the capacitance of the double layer ( $C$ ) normalized to  $C(t = 0)$  gained from EIS spectra in 0.5 M NaCl (curves 1 and 2) and 0.5 M NaCl + 0.1 M NaHCO<sub>3</sub> solutions (curves 3 and 4). The curves 1 and 3 are for the coating without LDH/MoO<sub>4</sub><sup>2-</sup> whereas the curves 2 and 4 are for the coating with LDH/MoO<sub>4</sub><sup>2-</sup> fillers.

LDH/MoO<sub>4</sub><sup>2-</sup> (curve 1) fillers. This can be interpreted as the absence of any effect of LDH/MoO<sub>4</sub><sup>2-</sup> fillers on the delamination of coated system. In contrast, comparing the behavior of the system with and without LDH/MoO<sub>4</sub><sup>2-</sup> fillers in 0.5 M NaCl + 0.1 M NaHCO<sub>3</sub> (curve 4 with and curve 3 without fillers) one can conclude that in the presence of carbonates disbonding is decreased in the coating with LDH/MoO<sub>4</sub><sup>2-</sup> fillers.

## 8.4 Discussion

### 8.4.1 Mechanisms of MoO<sub>4</sub><sup>2-</sup> release from Zn<sub>2</sub>Al/-LDH framework

Two different mechanisms of the ion release from LDH framework were described in the literature [131, 132, 153, 255, 256]: weathering and ion exchange. In the case of weathering, the partial dissolution of LDH framework in aggressive medias defines the release of an entrapped ion [153, 255]. The preferential dissolution of Al(III) from Zn<sub>2</sub>Al/-LDH framework at alkaline pH can alter the charge balance and hence, decrease the positive charge of the layers and decrease the amount of the intercalated anions enhancing MoO<sub>4</sub><sup>2-</sup> release. Therefore, at pH 12, which is out of the range of the pH stability of Zn<sub>2</sub>Al/-LDH framework (pH from 6.5 to 10.5) [18, 254], the partial dissolution of LDH framework with the preferential dissolution of Al(III) along with a complete release of MoO<sub>4</sub><sup>2-</sup> was observed. Incomplete dissolution of Al(III) (about 18 %, Fig. 8.7) indicates the contribution of both ion exchange and weathering mechanisms to the release of MoO<sub>4</sub><sup>2-</sup>.

In the case of the anion exchange mechanism when the LDH framework does not undergo changes, the release of an intercalated anion can be described by the sequence schematically represented in Fig. 8.12 [130, 132, 256, 268]:

8. FACTORS AFFECTING  $\text{MoO}_4^{2-}$  INHIBITOR RELEASE FROM A  $\text{Zn}_2\text{Al}$ -BASED LDH AND THEIR IMPLICATION IN PROTECTING HDG BY MEANS OF ORGANIC COATINGS.

1. the adsorption of an external anion such as  $\text{Cl}^-$ ,  $\text{HCO}_3^-$  etc. on the LDH plates
2. the exchange of the adsorbed species with the intercalated anions at the edge of LDH plates
3. the diffusion of the extraneous anion into the depth of the LDH framework

The rate determining step (RDS) of the ion exchange mechanism defines the kinetics of the anion release. The review of Costa et al. [130] provides a comprehensive description of the commonly used kinetic models to fit the experimental data and to identify the RDS. Herein, the Peppas model [130, 133] is used that includes most of the other models such as Higuchi, zero order, first order models etc. The equation that describes the Peppas model is:

$$\frac{Q_{released}^{Mo}}{Q_{total}^{Mo}} = kt^n; \quad \log \frac{Q_{released}^{Mo}}{Q_{total}^{Mo}} = \log k + n \cdot \log t \quad (8.1)$$

where  $t$  is time,  $k$  is the kinetic release constant and  $n$  is the order of the release process, which characterizes the RDS of the release mechanism. For the release from spherical particles,  $n = 0.5$  corresponds to the rate determining step (RDS), which is described by Fick diffusion (step 3 in Fig. 8.12) and  $n = 1.0$  corresponds to the surface reaction controlled kinetics (step 1 or/and 2 in Fig. 8.12) [130]. In the case of the cylindrical geometry of containers,  $n$  should decrease to approximately 0.4 and 0.8 instead of 0.5 and 1.0 respectively [130, 133]. The LDH particles used in this work were neither spherical nor cylindrical but had a platelet-like shape. The decrease of the symmetry in plates compared to spheres should result in modifying of  $n$  in the same direction as for the case of cylindrical particles. Therefore, the decrease of  $n$  from 0.5 or 1.0 should be expected. The values of  $n$  of about 0.35 and 0.70 in the present work were associated with the RDS being Fick diffusion and a surface reaction respectively.

The experimental data suggests the Fick diffusion as the RDS for the monovalent  $\text{Cl}^-$  and  $\text{NO}_3^-$  ions, and the surface reaction as the RDS in the case of the exchange with the divalent  $\text{CO}_3^{2-}$  and  $\text{SO}_4^{2-}$  ions. The change of the RDS when replacing monovalent anions in the electrolyte by divalent ions implies quicker diffusion of the divalent ions ( $\text{CO}_3^{2-}$  and  $\text{SO}_4^{2-}$ ) inside the LDH particles than the diffusion of monovalent ions ( $\text{Cl}^-$  and  $\text{NO}_3^-$ ). The driving force of the diffusion is determined by the difference of the electrochemical potentials ( $\mu$ ) [124] inside and outside LDH plates

$$J \sim \frac{\partial \mu}{\partial x} \quad (8.2)$$

where  $J$  is the flux of anions and  $x$  is the distance. The electrochemical potential is defined as [124]:

$$\mu = \mu^0 + zFE \quad (8.3)$$

where  $\mu^0$  is the standard electrochemical potential,  $z$  is the anion charge,  $F$  is the Faraday constant and  $E$  is the electric potential inside the LDH framework. The rate of the

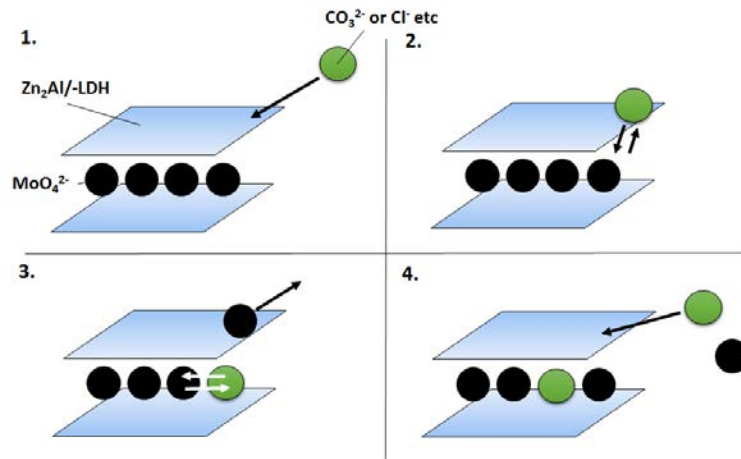


Figure 8.12: Schematic representation of the anion exchange mechanism into LDH framework where (1) is adsorption on LDH plates, (2) is exchange of absorbed species, (3) is diffusion inside LDH and (4) is adsorption of new anion from the media on LDH plates, and so on.

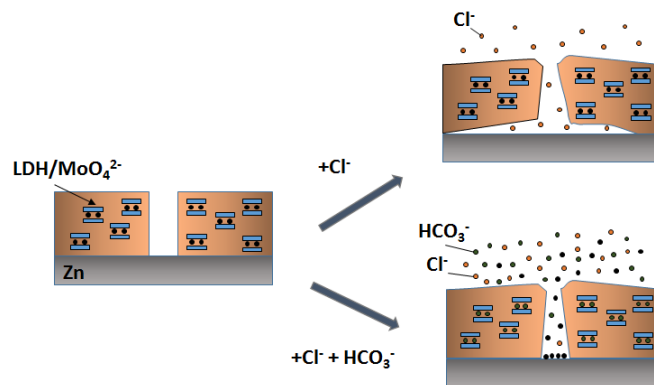


Figure 8.13: Schematic representation of the action of LDH/Mo hybrid coating on Zn in  $\text{Cl}^-$  and  $\text{Cl}^- + \text{HCO}_3^-$  medias: the loss of the adhesion of the coating in  $\text{Cl}^-$  due to Zn corrosion and the inhibition of the Zn corrosion in  $\text{Cl}^- + \text{HCO}_3^-$  due to the release of  $\text{MoO}_4^{2-}$  water soluble inhibitor.

diffusion should be directly related to the charge of the anion if the steric factors can be neglected:

$$J \sim z \quad (8.4)$$

### 8.4.2 Effect of carbonates on the corrosion behavior of coated samples

The reduced Zn dissolution, detached area of polymer and higher  $R_{ct}$  values for HDG coated with  $\text{Zn}_2\text{Al}/\text{MoO}_4^{2-}$  LDH fillers can be associated with the release of  $\text{MoO}_4^{2-}$  from the hybrid coating system in the presence of 0.1 M  $\text{NaHCO}_3$  confirming the reported earlier [187] inhibiting properties of soluble molybdates on HDG. The rapid release of  $\text{MoO}_4^{2-}$  in the presence of  $\text{CO}_3^{2-}$  was related to the high affinity of  $\text{CO}_3^{2-}$  and rapid kinetics of the ion exchange described as the surface controlled reaction (Fig. 8.13). The absence of any measurable effect of LDH/Mo fillers in only  $\text{Cl}^-$  media can be explained by the initial low exchange of  $\text{MoO}_4^{2-}$  with monovalent  $\text{Cl}^-$  ions.

To summarize, the release of  $\text{MoO}_4^{2-}$  water-soluble inhibitor from  $\text{Zn}_2\text{Al}/$ -LDH framework is directly related to the composition of the media providing a tool to control release kinetics and hence, inhibition of the substrate in the coated system. In the comprehensive investigation of the LDH/Mo system and the hybrid LDH/Mo coating system, the  $\text{CO}_3^{2-}$  ions serve as a trigger defining the release kinetics of  $\text{MoO}_4^{2-}$  ions.

## 8.5 Conclusions

In this work,  $\text{Zn}_2\text{Al}/\text{MoO}_4^{2-}$  LDH was considered as a potential filler for hybrid coatings on Zn based substrates. The factors controlling the release kinetics of  $\text{MoO}_4^{2-}$  water-soluble inhibitor were studied by XRD, in situ ATR-IR spectroscopy and ICP-AES. Results of the leaching tests from the LDH/ $\text{MoO}_4^{2-}$  powders and their numerical treatment demonstrated that:

1. In carbonate free neutral NaCl (pH 6-10) the release was incomplete (less than 40% after 24 of the immersion in 0.005 M, 0.05M and 0.5 M NaCl). The addition of carbonates in the NaCl solutions promoted the complete (100%) release after 60 minutes of the immersion. The release mechanism was the anion exchange with  $\text{CO}_3^{2-}$  even its ratio in carbonate solution at neutral pH was less than 0.5 %.
2. In strong alkaline solutions (pH 12), 100 % release was observed after 1 hour of the immersion. Under these conditions, along with the ion exchange mechanism the partial dissolution of the  $\text{Zn}_2\text{Al}/$ -LDH framework was involved in the release process.
3. The anion exchange kinetics of molybdate with monovalent anions (such as  $\text{Cl}^-$  and  $\text{NO}_3^-$ ) was described by a rate law with  $n=0.35 \pm 0.05$  and with divalent anions (such as  $\text{CO}_3^{2-}$  and  $\text{SO}_4^{2-}$ ) by  $n = 0.70 \pm 0.05$ . The values of n were related to the symmetry of the LDH plates and the rate determining step of the exchange reaction. The rate determining step of anion exchange was suggested to depend on the charge of exchange anions: Fick's diffusion of the exchangeable anions inside LDH plates for monovalent anions and the interface reaction (adsorption on the LDH plates) for divalent anions.

The behavior of the coated HDG with and without  $\text{Zn}_2\text{Al}/\text{MoO}_4^{2-}$  LDH fillers during the immersion was monitored by EIS and the leaching measurements. The results were

analyzed focusing on the role of the environment for the release kinetics of  $\text{MoO}_4^{2-}$ . In these experiments, lower Zn dissolution and polymer detachment were associated with the release of  $\text{MoO}_4^{2-}$  from  $\text{Zn}_2\text{Al}/\text{-MoO}_4^{2-}$  hybrid coatings controlled by the anion composition of the corrosive media. In 0.5 M NaCl solution under air of the release of  $\text{MoO}_4^{2-}$  was delayed for 24 h which was explained by a lower affinity of  $\text{Cl}^-$  to  $\text{Zn}_2\text{Al}/\text{-LDH}$  than  $\text{MoO}_4^{2-}$ . The presence of 0.1 M  $\text{NaHCO}_3$  in 0.5 M NaCl resulted in the immediate release of  $\text{MoO}_4^{2-}$  and measurable inhibiting effect providing a potential tool for controlling behavior of LDH hybrid coatings.

## Summary

---

- ✓ **The results of the work demonstrated that the composition of the corrosive environment provides a potential tool for controlling a performance of LDH hybrid anticorrosion coatings. The kinetics of the inhibitor release significantly varied with carbonate concentration in the solutions. The accumulation of carbonate species increased the total molybdate release and the release kinetics. The data permit to give a possible explanation for the results observed in salt spray tests (SST) of tested coatings on galvanized steel (Appendix G). SST demonstrated that at short exposure times there was no benefit effect of LDH/Mo anticorrosion coating, however at longer times a clear inhibiting effect was observed probably caused by the time delayed inhibitor release due to the accumulation of carbonates from the atmosphere.**
-



---

## D. Concluding remarks

---

This section comprises the final Chapter 9, which presents the general conclusions and perspectives brought by this PhD work.



---

## Conclusions and perspectives

---

In the recent decades, hybrid polymer coatings with a corrosion inhibitor embarked in a host reservoir of a nanometric size attracted considerable attention of corrosion scientists. This is due to their potential ability to control the release of the inhibitor and hence, to provide the long-term corrosion protection of a metal substrate [1,3–5,7]. However, the choice of an effective inhibitor and the understanding of the mechanisms of its inhibiting action in a specific underpaint corrosion conditions are not trivial tasks. A combined approach for coated systems taking into account different aspects affecting inhibitor action in such conditions was not previously proposed. This work attempts to propose such a complex approach for the mechanisms of the active corrosion protection of galvanized steel by  $\text{Zn}_2\text{Al-LDH}$ /inhibitor hybrids in polymer coatings. The novelty of the work consists in the combined global methodology, which includes different aspects of the system reactivity schematically presented in Fig. 9.1:

1. the corrosion reactions like metal dissolution (process  $1_a$  in Fig. 9.1) accompanied by cathodic oxygen reduction (process  $1_b$ ) and the formation of insoluble films (process  $1_c$ ) in the presence of the inhibitors are studied using electrochemical AESEC methods and completed by SEM, EDX, Raman, XPS and GD-OES characterization;
2. factors affecting leaching of the inhibitor from the host LDH (process 2 in Fig. 9.1) in corrosive media were identified by the comparison of the leaching kinetics in different environments surveyed by ICP-AES, XRD and in situ ATR-IR;
3. the degradation of the complete system during immersions in different electrolytes, including delamination of the polymer coating with  $\text{Zn}_2\text{Al-LDH}$ /inhibitor fillers (process 3 in Fig. 9.1) and the corrosion of the substrate, was described using simultaneous measurements of the Zn dissolution, the inhibitor release and the evolution of the EIS response giving access to the evolution of the active (disbonded from the organic coating) metal surface area and the corrosion rates of the substrate.

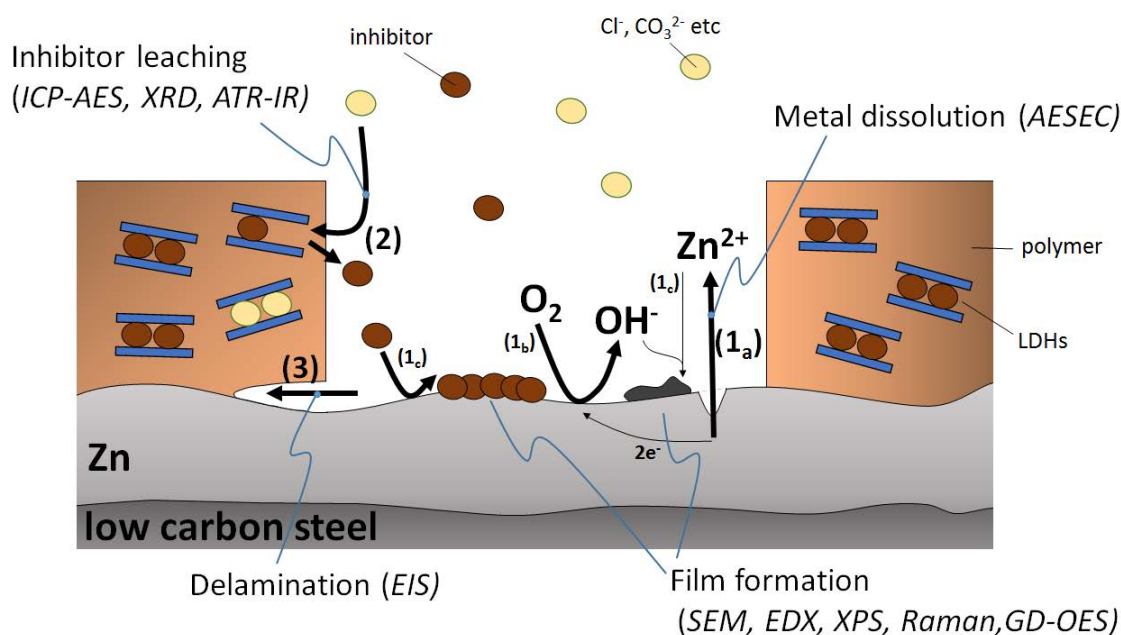


Figure 9.1: Schema of the corrosion inhibition of galvanized steel by LDH – inhibitor hybrids in the coating formulation. The main processes studied in this work are highlighted: (1<sub>a</sub>) electrochemical dissolution of the substrate accompanied by (1<sub>b</sub>) cathodic oxygen reduction and the formation of insoluble films (process 1<sub>c</sub>), (2) leaching of the inhibitor from LDH samples and (3) delamination of the coating.

The main results of the work are summarized below in connection with the considered processes.

### Intelligent screening of water soluble inhibitors for application in hybrid coating (processes 1 in Fig. 9.1)

The desired water soluble inhibitors in the coating formulation for galvanized steel need to be active in alkaline solutions, dictated by a high local alkalinization in confined zones due to oxygen or/and water reduction on Zn. This work gives the first systematic investigation of the effect of the water soluble inhibitors on the reactivity of Zn in large range of pH including alkaline solutions.

A new way of rapid screening of the inhibitor action on galvanized steel using AESEC measurement of Zn dissolution was applied to 3 potentially interesting inhibitors (2 organic and one inorganic). The method was compared with conventional methods of the determination of corrosion rates: based on Tafel extrapolation, estimation of  $R_p$  from EIS, mass balance of dissolved species in immersion tests.

The results confirmed that in a general case, one cannot rely on the estimation of the corrosion current from the conventional Tafel extrapolation due to possible contribution of the anodic dissolution to the total current under cathodic polarization (Fig. 9.2). Valid

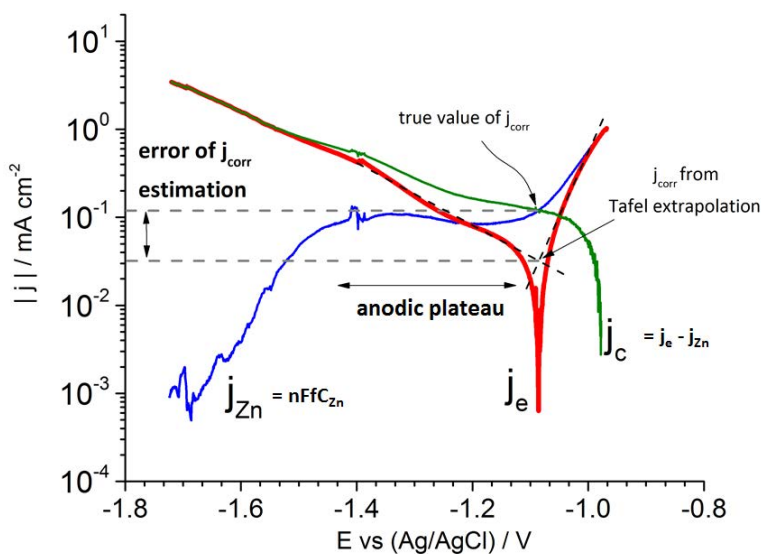


Figure 9.2: Illustration of corrosion rate estimation from AESEC polarization data and from the conventional Tafel extrapolation. Total current ( $j_e$ ), Zn dissolution current ( $j_{Zn}$ ), cathodic current ( $j_c$ ) and corrosion current ( $j_{corr}$ ) are shown.

estimation of the corrosion rates from  $R_p$  values essentially required a system stability, which was difficult to achieve during the corrosion of studied systems. From the tested electrochemical methods, AESEC provided the most appropriate values of corrosion currents. However, AESEC corrosion currents did not include the currents consumed to the formation of slightly soluble Zn(II) intermediates and hence, can underestimate its values.

Obviously, the conditions of AESEC experiments differ significantly from the conditions of immersion tests and atmospheric corrosion in terms of time and flow conditions resulting in disfavoring of the accumulation of corrosion products and their ageing, but AESEC has a major advantage in the investigation of elemental steps of the corrosion mechanisms giving the access to the kinetic data of the metal dissolution.

### Action of L-cysteine and L-phenylalanine amino acids

L-phenylalanine showed a weak inhibiting effect on Zn dissolution only at pH 2 and 12 and an accelerating at pH 10 in a whole studied pH range of 2-13 (see Appendix B). L-phenylalanine was not considered in details due to its weak inhibiting properties.

In this work for the first time L-cysteine was considered as a potential water soluble inhibitor on Zn in wide pH range of 2 – 13 and wide concentration range of  $10^{-5}$  M –  $10^{-2}$  M. L-cysteine accelerated Zn dissolution at high ( $10^{-2}$  M) concentration in the whole studied pH range of 2-13, which was defined by its strong complexation with  $Zn^{2+}$  forming soluble complexes and hence, the dissolution of native Zn protection oxides. At intermediate  $10^{-4}$  -  $10^{-3}$  M concentrations, L-cysteine inhibited Zn dissolution with the

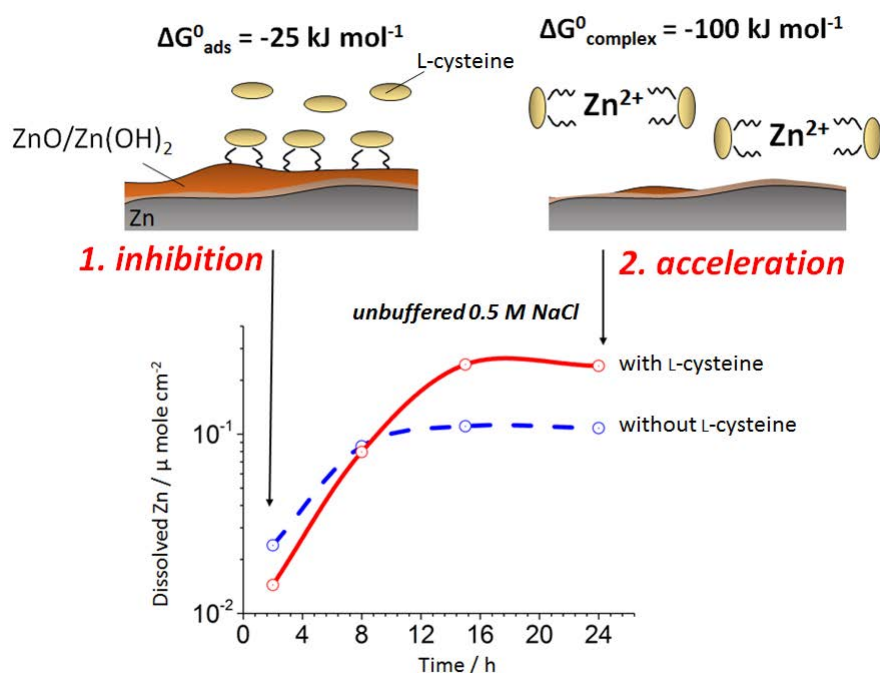


Figure 9.3: Action of  $10^{-4}$  -  $10^{-3}$  M L-cysteine on Zn dissolution at neutral pH: initial adsorption of L-cysteine on Zn oxides defines its inhibiting effect however, the dissolution of Zn oxides with time favored by thermodynamics leads to the acceleration of Zn dissolution.

inhibition efficiency of less than 70 % defined by a weak physisorption on the surface of Zn oxides. At neutral pH, the inhibiting effect turned into the acceleration after 8 hours of the immersion coherent with the time-delayed but thermodynamically favorable dissolution of Zn native oxides (Fig. 9.3). At pH 12, the inhibiting effect did not disappear even after 24 hours of the immersion. The origins of this effect still needs to be understood. The surface characterizations after 24 hours of the immersion demonstrated that the morphology and the nature of Zn corrosion products on the surface was different with and without L-cysteine underlying the effect of the inhibitor not only on the dissolution but also on the following precipitation processes.

The polarization of HDG in the presence of L-cysteine revealed a hidden plateau current of Zn dissolution at neutral and alkaline pH (Fig. 9.2) presumably determined by the diffusion of L-cysteine species to the metal surface. The major effect of L-cysteine additions on Zn dissolution was (i) to induce a cathodic shift of the onset for Zn dissolution, and (ii) to enhance the plateau current. Both effects were attributed to the complexation of Zn<sup>2+</sup> with L-cysteine.

**The dual action of L-cysteine as both the accelerator at high and the inhibitor at low concentrations render dubious its practical use in LDH hybrids coatings on galvanized steel.**

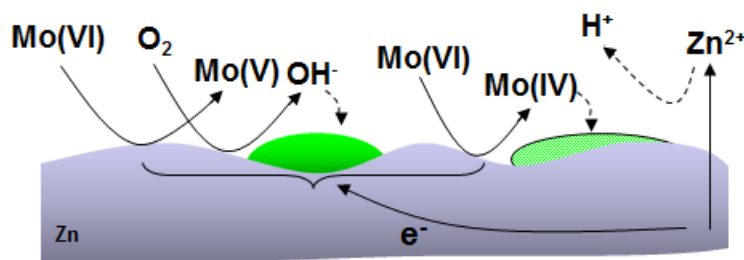


Figure 9.4: Schema of  $\text{MoO}_4^{2-}$  water soluble inhibitor action on Zn: preferential formation and precipitation of Mo(V) species on cathodic sites because of a local alkalinization and preferential formation and precipitation of Mo(IV) species on anodic sites because of a local acidification at neutral and slightly alkaline pH.

### Action of $\text{MoO}_4^{2-}$ water soluble inhibitor

$\text{MoO}_4^{2-}$  anions were considered then as the potential inhibitor for the application in hybrid coatings. The action of  $\text{MoO}_4^{2-}$  ions on galvanized steel has been well documented for the application in conversion coating in acid pH and with additives [64–68] with a **poor literature reported for action of  $\text{MoO}_4^{2-}$  as a water soluble inhibitor**. The novelty of this work consists in considering of  $\text{MoO}_4^{2-}$  as a water soluble inhibitor in alkaline solutions and in the identification of the species in the dynamically formed film which could be responsible for the inhibiting action.

The inhibiting effect of  $\text{MoO}_4^{2-}$  anions on galvanized steel was associated with the formation of Mo-rich protective films due to the reduction of Mo(VI) to lower oxidation states. In strong alkaline electrolyte (pH 13) no Mo-rich film was formed, correlated with low oxidizing capacity of Mo(VI) at this pH, and hence, no inhibiting effect was observed.

In neutral and slightly alkaline solutions (pH of 6-10) under both homogeneous electrolyte flow (achieved by the use of the mask) and heterogeneous electrolyte flow at alkaline pH, Mo(V)-rich films were formed within 2 s of the contact with Zn. The inhibition efficiency associated with the films was higher than 92 %. Inhomogeneities of the flow conditions in the experiments without the mask resulted in the decrease of the inhibiting efficiency from 95 % to 50 % after about 500 s of the exposure. The composition of Mo-rich protective film revealed the formation of local regions with the Mo(IV)-rich films on the border of the cell and Mo(V)-rich regions in the center of the cell. The local formation of the Mo(IV)-rich films was explained by the local pH decrease due to  $\text{Zn}^{2+}$  stagnation and its hydrolysis, and depletion of  $\text{O}_2$  due to slowed renewal (Fig. 9.4). This hypothesis correlated with the high Mo(IV) fraction in the films formed in acid solutions and their low inhibiting efficiency. The stagnation of  $\text{Zn}^{2+}$  was confirmed by the numerical simulation of the flow cell (Chapter A) . **Comparison of the films formed in different conditions and associated with their inhibition efficiencies suggested that Mo(V) is the most important component of the protective film.**

In addition to the highest (between the selected inhibitors) inhibiting effect of  $\text{MoO}_4^{2-}$

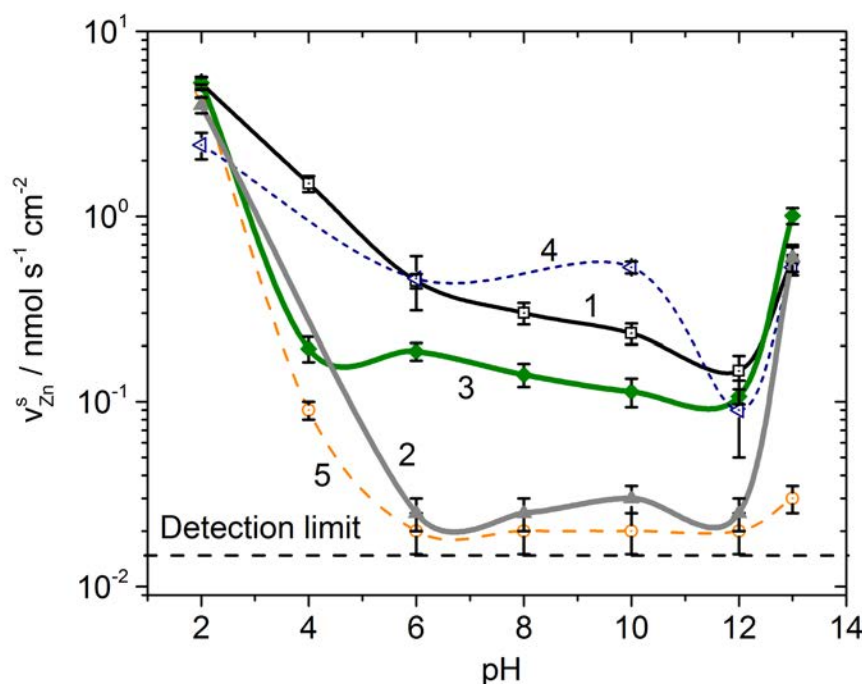


Figure 9.5: Steady state Zn dissolution rates ( $v_{Zn}^s$ ) as a function of pH in 0.5 M NaCl in (1) inhibitor free solution, (2)  $10^{-2}$  M  $\text{Na}_2\text{MoO}_4$  in homogeneous flow and (3)  $10^{-3}$  M L-cysteine, (4)  $10^{-2}$  M L-phenylalanine and (5)  $10^{-2}$  M  $\text{K}_2\text{CrO}_4$  in heterogeneous flow.

on Zn dissolution from galvanized steel (Fig. 9.5), it showed the highest inhibiting performance on low carbon steel (see Fig. 3.1 in Appendix C). Therefore,  $\text{MoO}_4^{2-}$  inhibitor was chosen for the further intercalation into LDH host systems and consideration of its action in smart coatings.

### Mechanisms of $\text{MoO}_4^{2-}$ release from $\text{Zn}_2\text{Al}/\text{-LDH}$ (process 2 in Fig. 9.1)

The delamination and degradation of the final coated system (Fig. 9.1) is controlled by both, the inhibitor action (processes  $1_{a-c}$  in Fig. 9.1) on galvanized steel and the inhibitor release from the LDH hybrid coating (process 2 in Fig. 9.1).  $\text{MoO}_4^{2-}$  as water soluble inhibitor immediately affected Zn dissolution. Therefore, only the release of the inhibitor from LDHs should determine the anticorrosion effect of the coating.

In the present work the mechanism of  $\text{MoO}_4^{2-}$  release from  $\text{Zn}_2\text{Al}/\text{-MoO}_4^{2-}$  fillers was studied as well as the release kinetics in different environments containing aggressive species typical to corrosive environments and underpaint conditions was measured for the first time.

---

In neutral and slightly alkaline solutions, the presence of only  $\text{Cl}^-$  resulted in the incomplete release of  $\text{MoO}_4^{2-}$  anions from  $\text{Zn}_2\text{Al}/\text{-LDH}$  (less than 40 % of the total intercalated molybdate after 24 h of the immersion in 0.5 M NaCl). The addition of 0.1 M  $\text{NaHCO}_3$  in the solutions containing  $\text{Cl}^-$  and  $\text{OH}^-$  resulted in the complete 100 % release after 1 h of the immersion. The in-situ measurement by ATR-IR confirmed the anion exchange mechanism of the replacement of  $\text{MoO}_4^{2-}$  by  $\text{CO}_3^{2-}$ . In strong alkaline media, 100 % release was observed driven by the dissolution of  $\text{Zn}_2\text{Al}/\text{-LDH}$  framework.

The measurements of the release kinetics by ICP-AES demonstrated that the ion exchange with the monovalent anions such as  $\text{Cl}^-$  and  $\text{NO}_3^-$  obeyed parabolic rate law and the exchange of molybdate with divalent anions such as  $\text{CO}_3^{2-}$  and  $\text{SO}_4^{2-}$  obeyed first order rate law. **Using the kinetic models developed for leaching processes in drug applications, we attributed the rate determining step of the anion exchange as a function of the charge of the exchanged anion. It was the Fick's diffusion of the exchangeable anions between LDH plates for monovalent anions and adsorption on the edges of LDH plates for divalent anions.**

### **Active inhibition of LDH/ $\text{MoO}_4^{2-}$ hybrid coatings in the presence of carbonates (process 3 in Fig. 9.1)**

Fully coated system (low carbon steel/galvanization layer/primer with LDH- $\text{MoO}_4^{2-}$  fillers/topcoat) was tested in immersion tests with and without the additions of carbonates in the solution since the presence of carbonates controlled the release of  $\text{MoO}_4^{2-}$  from  $\text{Zn}_2\text{Al}/\text{-LDH}$  host systems. The high impact of carbonates on the release of intercalated ions was numerously reported [129, 131, 132, 134–136, 254, 261] however, no literature can be found on the role of carbonates in the active corrosion protection of LDH hybrid coatings. **New methodology was proposed and used to study the full system which consisted in the simultaneous measurement of the inhibitor release and Zn dissolved by ICP-AES analysis of the solution and the monitoring of the coating degradation by EIS.**

The results showed that the inhibition of the Zn dissolution and the reduced coating degradation were associated with the release of  $\text{MoO}_4^{2-}$  from  $\text{Zn}_2\text{Al}/\text{-MoO}_4^{2-}$  hybrid coatings (processes 1 in Fig. 9.1), which in turn is directly related to the nature of the anions in the corrosive media as predicted from the leaching tests made for LDH/ $\text{MoO}_4^{2-}$  powder (process 2 in Fig. 9.1). In 0.5 M NaCl solution under air the 24 hours of  $\text{MoO}_4^{2-}$  delay was observed explained by a lower affinity of  $\text{Cl}^-$  to  $\text{Zn}_2\text{Al}/\text{-LDH}$  than  $\text{MoO}_4^{2-}$ . In contrast, the presence of 0.1 M  $\text{NaHCO}_3$  in 0.5 M NaCl resulted in an immediate release of  $\text{MoO}_4^{2-}$  (Fig. 9.6) providing a potential tool for controlling an inhibition performance of LDH hybrid coatings.

### **Perspectives**

Although this work has clarified some aspects of the mechanisms of the release and the active inhibition of galvanized steel by LDH hybrid coatings and the role of carbonates there are still many open questions.

First of all, from the mechanistic point of view the origin of the inhibiting effect of

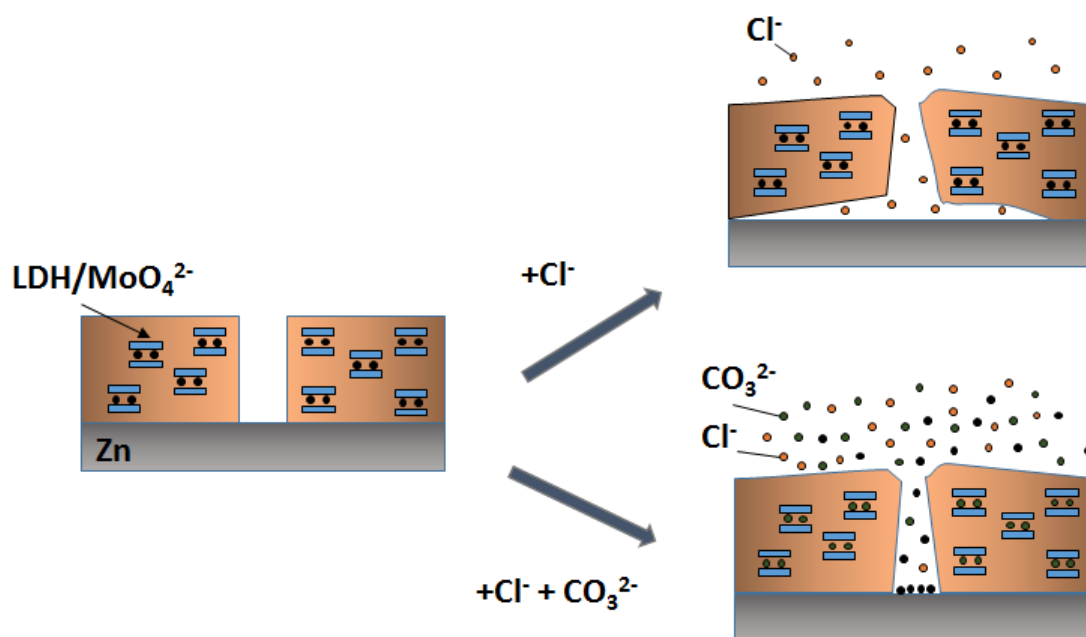


Figure 9.6: Schematic representation of the action of LDH/Mo hybrid coating on Zn in Cl<sup>-</sup> and Cl<sup>-</sup> + HCO<sub>3</sub><sup>-</sup> medias: the loss of the adhesion of the coating in Cl<sup>-</sup> due to Zn corrosion and the inhibition of the Zn corrosion in Cl<sup>-</sup> + HCO<sub>3</sub><sup>-</sup> due to the release of MoO<sub>4</sub><sup>2-</sup> water soluble inhibitor.

L-cysteine in alkaline solutions and at long immersion times remains still unsolved. The results of the Raman spectroscopy demonstrated that L-cysteine enhanced the formation of defective Zn<sub>1+x</sub>O oxide, which in the literature is considered to be formed by the partial reduction of Zn(II) trapped inside the oxide layer [218]. These results could be interpreted as an indicator of a parallel oxydo-reduction reactions in which Zn(II) is reduced under the precipitated corrosion products in couple with the oxidation of L-cysteine to L-cystine. This hypothesis merits a further verification.

For the action of the selected inhibitor, more profound study of the effect on the underlying steel needs to be conducted with a separate investigation of the galvanic coupling between low carbon steel and zinc. On the cut-edge, anodically dissolved Zn<sup>2+</sup> ions form protective films on the steel surface inhibiting the cathodic reaction [29, 278–280]. From our work, MoO<sub>4</sub><sup>2-</sup> in contact with Zn formed Mo(V), Mo(IV)-protective films, which can interfere the self-healing properties of Zn(II) corrosion products on steel. This hypothesis needs to be verified and deeper understood. Some works showed that the profound inhibition of the corrosion of galvanized layer by carbonates may result in the activation of underlying steel with the loss of its cathodic protection [31, 97, 281]. The latter phenomena needs to be verified for the studied system in the presence of MoO<sub>4</sub><sup>2-</sup>.

Concerning the leaching kinetics, the effect of various factors controlling the release

---

of the inhibitor from LDH coated system needs to be understood. The investigation of leaching from  $Zn_2Al$ - $MoO_4^{2-}$  LDHs have shown a strong influence of pH and divalent ions such as  $SO_4^{2-}$  and  $CO_3^{2-}$  on the release kinetics but only the effect of  $CO_3^{2-}$  was verified. Other parameters are also important for the consideration of the exploitation of LDH hybrid coatings: pH can be used as the universal trigger associated with the corrosion propagation [87,127,128,262] and  $SO_4^{2-}$  anions are always present in a corrosive environment under atmospheric exposure [151]. The influence of these parameters on performance of LDH coated systems deserves a separate investigation.

The kinetics of the inhibitor release from the LDH framework directly correlated with the nature of exchanged ions but the resulting kinetics of the inhibitor release from the coating systems along with its influence on the local mechanisms of delamination process are still poorly documented. Such an investigation would require the application of local techniques for the monitoring of the delamination front. The following two techniques could give a deeper insight of the overall process: Scanning Kelvin Probe studies [9,227,282,283] or/and scanning vibrating electrode technique [11,29,284] for the measurement of the local activity of anodic and cathodic zones in the coatings cracks both as a function of the environment composition. They can be completed by the local measurements of pH,  $MoO_4^{2-}$  or other inhibitor,  $Na^+$ ,  $Cl^-$  etc. distribution into the cut edge by ion selective electrodes [285,286] and of spatial resistivity of the delaminated zone [287]. This study should provide a comprehensive picture of the action of LDH hybrid anticorrosion coatings allowing to propose a future mathematical model for the system.



---

# On the time resolution of AESEC method

---

The time resolution of the atomic emission spectroelectrochemical (AESEC) flow cell has been investigated by numerical simulations. The results demonstrate that the resolution of the AESEC electrochemical flow cell may be simulated numerically based on the consideration of electrolyte flow patterns and ion transport in the cell. The time constant distribution closely approximates a log-normal distribution for both experiment and simulation. Time resolution may be improved by increasing the flow rate, however this also leads to marked heterogeneities in the flow rate vectors near the surface. The problem may be avoided somewhat by using a mask to cover all the surface except for a small portion near the center of the flow cell.<sup>1</sup>

## Introduction

Corrosion, dissolution and passivation occur spontaneously on the surface of metals in the presence of aggressive electrolytes. In order to accurately predict the evolution of these systems it is necessary to have real-time kinetic data so that the rate laws of the different reactions may be identified. Atomic emission spectroelectrochemistry (AESEC) is an analytical technique that allows monitoring the reaction of a material with an aggressive electrolyte in real-time. References [94, 160, 161, 288, 289] describe the instrumentation and the typical applications of this technique. Similar systems have been proposed using with a flow electrochemical cell mainly coupled with inductively coupled plasma mass spectrometry [?, 162–165, 290]

Briefly, an inductively coupled plasma atomic emission spectrometry (ICP-AES) is used to continuously monitor the concentration of dissolved elements downstream from an electrochemical flow cell (Fig. 1.1). At steady state flow conditions, the instantaneous concentration in the cell ( $C_M(t)$ ) and the instantaneous dissolution rate ( $v_M(t)$ ) are

---

<sup>1</sup>V. Shkirskiy, P. Maciel, J. Deconinck, K. Ogle, "On time resolution of the atomic emission spectroelectrochemistry method", submitted to Journal of The Electrochemical Society. **All simulations in this chapter were performed by P. Maciel and J. Deconinck.**

directly related to each other as follows:

$$v_M(t) = f_e C_M(t) \quad (\text{A.1})$$

where  $f_e$  is the flow rate through the cell. However, after dissolved ions are formed at the metal/electrolyte interface, they must diffuse into the electrolyte with mixing in the cell, and then pumped out of the electrochemical flow cell, carried along capillaries to the nebulizer – aspiration system of the ICP-AES. The mixing results in a significant broadening of the concentration transients,  $C_M(t)$ , with respect to the instantaneous dissolution rate transient at the working electrode surface, leading to a convolution integral relationship between  $v_M(t)$  and  $f_e C_M(t)$ :

$$f_e C_M(t) = \int_0^t v_M(i) h(t-i) di \quad (\text{A.2})$$

where  $h(t)$  is the time constant distribution or transfer function of the electrochemical flow cell. Herein,  $h(t)$  is defined as the response of the system, i.e. the flow of the substance from output of the flow cell, for 1 s uniform mass pulse of the dissolved species from the working electrode. Experimental measurement of  $h(t)$  can be closely approximated by a simplified version of the log-normal function in which the pre-exponential factor is constant [160]:

$$h(t) = \begin{cases} \sqrt{\frac{\beta}{\pi\tau^2}} \cdot e^{-\frac{1}{4\beta}} \cdot e^{-\beta \ln^2 \frac{t}{\tau}} & \text{if } t > 0 \\ 0 & \text{if } t = 0 \end{cases} \quad (\text{A.3})$$

where  $\tau$  is located at the peak maximum. The simplified version of the log-normal function is used only for the convenience of the approximation of the experimental data.

It is obvious that the choice of flow rate plays an important role in AESEC analysis. Considering  $f_e$  as a purely instrumental parameter, the sensitivity of the technique is inversely proportional to  $f_e$  by Eq A.1, and in addition, the nebulization – aspiration system is more efficient at lower flow rates. Nevertheless, high flow rates may be preferred to improve the time resolution of the experiment and to avoid the build-up of high concentrations of dissolved species which might alter the reaction rate. Finally, the flow rate will also play a role in the reaction rate and mechanisms especially if certain electrode processes are diffusion limited.

With this in mind, we would like to optimize the flow rate to obtain the most uniform flow pattern while increasing the time resolution. In this work a numerical simulation of the flow patterns in the cell have been determined. The approach was to calculate the time constant distribution and compare it with the experimental measurements.

## Numerical model

For the simulation of the electrochemical process in the flow cell (Fig. 1.1), we propose an approach that combines numerical models for the electrolyte flow and ion transport. To describe the flow in the cell, the mass and momentum conservation of the

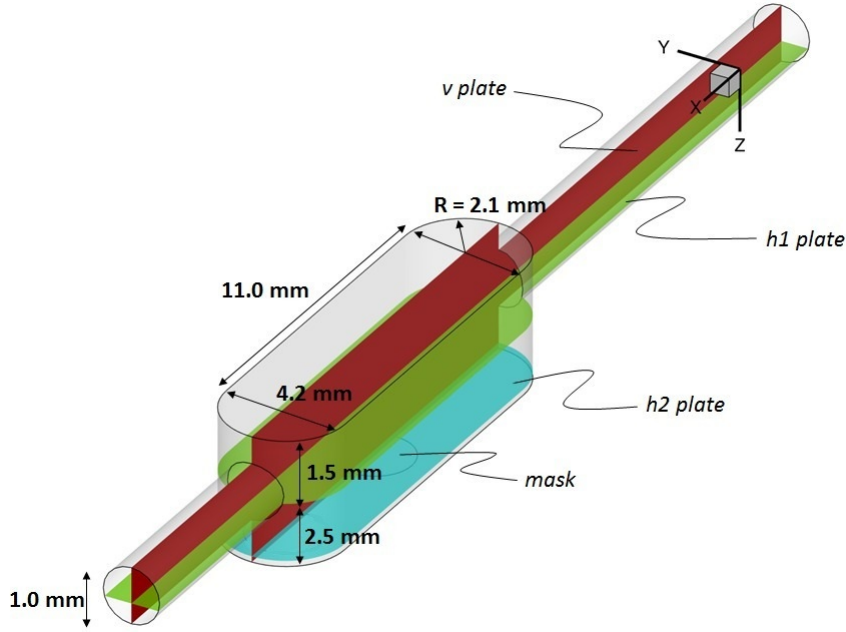


Figure 1.1: The scheme of the flow electrochemical cell. A working electrode (WE) is placed on the bottom of the cell with or without a mask. The mask leaves uncovered a circle with 1.3 mm radius in the center of the WE.  $v$  and  $h1$  plates cross the cell trough the center of the feed capillary in vertical and horizontal dimensions correspondingly.  $h2$  plate lies 0.2 mm above the WE.

electrolyte flow is modelled by the incompressible Navier-Stokes equations, solving for the fluid velocity  $\mathbf{u}$  and the pressure  $p$ :

$$\nabla \mathbf{u} = 0 \quad (\text{A.4})$$

$$\frac{\partial \mathbf{u}}{\partial t} + (\mathbf{u} \cdot \nabla) \mathbf{u} + \frac{1}{\rho} \nabla p - \nu \nabla^2 \mathbf{u} = 0 \quad (\text{A.5})$$

where  $\rho$  is the electrolyte density and  $\nu$  is the kinematic viscosity. The Reynolds number ( $Re$ ) of the system defined as

$$Re = \frac{\mathbf{u}L}{\nu} \quad (\text{A.6})$$

where  $L$  the traveled length of the fluid, is less than 1 indicating the laminar flow defined by the small cell geometry (Fig. 1.1) and the small (less than  $5 \text{ ml min}^{-1}$ ) the rate of electrolyte flow.

Assuming the anodic pulse and the time evolution of the concentration of species in the flow does not influence the flow in the cell, the Eq. A.4 and A.5 are decoupled from the species transport equations, and solved stationary. The density and viscosity of the electrolyte were assumed constant  $\rho = 10 \text{ kg m}^{-3}$  and  $\nu = 10^{-6} \text{ m}^2 \text{ s}$  characteristic for water as a main electrolyte component.

For the solution of the species concentration in the electrolyte, based on the MITReM model [291,292] we can state a balance equation for each species in the system:

$$\frac{\partial C_i}{\partial t} = -\nabla \cdot \mathbf{J}_i + \sum_{r=1}^R s_{ir} v_r \quad (\text{A.7})$$

where  $C_i$  is the concentration of species  $i$ . The source term on the right hand side of Eq. A.7 comes from the homogeneous reactions, where  $v_r$  is the rate of reaction  $r$  and  $s_{ir}$  is the stoichiometric coefficient of species  $i$  in this reaction. The flux  $\mathbf{N}_i$  is given by convection, diffusion and migration as follows:

$$\mathbf{J}_i = -C_i \mathbf{u} + D_i \nabla C_i + \frac{z_i F D_i}{RT} C_i \nabla E \quad (\text{A.8})$$

where  $D_i$  is the diffusion coefficient,  $z_i$  is the charge,  $F$  is the Faraday's constant,  $R$  is the universal gas constant,  $T$  is the temperature and  $E$  is the potential. The flux perpendicular to an electrode is given by the heterogeneous reactions:

$$\mathbf{J}_i \cdot \mathbf{1}_n = \sum_{y=1}^Y s_{iy} v_y \quad (\text{A.9})$$

In order to obtain the transfer function of the cell, a 1 s pulse of a single species was simulated perpendicular to the surface of the electrode. By injecting a mass pulse instead of applying a current pulse we avoid considering migration in Eq. A.8. This pulse is integrated in time (time-accurate simulation) and over the surface of the electrode to obtain the total amount of the substance injected into the electrolyte. This species then follows diffusion (close to the electrode) and convection in the electrolyte carrying it out of the cell. For the diffusivity of the medium,  $D_i$  is assigned to  $10^{-9} \text{ m}^2 \text{ s}^{-1}$  [291,292].

Two geometries of the working electrode were used: (i) when the whole surface is active and (ii) when a mask covers all the surface except for a circle with 1.3 mm radius in center of the surface (Fig. 1.1). The simulated area includes the flow cell, its input and output channels. The species injection pulse occurred at 1 s - 2 s ( $\Delta t = 1\text{s}$ ) with the computing time of 300 s. The simulated flow rates were 1.00, 1.25, 1.50, ..., 5.00 ml  $\text{min}^{-1}$  with the amount of substance injected to the cell of  $10^{-8}$  or/and  $10^{-7}$  mole for the experiment without the mask. For the experiments with the mask, the flow rate was 3 ml  $\text{min}^{-1}$  with the mass pulse of  $10^{-7}$  mole.

## Experimental

### Materials

Spectropure<sup>TM</sup> copper (Johnson Mathhey, 99.9995%) was used as a working electrode. Prior to each experiment the surface of sample was manually grounded with 4000 grid SiC paper then rinsed with ethanol (analytical grade, VWR Prolabo) and purified water. The experiments were performed in deaerated 1 M HCl (analytical grade, VWR Prolabo) solutions in purified water (Millipore<sup>TM</sup> system,  $18 \Omega \text{ cm}^2$ ). A flow of nitrogen was used to deaerate the solutions. The deaeration started 1 hour prior to each experiment and was continued until the end of the experiment.

---

## AESEC parameters

The emission intensity for Cu was monitored at 324.754 nm. The detection limit defined as two times standard deviation of the blank solution was  $2.7 \pm 0.2 \mu\text{g/L}$  under conditions of the experiments.

The exposure of Cu electrode was made in two geometries: (i) the whole  $0.51 \pm 0.01 \text{ cm}^2$  surface limited by O-ring was exposed to the electrolyte and (ii) only central part of the surface was exposed to the electrolyte (Fig. 1.1). In case (ii) a mask consisted of an insulating and impermeable electroplating tape (1 mm thick, 3M 470 Gamry Instruments) that covered the periphery of the cell but leaved uncovered a circle with  $1.3 \pm 0.1 \text{ mm}$  radius (or  $0.053 \pm 0.005 \text{ cm}^2$ ) of Cu electrode. The areas of the surfaces in both cases were measured from the reactive zone of Cu electrode by optical microscope appeared after anodic pulses.

The flow rate of the electrolyte was  $1.1 \pm 0.1 \text{ ml min}^{-1}$ ,  $3.1 \pm 0.1 \text{ ml min}^{-1}$  and  $5.0 \pm 0.1 \text{ ml min}^{-1}$ .

The transfer function for different flow rate of the electrolyte was measured by applying 1 s galvanostatic pulses of 1 and 10 mA (equivalent to  $10^{-8}$  and  $10^{-7}$  mol for Cu oxidation to  $\text{Cu}^+$ ) to Cu electrode in the experiment without the mask. 1 s pulse of 10 mA at  $3.1 \text{ ml min}^{-1}$  was used for the experiment with the mask. The experimental profiles of concentration evolution were fitted to an empirical function in the form of a log-normal distribution. The time offset due to transport through the capillaries has been removed for all data. Therefore, the onset of the galvanostatic pulse is fixed at  $t = 1 \text{ s}$  for each curve.

The application of galvanostatic pulses were performed with a Gamry Reference 600<sup>TM</sup> potentiostat with Ag/AgCl saturated reference electrode and a Pt sheet counter electrode. The analog potential and current signals were routed into the measuring circuit of the ICP-AES to guarantee the same time scale for the measurements of Cu current, potential and total current. Data acquisition of all signals from ICP-AES equaled to 1 point per second.

## Results

A schematic diagram of the electrochemical flow cell used for the numerical simulation is given in Fig. 1.1. This model is identical to the experimental flow cell in every respect except that the O-ring at the edge of the sample compartment is not taken into account. The working electrode (WE) is placed at the bottom of the cell with or without the mask. For the purpose of the numerical simulation, several different planes are defined in Fig. 1.1. The  $v$  and  $h1$  planes cross the cell trough the center of the feed capillary in the vertical and horizontal dimensions respectively. The  $h2$  plane lies 0.2 mm above the WE.

A series of numerical simulations of the velocity distributions in the cell was performed at various flow rates as shown in Fig. 1.2. The “steady – state” velocity vector distributions ( $u$ ) in the  $h1$  and the  $v$  plane are shown to the left and right respectively.

It is noted that a markedly increased flow rate is observed near the entrance to the cell which ultimately leads to the formation of a vortex at higher flow rates.

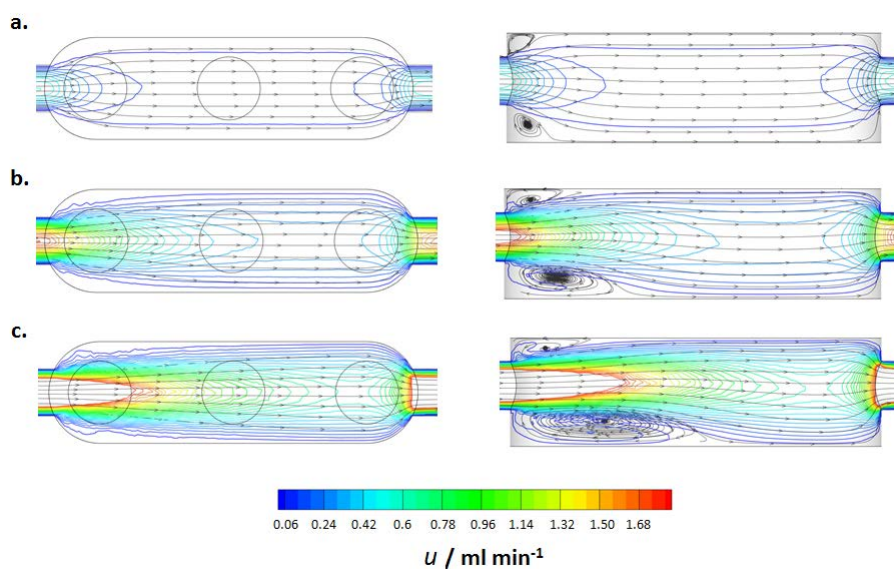


Figure 1.2: The “steady – state” velocity vector distribution ( $u$ ) into the cell in  $h1$  (on the left) and  $v$  (on the right) cross sections. a, b and c correspond to the 1, 3 and 5  $\text{ml min}^{-1}$  flow rates into the feed capillary ( $f_e$ ). The circulation of the flow near the entrance of the cell is observed.

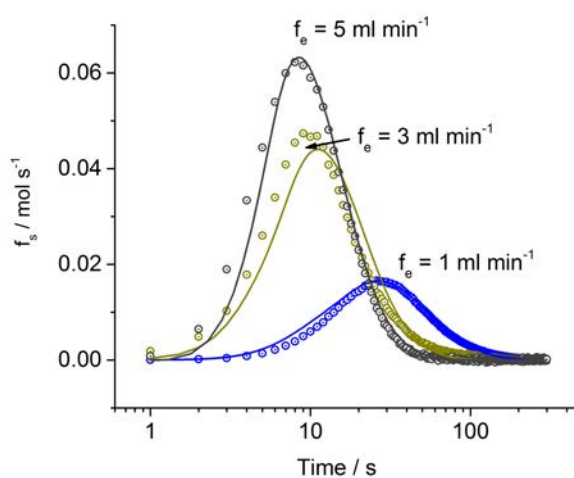


Figure 1.3: The experimental (in circles) and simulated (solid lines) flows of substance ( $f_s$ ) for 1 s mole mass of  $10^{-8}$  and  $10^{-7}$  mole pulses for 1, 3 and 5  $\text{ml min}^{-1}$  flow rate into the feed capillary ( $f_e$ ). The areas of the curves are normalized and the mean of two curves for each flow rate is presented on the slides.

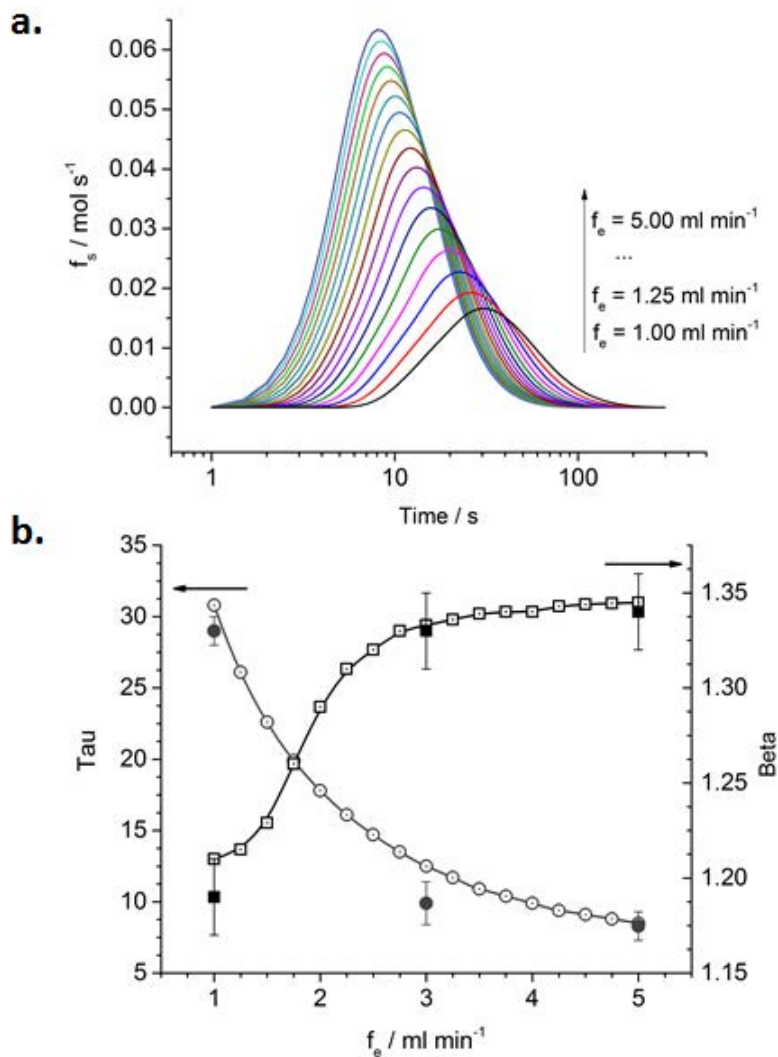


Figure 1.4: (a) shows the simulated flow of substance ( $f_s$ ) for 1 s mole mass of  $10^{-7}$  mole pulses for 1.00, 1.25, 1.50, ..., 5.00  $\text{ml min}^{-1}$  flow rate into the feed capillary ( $f_e$ ). The areas of the curves are normalized. (b) shows the  $\tau$  and  $\beta$  parameters of each curve in (a) as a function of  $f_e$ . Filled points show the experimental data obtained under conditions.

The transfer function (or residence time distribution) of the flow cell was measured by the copper pulse dissolution experiment and compared with the simulated response to a pulse release from the working electrode (Fig. 1.3). The numerical simulation assumed the pulse to be perfectly distributed over the active surface area at  $t=1$  s.

It is clear from Fig. 1.3 that the experimental results are in reasonably good agreement with the numerical simulation supporting the assumption that the mass transfer in the flow cell actually controls the residence time distribution. Fig. 1.4a shows the

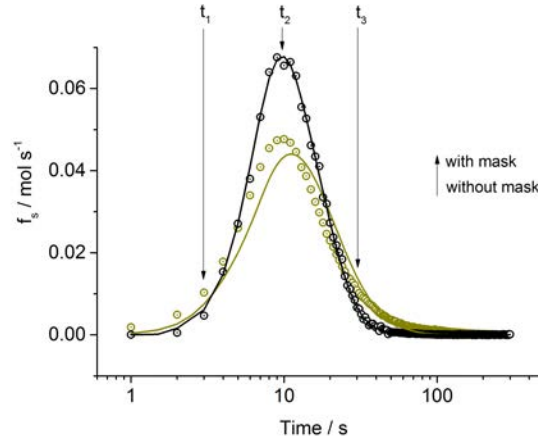


Figure 1.5: The experimental (in circles) and simulated (solid lines) flows of substance ( $f_s$ ) for 1 s mole mass pulses of  $10^{-7}$  mole at  $3 \text{ ml min}^{-1}$  flow rate into the feed capillary ( $f_e$ ) with the experiment with and without the mask.

simulated transfer function in a wide range of flow rates in the feed capillary ( $f_e$ ). Each curve in Fig. 1.3 and Fig. 1.4a was fitted to the log-normal distribution (Eq. A.3). The results are shown in Fig. 1.4b. It is clear that the increase of  $f_e$  from  $f_e = 1 \text{ ml min}^{-1}$  to  $f_e = 3 \text{ ml min}^{-1}$  results in the dramatic decrease of the position of the peak maximum (i.e.  $\tau$ ) and the half-width, which is inversely proportional to  $\beta$ . Further increase of  $f_e$  up to  $5 \text{ ml min}^{-1}$  slows the tendency of  $\tau$  and  $\beta$  change.

An attempt was made to limit the active surface area to a small surface in the center of the flow cell. The idea was to improve the overall time resolution of the flow cell system as well as the uniformity of the surface/electrolyte contact in term of the distribution of the velocity vectors. The results for the time constant distribution with and without the mask are shown in Fig. 1.5 with the fitting parameters for each curve in Table 1.1 for  $f_e = 3 \text{ ml min}^{-1}$ . The presence of the mask does not change the position of the peak maximum but reduces the half-width of the transfer function that can improve the resolution of the experimental data.

It is of interest to observe what is the concentration distribution at the active surface

Table 1.1: The parameters of  $\tau$  and  $\beta$  of log-normal transfer function shown in Fig. 1.5 for  $3 \text{ ml min}^{-1}$  flow rate in the feed capillary. Standart error of fitting for each data set was less than 0.1 for  $\tau$  and 0.01 for  $\beta$ .

	$\tau$		$\beta$	
	experimental	numerical	experimental	numerical
without the mask	9.9	12.5	1.21	1.33
with the mask	9.5	9.9	1.82	1.82

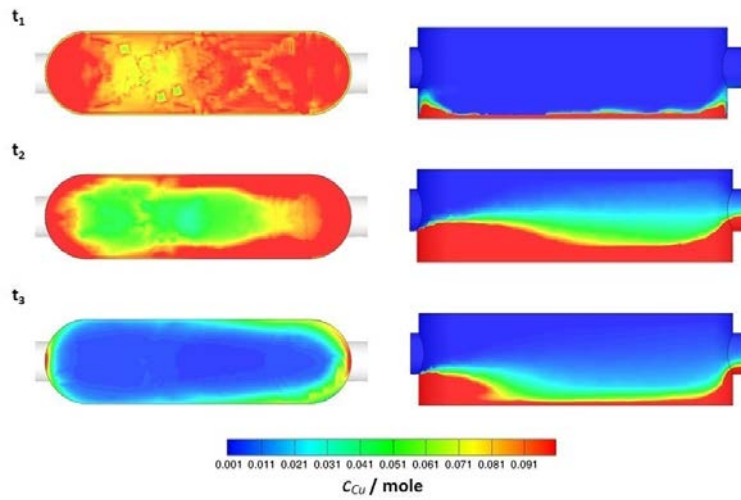


Figure 1.6: The substance distribution ( $C_{Cu}$ ) in mole in  $h2$  (on the left) and  $v$  (on the right) cross sections for  $3 \text{ mil min}^{-1}$  flow rate into the feed capillary without the mask for  $t_1$ ,  $t_2$  and  $t_3$  (3, 10 and 30 s) times after  $10^{-7}$  mole mass pulse.

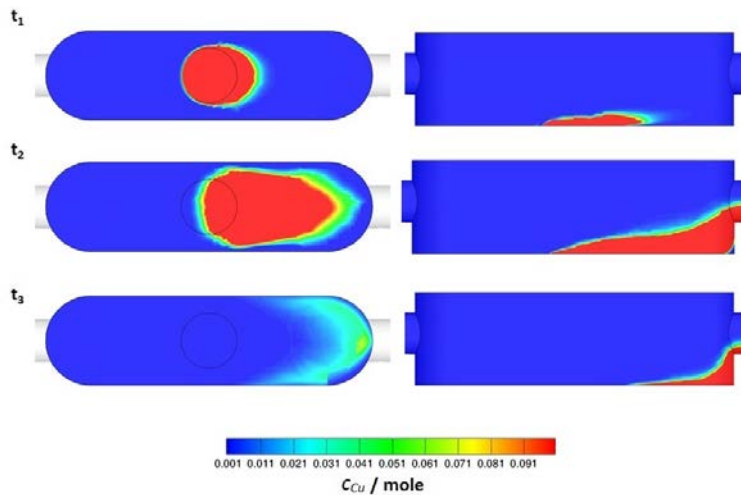


Figure 1.7: The substance distribution ( $C_{Cu}$ ) in mole in  $h2$  (on the left) and  $v$  (on the right) cross sections for  $3 \text{ mil min}^{-1}$  flow rate into the feed capillary with the mask for  $t_1$ ,  $t_2$  and  $t_3$  (3, 10 and 30 s) times after  $10^{-7}$  mole mass pulse.

for the different times:  $t_1$ ,  $t_2$  and  $t_3$  (3, 10 and 30 s), before, at, and after the maximum in Fig. 1.5 as indicated. This is shown in Fig. 1.6 without the mask and in Fig. 1.7 with the mask. **Marked heterogeneities are observed on the periphery of the flow cell without the mask indicated by the stagnation of the substance near the input of the flow cell.** The problem with the stagnation of the substance in

the confined zones of the cell was revolved using the mask.

## Discussion

It is obvious that the increase of the flow in the feed capillary ( $f_e$ ) increases the time resolution of the experiment decreasing the time required to wash out the species from the flow cell. However, it increases the heterogeneity in the velocity vector distribution visible by the propagation of the vortex like behavior of the flow the input of the flow cell (Fig. 1.2). From the tested flow rates of 1, 3 and 5 ml min<sup>-1</sup>, 3 ml min<sup>-1</sup> was chosen as the optimal  $f_e$  balanced between the essential requirements of the time resolution and homogeneity of the flow. **Therefore,  $f_e = 3 \text{ ml min}^{-1}$  was used in all AESEC experiments.**

The use of the mask additionally improves both the homogeneity of the flow and the time resolution, however it may significantly reduce the sensitivity of the currents of metal dissolution ( $j_M$ ) due to lower surface area of the anode. The reduction of anode area from 0.51 cm<sup>2</sup> without the mask to 0.053 cm<sup>2</sup> would reduce the sensitivity by a factor of 9.6 that can be critical for low currents, specially in the case of inhibiting systems. Therefore, further in the work, while screening MoO<sub>4</sub><sup>2-</sup> and L-cysteine water soluble inhibitors, experiments will be performed without the mask and only if the significant impact of the flow heterogeneities on electrochemical behavior of studied systems is suspected, the mask will be used.

## Conclusions

The results demonstrate conclusively that the time resolution of the AESEC electrochemical flow cell may be simulated numerically based on the consideration of the electrolyte flow patterns and ion transport in the cell. The time constant distribution closely approximates a log-normal distribution for both the experiment and the simulation. Time resolution may be improved by increasing the flow rate, however this also leads to marked heterogeneities in the flow rate vectors near the surface. **The heterogeneities in the flow rate inside the cell can result in differences in the mass transport of species between the center and the periphery of the cell. This can result in strong composition (pH, Cl<sup>-</sup>, O<sub>2</sub>, metal cation concentrations etc) gradient between these two zones. The impact of the flow inhomogeneities on the surface reactivity is verified in Chapter 7.** Based on both the experiment and the simulation, the optimal flow rate was defined as 3 ml min<sup>-1</sup>. The problem with flow heterogeneity may be avoided by using a mask to cover all the surface except for a small portion near the center of the flow cell, however it would reduce the detection limits of defined currents by a factor of 9.6. **In the work, the mask was be used only if the significant impact of heterogeneities on the studied systems was suspected.**

## Action of L-phenylalanine on galvanized steel

Action of  $10^{-2}$  M L-phenylalanine on galvanized steel in 0.5 M solutions was verified in the pH range of 2 - 13 (Fig. 2.1). The methodology of screening was similar as for L-cysteine (Chapter 6) and  $\text{MoO}_4^{2-}$  (Chapter 7) and consisted in the measurement of Zn spontaneous dissolution by AESEC at open circuit.

Inspection of Fig. 2.1 shows that L-phenylalanine acts as an inhibitor at pH 2 and pH 12, as an accelerator at pH 10 and no influence on Zn dissolution was observed at

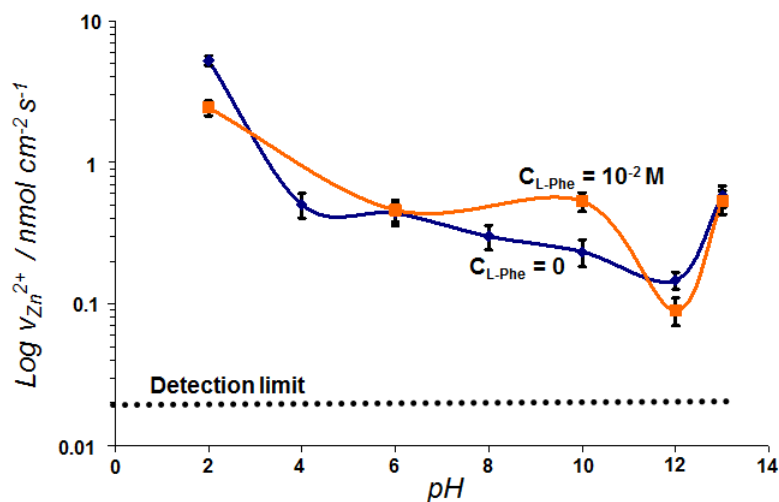


Figure 2.1: Zn spontaneous dissolution in 0.5 M NaCl with and without  $10^{-2}$  M L-phenylalanine as a function of pH. The mean value of two measurements with its deviation are shown for each point.

pH 6 and 13. The mechanism of L-phenylalanine action was not studied in details due to its poor performance as the corrosion inhibitor.

---

## Comparison the actions of L-cysteine, L-phenylalanine, $\text{CrO}_4^{2-}$ and $\text{MoO}_4^{2-}$ water soluble inhibitors on low carbon CRS

---

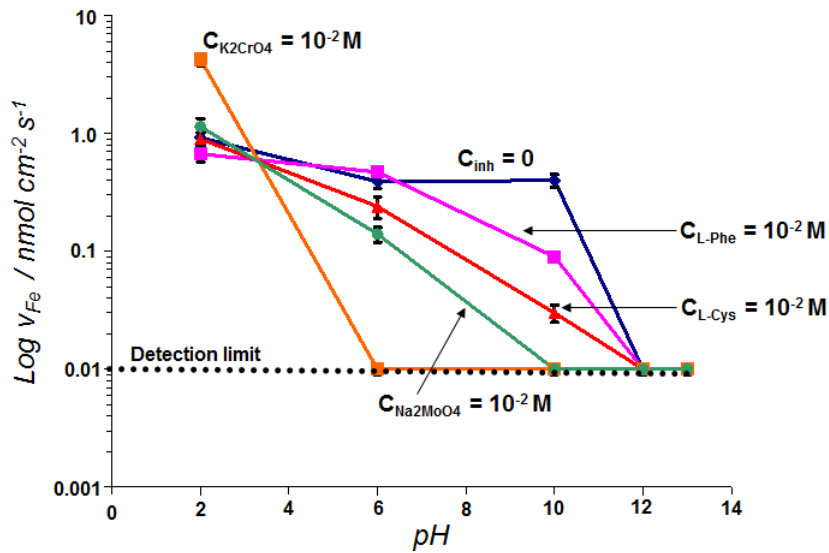


Figure 3.1: Fe spontaneous dissolution in 0.5 M NaCl with and without  $10^{-2}$  M of L-phenylalanine, L-cysteine,  $\text{CrO}_4^{2-}$  and  $\text{MoO}_4^{2-}$  as a function of pH. The mean value of two measurements with its deviation are shown for each point.

C. COMPARISON THE ACTIONS OF L-CYSTEINE, L-PHENYLALANINE,  $\text{CrO}_4^{2-}$  AND  $\text{MoO}_4^{2-}$  WATER SOLUBLE INHIBITORS ON LOW CARBON CRS

---

Action of potential inhibitors on galvanized steel (L-cysteine, L-phenylalanine,  $\text{CrO}_4^{2-}$  and  $\text{MoO}_4^{2-}$ ) was verified on low carbon steel in order to choose the best inhibitor for both systems and exclude species, which could inhibit Zn dissolution and accelerate Fe dissolution. The methodology of screening was similar as for L-cysteine (Chapter 6) and  $\text{MoO}_4^{2-}$  (Chapter 7) screening on galvanized steel and consisted in the measurement of Fe spontaneous dissolution by AESEC at open circuit.

Fig. 3.1 shows that all tested species showed the inhibiting action on Fe in pH range of 6 - 13 with an exception of L-phenilalanine at pH 6.  $10^{-2}$  M  $\text{CrO}_4^{2-}$  accelerates Fe dissolution at pH 2. From the all tested inhibitors and  $\text{CrO}_4^{2-}$  as the reference inhibitor,  $\text{MoO}_4^{2-}$  showed the best performance on low carbon steel and galvanized steel and hence, was chosen for the intercalation into  $\text{Zn}_2\text{Al}/\text{-LDH}$  samples and incorporation into LDH hybrid coating on galvanized steel.

## Methodology verification for leaching studies from LDH

---

Separation of LDH/Mo particles from the liquid phase by Nylon membranes and possible adsorption of Zn(II), Al(III) and Mo(VI) species on Teflon beaker were verified for the leaching study from LDH samples (Chapter 8).

### Size evaluation of LDH/Mo particles

A 50 ml of aqueous solutions with preliminary ground 0.1 g of LDH/Mo particles were prepared and filtered 3 times through 0.22  $\mu\text{m}$  Nylon membranes. Then, dynamic light scattering measurements were carried out for as prepared and filtered solutions using a Malvern Zetasizer NanoZS. The recorded values of derived count rate (DCR) were compared to the DCR value of the pure water to estimate the efficiency of the filter.

The value of derived count rate (DCR) for the pure water was equaled to 66 kilocounts per second (kcps). This value was taken as a reference for the solution without any amount of particles. The value of 43250 kcps found for the as prepared solution of LDH/Mo clearly shows the presence of LDH/Mo solid phase. One pass of the prepared solution containing LDH/Mo solid phase through the 0.22  $\mu\text{m}$  Nylon filter decreases the value of DCR to 186 kcps whereas a three-pass decreases DCR to 43 kcps. Thus, three pass of as prepared LDH/Mo solution through the 0.22  $\mu\text{m}$  filter separates the all LDH/Mo particles from the liquid phase. In addition, a size of the particles can be estimated. Since no particles were detected in the solution after a three-pass through 0.22  $\mu\text{m}$  filter, the major fraction of the LDH/Mo phase is more than 0.22  $\mu\text{m}$  in a diameter.

### Adsorption capacity of Zn, Al and Mo ions on Teflon beaker, precipitation of ions

In order to simulate the conditions of the leaching experiment, the 10.6 mM Zn(II) ( $\text{ZnCl}_2$ ), 5.3 mM Al(III) ( $\text{AlCl}_3$ ) and 2.7 mM  $\text{MoO}_4^{2-}$  ( $\text{Na}_2\text{MoO}_4$ ) were added in 0.5 M NaCl containing solutions. These values of ion concentrations correspond to the totally dissolved 0.1 g of LDH/Mo samples. The solution pH was adjusted to the value of

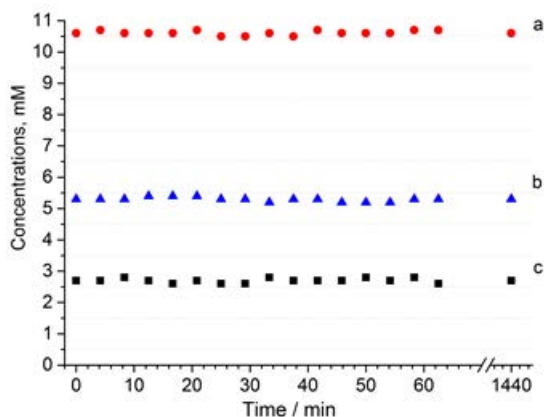


Figure 4.1: Evolution of (a) Zn(II), (b) Al(III) and (c) Mo(VI) concentrations in 0.5 M NaCl solution (50 ml) at pH 6 with the additions of 10.6 mM ZnCl<sub>2</sub>, 5.3 mM AlCl<sub>3</sub> and 2.7 mM Na<sub>2</sub>MoO<sub>4</sub>. The amounts of Zn, Al and Mo ions correspond to the totally dissolved 0.1 g LDH in 50 ml solution.

6 by 0.1 M NaOH solutions. From a continuously stirred solution 2 ml aliquots were sampled after approximately each 250 s during 1 hours and then after 24 hours. The sampled solutions were passed 3 times through the 0.22  $\mu\text{m}$  Nylon filter and then, the concentrations of Zn, Al and Mo were analyzed by ICP-AES. The possible change in the ion concentrations with time would be attributed to an adsorption of the ions on the walls of the beaker and/or to its precipitation in the solution bulk. Afterwards, the Teflon beaker was washed with 50 ml of distilled water and the concentrations of Zn, Al and Mo were analyzed in the washing solution too.

The chosen concentrations of the dissolved Zn, Al and Mo ions did not change during 24 hour in 0.5 M NaCl solution (Fig. 4.1). From the macroscopic observation, no ions precipitation in the solution was observed either. Moreover, the concentrations of Zn, Al and Mo ions in the washing solution after cleaning the Teflon beaker were below the detection limits for corresponding elements, which discards any significant amount of residual ions in the Teflon beaker. The results suggest absence of any effect regarding to neither Mo, Zn and Al ions adsorption on the Teflon beaker nor the precipitation of above-mentioned ions.

# Python code for numerical convolution and deconvolution of AESEC data

---

## Convolution

```
# convolution , Slava Shkirskiy

import math      # import math module

# transfer function

def trF(x):
    b = 1 # choose your parameters
    t = 2

    if x == 0:
        y = 0
    else:
        y = math.sqrt((b/math.pi/t/t))*math.exp(-1.0/4.0/b)
            *math.exp(-b*math.log(x/t)*math.log(x/t))

    return y

# reading a file into the dataX vector

f = open("c_input.txt", "r")

dataX = []
```

```
for line in f:
    dataX.append(line)

f.close()

# converting a data from string to float format

for i in range(len(dataX)):
    dataX[i] = dataX[i].strip('\n')
    dataX[i] = float(dataX[i])

# convolution algorithm

dataY = [0]*len(dataX) # create a vector for an output data

for i in range(len(dataX)):
    for j in range(i+1):
        dataY[i] += dataX[j]*trF(i-j)

# writing to a file

f = open("c_output.txt", "w")

for i in range(len(dataX)):
    f.write(str(dataY[i]) + "\n")

f.close()
```

## Deconvolution

```
# deconvolution, Slava Shkirskiy

import math # import math module

# transfer function

def trF(x):
    b = 1 # choose your parameters
    t = 10

    if x == 0:
        y = 0
    else:
        y = math.sqrt((b/math.pi/t/t))*math.exp(-1.0/4.0/b)
```

---

```

        *math.exp(-b*math.log(x/t)*math.log(x/t))

    return y

# function of Adjacent-Average smoothing of the data

def AAsm(data):

    Np = 20 # points of window, integer value
    N = Np/2
    dataI = [0]*len(data)

    for i in range(len(data)):

        sumN = 0
        Ni = 0

        for j in range(N*2+1):
            if ((i-N+j) >= 0) and ((i-N+j) <= (len(data)-1)):
                sumN += data[i-N+j]
                Ni += 1

        dataI[i] = sumN/Ni

    return dataI

# reading a file into the dataX vector

f = open("d_input.txt", "r")

dataX = []
for line in f:
    dataX.append(line)

f.close()

# converting a data from string to float format

for i in range(len(dataX)):
    dataX[i] = dataX[i].strip('\n')
    dataX[i] = float(dataX[i])

```

E. PYTHON CODE FOR NUMERICAL CONVOLUTION AND DECONVOLUTION OF  
AESEC DATA

---

```
# Adjacent-Averaging smoothing of the input data

dataX = AAsm(dataX)

# deconvolution algorithm

T = 3                                # start from Tth point
                                     # of transfer function since
                                     # the points before T are small
dataY = [0]*(len(dataX)-T) # create a vector for an output data

for i in range(0, (len(dataX)-T)):

    sumD = 0
    for j in range(1, (i+1)):
        sumD += trF(j+T)*dataY[i-j]

    dataY[i] = (dataX[i+T] - sumD)/trF(T)

# Adjacent-Averaging smoothing of the output data

dataY = AAsm(dataY)

# writing to a file

f = open("d_output.txt", "w")

for i in range(len(dataX)-T):
    f.write(str(dataY[i]) + "\n")

f.close()
```

# A novel coupling of EIS with AESEC: application to the open circuit dissolution of Zn

---

A novel coupling between atomic emission spectroelectrochemistry (AESEC) and electrochemical impedance spectrometry (EIS) is demonstrated. In this way, it is possible to distinguish situations in which the oxidation of the metal leads directly to the formation of dissolved ions or passes through a slightly soluble film intermediate. It was found that Zn dissolution in 0.1 M  $\text{NH}_4\text{Cl}$  occurs without any significant solid intermediate as evidenced by the excellent correlation between the AC components of the electrical current and the zinc dissolution rate. Analysis of the dissolution rate and total current transients as a function of potential directly yields the anodic and cathodic Tafel slopes for this system. In contrast, for Zn/0.5 M NaCl, electrochemical oxidation leads directly to the formation of an intermediate corrosion product film with subsequent dissolution.

<sup>1</sup>.

## Introduction

Spectroelectrochemical methods [293–297] are often used to identify the reaction products when electron transfer occurs at the metal/electrolyte interface and to quantify the stoichiometry and kinetics of the reactions. The idea is to correlate a spectroscopic signal due to a particular element or molecule with the electrical current or potential. The correlation between the spectroscopic and the electrochemical signal may be enhanced by applying a small amplitude AC perturbation to either the electrical current or potential and measuring the AC component of the spectroscopic signal using phase sensitive detection. Electrochemically modulated infrared spectroscopy [298] is a well-known technique based on this concept, and potential modulated in situ Raman spectroelec-

---

<sup>1</sup>V. Shkirskiy, K. Ogle, A novel coupling of electrochemical impedance spectroscopy with atomic emission spectroelectrochemistry: Application to the open circuit dissolution of zinc, *Electrochimica Acta*, 168, 2015, p. 167–172

trochemistry [299] has also been developed. These vibrational techniques are used to “tune in” to surface chemical bonds that form and dissipate in resonance with the modulated electrochemical potential. The phase sensitive detection greatly enhances the detection limit of the signal and the amplitude and phase variation of the signal with frequency may be used to extract kinetic information. Gabrielli et al. [300] have proposed a generalized transfer function formalism for the coupling of various techniques to a modulated electrochemical potential. It is of interest to note that this idea is not specific to electrochemistry: for example modulated reactive molecular beam scattering experiments [301,302] have been used to investigate surface catalyzed reactions, the amplitude ratio and phase angle between an incoming reactant beam and the scattered product beam were used to distinguish different reaction mechanisms.

The use of various analytical techniques coupled to electrochemistry is particularly pertinent to the investigation of oxide formation on Zn and Zn alloys. It is well known that the nature of the zinc corrosion products may determine the rate of corrosion of zinc or galvanized steel [140] and therefore the characterization of the insoluble oxidized zinc films is of considerable interest. Electrochemical characterization is highly pertinent as the semiconducting nature of the oxide film ultimately controls the oxygen reduction reaction [36]. The interfacial charge transfer properties may be accessed near the open circuit potential by electrochemical impedance spectroscopy [178, 180, 303]. The EIS approach however does not yield quantitative information concerning the quantity of oxidized zinc products formed at the interface. These films may be quantified by coupling the electrochemical methods to different types of solution analysis and performing a mass balance between oxidation and dissolution. A classic example would be the pioneering work of Hull et al. [304] who used the ring of a ring-disk electrode to measure dissolved Zn(II) species following dissolution at the disk.

More recently, atomic emission spectroelectrochemical (AESEC) technique was applied to quantify dissolved Zn and other alloying elements [40]. More recently Klemm et al. [163] and Laska et al. [37] have used a micro flow cell with downstream UV-visible detection to separate zinc oxidation and dissolution.

The AESEC technique (atomic emission spectroelectrochemistry) [160,161] is a method by which the dissolution rate of complex materials may be resolved into partial elemental dissolution rates. It involves the coupling of an electrochemical flow cell with an inductively coupled plasma atomic emission spectrometry (ICP-AES) which measures the time dependent concentrations of dissolved species downstream from the reaction cell. When all the oxidized elements are soluble, this method gives a complete picture of dissolution and may be used to directly measure the spontaneous corrosion rate of a material during an open circuit exposure, or, during polarization, to resolve the total anodic current into partial elemental currents. Unfortunately AESEC analysis may prove ambiguous if insoluble, and therefore undetectable products are formed. During anodic polarization experiments, when the cathodic current is negligible, this insoluble material may be quantified from a mass balance as it results in the sum of the elemental dissolution rates being less than the total anodic current. For spontaneous reaction systems (open circuit corrosion), the situation is difficult to apprehend as there is no external

---

current by which the elemental dissolution rates may be compared. In this Chapter, a novel approach to overcoming this problem is demonstrated by coupling the electrochemical impedance spectroscopy (EIS) to the AESEC method to directly correlate the dissolution rate and the electrical current. The correlation of AESEC dissolution rates with changes in potential has been used previously but only for large amplitude and long duration potential perturbations. For example, it has been used to detect the effect of potential on oxide film dissolution during the anodization of aluminum [305], the effect of cathodically generated hydroxide on oxide dissolution [92], and to quantify simultaneous oxide formation and dissolution of Zn in alkaline solution [94].

## Experimental

A commercial hot dip galvanized steel (HDG) sample of nearly pure Zn (approximately 0.1% Al) was used as the working electrode. The sample was cleaned sequentially with tetrahydrofuran, acetone, and ethanol for 10 minutes each in an ultrasonic bath and dried under flowing nitrogen, then dipped in 1M NaOH solution at 50° C for 30 s to remove residual aluminum oxides and simulate the oxidizing effect of a conventional alkaline degreasing. The experiments were performed in 0.1 M NH<sub>4</sub>Cl (analytical grade, VWR Prolabo) and 0.5 M NaCl (analytical grade, VWR Prolabo) prepared with purified water (Millipore™ system, 18.8 Ω cm<sup>2</sup>) at natural pH.

The AESEC technique and operating conditions were described previously in Chapter 4. The downstream zinc concentration,  $C_{Zn}$ , was determined from the emission at 213.856 nm using standard analytical procedures. The detection limit for Zn was determined to be  $2.1 \pm 0.2$  ppb (equivalent of  $0.6 \pm 0.1 \mu\text{A cm}^{-2}$ ) under the conditions of these experiments. Al was also monitored at 167.081 nm but was always below the detection limit of  $2.8 \pm 0.2$  ppb (equivalent of  $3.0 \pm 0.2 \mu\text{A cm}^{-2}$ ).

The data were expressed as an equivalent dissolution current density using

$$j_{Zn} = 2FfC_{Zn}/A \quad (\text{F.1})$$

where 2 is the assumed charge on the cation (Zn<sup>2+</sup>),  $F$  is the Faraday constant,  $f$  is the flow rate ( $0.050 \pm 0.002 \text{ cm}^3 \text{ s}^{-1}$ ), and  $A$  is the area of the exposed surface ( $0.51 \pm 0.01 \text{ cm}^2$ ). Electrochemical experiments (polarization and EIS) were performed with a Gamry Reference 600™ potentiostat using a Ag/AgCl reference electrode and a Pt plate counter electrode in the AESEC flow cell. EIS was measured from 10000 to 0.00398 Hz at 10 points per decade and 4 cycles per frequency with a 10 mV rms perturbation amplitude. Polarization curves were recorded from the lowest cathodic potential with a sweep rate of  $0.5 \text{ mV s}^{-1}$  in IR correction mode using the interrupt method on the Gamry potentiostat. However they were also recorded in analog mode without IR correction by the A/D convertor and software interface of the inductively coupled plasma atomic emission spectrometer (ICP-AES).

The time constant distribution or transfer function ( $h(t)$ ) of the electrochemical flow cell was used to convolute the electrical current ( $j_e$ ) to quantitatively compare the dissolution rate and electron transfer rate [160] as given by Eqs. (F.2)- (F.3):

$$h(t) = \sqrt{\frac{\beta}{\pi\tau^2}} e^{-\frac{1}{4\beta}} e^{-\beta \ln^2 \frac{t}{\tau}} \quad (\text{F.2})$$

$$j_e^*(t) = \sum_{\zeta=0}^t j_e(\zeta) h(t - \zeta) \quad (\text{F.3})$$

where  $j_e^*(t)$  is the convoluted electrical current. The time constant distribution was measured as previously described in Chapter 4 by applying a galvanostatic pulse of 1.0 mA for 1 s to pure Cu in deaerated 2.0 M HCl and fitting the resulting concentration transient to a log-normal distribution. In this work the parameters for log-normal distribution were found to be  $b = 0.99 \pm 0.02$  and  $\tau = 10.23 \pm 0.10$  s. The time offset due to transport through the capillaries was  $\Delta t = 14 \pm 0.5$  s.

## Results and Discussion

### Zn in 0.1 M NH<sub>4</sub>Cl

An overview of the chemistry of the Zn/0.1 M NH<sub>4</sub>Cl may be gained from a polarization curve obtained over a wide potential range as in Fig. 6.1. Shown are  $j_e$  and  $j_{Zn}$  vs.  $E$ , the later having been corrected for the ohmic drop of the cell using the current interrupt method of the Gamry software. It is noted that Zn dissolution begins to rise above the detection limit during the cathodic branch about 50 mV below the  $j_e = 0$  potential. As the potential increases, the Zn dissolution rate increases exponentially for three orders of magnitude, until the end of the experiment at -1.0 V with an apparent Tafel slope of  $b_a = 35 \pm 3$  mV decade<sup>-1</sup>. For  $E > -1.04$  V it is noted that  $j_e = j_{Zn}^{**}$  (within an error of 1%) demonstrating the equivalence of the Faradaic current and the elemental dissolution current. Between -1.25 V and -1.1 V, the cathodic branch shows a relatively constant plateau suggesting a diffusion limitation for oxygen reduction.

From a charge balance, the total electrical current is equal to the sum of the anodic and cathodic half reaction currents,  $j_e = j_c + j_a$ . The good agreement between  $j_e$  and  $j_{Zn}^{**}$  in the anodic branch and the well-defined linear Tafel region (after correction for IR drop) demonstrate that  $j_c$  and the formation of insoluble Zn(II) films in this electrolyte is negligible during the anodic branch. Hence, we may consider that  $j_{Zn}$  corresponds to the totality of the anodic current  $j_a$ , and the cathodic current may be estimated from a mass balance of the system:

$$j_c = j_e - j_{Zn}. \quad (\text{F.4})$$

The decoupling of  $j_e$  into  $j_c + j_a$  permits the construction of an Evan's diagram around the open circuit potential. This is shown as an inset to Fig. 6.1.

An investigation of the spontaneous, open circuit Zn dissolution of Zn/0.1 M NH<sub>4</sub>Cl with EIS is shown in Fig. 6.2. The dissolution profile consists of  $j_{Zn}$ ,  $j_e$  and  $E$  as a function of time and is divided into four time periods. Period I is simply the signal from the electrolyte used to define the background emission from the plasma. Period II

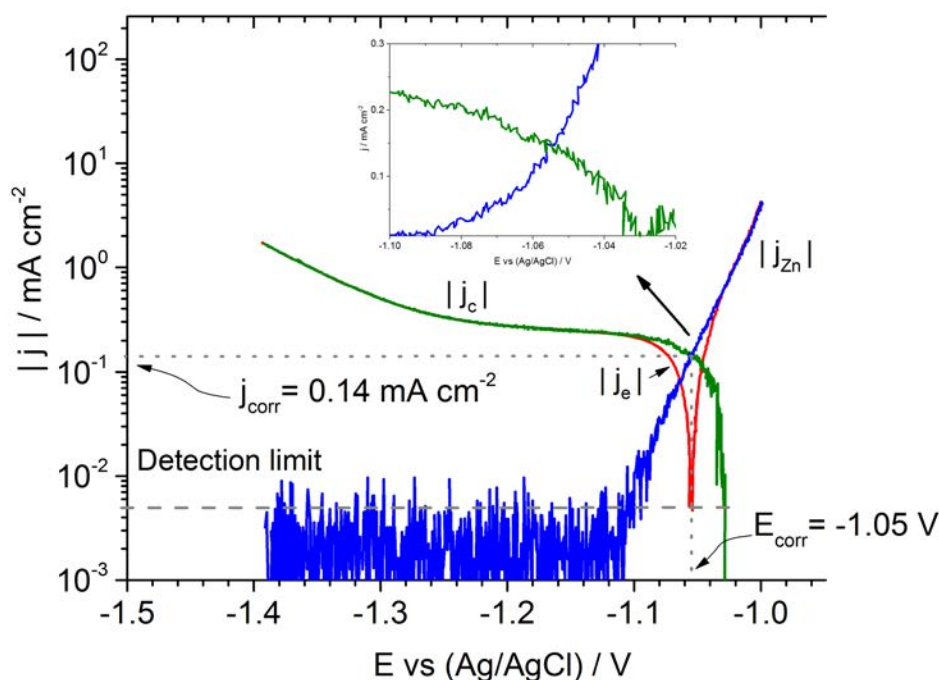


Figure 6.1: Polarization curve for Zn (galvanized steel) in 0.1 M  $\text{NH}_4\text{Cl}$  at  $0.5 \text{ mV s}^{-1}$ , corrected for ohmic drop, showing  $j_e$ ,  $j_{Zn}^{**}$  and  $j_c^{**} = j_e - j_{Zn}^{**}$ . The inset gives an expanded view (Evan's diagram) around the corrosion potential.

indicates the exposure of the electrolyte to Zn, at  $t = 0$  at which point the dissolution rate of Zn rises quickly from zero, reaching a maximum around  $0.2 \text{ mA cm}^{-2}$  and then falls off to a steady state value at  $0.16 \pm 0.01 \text{ mA cm}^{-2}$ . The EIS experiment begins at the second vertical dashed line indicated by period III. Period IV shows the return to the open circuit potential and spontaneous corrosion. The dissolution rates measured before and after the EIS experiment (Periods II and IV) were identical within experimental error, demonstrating the electrochemical stability of the Zn/0.1M  $\text{NH}_4\text{Cl}$  system.

Note that for the figure, the concentration, current, and potential were collected with the analog to digital convertor of the spectrometer with a data collection rate of 1 Hz. The Nyquist limit predicts that only the frequencies  $< 0.5 \text{ Hz}$  may be determined reliably in the time graph of Fig. 6.2. The current and potential data were also analyzed by the Gamry potentiostat to yield the conventional EIS spectrum that will be discussed later. The oscillations in the concentration transients become evident to the eye only around 0.05 Hz. The fact that the lower frequency oscillations in  $j_e$  are immediately visible in  $j_{Zn}$  demonstrates that zinc oxidation results almost exclusively in dissolved Zn ions. If an intermediate oxide film is formed, the time constants for its formation and dissolution

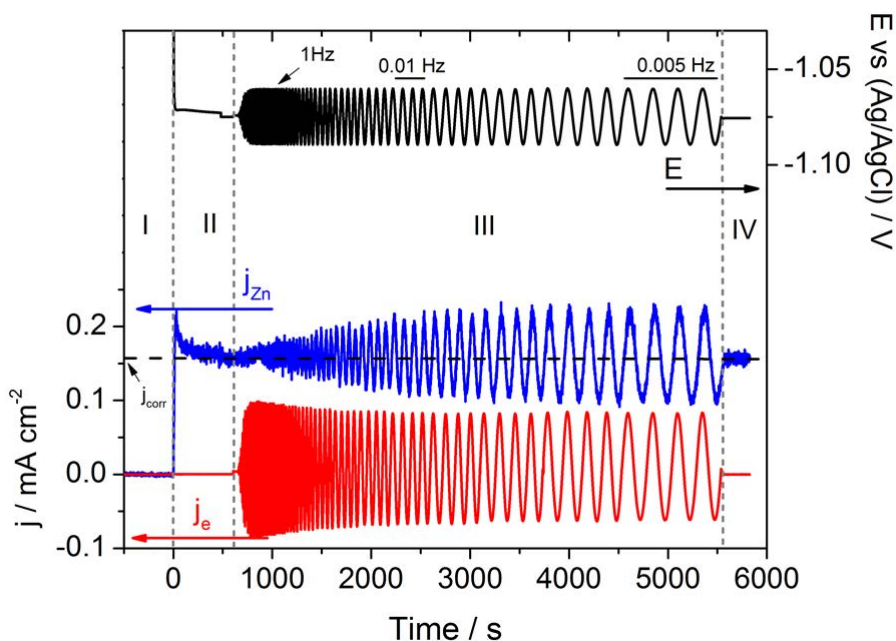


Figure 6.2: Open circuit dissolution of Zn (galvanized steel) in 0.1 M  $\text{NH}_4\text{Cl}$  showing  $j_{\text{Zn}}$ ,  $j_e$  and  $E$ , followed by an EIS experiment from 10 kHz to 0.00398 Hz.

are clearly below the time resolution of the AESEC technique.

As with the Evan's diagram of Fig.6.1, the EIS/AESEC combination may be used to decouple the total electrical current into partial anodic and cathodic currents. Fig. 6.3 gives  $j_e^*$ ,  $j_{\text{Zn}}$  ( $=j_a$ ) and  $j_c = j_e^* - j_{\text{Zn}}$ . The average value of the Faradaic efficiency is  $91\% \pm 7\%$  over the range of measurable frequencies and no significant frequency dependence is noted. A kinetic analysis of the current and dissolution transients will be presented in Section F.

### Zn in 0.5 M NaCl

Fig. 6.4 shows a similar AESEC polarization curve for Zn in 0.5 M NaCl electrolyte at  $\text{pH} = 6$ . As in the previous example, the cathodic current is essentially potential independent around the  $j_e = 0$  potential. The rapid onset of the anodic current density however, occurs without any significant increase in the Zn dissolution rate. Indeed,  $j_{\text{Zn}}$  rises above background only after +50 mV higher than the  $j_e = 0$  potential in the curve. This clearly indicates that the early stages of oxidation result exclusively in a corrosion product film rather than dissolved Zn ions. The fact that  $j_e \gg j_{\text{Zn}}$  throughout the anodic branch is also direct evidence for the formation of a corrosion product film. Due to problems with stability, the IR correction was not performed for this experiment, however

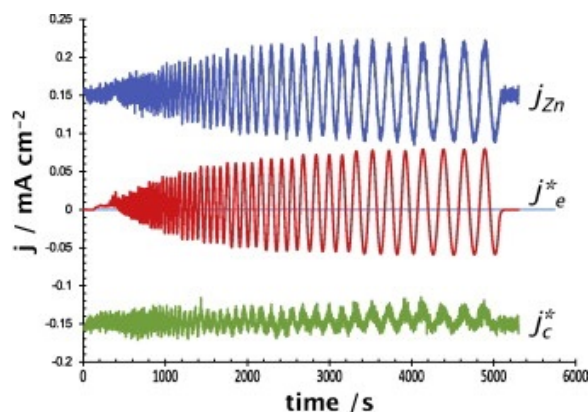


Figure 6.3: Comparison of the convoluted current,  $j_e^*$ ,  $j_{Zn}$  and,  $j_c = j_e^* - j_{Zn}$  the  $\text{NH}_4\text{Cl}$  electrolyte.

this is of no consequence since neither  $j_e$  nor  $j_{Zn}$  show a characteristic Tafel region with or without  $iR$  correction. Since  $j_{Zn}$  is essentially zero at  $j_e = 0$ , it is impossible to directly measure the corrosion rate, however extrapolation of the anodic and cathodic branches to  $j_e = 0$  yields an estimated corrosion rate of approximately  $0.05 \text{ mA cm}^{-2}$ .

An estimate of the quantity of insoluble Zn corrosion products,  $Q_{ins}$ , may be determined as

$$Q_{ins} = \int_0^t (j_e - j_{Zn}) dt \quad (\text{F.5})$$

with the assumption that the cathodic reaction makes a negligible contribution to the overall current. The integral is indicated by the shaded area in Fig. 3. This integration, between  $j_e = 0$  to the end of the anodic polarization, yields  $Q_{ins} = 85 \text{ mC cm}^{-2}$  corresponding to the oxidation of  $2.5 \mu\text{mole cm}^{-2}$ . This quantity is probably overestimated due to the broadening of the ICP-AES signal.

The open circuit – EIS transient for Zn in 0.5 M NaCl electrolyte at  $\text{pH} = 6$  is shown in Fig. 6.5. The important point here is that the oscillations of  $j_e$  do not appear in  $j_{Zn}$  even at the lowest frequencies. Since the cathodic reaction is nearly potential independent (Fig. 6.4) we attribute this to a mechanism in which the electrochemical reaction leads almost exclusively to the formation of insoluble corrosion products. The results in Fig. 6.5 also demonstrate a marked instability of the Zn/0.5M NaCl system: the central value of the AC current rises progressively above  $j_e = 0$  in Fig. 6.5, such that at the end of the experiment  $j_e$  is entirely anodic. This is indicative of the formation of insoluble corrosion products and the absence of a steady state.

The results of Fig. 6.5 do suggest that the dissolution rate varies with the applied potential. Curiously, as soon as the EIS experiment is applied there is an increase in the zinc dissolution rate by nearly a factor of two with  $j_{Zn}$  varying between  $0.07 \text{ mA cm}^{-2}$  at the initial open circuit potential and  $0.14 \text{ mA cm}^{-2}$  after application of the EIS experiment. Following the EIS experiment, the open circuit potential drops about

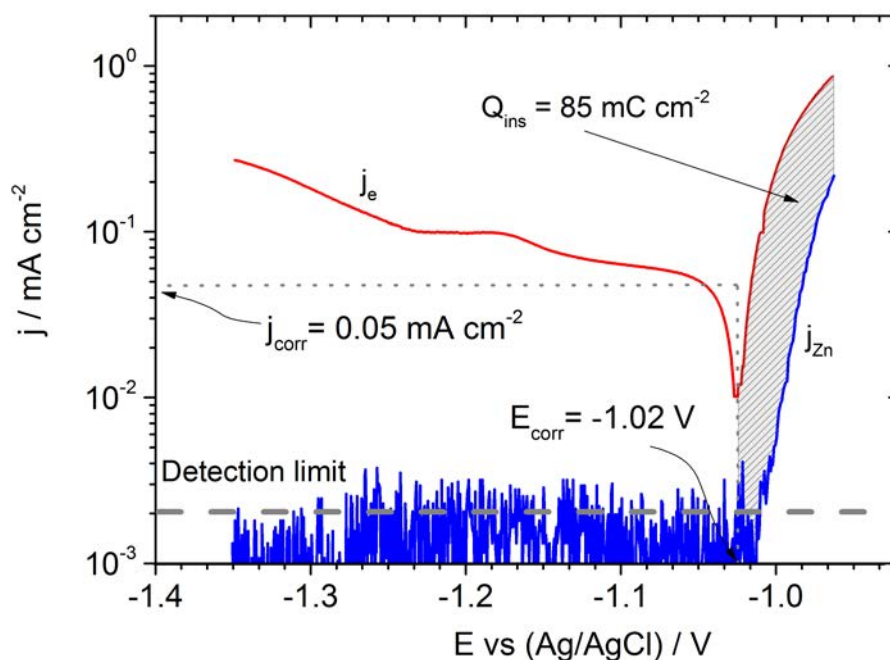


Figure 6.4: Polarization curve for Zn (galvanized steel) in 0.5 M NaCl at  $0.5 \text{ mV s}^{-1}$ , showing  $j_e$  and  $j_{Zn}$ . The dashed area shows the integral used to calculate  $Q_{ins}$ .

20 mV below the initial value and the Zn dissolution rate approaches its original value prior to EIS. The initial and final open circuit Zn dissolution rates are in reasonably good agreement with the corrosion rate predicted from Fig. 6.4 by extrapolation of the cathodic current to the  $j_e = 0$  limit, yielding approximately 0.05 to 0.07  $\text{mA cm}^{-2}$ .

Fig. 6.6 presents the impedance spectra in Nyquist format for the two systems measured during the experiments of Figs. 6.2 and 6.5. Note that the high frequency intercept of the real axis has been removed so as to facilitate comparison. Two time constants are clearly detected for both systems. The high frequency time constant is very similar for both electrolytes, between 100 kHz and 0.5 Hz with nearly identical resistance and a constant phase element values (see Figure caption). The low frequency time constant is clearly defined in 0.1 M  $\text{NH}_4\text{Cl}$  system as a semicircle. It is considerably distorted in 0.5 M NaCl however probably due to continual formation of the oxide film and the non-steady state conditions. Nevertheless, the results show that the zinc surface is active, consistent with the significant dissolution rate observed at open circuit, which would imply that the oxide film formed under these conditions does not significantly impede the cathodic reaction. This is in agreement with the conclusions of Bonk et al. [180]. A variety of different mechanisms and equivalent circuits may be used to explain the appearance of two time constants in the investigated frequency range. The high frequency

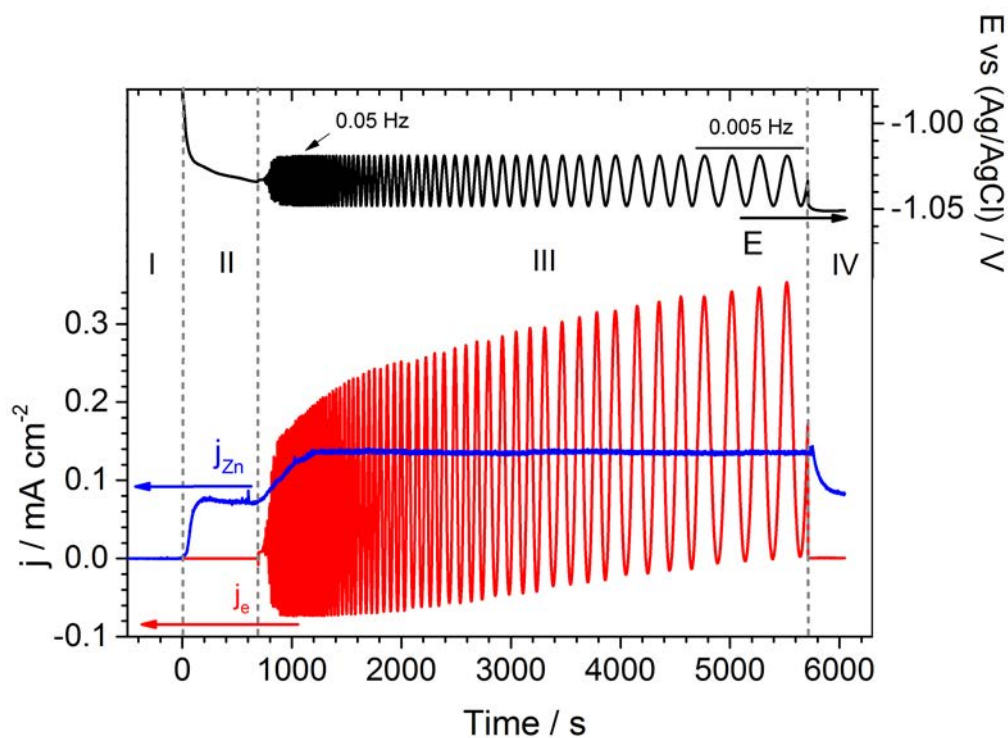


Figure 6.5: Open circuit dissolution of Zn (galvanized steel) in 0.5 M NaCl followed by an EIS experiment from 10 kHz to 0.00398 Hz.

time constant might be attributed to an adsorbed Zn(I) intermediate as discussed by Ganne et al. [273], however the AESEC has insufficient time resolution to access these kinetics and we will not discuss this further. The low frequency time constant mechanism is clearly the mechanism that gives rise to soluble Zn(II) ions and therefore reflects the rate limiting step of corrosion.

## Data Analysis

The combination of electrochemical data with the direct measurement of the dissolution rate permits the determination of the anodic and cathodic kinetic parameters. Fig. 6.7 gives the variation of  $j_{Zn}$ ,  $j_e$  and  $j_e - j_{Zn}$  as a function of potential ( $E$ ) for four cycles of the lowest frequency 0.00398 Hz experiments. Note that the potential has been corrected for the IR drop. The continuous curve shown in the center of each profile represents the calculated variation assuming a Tafel rate law expression according to Eq. (F.4):

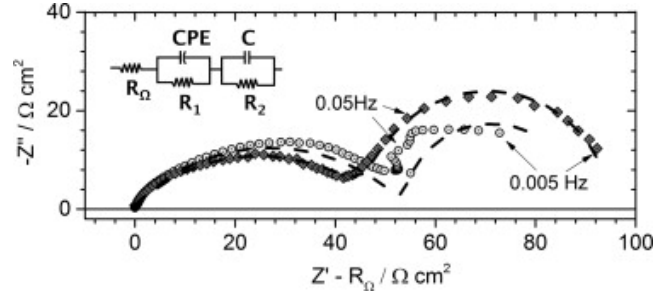


Figure 6.6: Impedance spectra in Nyquist format for Zn (galvanized steel) in (A) 0.1 M  $\text{NH}_4\text{Cl}$  and (B) 0.5 M  $\text{NaCl}$  from 10 kHz to 0.0398 Hz. The two time constant equivalent circuit used to simulate the impedance response is shown as an inset. The fitting parameters for the high frequency time constant were: (A) 0.1 M  $\text{NH}_4\text{Cl}$ :  $R_1 = 49 \pm 1 \Omega \text{ cm}^2$ ,  $Q_1 = 0.92 \pm 0.06 \times 10^{-3} \text{ F s}^{\alpha-1}$  and  $\alpha = 0.52$ ; (B) 0.5 M  $\text{NaCl}$ :  $R_1 = 49 \pm 1 \Omega \text{ cm}^2$ ,  $Q_1 = 0.25 \pm 0.09 \times 10^{-3} \text{ F s}^{\alpha-1}$  and  $\alpha = 0.59$ . Fitting parameters for the low frequency time constant for the 0.1 M  $\text{NH}_4\text{Cl}$  electrolyte were  $R_2 = 45 \pm 1 \Omega \text{ cm}^2$ ,  $C = 0.085 \pm 0.003 \text{ F}$ .

$$\begin{aligned} j_a &= j_a^- \exp(2.303(E - E^- - j_e AR_\Omega)/b_a) \\ j_c &= j_c^- \exp(-2.303(E - E^- - j_e AR_\Omega)/b_c) \\ j_e &= j_a + j_c \end{aligned} \quad (\text{F.6})$$

were  $j^-$  is the current density measured at  $E^-$ , the low potential extreme of the cycle and the term  $j_e AR_\Omega$  corrects for the uncompensated electrolyte charge resistance. The anodic Tafel slope ( $b_a$ ) was estimated by Eq. (F.7) (shown for  $b_a$ ) and adjusted according to the best fit to the data.

$$b_a = 2.303 \Delta E / \ln(j_{Zn}^+ / j_{Zn}^-) \quad (\text{F.7})$$

were  $\Delta E$  is the difference between the high and low potentials of the cycle corrected for the ohmic drop, and  $j_{Zn}^+$  and  $j_{Zn}^-$  are the corresponding values of  $j_{Zn}$ . The results of Fig. 6.7 yield a Tafel of  $45.6 \pm 0.9 \text{ mV decade}^{-1}$ , somewhat larger than the value of  $b_a = 35 \pm 3 \text{ mV decade}^{-1}$  determined from Fig. 6.1. This value is in good agreement with previous results for Zn in alkaline solution [40] where a value of 41 to 46 mV  $\text{mV decade}^{-1}$  was measured. This is also consistent with previous publications [306–308] for Zn in alkaline solution.

Fig. 6.7 gives the rate of the cathodic reaction, determined as  $j_c = j_e - j_{Zn}$  (assuming  $j_{Zn}$  to be the total anodic current, i.e. there is no film formation). From this analysis,  $j_c^- = -0.16 \text{ mA cm}^{-2}$  and  $j_c^+ = -0.13 \text{ mA cm}^{-2}$ , yielding a cathodic Tafel slope of approximately  $161 \text{ mV decade}^{-1}$  with a significant error due to the small difference in the two endpoints. Despite the error, the large estimated Tafel slope is consistent with the hypothesis of a diffusion limited oxygen reduction reaction as evoked previously in the

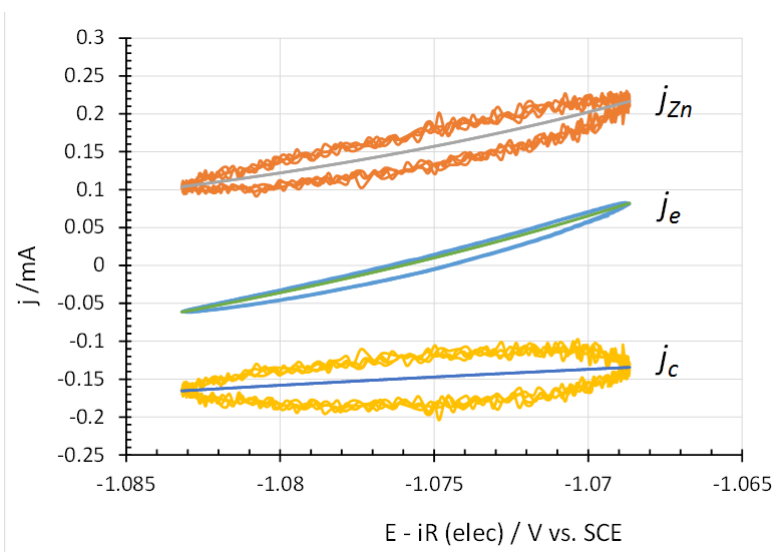


Figure 6.7: Kinetic analysis of the low frequency potential perturbation for the  $\text{NH}_4\text{Cl}$  electrolyte (Fig. 6.2) showing  $j_{Zn}$ ,  $j_e$  and  $j_c$  as a function of IR corrected potential during the low frequency perturbation of Fig. 6.2. The continuous curve in the center of each profile represents the calculated current variation using the best estimate of the anodic and cathodic Tafel slopes.

discussion of Fig. 6.1. Fig. 6.7 gives the total current variation with the theoretical fit for  $b_a$  and  $b_c$  determined above. As determined from the polarization curve, the variation of  $j_e$  with potential is almost exclusively determined by the anodic Tafel slope.

From the EIS experiment for 0.1 M  $\text{NH}_4\text{Cl}$ , the Stern Geary equation may also be used to estimate the corrosion rate:

$$j_{corr} = \left[ \frac{b_a b_c}{2.3(b_a + b_c)} \right] \left( \frac{1}{R_p} \right) \quad (\text{F.8})$$

with the polarization resistance,  $R_p = R_1 + R_2 = 94 \pm 2 \Omega \text{ cm}^2$ , with  $R_1$  and  $R_2$  representing the real component of the impedance for the high and low frequency time constant respectively. Using the values of  $b_a$  and  $b_c$  calculated above, Eq. (F.8) gives  $j_{corr} = 0.17 \text{ mA cm}^{-2}$  in reasonably good agreement with the open circuit AESEC data.

## Conclusions

The AESEC method may distinguish between mechanisms involving direct electrochemical dissolution and dissolution mediated by the presence of a corrosion product film by imposing a low frequency potential perturbation to the system. For the  $\text{NH}_4\text{Cl}$  system, the alternating electrical current is correlated with a nearly identical alternating Zn dissolution current. This demonstrates that the oxidation of Zn leads to the formation of dissolved Zn ions on the time scale of these experiments (frequency range of 0.00398 Hz to 0.05 Hz). Analysis of the potential dependence of the anodic and cathodic rates

at 0.00398 Hz independently yields a Tafel slope of  $45.6 \pm 0.9$  mV decade<sup>-1</sup> and 161 mV decade<sup>-1</sup>, which is somewhat larger than that obtained from the polarization curve measured for this system.

For the NaCl electrolyte, the AC perturbations of current do not appear in the Zn dissolution rate as a function of time and the system appears to be unstable. The continual growth of an oxide film on the surface is apparent. The quantity of Zn<sup>2+</sup> ions in the oxide film formed during polarization may be estimated from a mass balance between  $j_e$  and  $j_{Zn}$ .

---

## Salt spray test results of HDG panels coated with a model coating

---

Fig. 7.1 shows the results of salt spray tests for galvanized steel coated with a model coating with and without LDH/MoO<sub>4</sub><sup>2-</sup> fillers. The model coating was designed to fail after 360 h of exposure in order to evaluate the impact of anticorrosion additives (see details of preparation in Chapter 8).

The delay of inhibiting effect of LDH anticorrosion coating is observed. No difference can be noticed between two samples after 168 hours of exposure however, the marked inhibiting effect of LDH hybrid coating is observed after 360 hours of exposure. One of the possible explanations include time delayed inhibitor release controlled by the adsorption of carbonates from the atmosphere (see Chapter 8).



Figure 7.1: Salt spray test of galvanized steel coated with (2) and without (1) LDH/MoO<sub>4</sub><sup>2-</sup> fillers after 168 and 360 hours of exposure



---

## Bibliography

---

- [1] G. Grundmeier, W. Schmidt, and M. Stratmann, “Corrosion protection by organic coatings: electrochemical mechanism and novel methods of investigation,” *Electrochimica Acta*, vol. 45, no. 15-16, pp. 2515–2533, May 2000.
- [2] M. Rohwerder and A. Michalik, “Conducting polymers for corrosion protection: What makes the difference between failure and success?” *Electrochimica Acta*, vol. 53, no. 3, pp. 1300–1313, Dec. 2007.
- [3] E. Brooman, “Modifying organic coatings to provide corrosion resistance—Part I: Background and general principles,” *Metal Finishing*, vol. 100, no. 1, pp. 48–53, Jan. 2002.
- [4] —, “Modifying organic coatings to provide corrosion resistance: Part II—Inorganic additives and inhibitors,” *Metal Finishing*, vol. 100, no. 5, pp. 42–53, May 2002.
- [5] —, “Modifying organic coatings to provide corrosion resistance—Part III: Organic additives and conducting polymers,” *Metal Finishing*, vol. 100, no. 6, pp. 104–110, Jun. 2002.
- [6] A. Goldschmidt and H.-J. Streitberger, *BASF Handbook on Basics of Coating Technology*, 2nd ed., 2007.
- [7] H. Hintze-Bruening and F. Leroux, “Nanocomposite Based Multifunctional Coatings,” in *New Advances in Vehicular Technology and Automotive Engineering*, J. Carmo, Ed., 2012, ch. 2.
- [8] R. Posner, N. Fink, G. Giza, and G. Grundmeier, “Corrosive delamination and ion transport along stretch-formed thin conversion films on galvanized steel,” *Surface & Coatings Technology*, vol. 253, pp. 227–233, 2014.
- [9] R. Posner, P. E. Sundell, T. Bergman, P. Roose, M. Heylen, G. Grundmeier, and P. Keil, “UV-Curable Polyester Acrylate Coatings: Barrier Properties and Ion

- Transport Kinetics Along Polymer/Metal Interfaces,” *Journal of The Electrochemical Society*, vol. 158, no. 6, p. C185, 2011.
- [10] M. Zheludkevich, J. Tedim, and M. Ferreira, ““Smart” coatings for active corrosion protection based on multi-functional micro and nanocontainers,” *Electrochimica Acta*, vol. 82, pp. 314–323, Nov. 2012.
- [11] M. L. Zheludkevich, D. G. Shchukin, K. a. Yasakau, H. Möhwald, and M. G. S. Ferreira, “Anticorrosion coatings with self-healing effect based on nanocontainers impregnated with corrosion inhibitor,” *Chemistry of Materials*, vol. 19, no. 3, pp. 402–411, 2007.
- [12] T. Stimpfling, F. Leroux, and H. Hintze-Bruening, “Organo-modified layered double hydroxide in coating formulation to protect AA2024 from corrosion,” *Colloids and Surfaces A: Physicochemical and Engineering Aspects*, vol. 458, pp. 147–154, Sep. 2014.
- [13] R. G. Buchheit, H. Guan, S. Mahajanam, and F. Wong, “Active corrosion protection and corrosion sensing in chromate-free organic coatings,” *Progress in Organic Coatings*, vol. 47, no. 3-4, pp. 174–182, Sep. 2003.
- [14] G. Williams and H. N. McMurray, “Anion-Exchange Inhibition of Filiform Corrosion on Organic Coated AA2024-T3 Aluminum Alloy by Hydrotalcite-Like Pigments,” *Electrochemical and Solid-State Letters*, vol. 6, no. 3, p. B9, Mar. 2003.
- [15] —, “Inhibition of Filiform Corrosion on Polymer Coated AA2024-T3 by Hydrotalcite-Like Pigments Incorporating Organic Anions,” *Electrochemical and Solid-State Letters*, vol. 7, no. 5, p. B13, 2004.
- [16] M. Zheludkevich, S. Poznyak, L. Rodrigues, D. Raps, T. Hack, L. Dick, T. Nunes, and M. Ferreira, “Active protection coatings with layered double hydroxide nanocontainers of corrosion inhibitor,” *Corrosion Science*, vol. 52, no. 2, pp. 602–611, Feb. 2010.
- [17] J. Tedim, S. K. Poznyak, a. Kuznetsova, D. Raps, T. Hack, M. L. Zheludkevich, and M. G. S. Ferreira, “Enhancement of active corrosion protection via combination of inhibitor-loaded nanocontainers,” *ACS Applied Materials and Interfaces*, vol. 2, no. 5, pp. 1528–1535, 2010.
- [18] T. Stimpfling, F. Leroux, and H. Hintze-Bruening, “Phosphate-Based Organic Molecules Interleaved with Layered Double Hydroxide: Unraveling the Roles of Host Cations and the Guest-Inhibiting Effect in Aluminum Corrosion Protection,” *European Journal of Inorganic Chemistry*, vol. 2012, no. 32, pp. 5396–5404, Nov. 2012.
- [19] T. T. X. Hang, T. A. Truc, N. T. Duong, N. Pébère, M.-G. G. Olivier, N. Pébre, and M.-G. G. Olivier, “Layered double hydroxides as containers of inhibitors in

- organic coatings for corrosion protection of carbon steel,” *Progress in Organic Coatings*, vol. 74, no. 2, pp. 343–348, Jun. 2012.
- [20] W. Fürbeth and M. Stratmann, “Delamination of polymeric coatings from electrogalvanized steel - a mechanistic approach. Part 2: Delamination from a defect down to steel,” *Corrosion Science*, vol. 43, pp. 229–241, 2001.
- [21] —, “The delamination of polymeric coatings from electrogalvanised steel – a mechanistic approach.” *Corrosion Science*, vol. 43, pp. 207–227, 2001.
- [22] —, “The delamination of polymeric coatings from electrogalvanised steel—a mechanistic approach.—Part 1: delamination from a defect with intact zinc layer,” *Corrosion Science*, vol. 43, pp. 207–227, 2001.
- [23] X. G. Zhang, *Corrosion and Electrochemistry of Zinc*, plenum pre ed., New York, 1996.
- [24] S. Maeda, “Surface chemistry of galvanized steel sheets relevant to adhesion performance,” *Progress in Organic Coatings*, vol. 28, no. 4, pp. 227–238, Aug. 1996.
- [25] S. Yeomans, *Galvanized Steel Reinforcement in Concrete*. Elsevier, 2004.
- [26] T. N. Vu, P. Volovitch, and K. Ogle, “The effect of pH on the selective dissolution of Zn and Al from Zn–Al coatings on steel,” *Corrosion Science*, vol. 67, pp. 42–49, Feb. 2013.
- [27] Z. Mekhalif, L. Forget, and J. Delhalle, “Investigation of the protective action of chromate coatings on hot-dip galvanized steel: role of wetting agents,” *Corrosion Science*, vol. 47, no. 3, pp. 547–566, Mar. 2005.
- [28] R. Krieg, M. Rohwerder, S. Evers, B. Schuhmacher, and J. Schauer-Pass, “Cathodic self-healing at cut-edges: The effect of  $\text{Zn}^{2+}$  and  $\text{Mg}^{2+}$  ions,” *Corrosion Science*, vol. 65, pp. 119–127, 2012.
- [29] F. Thébault, B. Vuillemin, R. Oltra, C. Allely, and K. Ogle, “Protective mechanisms occurring on zinc coated steel cut-edges in immersion conditions,” *Electrochimica Acta*, vol. 56, no. 24, pp. 8347–8357, Oct. 2011.
- [30] K. Ogle, V. Baudu, L. Garrigues, and X. Philippe, “Localized Electrochemical Methods Applied to Cut Edge Corrosion,” *Journal of The Electrochemical Society*, vol. 147, no. 10, p. 3654, 2000.
- [31] J. Yoo, K. Ogle, and P. Volovitch, “The effect of synthetic zinc corrosion products on corrosion of electrogalvanized steel. II. Zinc reactivity and galvanic coupling zinc/steel in presence of zinc corrosion products,” *Corrosion Science*, vol. 83, pp. 32–37, Jun. 2014.

- [32] ———, “The effect of synthetic zinc corrosion products on corrosion of electrogalvanized steel: I. Cathodic reactivity under zinc corrosion products,” *Corrosion Science*, vol. 81, pp. 11–20, Apr. 2014.
- [33] I. Puigdomenech, “Hydra/Medusa Chemical Equilibrium Database and Plotting Software KTH Royal Institute of Technology,” Consulted 07/05/2015.
- [34] R. W. Powers and M. W. Breiter, “The Anodic Dissolution and Passivation of Zinc in Concentrated Potassium Hydroxide Solutions,” *Journal of The Electrochemical Society*, vol. 116, no. 6, p. 719, 1969.
- [35] R. Powers, “Film Formation and Hydrogen Evolution on the Alkaline Zinc Electrode,” *Journal of The Electrochemical Society*, vol. 118, no. 5, p. 685, 1971.
- [36] S. Thomas, I. Cole, M. Sridhar, and N. Birbilis, “Revisiting zinc passivation in alkaline solutions,” *Electrochimica Acta*, vol. 97, pp. 192–201, May 2013.
- [37] C. a. Laska, M. Auinger, P. Biedermann, D. Iqbal, N. Laska, J. De Strycker, and K. J. Mayrhofer, “Effect of hydrogen carbonate and chloride on zinc corrosion investigated by a scanning flow cell system,” *Electrochimica Acta*, vol. 159, pp. 198–209, 2015.
- [38] D. D. Macdonald, K. M. Ismail, and E. Sikora, “Characterization of the Passive State on Zinc,” *Journal of Electrochemical Society*, vol. 145, no. 9, pp. 3141–3149, 1998.
- [39] L. Baugh and a. Higginson, “Passivation of zinc in concentrated alkaline solution—I. Characteristics of active dissolution prior to passivation,” *Electrochimica Acta*, vol. 30, no. 9, pp. 1163–1172, Sep. 1985.
- [40] M. Mokaddem, P. Volovitch, and K. Ogle, “The anodic dissolution of zinc and zinc alloys in alkaline solution. I. Oxide formation on electrogalvanized steel,” *Electrochimica Acta*, vol. 55, no. 27, pp. 7867–7875, Nov. 2010.
- [41] S. Thomas, N. Birbilis, M. Venkatraman, and I. Cole, “Self-repairing oxides to protect zinc: Review, discussion and prospects,” *Corrosion Science*, vol. 69, pp. 11–22, Apr. 2013.
- [42] B. Harvey, *Zinc oxide: Properties and applications*. International Lead Zinc Research Organization, 1976.
- [43] A. Goux, T. Pauporté, and D. Lincot, “Oxygen reduction reaction on electrodeposited zinc oxide electrodes in KCl solution at 70°C,” *Electrochimica Acta*, vol. 51, no. 15, pp. 3168–3172, Apr. 2006.
- [44] M. S. Venkatraman, I. S. Cole, and B. Emmanuel, “Corrosion under a porous layer: A porous electrode model and its implications for self-repair,” *Electrochimica Acta*, vol. 56, no. 24, pp. 8192–8203, Oct. 2011.

- 
- [45] Y. Chen, S. Chung, and H. Shih, "Studies on the initial stages of zinc atmospheric corrosion in the presence of chloride," *Corrosion Science*, vol. 48, no. 11, pp. 3547–3564, Nov. 2006.
- [46] I. Odnevall Wallinder and C. Leygraf, "Reaction sequences in atmospheric corrosion of zinc," in *Atmospheric Corrosion*, W. Kirk and H. Lawson, Eds. Philadelphia: ASTM STP 1239, 1995, p. 215.
- [47] W. Feitknecht, "Chemical and thermochemical principles relating to corrosion of metals in aqueous solutions with Zn metal as an example," *Metaux et Corrosion*, vol. 23, pp. 192–203, 1947.
- [48] I. S. Cole, T. H. Muster, S. Furman, N. Wright, and A. Bradbury, "Products Formed during the Interaction of Seawater Droplets with Zinc Surfaces: I. Results from 1- and 2.5-Day Exposures," *Journal of The Electrochemical Society*, vol. 155, no. 5, p. C244, 2008.
- [49] B. E. Roetheli, G. L. Cox, and W. Literal, "Effect of pH on the corrosion products and corrosion rate of zinc in oxygenated aqueous solutions," *Met. Alloy*, vol. 3, pp. 73–76, 1932.
- [50] T. Prosek, D. Thierry, C. Taxén, and J. Maixner, "Effect of cations on corrosion of zinc and carbon steel covered with chloride deposits under atmospheric conditions," *Corrosion Science*, vol. 49, no. 6, pp. 2676–2693, Jun. 2007.
- [51] C. Cachet, S. Joiret, G. Maurin, R. Nogueira, and V. Vivier, "Relationship between zinc corrosion process and corrosion products: an EIS and raman spectroscopy study," in *203rd Meeting of the ElectroChemical Society*, 2003, p. abstract 206.
- [52] Z. Pilbáth and L. Sziráki, "The electrochemical reduction of oxygen on zinc corrosion films in alkaline solutions," *Electrochimica Acta*, vol. 53, no. 7, pp. 3218–3230, Feb. 2008.
- [53] Q. Qu, L. Li, W. Bai, C. Yan, and C.-n. Cao, "Effects of NaCl and NH<sub>4</sub>Cl on the initial atmospheric corrosion of zinc," *Corrosion Science*, vol. 47, no. 11, pp. 2832–2840, Nov. 2005.
- [54] M. Maja, N. Penazzi, G. Farnia, and G. Sandona, "Zinc corrosion in NH<sub>4</sub>Cl and effect of some organic inhibitors," *Electrochimica Acta*, vol. 38, no. 10, pp. 1453–1459, 1993.
- [55] M. Salgueiro Azevedo, C. Allély, K. Ogle, and P. Volovitch, "Corrosion mechanisms of Zn(Mg,Al) coated steel: The effect of HCO<sub>3</sub><sup>-</sup> and NH<sub>4</sub><sup>+</sup> ions on the intrinsic reactivity of the coating," *Electrochimica Acta*, vol. 153, pp. 159–169, Jan. 2015.
- [56] E. McCafferty, "Thermodynamics of chromate replacements by various homologous transition metal oxyanions," *Journal of Applied Electrochemistry*, vol. 40, no. 3, pp. 543–549, Oct. 2010.

- [57] S. Langård and T. Vigander, "Occurrence of lung cancer in workers producing chromium pigments." *British journal of industrial medicine*, vol. 40, no. 1, pp. 71–4, Feb. 1983.
- [58] S. Hong, E. Kim, D. Kim, T. Sung, and K. No, "On measurement of optical band gap of chromium oxide films containing both amorphous and crystalline phases," pp. 245–254, 1997.
- [59] W. J. Clark and R. L. McCreery, "Inhibition of Corrosion-Related Reduction Processes via Chromium Monolayer Formation," *Journal of The Electrochemical Society*, vol. 149, no. 9, p. B379, 2002.
- [60] D. Landolt, *Corrosion and surface chemistry of metals*, 1st ed. EPFL Press, 2007, vol. 10, no. 5.
- [61] D. Wang, X. Tang, Y. Qiu, F. Gan, and G. Zheng Chen, "A study of the film formation kinetics on zinc in different acidic corrosion inhibitor solutions by quartz crystal microbalance," *Corrosion Science*, vol. 47, no. 9, pp. 2157–2172, Sep. 2005.
- [62] I. Baghni, S. Lyon, and B. Ding, "The effect of strontium and chromate ions on the inhibition of zinc," *Surface and Coatings Technology*, vol. 185, no. 2-3, pp. 194–198, Jul. 2004.
- [63] K. Aramaki, "The inhibition effects of chromate-free, anion inhibitors on corrosion of zinc in aerated 0.5 M NaCl," *Corrosion Science*, vol. 43, pp. 591–604, 2001.
- [64] C. da Silva, I. Margarit-Mattos, O. Mattos, H. Perrot, B. Tribollet, and V. Vivier, "The molybdate–zinc conversion process," *Corrosion Science*, vol. 51, no. 1, pp. 151–158, Jan. 2009.
- [65] A. Magalhães, I. Margarit, and O. Mattos, "Molybdate conversion coatings on zinc surfaces," *Journal of Electroanalytical Chemistry*, vol. 572, no. 2, pp. 433–440, Nov. 2004.
- [66] D. Gabe and S. Gould, "Black molybdate conversion coatings," *Surface and Coatings Technology*, vol. 35, no. 1-2, pp. 79–91, Oct. 1988.
- [67] L. Fachikov and D. Ivanova, "Surface treatment of zinc coatings by molybdate solutions," *Applied Surface Science*, vol. 258, no. 24, pp. 10 160–10 167, Oct. 2012.
- [68] B.-i. Lin, J.-t. Lu, G. Kong, and J. Liu, "Growth and corrosion resistance of molybdate modified zinc phosphate conversion coatings on hot-dip galvanized steel," *Transactions of Nonferrous Metals Society of China*, vol. 17, no. 4, pp. 755–761, Aug. 2007.
- [69] P. A. Nikolaychuk and A. G. Tyurin, "The Revised Pourbaix Diagram for Molybdenum," *Butlerov Communications*, vol. 24, no. 2, pp. 101–105, 2011.

- 
- [70] W. D. Robertson, "Molybdate and Tungstate as Corrosion Inhibitors and the Mechanism of Inhibition," *Journal of The Electrochemical Society*, vol. 98, no. 3, p. 94, 1951.
- [71] B. R. W. Hinton and L. Wilson, "The corrosion inhibition of Zn with cerous chloride," *Corrosion Science*, vol. 29, no. 8, pp. 967–985, 1989.
- [72] M. Arenas and J. de Damborenea, "Interference by cerium cations during the multi-step zinc dissolution process in a chloride-containing electrolyte," *Corrosion Science*, vol. 48, no. 10, pp. 3196–3207, Oct. 2006.
- [73] K. Aramaki, "The inhibition effects of cation inhibitors on corrosion of zinc in aerated 0.5 M NaCl," *Corrosion Science*, vol. 43, no. 8, pp. 1573–1588, Aug. 2001.
- [74] E. Diler, S. Rioual, B. Lescop, D. Thierry, and B. Rouvellou, "Chemistry of corrosion products of Zn and MgZn pure phases under atmospheric conditions," *Corrosion Science*, vol. 65, pp. 178–186, Dec. 2012.
- [75] M. Salgueiro Azevedo, C. Allély, K. Ogle, and P. Volovitch, "Corrosion mechanisms of Zn(Mg,Al) coated steel: 2. The effect of Mg and Al alloying on the formation and properties of corrosion products in different electrolytes," *Corrosion Science*, vol. 90, pp. 482–490, Jan. 2015.
- [76] F. Thébault, B. Vuillemin, R. Oltra, C. Allely, K. Ogle, and O. Heintz, "Influence of magnesium content on the corrosion resistance of the cut-edges of Zn – Mg-coated steel," vol. 97, pp. 100–106, 2015.
- [77] E. Tada, S. Katakami, and A. Nishikata, "Electrochemical behavior of iron covered with simulated zinc corrosion products formed in MgCl<sub>2</sub> and NaCl containing Zn<sup>2+</sup>," in *11th International Symposium on electrochemical methods in corrosion research*, 2015, p. 7.
- [78] P. Volovitch, T. Vu, C. Allély, a. Abdel Aal, and K. Ogle, "Understanding corrosion via corrosion product characterization: II. Role of alloying elements in improving the corrosion resistance of Zn–Al–Mg coatings on steel," *Corrosion Science*, vol. 53, no. 8, pp. 2437–2445, Aug. 2011.
- [79] P. Volovitch, C. Allely, and K. Ogle, "Understanding corrosion via corrosion product characterization: I. Case study of the role of Mg alloying in Zn–Mg coating on steel," *Corrosion Science*, vol. 51, no. 6, pp. 1251–1262, Jun. 2009.
- [80] N. Hosking, M. Ström, P. Shipway, and C. Rudd, "Corrosion resistance of zinc–magnesium coated steel," *Corrosion Science*, vol. 49, no. 9, pp. 3669–3695, Sep. 2007.
- [81] S. Schuerz, M. Fleischanderl, G. Luckeneder, K. Preis, T. Haunschmied, G. Mori, and A. Kneissl, "Corrosion behaviour of Zn–Al–Mg coated steel sheet in

- sodium chloride-containing environment,” *Corrosion Science*, vol. 51, no. 10, pp. 2355–2363, Oct. 2009.
- [82] D. Persson, D. Thierry, N. LeBozec, and T. Prosek, “In situ infrared reflection spectroscopy studies of the initial atmospheric corrosion of Zn–Al–Mg coated steel,” *Corrosion Science*, vol. 72, pp. 54–63, Jul. 2013.
- [83] T. Ishikawa, M. Ueda, K. Kandori, and T. Nakayama, “Air permeability of the artificially synthesized Zn–Al–Mg alloy rusts,” *Corrosion Science*, vol. 49, no. 6, pp. 2547–2556, Jun. 2007.
- [84] M. Zheludkevich, R. Serra, M. Montemor, and M. Ferreira, “Oxide nanoparticle reservoirs for storage and prolonged release of the corrosion inhibitors,” *Electrochemistry Communications*, vol. 7, no. 8, pp. 836–840, Aug. 2005.
- [85] M. Zheludkevich, R. Serra, M. Montemor, K. Yasakau, I. M. Salvado, and M. Ferreira, “Nanostructured sol–gel coatings doped with cerium nitrate as pre-treatments for AA2024-T3,” *Electrochimica Acta*, vol. 51, no. 2, pp. 208–217, Oct. 2005.
- [86] S. Lamaka, M. Zheludkevich, K. Yasakau, R. Serra, S. Poznyak, and M. Ferreira, “Nanoporous titania interlayer as reservoir of corrosion inhibitors for coatings with self-healing ability,” *Progress in Organic Coatings*, vol. 58, no. 2-3, pp. 127–135, Feb. 2007.
- [87] S. Dias, S. Lamaka, C. Nogueira, T. Diamantino, and M. Ferreira, “Sol–gel coatings modified with zeolite fillers for active corrosion protection of AA2024,” *Corrosion Science*, vol. 62, pp. 153–162, Sep. 2012.
- [88] S. Bohm, H. N. McMurray, D. a. Worsley, and S. M. Powell, “Novel environment friendly corrosion inhibitor pigments based on naturally occurring clay minerals,” *Materials and Corrosion / Werkstoffe und Korrosion*, vol. 52, no. 12, pp. 896–903, 2001.
- [89] B. Liu, X. Zhang, G.-y. Xiao, and Y.-p. Lu, “Phosphate chemical conversion coatings on metallic substrates for biomedical application: a review.” *Materials science & engineering. C, Materials for biological applications*, vol. 47, pp. 97–104, Feb. 2015.
- [90] M. R. Yuan, J. T. Lu, and G. Kong, “Effect of SiO<sub>2</sub>:Na<sub>2</sub>O molar ratio of sodium silicate on the corrosion resistance of silicate conversion coatings,” *Surface and Coatings Technology*, vol. 204, no. 8, pp. 1229–1235, 2010.
- [91] A. Amirudin and D. Thierry, “Corrosion mechanisms of phosphated zinc layers on steel as substrates for automotive coatings,” *Progress in Organic Coatings*, vol. 28, no. 1, pp. 59–75, May 1996.

- 
- [92] L. Jiang, M. Wolpers, P. Volovitch, and K. Ogle, "The degradation of phosphate conversion coatings by electrochemically generated hydroxide," *Corrosion Science*, vol. 55, pp. 76–89, Feb. 2012.
- [93] A. Losch, E. Klusmann, and J. Schultze, "Electrochemical investigations of phosphate layers by metal deposition and cataphoretic painting," *Electrochimica Acta*, vol. 39, no. 8-9, pp. 1183–1187, Jun. 1994.
- [94] L. Jiang, M. Wolpers, P. Volovitch, and K. Ogle, "An atomic emission spectroelectrochemical study of passive film formation and dissolution on galvanized steel treated with silicate conversion coatings," *Surface and Coatings Technology*, vol. 206, no. 13, pp. 3151–3157, Feb. 2012.
- [95] V. S. Sastri, *Green Corrosion Inhibitors: Theory and Practice*. John Wiley & Sons, 2012.
- [96] P. Delahay, M. Pourbaix, and P. Van Rysselberghe, "Potential-pH Diagram of Zinc and its Applications to the Study of Zinc Corrosion," *Journal of The Electrochemical Society*, vol. 98, no. 3, p. 101, 1951.
- [97] H. Kaesche, "The passivity of zinc in aqueous solutions of sodium carbonate and sodium bicarbonate," *Electrochimica Acta*, vol. 9, no. 4, pp. 383–394, Apr. 1964.
- [98] L. Baugh, "Corrosion and polarization characteristics of zinc in neutral—acid media — I. Pure zinc in solutions of various sodium salts," *Electrochimica Acta*, vol. 24, no. 6, pp. 657–667, Jun. 1979.
- [99] R. L. David, *Handbook of Chemistry and Physics*, 88th ed. Chemical Rubber Company, 2007.
- [100] D. Kesavan, M. Gopiraman, and N. Sulochana, "Green Inhibitors for Corrosion of Metals : A Review," *Chemical Science Review and Letters*, vol. 1, no. 1, pp. 1–8, 2012.
- [101] N. K. Allam, A. A. Nazeer, and E. A. Ashour, "A review of the effects of benzotriazole on the corrosion of copper and copper alloys in clean and polluted environments," *Journal of Applied Electrochemistry*, vol. 39, no. 7, pp. 961–969, Jan. 2009.
- [102] G. Gece, "Drugs: A review of promising novel corrosion inhibitors," *Corrosion Science*, vol. 53, no. 12, pp. 3873–3898, Dec. 2011.
- [103] S. Hooshmand Zaferani, M. Sharifi, D. Zaarei, and M. R. Shishesaz, "Application of eco-friendly products as corrosion inhibitors for metals in acid pickling processes - A review," *Journal of Environmental Chemical Engineering*, vol. 1, no. 4, pp. 652–657, 2013.

- [104] R. Palou, O. Olivares-Xomelt, and N. Lickanova, "Environmentally Friendly Corrosion Inhibitors, Developments in Corrosion Protection," in *Green corrosion inhibitors: theory and practice*, D. M. Aliofkhazraei, Ed., 2014, ch. 19, pp. 431–465.
- [105] R. Twite and G. Bierwagen, "Review of alternatives to chromate for corrosion protection of aluminum aerospace alloys," *Progress in Organic Coatings*, vol. 33, no. 2, pp. 91–100, Feb. 1998.
- [106] C. Dariva and G. Alexandre, "Corrosion Inhibitors – Principles, Mechanisms and Applications," in *Developments in Corrosion Protection*, M. Aliofkhazraei, Ed. InTech, Feb. 2014.
- [107] S. Manov, F. Noli, A. Lamazouere, and L. Aries, "Surface treatment for zinc corrosion protection by a new organic chelating reagent," *Journal of Applied Electrochemistry*, vol. 29, no. 8, pp. 995–1003, 1999.
- [108] M. S. Abdel-All, Z. A. Ahmed, and M. S. Hassan, "Inhibiting and accelerating effects of some quinolines on the corrosion of zinc and some binary zinc alloys in HCl solution," *Journal of Applied Electrochemistry*, vol. 22, no. 11, pp. 1104–1109, Nov. 1992.
- [109] S. Manov, L. Arie, A. Lamazouère, and L. Ariès, "Electrochemical study of the corrosion behaviour of zinc treated with a new organic chelating inhibitor," *Corrosion Science*, vol. 42, no. 7, pp. 1235–1248, Jul. 2000.
- [110] R. L. LEROY, "Polythioglycolate Passivation of Zinc," *Corrosion*, vol. 34, no. 4, pp. 113–119, Apr. 1978.
- [111] R. L. Leroy, "Chelate Inhibitors for Zinc and Galvanized Products," *Corrosion*, vol. 34, no. 3, pp. 98–110, Mar. 1978.
- [112] K. Wippermann, J. Schultze, R. Kessel, and J. Penninger, "The inhibition of zinc corrosion by bisaminotriazole and other triazole derivatives," *Corrosion Science*, vol. 32, no. 2, pp. 205–230, 1991.
- [113] B. Müller and G. Imblo, "Heterocycles as corrosion inhibitors for zinc pigments in aqueous alkaline media," *Corrosion Science*, vol. 38, no. 2, pp. 293–300, 1996.
- [114] F. Berrekhis, Y. Roques, L. Aries, and M. Hajjaji, "Electrodeposition and characterization of casein coatings on a zinc alloy," *Progress in Organic Coatings*, vol. 33, no. 1, pp. 7–13, 1998.
- [115] M. Troquet, J. Labbe, and J. Pagetti, "The mechanism of the inhibition of zinc corrosion in 1N HCl solution by tetraphenylphosphonium bromide," *Corrosion Science*, vol. 21, no. 2, pp. 101–117, 1981.

- [116] M. Troquet and J. Pageiti, "Etude du mecanisme de l'inhibition du zinc en milieu HCl par les sels de phoshonium," *Electrochimica Acta*, vol. 27, no. 2, pp. 197–203, 1982.
- [117] K. Aramaki, "Effects of organic inhibitors on corrosion of zinc in an aerated 0.5 M NaCl solution," *Corrosion Science*, vol. 43, no. 10, pp. 1985–2000, Oct. 2001.
- [118] A. G. G. Allah and H. Moustafa, "Quantum mechanical calculations of amino pyrazole derivatives as corrosion inhibitors for zinc, copper and brass in acid chloride solution," *Journal of Applied Electrochemistry*, vol. 22, no. 7, pp. 644–648, Jul. 1992.
- [119] E. Stupnišek-Lisac, S. Podbršček, and T. Sorić, "Non-toxic organic zinc corrosion inhibitors in hydrochloric acid," *Journal of Applied Electrochemistry*, vol. 24, no. 8, pp. 779–784, Aug. 1994.
- [120] M. S. Morad, "Inhibition of phosphoric acid corrosion of zinc by organic onium compounds and their adsorption characteristics," *Journal of Applied Electrochemistry*, vol. 29, pp. 619–626, 1999.
- [121] M. S. A. Aal, A. A. A. Wahab, and A. E. Saied, "A Study of the Inhibiting Action of Benzene Thiols and Related Compounds on the Corrosion of Zinc in Acidic Media," Mar. 2012.
- [122] H. Rudresh and S. Mayanna, "The synergistic effect of Halide ions on the corrosion inhibition of zinc by n-decylamine," *Corrosion Science*, vol. 19, no. 6, pp. 361–370, 1979.
- [123] F. Donahue and K. Nobe, "Theory of Organic Corrosion Inhibitors Adsorption and Linear Free Energy Relationships," *Journal of Electrochemical Society*, vol. 122, no. 9, pp. 886–891, 1965.
- [124] P. Atkins, *Physical Chemistry*, 4th ed. Oxford University Press, 1990.
- [125] N. Helal and W. Badawy, "Environmentally safe corrosion inhibition of Mg–Al–Zn alloy in chloride free neutral solutions by amino acids," *Electrochimica Acta*, vol. 56, no. 19, pp. 6581–6587, Jul. 2011.
- [126] D. G. Shchukin, S. V. Lamaka, K. a. Yasakau, M. L. Zheludkevich, M. G. S. Ferreira, and H. Möhwald, "Active anticorrosion coatings with halloysite nanocontainers," *Journal of Physical Chemistry C*, vol. 112, no. 4, pp. 958–964, 2008.
- [127] D. G. Shchukin, M. Zheludkevich, and H. Mohwald, "Feedback active coatings based on incorporated nanocontainers," *Journal of Materials Chemistry*, vol. 16, no. 47, p. 4561, 2006.

- [128] D. G. Shchukin, M. Zheludkevich, K. Yasakau, S. Lamaka, M. G. S. Ferreira, and H. Möhwald, "Layer-by-layer assembled nanocontainers for self-healing corrosion protection," *Advanced Materials*, vol. 18, no. 13, pp. 1672–1678, 2006.
- [129] M. Barzegar-jalali, K. Adibkia, H. Valizadeh, M. Reza, and S. Shadbad, "Kinetic Analysis of Drug Release From Nanoparticles," vol. 11, no. 1, pp. 167–177, 2008.
- [130] P. Costa and J. M. Sousa Lobo, "Modeling and comparison of dissolution profiles," *European Journal of Pharmaceutical Sciences*, vol. 13, no. 2, pp. 123–133, May 2001.
- [131] R. Rojas, A. Jimenez-Kairuz, R. Manzo, and C. Giacomelli, "Release kinetics from LDH-drug hybrids: Effect of layers stacking and drug solubility and polarity," *Colloids and Surfaces A: Physicochemical and Engineering Aspects*, vol. 463, pp. 37–43, Dec. 2014.
- [132] R. Rojas, M. Palena, a.F. Jimenez-Kairuz, R. Manzo, and C. Giacomelli, "Modeling drug release from a layered double hydroxide–ibuprofen complex," *Applied Clay Science*, vol. 62-63, pp. 15–20, Jul. 2012.
- [133] P. L. Ritger and N. A. Peppas, "A simple equation for description of solute release II. Fickian and anomalous release from swellable devices," *Journal of Controlled Release*, vol. 5, no. 1, pp. 37–42, Jun. 1987.
- [134] X. Gao, L. Lei, D. O'Hare, J. Xie, P. Gao, and T. Chang, "Intercalation and controlled release properties of vitamin C intercalated layered double hydroxide," *Journal of Solid State Chemistry*, vol. 203, pp. 174–180, 2013.
- [135] M. S. Gasser, "Inorganic layered double hydroxides as ascorbic acid (vitamin C) delivery system-Intercalation and their controlled release properties," *Colloids and Surfaces B: Biointerfaces*, vol. 73, no. 1, pp. 103–109, 2009.
- [136] V. Rives, M. del Arco, and C. Martín, "Intercalation of drugs in layered double hydroxides and their controlled release: A review," *Applied Clay Science*, vol. 88-89, pp. 239–269, Feb. 2014.
- [137] M. L. Zheludkevich, I. M. Salvado, and M. G. S. Ferreira, "Sol-gel coatings for corrosion protection of metals," *Journal of Materials Chemistry*, vol. 15, no. 48, p. 5099, 2005.
- [138] M. L. Zheludkevich, R. Serra, M. F. Montemor, I. M. Miranda Salvado, and M. G. S. Ferreira, "Corrosion protective properties of nanostructured sol-gel hybrid coatings to AA2024-T3," *Surface and Coatings Technology*, vol. 200, no. 9, pp. 3084–3094, 2006.
- [139] N. Birbilis and B. Hinton, *Fundamentals of Aluminium Metallurgy*. Elsevier, 2011.

- [140] S. Thomas, N. Birbilis, M. S. Venkatraman, and I. S. Cole, "Corrosion of Zinc as a Function of pH," *Corrosion*, vol. 9312, no. January, pp. 1–9, 2012.
- [141] G. Busca, *Heterogeneous Catalytic Materials*. Elsevier, 2014.
- [142] F. Cavani, F. Trifiro, and A. Vaccari, "Hydrotalcite-type anionic clays: preparation, properties and applications," *Catalysis Today*, no. 11, pp. 173–301, 1991.
- [143] C. Frondel, "Constitution and polymorphism of the pyroaurite and sjogrenite groups," *American Mineralogist*, vol. 26, no. 5, pp. 295–315, 1941.
- [144] W. Feitknecht and M. Gerber, "Zur Kenntnis der Doppelhydroxyde und basischen Doppelsalze III. Über Magnesium-Aluminiumdoppelhydroxyd," *Helvetica Chimica Acta*, vol. 25, no. 1, pp. 131–137, Feb. 1942.
- [145] W. Feitknecht, "Über die Bildung von Doppelhydroxyden zwischen zwei- und dreiwertigen Metallen," *Helvetica Chimica Acta*, vol. 25, no. 3, pp. 555–569, May 1942.
- [146] V. Rives, *Layered Double Hydroxides: Present and Future*. Nova Publishers, 2001.
- [147] J. Tedim, A. Kuznetsova, A. Salak, F. Montemor, D. Snihirova, M. Pilz, M. Zheludkevich, and M. Ferreira, "Zn–Al layered double hydroxides as chloride nanotraps in active protective coatings," *Corrosion Science*, vol. 55, pp. 1–4, Feb. 2012.
- [148] R. G. Buchheit, S. B. Mamidipally, P. Schmutz, and H. Guan, "Active Corrosion Protection in Ce-Modified Hydrotalcite Conversion Coatings," *Corrosion*, vol. 58, no. 1, pp. 3–14, Jan. 2002.
- [149] S. K. Poznyak, J. Tedim, L. M. Rodrigues, A. N. Salak, M. L. Zheludkevich, L. F. P. Dick, and M. G. S. Ferreira, "Novel inorganic host layered double hydroxides intercalated with guest organic inhibitors for anticorrosion applications," *ACS Applied Materials and Interfaces*, vol. 1, no. 10, pp. 2353–2362, 2009.
- [150] H. Hintze-Bruening, J.-B. Kues, S. Sinnwell, K. Wapner, F. Leroux, and T. Stimpfling, "Method for production of anticorrosive coatings containing layered double hydroxides," 2013.
- [151] M. Salgueiro Azevedo, C. Allély, K. Ogle, and P. Volovitch, "Corrosion mechanisms of Zn(Mg, Al) coated steel in accelerated tests and natural exposure: 1. The role of electrolyte composition in the nature of corrosion products and relative corrosion rate," *Corrosion Science*, vol. 90, pp. 472–481, Jan. 2015.
- [152] S. Miyata, "Anion-exchange properties of hydrotalcite-like compounds," *Clays and Clay Minerals*, vol. 31, no. 4, pp. 305–311, 1983.

- [153] M. L. Parello, R. Rojas, and C. E. Giacomelli, "Dissolution kinetics and mechanism of Mg-Al layered double hydroxides: A simple approach to describe drug release in acid media," *Journal of Colloid and Interface Science*, vol. 351, no. 1, pp. 134–139, 2010.
- [154] K. Ogle, "Atomic emission spectroelectrochemistry: A new look at the corrosion, dissolution and passivation of complex materials," *Corrosion and Materials*, vol. 37, no. 3, pp. 58–65, 2012.
- [155] K. Vetter, *Electrochemical kinetics. Theoretical and experimental aspects*. New York: Academic Press, 1967.
- [156] B. Tribollet and M. E. Orazem, *Electrochemical Impedance Spectroscopy*. John Wiley & Sons, 2008.
- [157] D. Jones, *Principles and prevention of corrosion*, 2nd ed. Prentice Hall, 1996.
- [158] P. Marcus, *Corrosion Mechanisms in Theory and Practice*, 2nd ed. New York: Marcel Dekker, 2002.
- [159] W. Albery and M. Hitchman, *Ring-Disk Electrodes*. Oxford University Press, 1971.
- [160] K. Ogle and S. Weber, "Anodic Dissolution of 304 Stainless Steel Using Atomic Emission Spectroelectrochemistry," *Journal of The Electrochemical Society*, vol. 147, no. 5, p. 1770, May 2000.
- [161] K. Ogle, J. Baeyens, J. Swiatowska, and P. Volovitch, "Atomic emission spectroelectrochemistry applied to dealloying phenomena: I. The formation and dissolution of residual copper films on stainless steel," *Electrochimica Acta*, vol. 54, no. 22, pp. 5163–5170, Sep. 2009.
- [162] Q. Van Overmeere, D. Mercier, R. Santoro, and J. Proost, "In Situ Optical Emission Spectrometry during Porous Anodic Alumina Initiation and Growth in Phosphoric Acid," *Electrochemical and Solid-State Letters*, vol. 15, no. 1, p. C1, 2012.
- [163] S. O. Klemm, A. a. Topalov, C. a. Laska, and K. J. Mayrhofer, "Coupling of a high throughput microelectrochemical cell with online multielemental trace analysis by ICP-MS," *Electrochemistry Communications*, vol. 13, no. 12, pp. 1533–1535, Dec. 2011.
- [164] N. Ott, A. Beni, A. Ulrich, C. Ludwig, and P. Schmutz, "Flow microcapillary plasma mass spectrometry-based investigation of new Al-Cr-Fe complex metallic alloy passivation." *Talanta*, vol. 120, pp. 230–8, Mar. 2014.

- [165] N. Homazava, a. Ulrich, and U. Krähenbühl, “Spatially and time-resolved element-specific in situ corrosion investigations with an online hyphenated microcapillary flow injection inductively coupled plasma mass spectrometry set-up,” *Spectrochimica Acta - Part B Atomic Spectroscopy*, vol. 63, no. 7, pp. 777–783, 2008.
- [166] X. Wang, M. Bernard, C. Deslouis, S. Joiret, and P. Rousseau, “Kinetic reactions in thin polyaniline films revisited through Raman–impedance dynamic coupling,” *Electrochimica Acta*, vol. 56, no. 10, pp. 3485–3493, Apr. 2011.
- [167] C. Gabrielli, M. Keddam, F. Minouffet-Laurent, K. Ogle, and H. Perrot, “Investigation of zinc chromatation. I. Application of QCM–ICP coupling,” *Electrochimica Acta*, vol. 48, no. 8, pp. 965–976, Apr. 2003.
- [168] M. Thompson and N. Walsh, *Handbook of Inductively Coupled Plasma Atomic Emission Spectrometry*. CRC Press, 1990.
- [169] P. Boumans, *Inductively Coupled Plasma Emission Spectroscopy, Methodology, Instrumentation and Performance (Chemical Analysis: A Series of Monographs on Analytical Chemistry and Its Applications) (Part 1)*. Wiley-Interscience, 1987.
- [170] S. Greenfield, I. L. Jones, and C. T. Berry, “High-pressure plasmas as spectroscopic emission sources,” *The Analyst*, vol. 89, no. 1064, p. 713, 1964.
- [171] M. Serdechnova, P. Volovitch, and K. Ogle, “Atomic emission spectroelectrochemistry study of the degradation mechanism of model high-temperature paint containing sacrificial aluminum particles,” *Surface and Coatings Technology*, vol. 206, no. 8-9, pp. 2133–2139, Jan. 2012.
- [172] M. Mokaddem, P. Volovitch, F. Rechou, R. Oltra, and K. Ogle, “The anodic and cathodic dissolution of Al and Al–Cu–Mg alloy,” *Electrochimica Acta*, vol. 55, no. 11, pp. 3779–3786, Apr. 2010.
- [173] D. Tissue, “Inductively-Coupled Plasma (ICP) Excitation Source (<https://www.uam.es/docencia/quimcursos/Scimedia/chemed/spec/atomic/emission/icp.htm>),” 1996.
- [174] S. Lebouil, “Etude et réalisation d’un couplage instrumental pour la mesure du dégagement d’hydrogène ne temps réel: apports des outils microfluidiques,” Ph.D. dissertation, UMPC, 2013.
- [175] I. S. Cole, T. H. Muster, D. Lau, N. Wright, and N. S. Azmat, “Products Formed during the Interaction of Seawater Droplets with Zinc Surfaces,” *Journal of The Electrochemical Society*, vol. 157, no. 6, p. C213, 2010.
- [176] T. H. Muster and I. S. Cole, “The protective nature of passivation films on zinc: surface charge,” *Corrosion Science*, vol. 46, no. 9, pp. 2319–2335, Sep. 2004.

- [177] D. D. Macdonald, "Passivity—the key to our metals-based civilization," *Pure and Applied Chemistry*, vol. 71, no. 6, pp. 951–978, 1999.
- [178] S. Walkner and A. W. Hassel, "Combined chemical and EIS study of the reaction of zinc coatings under alkaline conditions," *Electrochimica Acta*, vol. 131, pp. 130–136, 2014.
- [179] N. A. Hampson and M. J. Tarbox, "The Anodic Behavior of Zinc in Potassium Hydroxide Solution," *Journal of The Electrochemical Society*, vol. 110, no. 2, p. 95, 1963.
- [180] S. Bonk, M. Wicinski, A. W. Hassel, and M. Stratmann, "Electrochemical characterizations of precipitates formed on zinc in alkaline sulphate solution with increasing pH values," *Electrochemistry Communications*, vol. 6, no. 8, pp. 800–804, Aug. 2004.
- [181] K. M. Ismail, "Evaluation of cysteine as environmentally friendly corrosion inhibitor for copper in neutral and acidic chloride solutions," *Electrochimica Acta*, vol. 52, no. 28, pp. 7811–7819, Nov. 2007.
- [182] S. Shen, X.-y. Guo, P. Song, Y.-C. Pan, H.-q. Wang, Y. Wen, and H.-F. Yang, "Phytic acid adsorption on the copper surface: Observation of electrochemistry and Raman spectroscopy," *Applied Surface Science*, vol. 276, pp. 167–173, Jul. 2013.
- [183] V. Shkirskiy, P. Keil, H. Hintze-Bruening, F. Leroux, K. Ogle, and P. Volovitch, "The effects of L-cysteine on the inhibition and accelerated dissolution processes of zinc metal," *Corrosion Science*, p. Submitted.
- [184] G. Berton, "The stability constants of metal complexes of amino acids with polar side chains," *Pure and Applied Chemistry*, vol. 67, no. 7, pp. 1117–1240, 1995.
- [185] V. Shkirskiy, P. Keil, H. Hintze-Bruening, F. Leroux, P. Vialat, K. Ogle, and P. Volovitch, "Role of environment on release kinetics of intercalated MoO<sub>4</sub><sup>2-</sup> inhibitor from Zn<sub>2</sub>Al/- layered double hydroxides." in *Eurocorr 2015*.
- [186] V. Shkirskiy, A. D. King, O. Gharbi, P. Volovitch, J. R. Scully, K. Ogle, and N. Birbilis, "Revisiting the electrochemical impedance spectroscopy of magnesium with online inductively coupled plasma atomic emission spectroscopy." *ChemPhysChem*, vol. 16, no. 3, pp. 536–9, Nov. 2014.
- [187] V. Shkirskiy, P. Keil, H. Hintze-Bruening, F. Leroux, T. Stimpfling, D. Dragoe, K. Ogle, and P. Volovitch, "MoO<sub>4</sub><sup>2-</sup> as a soluble inhibitor for Zn in neutral and alkaline solutions," *Corrosion Science*, p. in press, May 2015.
- [188] L. G. Bela, *Instrument Engineers' Handbook, Fourth Edition, Volume Two: Process Control and Optimization*, 4th ed. CRC Press, 2006.

- 
- [189] W. J. Lorenz, "Determination of corrosion rates by electrochemical DC and AC methods," *Corrosion Science*, vol. 21, no. February, pp. 647–672, 1981.
- [190] A. Aksut, W. Lorenz, and F. Mansfeld, "The determination of corrosion rates by electrochemical DC and AC methods - II. System with discontinuous steady state polarization behavior," *Corrosion Science*, vol. 22, no. 7, pp. 611–619, 1982.
- [191] I. Epelboin, M. Keddam, and H. Takenouti, "Use of impedance measurements for the determination of the instant rate of metal corrosion," *Journal of Applied Electrochemistry*, vol. 2, no. 1, pp. 71–79, Feb. 1972.
- [192] F. Mansfeld, M. W. Kendig, and S. Tsa, "Recording and Analysis of AC Impedance Data for Corrosion Studies II . Experimental Approach and Results," vol. 35, no. 1979, pp. 570–580, 1982.
- [193] J. R. Scully, "Polarization Resistance Method for Determination of Instantaneous Corrosion Rates," *Corrosion*, vol. 56, no. 2, pp. 199–218, Feb. 2000.
- [194] M. Stern and A. Geary, "Electrochemical Polarization: I. A Theoretical Analysis of the Shape of Polarization Curves," *Journal of Electrochemical Society*, vol. 104, no. 1, pp. 56–63, 1957.
- [195] Y.-C. Chang, "A Model for the Anodic Dissolution of the Zinc Electrode in the Prepassive Region," *Journal of The Electrochemical Society*, vol. 136, no. 11, p. 3398, 1989.
- [196] X. Zhang, W. Sloof, A. Hovestad, E. van Westing, H. Terryn, and J. de Wit, "Characterization of chromate conversion coatings on zinc using XPS and SKPFM," *Surface and Coatings Technology*, vol. 197, no. 2-3, pp. 168–176, Jul. 2005.
- [197] A. Pilbáth, L. Nyikos, I. Bertóti, and E. Kálmán, "Zinc corrosion protection with 1,5-diphosphono-pentane," *Corrosion Science*, vol. 50, no. 12, pp. 3314–3321, Dec. 2008.
- [198] T. R. Ralph, M. L. Hitchman, J. P. Millington, and F. C. Walsh, "The electrochemistry of L-cystine and L-cysteine and kinetic studies Part 1: Thermodynamic and kinetic studies," *Journal of Electroanalytical Chemistry*, vol. 375, pp. 1–15, 1994.
- [199] E. Kendall and F. Nord, "Reversible oxidation-reduction systems of cysteine-cystine and reduced and oxydezed clutathione," *The journal of Bioloical Chemistry*, vol. 69, pp. 295–337, 1926.
- [200] A. Aksüt and S. Bilgiç, "The effect of amino acids on the corrosion of nickel in H<sub>2</sub>SO<sub>4</sub>," *Corrosion Science*, vol. 33, no. 3, pp. 379–387, 1992.

- [201] A. Silva, S. Agostinho, O. Barcia, G. Cordeiro, and E. D'Elia, "The effect of cysteine on the corrosion of 304L stainless steel in sulphuric acid," *Corrosion Science*, vol. 48, no. 11, pp. 3668–3674, Nov. 2006.
- [202] G. M. A. El-Hafez and W. A. Badawy, "The use of cysteine, N-acetyl cysteine and methionine as environmentally friendly corrosion inhibitors for Cu–10Al–5Ni alloy in neutral chloride solutions," *Electrochimica Acta*, vol. 108, pp. 860–866, Oct. 2013.
- [203] M. B. Petrović, M. B. Radovanović, A. T. Simonović, and S. M. Milić, "The Effect of Cysteine on the Behaviour of Copper in Neutral and Alkaline Sulphate Solutions," *International Journal of Electrochemical Science*, vol. 7, pp. 9043–9057, 2012.
- [204] J. Matos, L. Pereira, S. Agostinho, O. Barcia, G. Cordeiro, and E. D'Elia, "Effect of cysteine on the anodic dissolution of copper in sulfuric acid medium," *Journal of Electroanalytical Chemistry*, vol. 570, no. 1, pp. 91–94, Aug. 2004.
- [205] K. Barouni, M. Mihit, L. Bazzi, R. Salghi, B. Hammouti, and A. Albourine, "The Inhibited Effect of Cysteine Towards the Corrosion of Copper in Nitric Acid Solution," *The Open Corrosion Journal*, vol. 3, pp. 58–63, 2010.
- [206] A. A. Nazeer, A. S. Fouda, and E. A. Ashour, "Inhibition Effect of Cysteine and Glycine towards the Corrosion of Cu10Ni Alloy in Sulfide Polluted Saltwater : Electrochemical and Impedance Study," *J. Mater. Environ. Sci.*, vol. 2, no. 1, pp. 24–38, 2011.
- [207] M. S. Morad, "Effect of amino acids containing sulfur on the corrosion of mild steel in phosphoric acid solutions containing Cl<sup>-</sup>, F<sup>-</sup> and Fe<sup>3+</sup> ions: Behavior under polarization conditions," *Journal of Applied Electrochemistry*, vol. 35, no. 9, pp. 889–895, 2005.
- [208] V. Hluchan, B. Wheeler, and N. Hackerman, "Amino acids as corrosion inhibitors in hydrochloric acid solutions," *Werkstoffe und Korrosion*, vol. 39, pp. 512–517, 1988.
- [209] H. Hintze-Bruening, F. Leroux, T. Stimpfling, P. Keil, and H. Theil, "Method for producing an anti-corrosion coating," 2014.
- [210] P. Volovitch, I. Gazizzullin, F. Ruel, and K. Ogle, "An atomic emission spectroelectrochemical study of corrosion inhibition: The effect of hexamethylenetetramine on the reaction of mild steel in HCl," *Corrosion Science*, vol. 53, no. 4, pp. 1362–1368, Apr. 2011.
- [211] D. Landolt, *Corrosion et chimie de surface des metaux, Traité des Matériaux*, presses po ed., 1993.

- [212] A. Pasupathy, S. Nirmala, G. Abirami, A. Satish, and R. Paul Milton, "Cystein as a Corrosion Inhibitor for Zinc in Acidic Solutions," *International Journal of Scientific and Research Publications*, vol. 4, no. 3, pp. 1–3, 2014.
- [213] V. Shkirskiy, P. Keil, H. Hintze-Bruening, F. Leroux, P. Volovitch, and K. Ogle, "Observation of anodic zinc dissolution during cathodic polarization and its consequences for corrosion rate measurements," *Submitted to Electrochimica Acta*, 2015.
- [214] E. Johnson, *UV atlas of organic compounds*, 5th ed., 1971.
- [215] J. Yoo, P. Volovitch, A. Abdel Aal, C. Allely, and K. Ogle, "The effect of an artificially synthesized simonkolleite layer on the corrosion of electrogalvanized steel," *Corrosion Science*, vol. 70, pp. 1–10, May 2013.
- [216] R. Dawson, D. Elliot, W. Elliot, and K. Jones, *Data for Biochemical Research*. Clarendon Press, Oxford, 1986.
- [217] M. Bernard, A. Hugot-Le Goff, D. Massinon, and N. Phillips, "Underpaint corrosion of zinc-coated steel sheet studied by in situ raman spectroscopy," *Corrosion Science*, vol. 35, no. 5-8, pp. 1339–1349, Jan. 1993.
- [218] Y. Chen, P. Schneider, B.-J. Liu, S. Borodin, B. Ren, and A. Erbe, "Electronic structure and morphology of dark oxides on zinc generated by electrochemical treatment." *Physical chemistry chemical physics : PCCP*, vol. 15, no. 24, pp. 9812–22, Jun. 2013.
- [219] L. Baugh and A. Baikie, "Passivation of zinc in concentrated alkaline solution—II. Role of various experimental factors and the distinction between the solid-state and dissolution—precipitation mechanisms," *Electrochimica Acta*, vol. 30, no. 9, pp. 1173–1183, Sep. 1985.
- [220] A. P. Gondikas, E. K. Jang, and H. Hsu-Kim, "Influence of amino acids cysteine and serine on aggregation kinetics of zinc and mercury sulfide colloids," *Journal of Colloid and Interface Science*, vol. 347, no. 2, pp. 167–171, 2010.
- [221] T. Ishikawa, M. Murai, K. Kandori, and T. Nakayama, "Structure and composition of artificially synthesized rusts of Zn-Fe and Zn-Ti alloys," *Corrosion Science*, vol. 48, no. 10, pp. 3172–3185, 2006.
- [222] H. Tanaka, A. Fujioka, A. Futoyu, K. Kandori, and T. Ishikawa, "Synthesis and characterization of layered zinc hydroxychlorides," *Journal of Solid State Chemistry*, vol. 180, no. 7, pp. 2061–2066, 2007.
- [223] A.-L. Troutier-Thuilliez, C. Taviot-Guého, J. Cellier, H. Hintze-Bruening, and F. Leroux, "Layered particle-based polymer composites for coatings: Part I. Evaluation of layered double hydroxides," *Progress in Organic Coatings*, vol. 64, no. 2-3, pp. 182–192, Feb. 2009.

- [224] K. Ogle, S. Morel, and N. Meddahi, "An electrochemical study of the delamination of polymer coatings on galvanized steel," *Corrosion Science*, vol. 47, no. 8, pp. 2034–2052, Aug. 2005.
- [225] H. Dafydd, D. Worsley, and H. McMurray, "The kinetics and mechanism of cathodic oxygen reduction on zinc and zinc–aluminium alloy galvanized coatings," *Corrosion Science*, vol. 47, no. 12, pp. 3006–3018, Dec. 2005.
- [226] P. J. Gellings, H. C. Ekama, and V. U. Shipyards, "The change pH under paint film due to corrosion protection," *Corrosion Science*, vol. 15, no. January, pp. 529–535, 1975.
- [227] A. Leng, H. Streckel, and M. Stratmann, "The delamination of polymeric coatings from steel. Part 1: Calibration of the Kelvinprobe and basic delamination mechanism," *Corrosion Science*, vol. 41, pp. 547–579, 1999.
- [228] C. Gabrielli, M. Keddam, F. Minouflet-Laurent, K. Ogle, and H. Perrot, "Investigation of zinc chromatisation," *Electrochimica Acta*, vol. 48, no. 11, pp. 1483–1490, May 2003.
- [229] E. Almeida, T. C. Diamantino, M. O. Figueiredo, and C. Sa, "Oxidising alternative species to chromium VI in zinc galvanised steel surface treatment . Part 1 — A morphological and chemical study," *Surface and Coatings Technology*, vol. 106, pp. 8–17, 1998.
- [230] A. C. Guy and A. M. Daniel, "Molybdate-containing corrosion inhibitors," Mar. 1991.
- [231] G. M. Treacy, G. D. Wilcox, M. O. W. Richardson, and G. Britain, "Behaviour of molybdate-passivated zinc coated steel exposed to corrosive chloride environments," *Journal of Applied Electrochemistry*, vol. 29, no. 5, pp. 647–654, 1999.
- [232] R.-C. Zeng, Z.-G. Liu, F. Zhang, S.-Q. Li, H.-Z. Cui, and E.-H. Han, "Corrosion of molybdate intercalated hydrotalcite coating on AZ31 Mg alloy," *Journal of Materials Chemistry A*, vol. 2, no. 32, p. 13049, Jun. 2014.
- [233] B. Bhanvase, M. Patel, and S. Sonawane, "Kinetic properties of layer-by-layer assembled cerium zinc molybdate nanocontainers during corrosion inhibition," *Corrosion Science*, vol. 88, pp. 170–177, Nov. 2014.
- [234] W. D. Robertson, "Closure to 'Discussion of 'Molybdate and Tungstate as Corrosion Inhibitors and the Mechanism of Inhibition' [W. D. Robertson (pp. 94–100)]'," *Journal of The Electrochemical Society*, vol. 98, no. 12, p. 515, Dec. 1951.

- [235] C.-Y. Tsai, J.-S. Liu, P.-L. Chen, and C.-S. Lin, "A two-step roll coating phosphate/molybdate passivation treatment for hot-dip galvanized steel sheet," *Corrosion Science*, vol. 52, no. 10, pp. 3385–3393, Oct. 2010.
- [236] D.-l. Liu, Z.-g. Yang, Z.-q. Wang, and C. Zhang, "Synthesis and evaluation of corrosion resistance of molybdate-based conversion coatings on electroplated zinc," *Surface and Coatings Technology*, vol. 205, no. 7, pp. 2328–2334, Dec. 2010.
- [237] K. Emregül and A. Aksüt, "The effect of sodium molybdate on the pitting corrosion of aluminum," *Corrosion Science*, vol. 45, no. 11, pp. 2415–2433, Nov. 2003.
- [238] T. R. Weber, M. A. Stranick, and M. S. Vukasovich, "Molybdate Corrosion Inhibition in Deaerated and Low-Oxygen Waters," *Corrosion*, vol. 42, no. 9, pp. 542–545, Sep. 1986.
- [239] W. C. Moshier and G. D. Davis, "Interaction of Molybdate Anions with the Passive Film on Aluminum," *Corrosion*, vol. 46, no. 1, pp. 43–50, Jan. 1990.
- [240] A. Shams El Din and L. Wang, "Mechanism of corrosion inhibition by sodium molybdate," *Desalination*, vol. 107, no. 1, pp. 29–43, Sep. 1996.
- [241] M. Pryor and M. Cohen, "The Inhibition of the Corrosion of Iron by Some Anodic Inhibitor," *Journal of Electrochemical Society*, vol. 100, no. 5, pp. 203–215, 1953.
- [242] J.-G. Choi and L. Thompson, "XPS study of as-prepared and reduced molybdenum oxides," *Applied Surface Science*, vol. 93, no. 2, pp. 143–149, Feb. 1996.
- [243] D. Kim, S. V. Kagwade, and C. R. Clayton, "Identincation of Mo (V) Commonly Observed in Passive Films Formed on Stainless Steels," *Surface and interface analysis*, vol. 26, no. September 1997, pp. 155–159, 1998.
- [244] G. Lindbergh and D. Simonsson, "Inhibition of cathode reaction in sodium hydroxide solution containing chromate," *Electrochimica Acta*, vol. 36, no. 13, pp. 1985–1994, 1991.
- [245] Z. Long, Y. Zhou, and L. Xiao, "Characterization of black chromate conversion coating on the electrodeposited zinc–iron alloy," *Applied Surface Science*, vol. 218, no. 1-4, pp. 124–137, Sep. 2003.
- [246] B. Fernández, R. Pereiro, and A. Sanz-Medel, "Glow discharge analysis of nanostructured materials and nanolayers-A review." *Analytica chimica acta*, vol. 679, no. 1-2, pp. 7–16, Oct. 2010.
- [247] A. P. Yadav, A. Nishikata, and T. Tsuru, "Oxygen reduction mechanism on corroded zinc," *Journal of Electroanalytical Chemistry*, vol. 585, no. 1, pp. 142–149, Nov. 2005.

- [248] E. Samsonl, J. Marchandl, and K. A. Snyder, "Calculation of ionic diffusion coefficients on the basis of migration test results by Calculation of ionjc diffusjon coefficients on the basis of migration test results," *Materials and Structures*, vol. 36, no. 257, pp. 156–165, 2003.
- [249] E. Roussi, A. Tsetsekou, D. Tsiourvas, and A. Karantonis, "Novel hybrid organo-silicate corrosion resistant coatings based on hyperbranched polymers," *Surface and Coatings Technology*, vol. 205, no. 10, pp. 3235–3244, Feb. 2011.
- [250] a. N. Khramov, N. N. Voevodin, V. N. Balbyshev, and M. S. Donley, "Hybrid organo-ceramic corrosion protection coatings with encapsulated organic corrosion inhibitors," *Thin Solid Films*, vol. 447-448, pp. 549–557, 2004.
- [251] E. V. Skorb, D. Fix, D. V. Andreeva, H. Möhwald, and D. G. Shchukin, "Surface-Modified Mesoporous SiO<sub>2</sub> Containers for Corrosion Protection," *Advanced Functional Materials*, vol. 19, no. 15, pp. 2373–2379, Aug. 2009.
- [252] I. Kartsonakis, I. Daniilidis, and G. Kordas, "Encapsulation of the corrosion inhibitor 8-hydroxyquinoline into ceria nanocontainers," *Journal of Sol-Gel Science and Technology*, vol. 48, no. 1-2, pp. 24–31, Aug. 2008.
- [253] D. Fix, D. V. Andreeva, Y. M. Lvov, D. G. Shchukin, and H. Möhwald, "Application of Inhibitor-Loaded Halloysite Nanotubes in Active Anti-Corrosive Coatings," *Advanced Functional Materials*, vol. 19, no. 11, pp. 1720–1727, Jun. 2009.
- [254] A. Vaccari, *Layered double hydroxides: present and future*, Nov. 2002, vol. 22, no. 1-2.
- [255] R. Rojas, M. R. Perez, E. M. Erro, P. I. Ortiz, M. A. Ulibarri, and C. E. Giacomelli, "EDTA modified LDHs as Cu<sup>2+</sup> scavengers: Removal kinetics and sorbent stability," *Journal of Colloid and Interface Science*, vol. 331, no. 2, pp. 425–431, 2009.
- [256] T. Kameda, E. Kondo, and T. Yoshioka, "Treatment of Cr(VI) in aqueous solution by Ni–Al and Co–Al layered double hydroxides: Equilibrium and kinetic studies," *Journal of Water Process Engineering*, pp. 1–6, 2014.
- [257] M. a. Woo, T. Woo Kim, M. J. Paek, H. W. Ha, J. H. Choy, and S. J. Hwang, "Phosphate-intercalated CaFe-layered double hydroxides: Crystal structure, bonding character, and release kinetics of phosphate," *Journal of Solid State Chemistry*, vol. 184, no. 1, pp. 171–176, 2011.
- [258] L. Châtelet, J. Y. Bottero, J. Yvon, and a. Bouchelaghem, "Competition between monovalent and divalent anions for calcined and uncalcined hydrotalcite: Anion exchange and adsorption sites," *Colloids and Surfaces A: Physicochemical and Engineering Aspects*, vol. 111, no. 3, pp. 167–175, 1996.

- [259] A. Davantes and G. Lefevre, "In Situ Real Time Infrared Spectroscopy of Sorption of (Poly)molybdate Ions into Layered Double Hydroxides," *The journal of Physical Chemistry*, 2013.
- [260] L. M. Parker, N. B. Milestone, and R. H. Newman, "The Use of Hydrotalcite as an Anion Absorbent," *Industrial & Engineering Chemistry Research*, vol. 34, no. 4, pp. 1196–1202, Apr. 1995.
- [261] J. Chakraborty, S. Sengupta, S. Dasgupta, M. Chakraborty, S. Ghosh, S. Mallik, K. L. Das, and D. Basu, "Determination of trace level carbonate ion in Mg-Al layered double hydroxide: Its significance on the anion exchange behaviour," *Journal of Industrial and Engineering Chemistry*, vol. 18, no. 6, pp. 2211–2216, 2012.
- [262] L. Wenyan, B. Jerry, J. Scott, and C. Luz, "pH-sensitive microparticles with matrix-dispersed active agent," 2014.
- [263] D. Snihirova, S. V. Lamaka, M. Cardoso, J. A. Condeço, H. E. Ferreira, and M. de Fatima Montemor, "pH-sensitive polymeric particles with increased inhibitor-loading capacity as smart additives for corrosion protective coatings for AA2024," *Electrochimica Acta*, vol. 145, pp. 123–131, Nov. 2014.
- [264] G. Lefèvre, "In situ Fourier-transform infrared spectroscopy studies of inorganic ions adsorption on metal oxides and hydroxides." *Advances in colloid and interface science*, vol. 107, no. 2-3, pp. 109–23, Mar. 2004.
- [265] N. Kazuo, *Infrared and Raman Spectra of Inorganic and Coordination Compounds. Part A: Theory and Applications in Inorganic Chemistry.*, 6th ed. John Wiley & Sons: Hoboken, 2009.
- [266] C. Su and D. L. Suarez, "In situ infrared speciation of adsorbed carbonate on aluminum and iron oxides," no. 6, pp. 814–825, 1997.
- [267] T. Tanaka, Y. Kameshima, S. Nishimoto, and M. Miyake, "Determination of carbonate ion contents in layered double hydroxides by FTIR spectrometry," *Analytical Methods*, vol. 4, no. 12, p. 3925, Nov. 2012.
- [268] M. Jobbágy and A. E. Regazzoni, "Complexation at the edges of hydrotalcite: the cases of arsenate and chromate." *Journal of colloid and interface science*, vol. 393, pp. 314–8, Mar. 2013.
- [269] D. T. A. Amirudin, A. Amirudin, and D. Thierry, "Application of electrochemical impedance spectroscopy to study the degradation of polymer-coated metals," *Progress in Organic Coatings*, vol. 26, no. 3, pp. 1–28, 1995.
- [270] Y. Shao, C. Jia, G. Meng, T. Zhang, and F. Wang, "The role of a zinc phosphate pigment in the corrosion of scratched epoxy-coated steel," *Corrosion Science*, vol. 51, no. 2, pp. 371–379, 2009.

- [271] H. Weijde, *Impedance spectroscopy and organic barrier coatings; impossibilities*. Den Haag: Pasmass Offsetdrukkerij BV, 1996.
- [272] I. Klüppel, B. Schinkinger, and G. Grundmeier, “In situ electrochemical studies of forming-induced defects of organic coatings on galvanised steel,” *Electrochimica Acta*, vol. 54, no. 13, pp. 3553–3560, 2009.
- [273] F. Ganne, C. Cachet, G. Maurin, R. Wiert, E. Chauveau, and J. Petitjean, “Impedance spectroscopy and modelling of zinc deposition in chloride electrolyte containing a commercial additive,” *Journal of Applied Electrochemistry*, vol. 30, no. 6, pp. 665–673, 2000.
- [274] J.-B. Jorcin, M. E. Orazem, N. Pébère, and B. Tribollet, “CPE analysis by local electrochemical impedance spectroscopy,” *Electrochimica Acta*, vol. 51, no. 8-9, pp. 1473–1479, Jan. 2006.
- [275] N. LeBozec, D. Thierry, M. Rohwerder, D. Persson, G. Luckeneder, and L. Luxem, “Effect of carbon dioxide on the atmospheric corrosion of Zn-Mg-Al coated steel,” *Corrosion Science*, vol. 74, pp. 379–386, 2013.
- [276] F. Deflorian, L. Fedrizzi, and P. Bonora, “Determination of the reactive area of organic coated metals using the break-point method,” *Electrochimica Acta*, vol. 38, no. 12, pp. 1609–1613, 1993.
- [277] F. Mansfeld, “Discussion of “determination of the reactive area of organic coated metals: physical meaning and limits of the break-point method”, a comment on the paper by F. Deflorian et al.” *Electrochimica Acta*, vol. 39, no. 10, pp. 1451–1452, 1994.
- [278] A. Vu, B. Vuillemin, R. Oltra, and C. Allély, “Cut-edge corrosion of a Zn-55Al-coated steel: A comparison between sulphate and chloride solutions,” *Corrosion Science*, vol. 53, no. 9, pp. 3016–3025, Sep. 2011.
- [279] F. Thébault, B. Vuillemin, R. Oltra, C. Allely, and K. Ogle, “Reliability of numerical models for simulating galvanic corrosion processes,” *Electrochimica Acta*, vol. 82, pp. 349–355, Nov. 2012.
- [280] ———, “Modeling bimetallic corrosion under thin electrolyte films,” *Corrosion Science*, vol. 53, no. 1, pp. 201–207, Jan. 2011.
- [281] G. K. Glass and V. Ashworth, “The corrosion behavior of the Zn-mild steel galvanic cell in hot sodium bicarbonate solution,” *Corrosion Science*, vol. 25, no. 11, pp. 971–983, 1985.
- [282] M. Rohwerder and F. Turcu, “High-resolution Kelvin probe microscopy in corrosion science: Scanning Kelvin probe force microscopy (SKPFM) versus classical scanning Kelvin probe (SKP),” *Electrochimica Acta*, vol. 53, pp. 290–299, 2007.

- [283] M. Rohwerder, E. Hornung, and M. Stratmann, "Microscopic aspects of electrochemical delamination: an SKPFM study," *Electrochimica Acta*, vol. 48, no. 9, pp. 1235–1243, Apr. 2003.
- [284] A. de Vooy and H. van der Weijde, "Investigating cracks and crazes on coated steel with simultaneous SVET and EIS," *Progress in Organic Coatings*, vol. 71, no. 3, pp. 250–255, Jul. 2011.
- [285] E. A. Zdrachek, A. G. Karotkaya, V. A. Nazarov, K. A. Andronchyk, L. S. Stanishevskii, V. V. Egorov, M. G. Taryba, D. Snihirova, M. Kopylovich, and S. V. Lamaka, "H<sup>+</sup>-selective microelectrodes with optimized measuring range for corrosion studies," *Sensors and Actuators B: Chemical*, vol. 207, pp. 967–975, Feb. 2015.
- [286] A. Alvarez-Pampliega, M. Taryba, K. Van den Bergh, J. De Strycker, S. Lamaka, and H. Terryn, "Study of local Na<sup>+</sup> and Cl<sup>-</sup> distributions during the cut-edge corrosion of aluminum rich metal-coated steel by scanning vibrating electrode and micro-potentiometric techniques," *Electrochimica Acta*, vol. 102, pp. 319–327, Jul. 2013.
- [287] A. Rubin, R. Oltra, B. Vuillemin, and K. Ogle, "Impedance characterization of the electrochemical environment under a polymer film artificially delaminated," *Electrochimica Acta*, vol. 53, no. 22, pp. 6484–6488, Sep. 2008.
- [288] P. Lodi, K. Ogle, and A. Storhay, "Méthode d'analyse d'un échantillon métallique par dissolution de sa surface, et dispositif pour mise en oeuvre," 1992.
- [289] T. Vu, M. Mokaddem, P. Volovitch, and K. Ogle, "The anodic dissolution of zinc and zinc alloys in alkaline solution. II. Al and Zn partial dissolution from 5% Al-Zn coatings," *Electrochimica Acta*, vol. 74, pp. 130–138, Jul. 2012.
- [290] M. Voith, G. Luckeneder, and A. W. Hassel, "In situ identification and quantification in a flow cell with AAS downstream analytics," *Journal of Solid State Electrochemistry*, vol. 16, no. 11, pp. 3473–3478, Oct. 2012.
- [291] L. Bortels, J. Deconinck, and B. Van Den Bossche, "The multi-dimensional up-winding method as a new simulation tool for the analysis of multi-ion electrolytes controlled by diffusion, convection and migration. Part 1. Steady state analysis of a parallel plane flow channel," *Journal of Electroanalytical Chemistry*, vol. 404, no. 1, pp. 15–26, 1996.
- [292] J. Newman and K. Thomas-Alyea, *Electrochemical Systems*, 3rd ed. Wiley, 2004.
- [293] W. Kaim and J. Fiedler, "Spectroelectrochemistry: the best of two worlds." *Chemical Society reviews*, vol. 38, no. 12, pp. 3373–82, Dec. 2009.
- [294] R. Gale, *Spectroelectrochemistry: Theory and Practice*. New York: Plenum Press, 1988.

- [295] W. Kaim and A. Klein, *Spectroelectrochemistry*, Royal Society of Chemistry Publishing. Cambridge, 2008.
- [296] Y. Li, J.-B. He, M. Zhang, and X.-L. He, "Corrosion inhibition effect of sodium phytate on brass in NaOH media. Potential-resolved formation of soluble corrosion products," *Corrosion Science*, vol. 74, pp. 116–122, Sep. 2013.
- [297] Y.-H. Wang and J.-B. He, "Corrosion inhibition of copper by sodium phytate in NaOH solution: Cyclic voltabsorptometry for in situ monitoring of soluble corrosion products," *Electrochimica Acta*, vol. 66, pp. 45–51, Apr. 2012.
- [298] A. Bewick and K. Kunimatsu, "Infra red spectroscopy of the electrode-electrolyte interphase," *Surface Science*, vol. 101, no. 1-3, pp. 131–138, Dec. 1980.
- [299] X. Wang, M. Bernard, C. Deslouis, S. Joiret, and P. Rousseau, "A new transfer function in electrochemistry: Dynamic coupling between Raman spectroscopy and electrochemical impedance spectroscopy," *Electrochimica Acta*, vol. 55, no. 21, pp. 6299–6307, Aug. 2010.
- [300] C. Gabrielli and B. Tribollet, "A Transfer Function Approach for a Generalized Electrochemical Impedance Spectroscopy," *Journal of Electrochemical Society*, vol. 141, no. 5, pp. 1147–1157, 1994.
- [301] R. J. Madix, "Surface microcatalysis by MBRS: Molecular beam waveforms," *Surface Science*, vol. 45, no. 2, pp. 696–698, Oct. 1974.
- [302] G. Ertl, "Scattering of atomic and molecular beams at metal surfaces," *Surface Science*, vol. 89, no. 1-3, pp. 525–539, Jan. 1979.
- [303] C. Deslouis, M. Duprat, and C. Tulet-Tournillon, "The cathodic mass transport process during zinc corrosion in neutral aerated sodium sulphate solutions," *Journal of Electroanalytical Chemistry and Interfacial Electrochemistry*, vol. 181, no. 1-2, pp. 119–136, Dec. 1984.
- [304] M. N. Hull, J. E. Ellison, and J. E. Toni, "The Anodic Behavior of Zinc Electrodes in Potassium Hydroxide Electrolytes," *Journal of The Electrochemical Society*, vol. 117, no. 2, p. 192, Feb. 1970.
- [305] D. Mercier, Q. Van Overmeere, R. Santoro, and J. Proost, "In-situ optical emission spectrometry during galvanostatic aluminum anodising," *Electrochimica Acta*, vol. 56, no. 3, pp. 1329–1336, Jan. 2011.
- [306] J. O. Bockris, Z. Nagy, and A. Damjanovic, "On the Deposition and Dissolution of Zinc in Alkaline Solutions," *Journal of The Electrochemical Society*, vol. 119, no. 3, p. 285, Mar. 1972.

- [307] Y.-C. Chang, "A kinetic model for the anodic dissolution of zinc in alkaline electrolyte with sodium metasilicate additions," *Electrochimica Acta*, vol. 41, no. 15, pp. 2425–2432, 1996.
- [308] V. Muralidharan and K. Rajagopalan, "Kinetics and mechanism of corrosion of zinc in sodium hydroxide solutions by steady-state and transient methods," *Journal of Electroanalytical Chemistry*, vol. 94, pp. 21–36, 1978.